A study of the Hercules dwarf spheroidal galaxy

Adén, Daniel

2011

Daniel Adén

A study of the Hercules dwarf spheroidal galaxy

Daniel Adén
Department of Astronomy and Theoretical Physics
Lund Observatory, Lund University, 2011

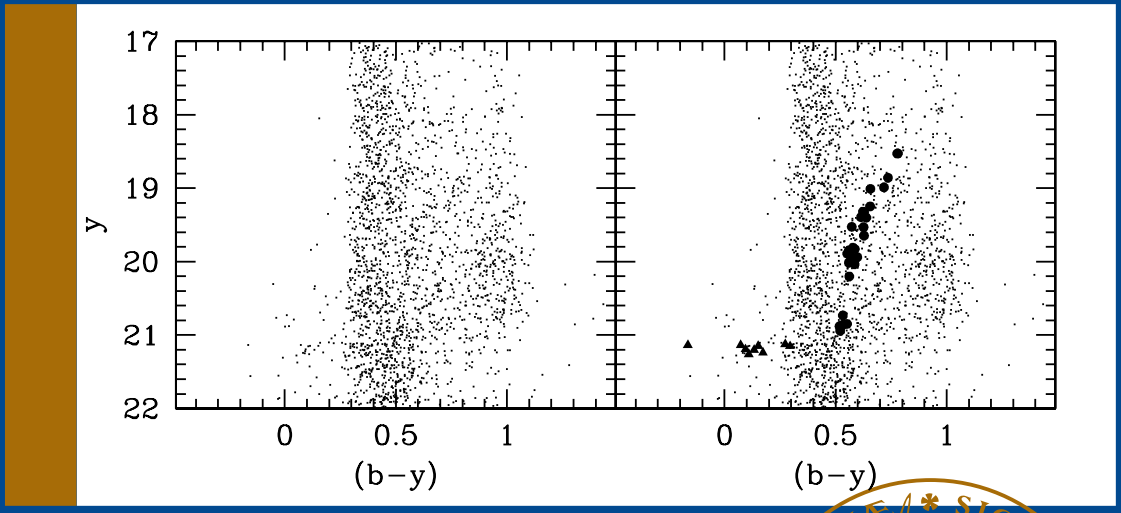

A study of the Hercules dwarf spheroidal galaxy

A study of the Hercules dwarf spheroidal galaxy

Daniel Adén

Lund Observatory
Department of Astronomy and Theoretical Physics
Lund University
Sweden

Thesis for degree of Doctor of Philosophy

Thesis advisors:
Sofia Feltzing, Professor
Ingemar Lundström, Docent
Thomas Bensby, Ph.D

To be presented with the permission of the Faculty of Science of Lund University, for public criticism in the Lundmark lecture hall (Lundmarksalen) at the Department of Astronomy and Theoretical Physics on Wednesday, the 6th of April, 2011 at 10.15.

Faculty Opponent

Professor Scott Trager
Kapteyn Astronomical Institute
University of Groningen

Evaluation Committee

Johan Rathsman
Department of Astronomy and Theoretical Physics
Lund University

Ulrike Heiter
Department of Astronomy and Physics
Uppsala University

Anja Andersen
Dark Cosmology Center
University of Copenhagen

Cover: Colour-magnitude diagrams towards the Hercules dSph galaxy. · indicate all stars towards the Hercules in a $\sim 0.5 \times 0.5$ arcmin field of view. • and solid triangles are stars identified as red-giant branch and horizontal branch members, respectively.

LUNFD6/(NFAS-1040)/1-130/(2011)

ISBN 978-91-7473-098-2
Printed by Wallin & Dalholm Digital AB, Lund 2011

Organization	Document name
LUND UNIVERSITY Dept. of Astronomy & Theoretical Physics Lund Observatory Box 43 SE-221 00, Lund, Sweden	DOCTORAL DISSERTATION
	Date of issue April 6, 2011
	Sponsoring organization

Author(s)
Daniel Adén

Title and subtitle

A study of the Hercules dwarf spheroidal galaxy

Abstract

Parts of large spiral galaxies, such as the Milky Way and Andromeda, are believed to have formed from the accretion of several smaller galaxies. Remnants of this chaotic merging era, such as dwarf spheroidal (dSph) galaxies, are visible in the outskirts of large galaxies. dSph galaxies are characterized by their low luminosity, low surface brightness and high fraction of dark matter. Determining the properties, such as mass, luminosity and metallicity, of the dSph galaxies provides key information in our understanding of galaxy formation and evolution.

In this thesis, we combine Strömgren photometry with low and high resolution spectroscopy, of the recently discovered Hercules dSph galaxy, to provide information about the evolutionary state of the stars and their radial velocities and metallicities. This enables us to select a clean sample of red-giant branch stars that belong to the Hercules dSph galaxy.

Based on the stars identified as members of the Hercules, we find: 1) a galaxy mass that is significantly lower than previous estimates: 2) an abundance trend such that [Ca/Fe] is higher for more metal-poor stars, and lower for more metal-rich stars. This trend suggests an early rapid enrichment through supernovae type II: 3) a tentative evidence for a velocity gradient in our kinematic data.

Additionally, we provide a study of the Draco, Sextans and UMaII dSph galaxies using Strömgren photometry. This enables us to establish a new metallicity calibration, based on [Fe/H] determined from high-resolution spectroscopy, from which we derive metallicity distribution functions for the Draco, Sextans and UMaII dSph galaxies.

Key words: Galaxies: dwarf - Galaxies: evolution - Galaxies: individual: Hercules - Galaxies: kinematics and dynamics - Stars: abundances

Classification system and/or index termes (if any):

Supplementary bibliographical information:		Language
ISSN and key title:		ISBN 978-91-7473-098-2
Recipient's notes	Number of pages 130	Price
	Security classification	

To Yvonne, Curt, Linda and Mari

This thesis is based on the following publications:

i **A photometric and spectroscopic study of the new dwarf spheroidal galaxy in Hercules. Metallicity, velocities, and a clean list of RGB members.**

D. Adén, S. Feltzing, A. Koch, M. I. Wilkinson, E. K. Grebel, I. Lundström, G. F. Gilmore, D. B. Zucker, V. Belokurov, N. W. Evans, D. Faria
Astronomy & Astrophysics, 2009, 506, 1147

ii **A New Low Mass for the Hercules dSph: The End of a Common Mass Scale for the Dwarfs.**

D. Adén, M. I. Wilkinson, J. I. Read, S. Feltzing, A. Koch, G. F. Gilmore, E. K. Grebel, I. Lundström
Astrophysical Journal, 2009, 706, L150

iii **An abundance study of red-giant-branch stars in the Hercules dwarf spheroidal galaxy**

D. Adén, K. Eriksson, S. Feltzing, E. K. Grebel, A. Koch, M. I. Wilkinson
Astronomy & Astrophysics, 2011, 525, 153

iv **An analysis of classical and ultra-faint dSph galaxies using Strömgren photometry**

D. Adén, S. Feltzing, G. F. Gilmore, M. I. Wilkinson
Astronomy & Astrophysics, in preparation.

Publications and conference proceedings not included in this thesis:

i **Chemical evolution of the Galactic bulge as traced by microlensed dwarf and subgiant stars. Detailed abundance analysis of OGLE-2008-BLG-209S**

T. Bensby, J. A. Johnson, J. Cohen, S. Feltzing, A. Udalski, A. Gould, W. Huang, I. Thompson, J. Simmerer, **D. Adén**
Astronomy & Astrophysics, 2009, 499, 737

ii **OGLE-2009-BLG-076S: The Most Metal-Poor Dwarf Star in the Galactic Bulge**

T. Bensby, S. Feltzing, J. A. Johnson, A. Gal-Yam, A. Udalski, A. Gould, C. Han, **D. Adén**, J. Simmerer
Astrophysical Journal, 2009, 699, 174

iii **Complexity in small-scale dwarf spheroidal galaxies**

A. Koch, **D. Adén**, E. K. Grebel, S. Feltzing
Astronomische Nachrichten, 2009, 330, 675

iv **Chemical evolution of the Galactic bulge as traced by microlensed dwarf and subgiant stars. II. Ages, metallicities, detailed elemental abundances, and connections to the Galactic thick disc**

T. Bensby, S. Feltzing, J. A. Johnson, A. Gould, **D. Adén**, M. Asplund, J. Meléndez, A. Gal-Yam, S. Lucatello, H. Sana, T. Sumi, N. Miyake, D. Suzuki, C. Han, I. Bond, A. Udalski
Astronomy & Astrophysics, 2010, 512, 41

v **Chemical evolution of the Galactic bulge as traced by microlensed dwarf and subgiant stars. III. Detection of lithium in the metal-poor bulge dwarf MOA-2010- BLG-285S.**

T. Bensby, M. Asplund, J. A. Johnson, S. Feltzing, J. Meléndez, S. Dong, A. Gould, C. Han, **D. Adén**, S. Lucatello, A. Gal-Yam, I. Thompson, G. Burley
Astronomy & Astrophysics, 2010, 521, 57

vi **Elemental abundances in the Galactic bulge from microlensed dwarf stars**

T. Bensby, S. Feltzing, J. A. Johnson, A. Gould, H. Sana, A. Gal-Yam, M. Asplund, S. Lucatello, J. Meléndez, A. Udalski, D. Kubas, G. James, **D. Adén**, J. Simmerer
International Astronomical Union Symposium, 2010, 265, 346

vii **Chemical evolution of the Galactic bulge as traced by microlensed dwarf and subgiant stars. IV. Two bulge populations**

T. Bensby, **D. Adén**, J. Meléndez, A. Gould, S. Feltzing, M. Asplund, J. A. Johnson, J. C. Yee, J. Cohen, I. Thompson, S. Lucatello, A. Gal-Yam
Astronomy & Astrophysics, in preparation

x

Contents

Chapter 1

Introduction

Galaxies come in a wide range of masses and shapes. From the most massive spiral and elliptical galaxies with total masses of about 10^{13} solar masses ($M_{\odot}$), to the least massive spheroidally shaped dwarf galaxies with total masses as low as $10^{6} M_{\odot}$. The baryonic masses of the smallest galaxies can be less than $10^{4} M_{\odot}$ (e.g., Martin et al. 2008). It is still to be determined when the first galaxies formed, but a recent study by Lehnert et al. (2010) suggests that galaxy formation could take place less than 600 million years after the Big Bang.

One of the key questions in modern astronomy is the formation and evolution of galaxies. To a first approximation, a galaxy is a gravitationally bound system that consists of stars, gas and dust. Given the results from studies on galaxies over the past few decades, galaxies are now believed to also host a large amount of dark matter and, for the most massive galaxies, a super massive black hole in the centre (e.g., Ferrarese & Ford 2005). It was not until the 1920s that Edwin Hubble was able to determine that the Andromeda galaxy was indeed a neighbouring galaxy, and not a cloud of gas (Hubble 1929). Prior to that discovery, astronomers believed that the Milky Way was the only galaxy in the universe. Even though a large amount of galaxies have been observed to date, the Milky Way is still unique since we can study it and its satellite companions in great detail. Future telescopes and instruments will be able to probe neighbouring galaxies, and beyond, in greater detail. However, to date the Milky Way is our best test bed for detailed studies.

The formation scenario for galaxies has historically been classified into two main paths. The first was introduced by Eggen et al. (1962). Their paper had the title "Evidence from the motion of old stars that the galaxy collapsed". They describe the formation of a galaxy as a proto-galaxy that fall together out of intergalactic material. The galaxy either had an initial angular momentum or acquired it from the forces exerted on the galaxy by nearby

condensations. Globular clusters and stars formed from condensations as the material fell together. The radial collapse of the galaxy was stopped by the rotation while it continued in the z-direction and finally settled in a disk. The collapse was very rapid and only a few times 10^8 years was required for the gas to settle in a circular orbit. This early model of galaxy formation has become known as the monolithic model.

The second scenario, the hierarchical formation scenario, was introduced by Searle & Zinn (1978) and is often seen as a counter scenario to the monolithic model. The monolithic model predicts that an abundance gradient will arise and persist in the stellar component which formed out of the contracting gas cloud. By studying globular clusters in the outer halo Searle & Zinn (1978) found no such gradient. Based on this empirical finding they proposed a more chaotic origin for the Galaxy. In their final conclusion they propose that "*the gas from which the clusters and stars of the outer halo formed continued to fall into the galaxy for some time after the collapse of its central region had been completed*" and "*these clusters could have formed in a number of small proto-galaxies that subsequently merged to form the present galactic halo*". This suggests that smaller galaxies, orbiting the Milky Way, and stellar streams that we observe today are the remnants of a violent past that formed the Milky Way halo.

The hierarchical formation scenario has become part of the modern cosmological model based on the Λ cold dark matter (ΛCDM) paradigm which has been very successful in explaining large scale structures in the universe, such as the "Sloan Great Wall" (Gott et al. 2005). The ΛCDM simulations (Springel et al. 2005) have shown that signatures of the hierarchical formation scenario may be detected nowadays in the form of coherent stellar structures in the halo region of their host galaxies. One of the most spectacular pieces of evidence for these coherent stellar structures is the formation of stellar streams which are wrapped around the host galaxy, e.g., the Sagittarius stream (Ibata et al. 2001). Stellar streams have been detected not only in the Milky Way galaxy, but also in more distant galaxies (Martínez-Delgado et al. 2008). Additionally, to date, a wealth of satellite galaxies have been observed not only in the Milky Way, but also in neighbouring galaxies (see, e.g., Brasseur et al. 2011). The least massive of these satellite galaxies are known as dwarf spheroidal (dSph) galaxies.

1.1 Dwarf spheroidal galaxies

Given that larger galaxies are assumed, based on simulations and theoretical predictions (e.g., Gallagher & Wyse 1994; Moore et al. 1999), to host several dSph galaxies, the dSph galaxies are believed to be the most common type of galaxies.

High-resolution simulations of galaxy formation, with a cosmological model based on a ΛCDM dominated universe, predict the existence of an overabundance of self-bound cold dark matter halos which orbit within halos of larger galaxies such as the Milky Way

and the Andromeda (e.g., Moore et al. 1999). Until a few years ago, the low number of observed dSph galaxies in the vicinity of the Milky Way and Andromeda did seem to disagree with this model. Assuming that the predictions from the ΛCDM simulations are true, this shortage of observed dSphs has become known as "The missing satellite problem" (Klypin et al. 1999).

However, astrophysical processes, such as photo-ionization, could have prevented the dark matter halos from acquiring enough gas to form stars, and thus making them invisible from todays surveys due to the lack of light from stars (Benson et al. 2002). Photoionization prevents galaxy formation in low-mass dark matter halos by heating of the intergalactic medium and reducing the rate of radiative cooling of gas within haloes, which implies that some of the dSph galaxies must be very faint. This solution has also gained support through the discovery of the ultra-faint dSph galaxies in the recent years.

Over the past decade, the number of known dSph galaxies that are companions to the Milky Way has more than doubled thanks to large wide-field photometric surveys such as the Sloan Digital Sky Survey (e.g., Zucker et al. 2006; Belokurov et al. 2007). Since most of the new dSph galaxies were discovered using the SDSS, which primarily covers parts of the northern hemisphere, it seems likely that additional dSphs will be detected once the southern hemisphere is studied with similar surveys (e.g., Keller et al. 2007; Walsh et al. 2009). Additionally, more sensitive surveys in the future may be able to detect additional objects beyond the Milky Way (Tollerud et al. 2008). The recently discovered dSph galaxies are similar to the ones previously known in many of their properties, but the majority of them have significantly lower surface brightnesses. Some of the most extreme dSph galaxies have luminosities lower than the average globular cluster $L_{\odot} \sim 10^2 - 10^4$. This is the main reason why they have not been discovered earlier, even though they are fairly close. Distances are typically 30 to 150 kpc from the Milky Way. Since these dSph galaxies are much fainter than the already known dSphs, they are often referred to as the "ultra-faint dSph galaxies" and the previously discovered dSphs are referred to as "classical dSph galaxies" (see, e.g., Koch 2009). In general, dSph galaxies, both classical and ultra-faint, are characterised not only by their low luminosity, but also by a low total stellar mass and a spheroidal shape that is consistent with a pressure supported system (Grebel et al. 2003). This makes them similar to globular clusters. However, given that the dSph galaxies have a much lower surface brightness, they usually have a much larger scale length for the distribution of stars than the stellar clusters. Follow-up kinematic observations of the dSph galaxies have shown that these small galaxies have a surprisingly high velocity dispersions when compared to globular clusters (e.g., Simon & Geha 2007; Martin et al. 2007). Estimates of the total mass using the velocity dispersions, based on Jeans analysis for a pressure supported system, has shown that the dSph galaxies are the most dark matter dominated systems known (e.g., Mateo 1998).

A plot of the mass-to-light ratio vs. the luminosity for classical dSph galaxies shows a trend where the mass-to-light ratio increase with decreasing luminosity. The study by

Mateo et al. (1993) was the first to point out that the trend indicates that all of the dSph galaxies harbour the same amount of dark matter, $1-5\cdot10^7\ M_{\odot}$, within the volume of the visible galaxy. This hypothesis puts a constraint on the minimum mass of dSph galaxies, where the mass of the dark matter is the lower limit. However, with the discovery of the new ultra-faint dSph galaxies, this picture has changed. These low-luminosity dSphs have significantly smaller mass-to-light ratios, and hence much lower halo masses than the more luminous dSph galaxies. It appears that the new dSph galaxies occupy a new trend in the mass-to-light ratio vs. luminosity plot where the mass-to-light ratio saturates at a few to several hundreds for $M_V > -9$ (Simon & Geha 2007). Additionally, Strigari et al. (2008) found that the amount of dark matter within a fixed central radius, 300 parsec, is about the same ($\sim 10^7 M_{\odot}$) for all the dSph galaxies, including the recently discovered ultra-faint dSph galaxies. This result implies a central density for dark matter of $\sim 0.1 M_{\odot}\,\mathrm{pc}^{-3}$ in these galaxies. A possible explanation is that dSph galaxies inhabit the smallest dark matter haloes in the Universe. However, in a recent study (Adén et al. 2009b) it was concluded that the total mass of the Hercules dSph galaxy was significantly lower if foreground contaminating dwarf stars were removed. This suggests that the total mass within 300 parsec may differ between dSph galaxies.

Given that the dSph galaxies are believed to play a very important role in the formation of larger galaxies, the study of these objects is key to our understanding of galaxies in general.

1.2 Dwarf spheroidal galaxies and the Milky Way halo

As described above, the number of known satellites in the Milky Way has increased significantly over the past decade. With the discovery of these new ultra-faint dSph galaxies in the northern hemisphere, our understanding of the missing satellite problem is being rapidly revised. For the first time there is reason to believe that the missing satellites are not missing, but instead hiding just behind the detection limit of our telescopes and instruments and in areas of the sky not yet surveyed.

Thus, there is hope that these missing satellites will be detected by surveys such as the Large Synoptic Survey Telescope (LSST) and Sky Mapper as they will cover more sky and provide deeper observations of our surroundings (see, e.g., Tollerud et al. 2008, for a recent review on the prospects of future surveys).

Since the dSph galaxies may be one of the building blocks of the Milky Way halo population, as predicted by simulations of the hierarchical merging scenario, it is interesting to compare the metallicity distribution functions to that of the field halo stars. If stars had formed within the dSph galaxies prior to the time of the merging, then the metallicity-distribution functions of the Galactic halo and the dSphs should agree.

Using medium-resolution spectra of the Milky Way dSph galaxies Sculptor, Sextans, Fornax and Carina, Helmi et al. (2006) found a significant lack of stars with [Fe/H]~ -3 in the dSph galaxies when compared to the stars of the Galactic halo. In Fig. 1.1 we show the result from Helmi et al. (2006). Note the lack of dSph galaxy stars with [Fe/H]< -3. This shortage of very metal-poor stars implies that the progenitors of the Milky Way halo and the dSph galaxies must have been different (i.e. that any merging of the nearby dSph galaxies with properties similar to todays dSph galaxies as a mechanism for building up the Galactic halo is ruled out) (Helmi et al. 2006). This shortage of observed metal-poor stars in dSphs has become known as "The missing metal-poor stars".

In contrast to this result, Kirby et al. (2008) discovered many metal-poor ([Fe/H]< -3.0) stars in the recently discovered ultra-faint dSph galaxies. Based on these stars, they show that the shape of the metal-poor halo metallicity distribution function agrees with that of the recently discovered ultra-faint dSph galaxies.

In agreement with the result in Kirby et al. (2008), Schörck et al. (2009) derived the metallicity-distribution function for stars in the Galactic halo from a sample of 1638 metal-poor stars, selected from the Hamburg/ESO objective-prism survey (HES), taking into account the selection function employed in the HES to correct the observed metallicity-distribution function. They found that the metallicity-distribution function of the Galactic halo stars is statistically indistinguishable from that of the stellar population of the nearest dSph galaxies.

These discoveries support the hierarchical formation scenario of galaxy formation, and motivates more detailed abundance studies of the dSph galaxies.

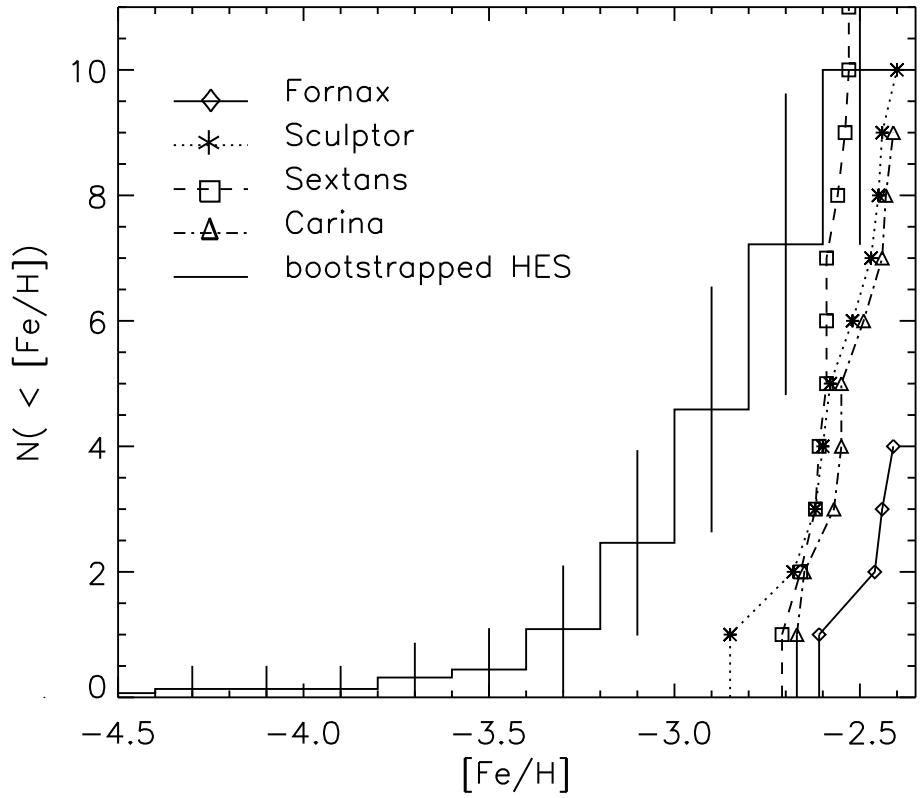

Figure 1.1: MDFs from Helmi et al. (2006) (their Fig. 3). The solid histogram indicates the MDF for halo stars from the Hamburg/ESO survey. The other lines represent the MDFs for the dSph galaxies, as indicated.

Chapter 2

Finding red-giant-branch stars in dSph galaxies

The line of sight towards dSph galaxies is often heavily contaminated with foreground stars, making it impossible to determine membership from the colour-magnitude diagram alone (e.g., Faria et al. 2007; Adén et al. 2009a). Even when radial velocities are added the selection remains uncertain, because the mean velocity of the dSph galaxy could coincide with the velocity of the disk stars in the Milky Way (e.g., Adén et al. 2009a). In Fig. 2.1 we show the colour-magnitude diagrams for all stars towards the Hercules and Draco dSph galaxies. The galactic longitude, and latitude, for Hercules and Draco are $l = 28.7°$, $b = 36.9°$, and $l = 86.4°$, $b = 34.7°$, respectively. Thus, an observation towards the Hercules dSph galaxy will contain more foreground dwarf stars than an observation towards the Draco dSph galaxy, since Hercules is more obscured by the Milky Way disk. We note that the RGB of the Hercules dSph is not distinguishable from the foreground contaminating dwarf stars that belong to the Milky Way. Additionally, in this figure, it is obvious that the Draco dSph galaxy is a much more populated galaxy than Hercules. However, even though the RGB of Draco is seen, it is still difficult to establish if the stars that fall on the apparent RGB are members of the dSph galaxy or not based on the colour-magnitude diagram alone.

2.1 Strömgren photometry

The Strömgren photometric system utilises three indices, $(b-y)$, m_1 and c_1, derived from the intermediate width filters u, v, b and y (Strömgren 1963). The $(b-y)$ index

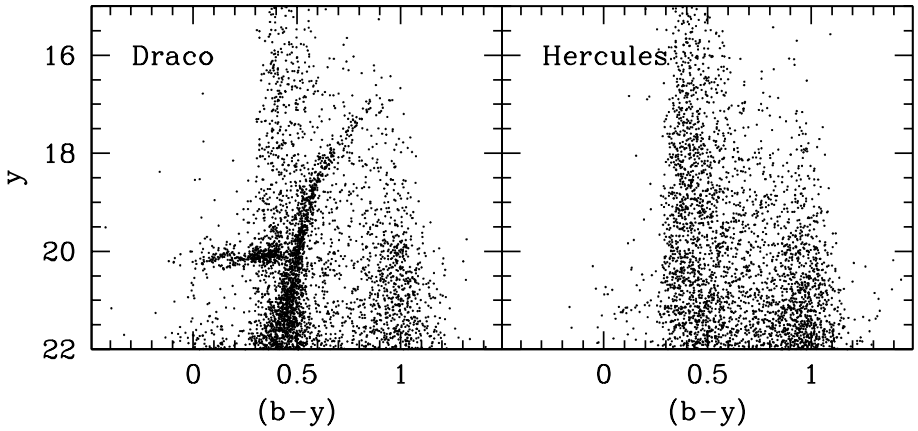

Figure 2.1: Colour-magnitude diagrams for all stars, in a $\sim 0.5 \times 0.5$ arcmin field of view, towards the Draco and Hercules dSph galaxies, as indicated.

is a relatively metallicity-insensitive colour index. The m_1 index is a measurement of the total intensity of the metal lines at $\lambda \sim 4110$ Å. The c_1 index is a measure of the Balmer discontinuity in a stellar spectrum and is defined as

$$c_1 = (u - v) - (v - b) \tag{2.1}$$

The strength of the Balmer discontinuity depends on the evolutionary stage of the star. Stars in a plot of $c_{1,0}$ vs. $(b - y)_0$ will therefore occupy different regions depending on their evolutionary stage. Thus, the c_1 index in the Strömgren system gives us the ability to disentangle the RGB and HB stars in a dSph galaxy from the foreground dwarf stars. Figure 2.2 shows which regions are occupied by stars at different evolutionary stages. This classification is adopted from Schuster et al. (2004). Additionally, for a more detailed definition of the RGB region, we use two 12 Gyr old isochrones with [Fe/H]$= -2.3$ and [Fe/H]$= 0.0$ by VandenBerg et al. (2006) and colour transformations by Clem et al. (2004).

As can be seen from Fig. 2.2, for giant stars, the c_1 index has a clear metallicity dependence. This is more pronounced for the reddest colours (i.e. the tip of the RGB). However, in spite of this, this index still provides a strong discriminant between giant and dwarf stars for cooler stars ($(b - y)_0 >\sim 0.55$).

Since the dwarf and RGB stellar sequences converge, in the $c_{1,0}$ vs. $(b-y)_0$ plane, around $(b - y)_0 \sim 0.5$ (compare Fig. 2.2) we can not distinguish between dwarfs and giants for colours bluewards ~ 0.5. Thus, we need to define a blue limit for stars that we identify as RGB stars. In Adén et al. (2009a) we analysed stars in the magnitude range $15 < V_0 < 18$

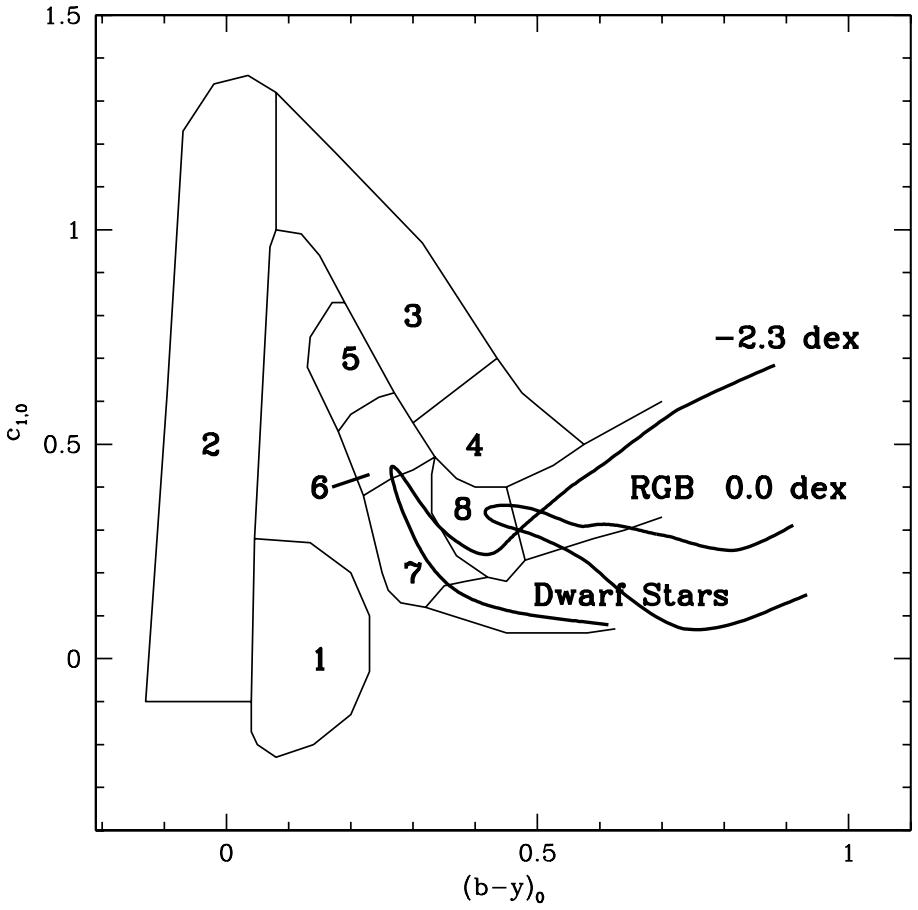

Figure 2.2: $c_{1,0}$ vs. $(b-y)_0$ diagram with evolutionary regions for metal-poor stars, as defined by Schuster et al. (2004). 1: the sub-luminous-blue-horizontal branch transition; 2: blue horizontal branch; 3: horizontal branch; 4: red-horizontal-branch-asymptotic-giant-branch transition; 5: blue stragglers; 6: blue-straggler-turnoff transition; 7: turnoff stars; 8: subgiant stars. The upper and lower thick solid lines indicate isochrones, for 12 Gyr old systems, by VandenBerg et al. (2006) with colour transformations by Clem et al. (2004). Their metallicities are -2.3 and 0.0 dex, respectively.

in $c_{1,0}$ vs. $(b-y)_0$. Stars fainter than $V_0 = 15$ are not saturated on the CCDs, and this magnitude range was bright enough not to contain any RGB stars in the Hercules dSph galaxy. We defined a line that follows the upper envelope of observed dwarf stars to separate the RGB stars from the dwarf stars in order to safely exclude any dwarf stars. In Adén et al. (2009a), no object bluer than this limit was considered as an RGB star since they have a high probability of belonging to the foreground dwarf contamination.

2.2 Radial velocities

Using radial velocity measurements to separate the stars belonging to a dSph galaxy from foreground stars has proven to be an efficient method for membership determination (see, e.g., Kleyna et al. 2002; Walker et al. 2006; Battaglia et al. 2010). The mean heliocentric velocity and internal velocity dispersion (σ) are determined, based on an initial sample of stars centred on the velocity peak for the system. Next, stars that deviate by more than 3σ from the heliocentric velocity are rejected from the sample as non-members. Finally, the procedure is repeated until no stars are rejected. The σ in the last iteration is defined as the velocity dispersion for the dSph galaxy, and the stars with radial velocities within 3σ are defined as member stars.

However, this method relies on the fact that the dSph galaxy has a different systemic velocity than the velocity distribution of the foreground dwarf stars belonging to the Milky Way. This is often, but not always, the case. The Hercules dSph galaxy has a systemic velocity that falls well within the velocity distribution of the foreground dwarf stars (compare Fig. 2.3). Thus making it difficult to rely on radial velocity measurements to separate the dSph galaxy from foreground stars. Hence, relying on the positions in a colour-magnitude diagram and radial velocity measurements for stars is not enough to identify RGB stars that are members of the Hercules dSph galaxy. In Fig. 2.3 we show the radial velocity distribution for ~ 100 stars towards the Hercules dSph galaxy, observed using the FLAMES spectrograph (Adén et al. 2009a), together with velocities from a Besançon model in the direction of Hercules. As can be seen, the velocity peak of the Hercules dSph galaxy lies within the radial velocity distribution of the Milky Way. A sample of member stars for the Hercules dSph galaxy, identified as members based on their radial velocity, is therefore likely to contain a non-negligible amount of foreground dwarf stars. In Adén et al. (2009a), we were able to get around this problem since we also had Strömgren photometry towards the Hercules (see Sect. 2.1). We found that about 30 per cent of the stars considered as members, based on the radial velocities, were in fact foreground contaminating (see Sect. 5.2 in Adén et al. 2009a).

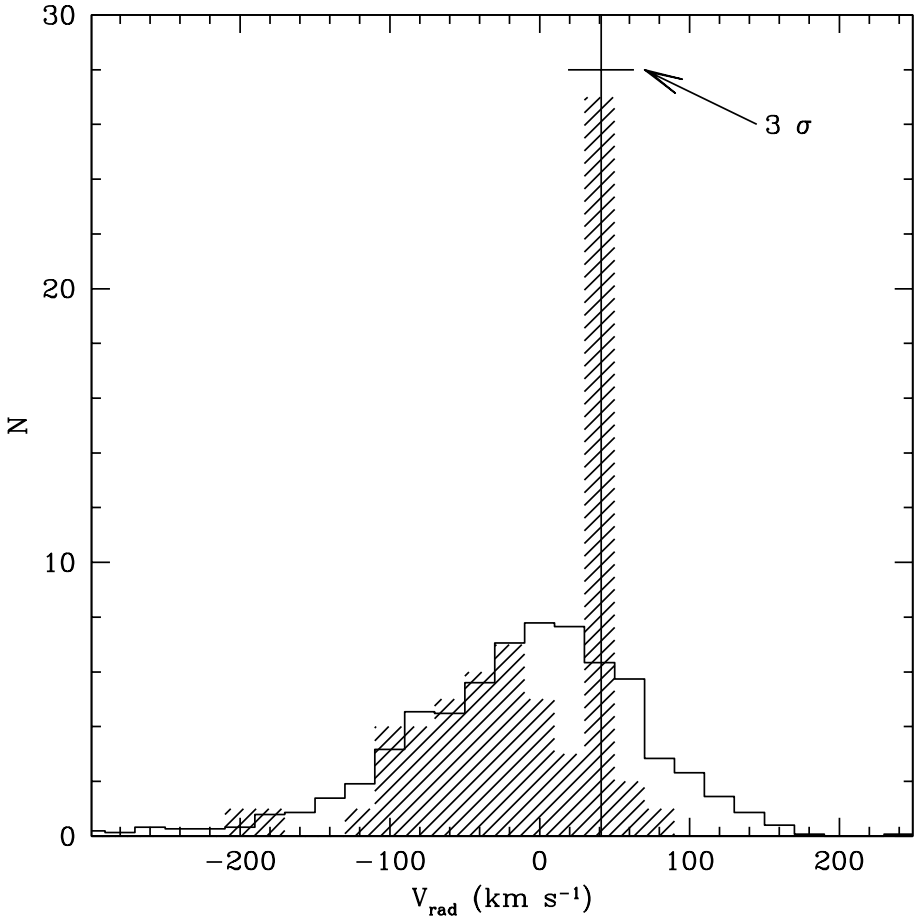

Figure 2.3: Distribution of radial velocities towards the Hercules dSph galaxy. The solid histogram shows the distribution of radial velocities from a Besançon model of the stars in the Milky Way in the direction of the Hercules dSph galaxy. The shaded histogram shows the observed distribution of radial velocities for $\sim$ 100 stars towards the Hercules dSph galaxy. The vertical solid line indicates the systemic velocity of the Hercules dSph galaxy. The horizontal solid line indicates $\pm 3\sigma$.

Chapter 3

Determining the metallicity

The metallicity distribution function (MDF) for dSph galaxies reflect their star formation histories. The mean metallicity for a dSph galaxy increases with increasing galaxy mass, since a deeper gravitational potential is able to sustain a larger amount of gas for star formation, as predicted by theory (e.g., Mateo 1998; Ferrara & Tolstoy 2000). Additionally, as described in Sect. 1.1, it is interesting to compare the MDFs for stars in the Milky Way with that of the dSph galaxies, since it may provide key information on how the dSph galaxies are accreted by larger galaxies. Since the average metallicity of a galaxy increases with time, as stars explode and pollute the interstellar medium with heavy elements, the stars at the metal-poor end of the distribution are likely to be related to the first stars formed in the dSph galaxy, given that these systems are old. This allows for a view of the physical processes and properties of the early universe.

The ability to estimate the metallicity for stars has improved significantly over the past few decades. The most obvious method to derive a value of [Fe/H] is to measure the equivalent width for iron lines through spectroscopy. However, when studying dSph galaxies, this method requires high-resolution spectroscopy of stars that often are very distant and thus faint. A competing method for the determination of [Fe/H] is to measure the equivalent width of the Ca II IR triplet lines (Alloin & Bica 1989). These absorption lines are, relative to iron lines, intrinsically strong and easily accessible. To date, there exists several calibrations that translates the strength of the Ca II IR triplet lines to [Fe/H] (e.g., Rutledge et al. 1997a; Starkenburg et al. 2010). Additionally, a spectrum, with a relatively low signal-to-noise level, of the wavelength region can provide a robust estimate of the radial velocity for the star (see, e.g., discussion in Adén et al. 2009a).

With the advent of multi-fibre spectrographs, it is now possible to cover hundreds of stars for abundance analysis in a reasonably short time span, if the stars are not too faint.

However, given that a photometric observation can cover a large area of the sky, relying on a calibration that translates photometric indices to an estimate of [Fe/H] is preferable in some studies.

In the following sections, we describe each of the three methods discussed above.

3.1 Using iron lines

The spectrum of a star contains a lot of information on the conditions in the atmosphere of the star. By measuring the equivalent width of the absorption lines from known elements and transitions, it is possible to determine fundamental stellar parameters for the atmosphere such as surface gravity, the effective temperature and elemental abundances (Gray 2005). For example, the equivalent width for an iron absorption line increases with increased iron abundance. The iron abundance is most often given relative to the sun using the following standard notation

$$[\mathrm{Fe/H}] = \log\left(\frac{\mathrm{N_{Fe}}}{\mathrm{N_H}}\right)_\star - \log\left(\frac{\mathrm{N_{Fe}}}{\mathrm{N_H}}\right)_\odot \tag{3.1}$$

where subscripts $\odot$ and $\star$ designate the sun and the star, respectively. [Fe/H] for the sun is thus defined to be 0.

Once the stellar parameters are known, it is possible to solve the radiative transfer equations, through a model atmosphere based on the stellar parameters, for the iron abundance of the star. The iron abundance that best reproduces the measured equivalent width is then chosen as [Fe/H]. This procedure is often iterated since the iron abundance is one of the parameters used when calculating the stellar model atmosphere. In Fig. 3.1b we show an example of a spectrum for an RGB star in the Hercules dSph galaxy. The signal-to-noise ratio is ~ 35 per pixel with a spectral resolution of R$\sim 20\,000$.

The method outlined above requires that it is possible to measure the equivalent width of the iron lines. However, in some cases, estimating the equivalent width can be difficult due to a low signal-to-noise ratio for the spectrum. Instead, it is possible to generate synthetic spectra with different values of [Fe/H]. Next, a χ^2-fitting routine can indicate which one of the synthetic spectra that best fits the observed spectrum. Recent applications of this technique includes Kirby et al. (2008); Adén et al. (2011).

Estimating the errors in [Fe/H] as derived using iron lines is difficult. One has to consider not only the uncertainties in the measurements of the equivalent widths, but also the uncertainties for the stellar parameters. However, if the signal-to-noise ratio for the spectrum is sufficiently high, the errors will be relatively small.

Estimating [Fe/H] for a star based on equivalent width measurements of iron lines is a

robust method. However, it requires a relatively high amount of photons from the star.

3.2 Using Ca II IR triplet lines

The Ca II IR triplet lines at $\lambda = 8498, 8542$ and 8662 Å are among the strongest features in the near-infrared for a stellar spectrum. Thus, the equivalent widths of these lines can be measured even for a relatively low-resolution spectrum with a modest signal-to-noise ratio (e.g., Rutledge et al. 1997a). Fortunately, the Ca II IR triplet lines are sensitive to the metallicity of a star (see, e.g., Alloin & Bica 1989; Rutledge et al. 1997a). In Fig. 3.1a we show an example of a spectrum, centred on the wavelength region for the Ca II IR triplet lines, for an RGB star in the Hercules dSph galaxy. The signal-to-noise ratio is ~ 30 per pixel with a spectral resolution of R$\sim$ 6 000. Even at this low resolution, and low signal-to-noise, the equivalent widths of the Ca II IR triplet lines are easily measurable.

In Adén et al. (2009a), we followed Rutledge et al. (1997b) in defining the line strength of the Ca II IR triplet lines as the weighted sum of the W, with lower weights for the weaker lines

$$\sum W = 0.5 \cdot W_1 + W_2 + 0.6 \cdot W_3 \tag{3.2}$$

where W_1, W_2 and W_3 are the widths of the individual Ca II IR triplet lines in the order of increasing wavelength.

As discussed, e.g., in Rutledge et al. (1997a), the strength of the Ca II IR triplet lines depend not only on metallicity but also on the surface gravity and effective temperature of the star. It is possible to remove the effect of gravity and temperature to first order by taking into account the position of the star on the RGB. This is done by defining the reduced W as

$$W' = \sum W + 0.64(\pm 0.02)(V - V_{HB}) \tag{3.3}$$

where $(V - V_{HB})$ is the difference between the V magnitude of the star and the V magnitude of the horizontal branch (V_{HB}). The final values of [Fe/H] in Adén et al. (2009a) were calculated using the calibration by Rutledge et al. (1997a) onto the metallicity scale of Carretta & Gratton (1997). The Rutledge et al. (1997a) calibration reads as follows

$$[\mathrm{Fe/H}]_{\mathrm{Ca\,II}} = -2.66(\pm 0.08) + 0.42(\pm 0.02)W' \tag{3.4}$$

and is valid down to at least -2.4 dex. Thus, [Fe/H] for more metal-poor stars as derived using this calibration is uncertain.

Estimating [Fe/H], of individual RGB stars, based on the strength of the Ca II IR triplet lines has been used extensively in the literature (e.g., Starkenburg et al. 2010; Battaglia et al. 2010). Especially for dSph galaxies since the RGB stars are often faint, and thus difficult for high-resolution, high signal-to-noise studies. However, even updated calibrations have difficulties estimating [Fe/H] for very metal-poor stars. The residuals may be as large as ~ 0.5 dex for stars with spectroscopic [Fe/H] below $\sim$–3.5 dex (Starkenburg et al. 2010). This since the calibrations often are based on RGB stars in globular clusters that are more metal-rich than the metal-poor stars discovered in dSph galaxies.

The uncertainties in [Fe/H], as derived using the Ca II IR triplet lines, depends not only on the uncertainties in the measurements of the equivalent widths, but also on the uncertainties in the calibration used to translate the Ca II IR triplet lines to [Fe/H].

3.3 Using photometry

As described in Sect. 2, the Strömgren photometric system provides an excellent index for the determination of the evolutionary stages of stars. Additionally, the Strömgren m_1 index provides a robust metallicity ranking for late-type stars (Eggen 1978; Bell & Gustafsson 1978). The m_1 index is a measure of the total intensity of the metal lines, centred on $\lambda \sim 4110$ Å, in a stellar spectrum and is defined as

$$m_1 = (v - b) - (b - y) \tag{3.5}$$

Thus, stars in a plot of m_1 vs. $(b-y)_0$ will therefore occupy different regions depending on their [Fe/H]. These regions are well approximated by straight lines. Several authors have derived calibrations that translates m_1 and $(b-y)_0$ to an estimate of [Fe/H] for giant stars (e.g., Bond 1980; Grebel & Richtler 1992; Hilker 2000; Ramírez & Meléndez 2004; Calamida et al. 2007, 2009). None of these are valid down to the very metal-poor stars, i.e., [Fe/H]~ -3, but stops where the globular clusters stops, -2.3 dex, as the globular clusters are the main calibrators.

In Fig. 3.2 we show m_1 vs. $(b - y)$ for dSph galaxy stars and Milky Way field stars. Additionally, in Fig. 3.2, we show iso-metallicity lines derived using our revised metallicity calibration (Adén et al., in preparation). We note that stars with different values of [Fe/H] indeed occupy different regions in this diagram, and that the revised calibration describes these regions well.

Many more calibrations are available for dwarf stars. A recent calibration is provided by Casagrande et al. (submitted), and a summary of available calibrations is given in Árnadóttir et al. (2010).

Estimating the errors in [Fe/H] as derived using photometry is similar to how the errors are determined using the Ca II IR triplet lines. However, instead of an uncertainty in the

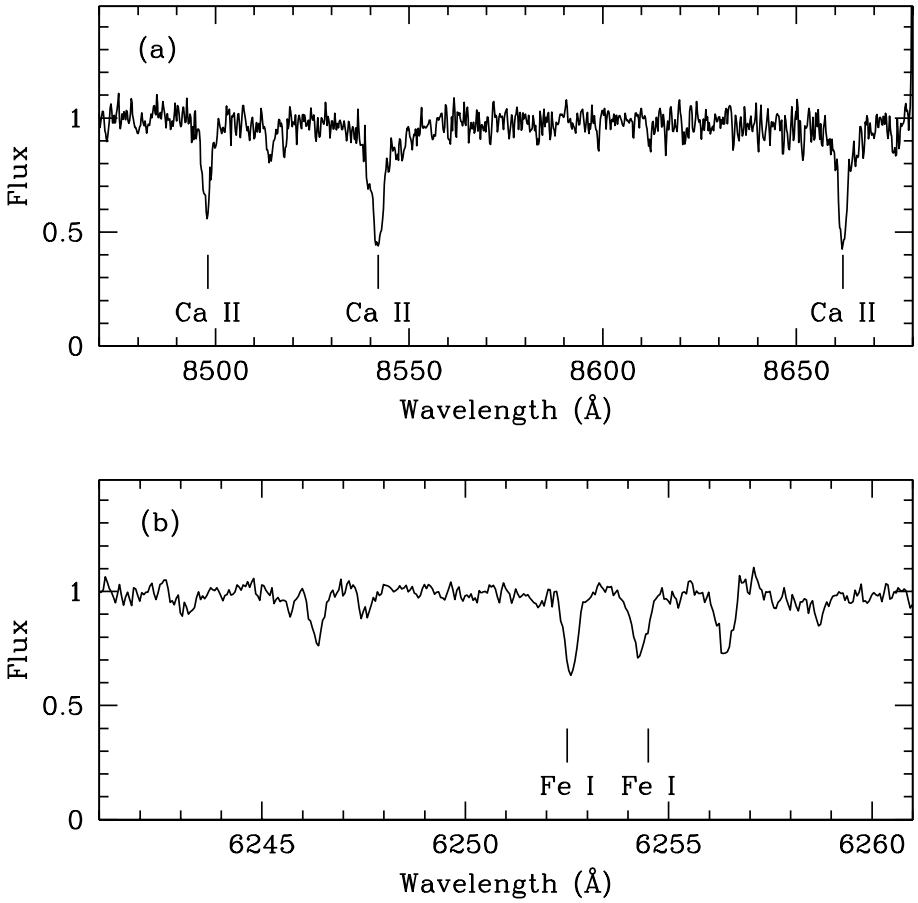

Figure 3.1: a) Portion of a stellar spectrum for an RGB star in the Hercules dSph galaxy. The three Ca II IR triplet lines are indicated by vertical lines. Spectral resolution is $\sim$ 6 000. **b)** Portion of a stellar spectrum for an RGB star in the Hercules dSph galaxy. Fe I lines used in the analysis in Adén et al. (2011) are indicated by vertical lines. Spectral resolution is $\sim$ 20 000.

measurement of the equivalent widths, the internal errors originate from the uncertainty in the photometry. Thus, it is important to have deep photometry, i.e., small photometric errors, when determining [Fe/H] using photometry.

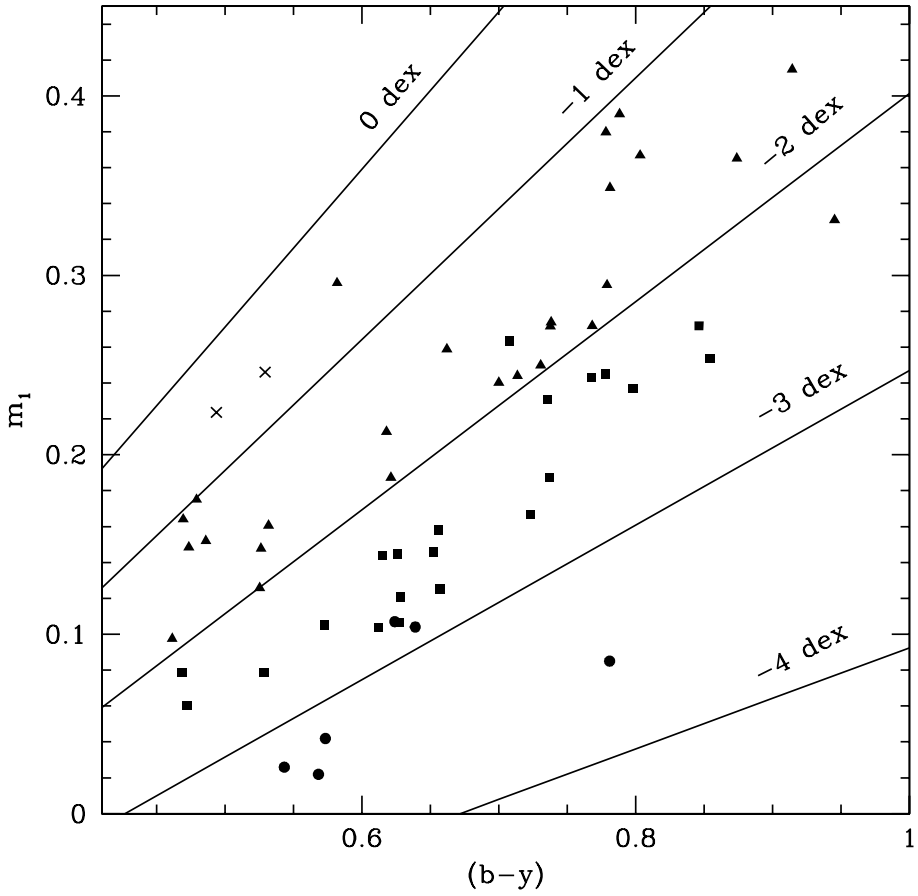

Figure 3.2: m_1 vs. $(b-y)$ for dSph galaxy stars and Milky Way field stars. The solid lines are iso-metallicity lines based on our revised calibration (Adén et al., in preparation) with metallicities as indicated. • are stars with spectroscopic [Fe/H]< -3. Solid rectangles indicate stars with spectroscopic -3 <[Fe/H]< -2. Solid triangles indicate stars with spectroscopic -2 <[Fe/H]$<$ -1 and *times* mark stars with spectroscopic -1 <[Fe/H]< 0

3.4 A metallicity calibration for Strömgren photometry

One of the difficulties when deriving a new metallicity calibration is to define the sample on which the calibration is based on. This sample will not only define the constants in the calibration, but also define for which range that the calibration is valid. For example, a calibration based on metal-rich stars only will only be valid for metal-rich stars. In

Adén et al. (2011) we derived a simple metallicity calibration that translates the Strömgren m_1 index to an estimate of [Fe/H] for metal-poor RGB stars such as those present in dSph galaxies. In order to increase the range for which the calibration was valid, we included spectroscopic [Fe/H] derived from high-resolution spectra available for stars in the Draco (Cohen & Huang 2009; Shetrone et al. 2001), Sextans (Shetrone et al. 2001), UMaII (Frebel et al. 2010) and Hercules Adén et al. (2011), and combined these data with our own Strömgren photometry where available. We found that, for these stars, the relation between [Fe/H], as derived from high-resolution spectroscopy, and m_1 was sufficiently linear for a calibration used for chemical labeling.

However, given that the metallicity of a stars is also colour dependant we have revised our calibration to include the Strömgren colour $(b-y)$. We note that the colour $(v-y)$ is more metallicity dependant that $(b-y)$ (e.g., Calamida et al. 2009), but given that it includes the filter v, which has a much lower transmission than both b and y, we chose $(b-y)$ for increased accuracy in the derived values.

In Adén et al. (in preparation), we followed Grebel & Richtler (1992) and used the relation

$$m_1 = \alpha + \beta \cdot (b-y) + \gamma \cdot [\mathrm{Fe/H}] + \delta \cdot (b-y) \cdot [\mathrm{Fe/H}] \tag{3.6}$$

to translate the Strömgren m_1 and $(b-y)$ index to an estimate of [Fe/H] based on photometry, [M/H]. Thus, the task was to determine the constants α, β, γ and δ.

For the calibration, we used the same set of stars for dSph galaxies as in Adén et al. (2011). In total, this gave us 29 dSph galaxy RGB stars for the calibration. Additionally, in order to increase the [Fe/H] calibration range and to increase the accuracy and precision of the multi-linear regression, we added 30 Milky Way RGB field stars from Cayrel et al. (2004) and Gratton et al. (1999) to the sample.

Given that most of the field stars are inside the dust disk of the Milky Way, we reduced the extinction (e.g., Beers et al. 2002; Árnadóttir et al. 2010) according to their position in the galaxy using

$$E(B-V) = \left(1 - e^{-|d \sin b|/h}\right) \cdot E(B-V)_{LOS} \tag{3.7}$$

where $E(B-V)_{LOS}$ is the full extinction along the line of sight (LOS), as determined from Schlegel et al. (1998), d is the distance to the star, b is the galactic latitude and h is the scale height of the Milky Way disk. We adopted a scale height of 125 kpc from Beers et al. (2002), and the distances from the Hipparcos catalogue (Perryman et al. 1997). Finally, we used a multilinear regression to solve Eq. 3.6 for α, β, γ and δ.

Given the amount of data required for a calibration (photometry, spectroscopy and a relation) it is difficult to define the error in [Fe/H] as determined using the calibration. In Adén et al. (in preparation) we used the residuals from the calibration to define the error.

The standard deviation for the residuals was $\sigma = 0.28$ dex. Thus, we adopted this error as the uncertainty in [Fe/H] as derived using the calibration.

To test if our calibration was valid for an independent sample, and to make sure that our errors were not underestimated, we applied our calibration on the stars in a recent study by Lind et al. (2010). They studied the metal-poor globular cluster NGC6397. Using high-resolution spectra, obtained with the FLAMES/UVES spectrograph, they determined [Fe/H] based on measurements of the equivalent widths of iron lines for 21 RGB stars. We found that the agreement, between [Fe/H] determined by their spectroscopy and our calibration, was very good, with no significant trend in the colours $(b - y)_0$ and $(v - y)_0$. The offset was $[\mathrm{Fe/H}]_{\mathrm{Lind}} - [\mathrm{M/H}] = -0.02$ with a standard deviation of about 0.05 dex. This is well within our error-bars for the new metallicity calibration. Thus, we concluded that our calibration was working as intended and that our errors were not underestimated.

3.5 Metallicity distribution functions

In Adén et al. (in preparation) we provide a new Strömgren metallicity calibration (see Sect. 3.4 in this thesis). [Fe/H] as determined using this calibration will henceforth be denoted [M/H]. This since the Strömgren m_1-index measures the total intensity of metal lines, and not only the intensity from iron lines. This calibration is formally valid for stars with $-3.3 <$[Fe/H]< -0.7. In Fig. 3.3 we show the MDFs for the Draco, Sextans and Hercules dSph galaxies, as derived using our metallicity calibration. We note that a small fraction of stars have [M/H] below or above the region for which the calibration is valid. However, these stars are included in the analysis as an extrapolation. In agreement with the metallicity-luminosity relation (e.g., Mateo 1998; Kirby et al. 2011), Hercules peaks at a lower [M/H]. The MDF for the Draco and Sextans dSph galaxies are similar in terms of peak value and the spread for [M/H]. They both appear to have a much wider spread in [M/H] than the Hercules dSph galaxy. However, we find that the MDF for the Draco dSph galaxy appears slightly more symmetric than the MDF for Sextans. i.e., the MDF for the Draco resembles a normal distribution more than the MDF for Sextans. The sharp peak, and change in slope on the metal poor end, for the Hercules dSph galaxy could be associated with a scenario where the Hercules has been able to access an additional supply of gas during its star formation (see, e.g., Kirby et al. 2011, for a discussion on chemical evolution models). On the other hand, the symmetry of the Draco MDF could be indicative of an association with a leaky box model. The dSph galaxy, in such a theoretical model, is allowed to lose gas, but never to acquire new gas for stars formation (see, e.g., Kirby et al. 2009, for a discussion on the leaky box model).

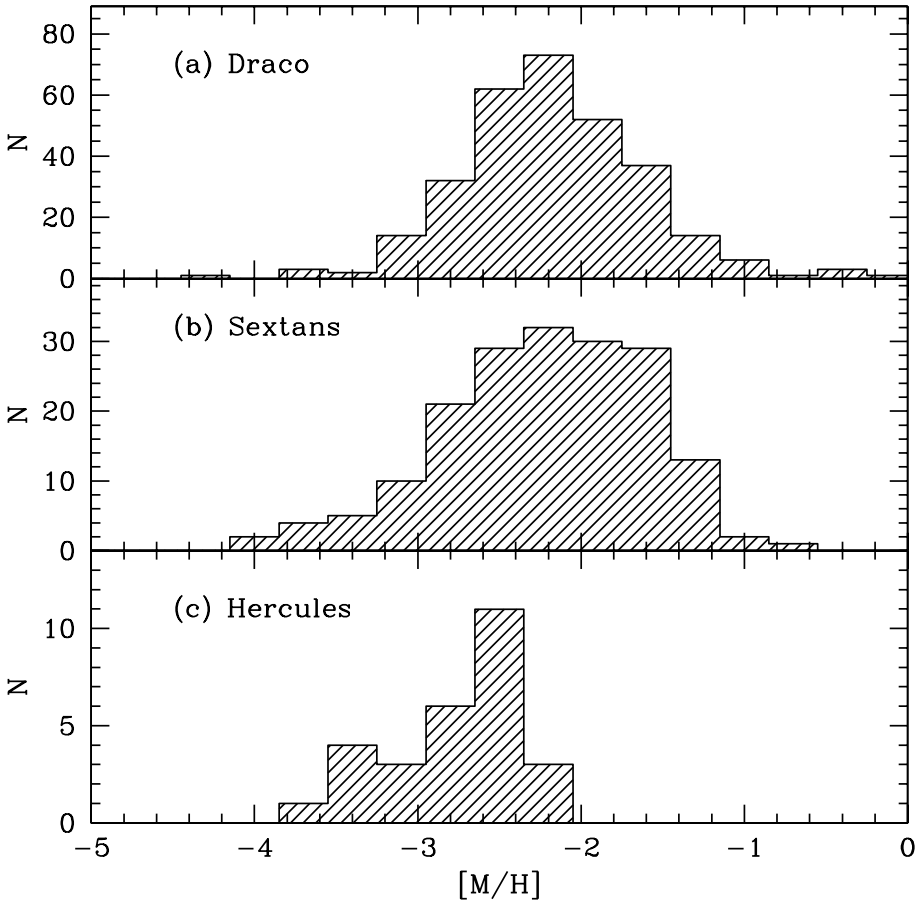

Figure 3.3: Metallicity distribution functions for the Draco, Sextans and Hercules dSph galaxies, as indicated.

Chapter 4

The mass of a dSph galaxy

Knowledge of dSph masses is essential for comparison with cosmological simulations of galaxy formation. Good mass estimates help us to establish whether the paucity in the number of observed systems (a few tens) to the number of predicted satellite haloes (several hundreds) represents a fundamental failure of our cosmological model (e.g. Moore et al. 1999), or whether it is simply telling us that galaxy formation is inefficient on small scales (e.g. Read et al. 2006). Recent studies have suggested that the dSph galaxies share a common mass within a certain radius (Walker et al. 2007; Strigari et al. 2008; Walker et al. 2009). If confirmed, this would be an important clue to the processes which regulate the formation of the lowest luminosity galaxies.

All mass estimates implicitly assume that contamination of the kinematic sample by foreground stars is negligible, and that the system is in (or close to) virial equilibrium. Since the mass of an equilibrium stellar system is proportional to its velocity dispersion squared, an over-estimate of the velocity dispersion will result in an inflated mass estimate.

Under the assumption that the system is in dynamical equilibrium, is spherically symmetric, has an isotropic velocity distribution, and a flat velocity dispersion profile, the Jeans equation for the mass distribution (Eq. 4.215 in Binney & Tremaine 2008) becomes:

$$\sigma_v^2 \frac{d\,\nu(r)}{dr} = -\frac{\nu(r)\,G\,M(r)}{r^2} \tag{4.1}$$

where r is the three-dimensional distance from the centre of the galaxy, $\nu(r)$ is the deprojected stellar density profile and $M(r)$ is the enclosed mass. Thus, the total mass, as derived using a stellar density profile that follows a Plummer or an exponential profile, is proportional to the velocity dispersion squared. In Adén et al. (2009a) we emphasised the importance of weeding out foreground contaminating dwarf stars when observing

dSph galaxies such as the Hercules, since its systemic velocity coincides with the bulk motion of dwarf stars in the Milky Way disk. For comparison, in Adén et al. (2009a), we derived the velocity dispersion for the Hercules dSph galaxy without the knowledge of the evolutionary stage for the stars as provided by the Strömgren photometry. Thus, the membership identification for this comparison was based on the location of the stars in the colour-magnitude diagram, and their radial velocities only. We found that the velocity dispersion was twice as large as for the clean sample, since many foreground contaminating dwarf stars were included in the calculation of the velocity dispersion. Given that the total mass is proportional to the velocity dispersion squared, this has a significant impact on the result. In Fig. 4.1 we show the probability distribution for the galaxy mass within the central 300 pc, based on both the clean and contaminated samples.

Our clean revised velocity dispersion implies a mass within the inner 300 pc (M_{300}) of only $1.9^{+1.1}_{-0.8} \times 10^6\, M_\odot$. This indicates that Hercules falls considerably below the "common mass scale" for dSphs as presented by Strigari et al. (2008). They suggests that all observed dSph galaxies have masses of about $\sim 10^7 M_\odot$ within a fixed radius of 300 pc.

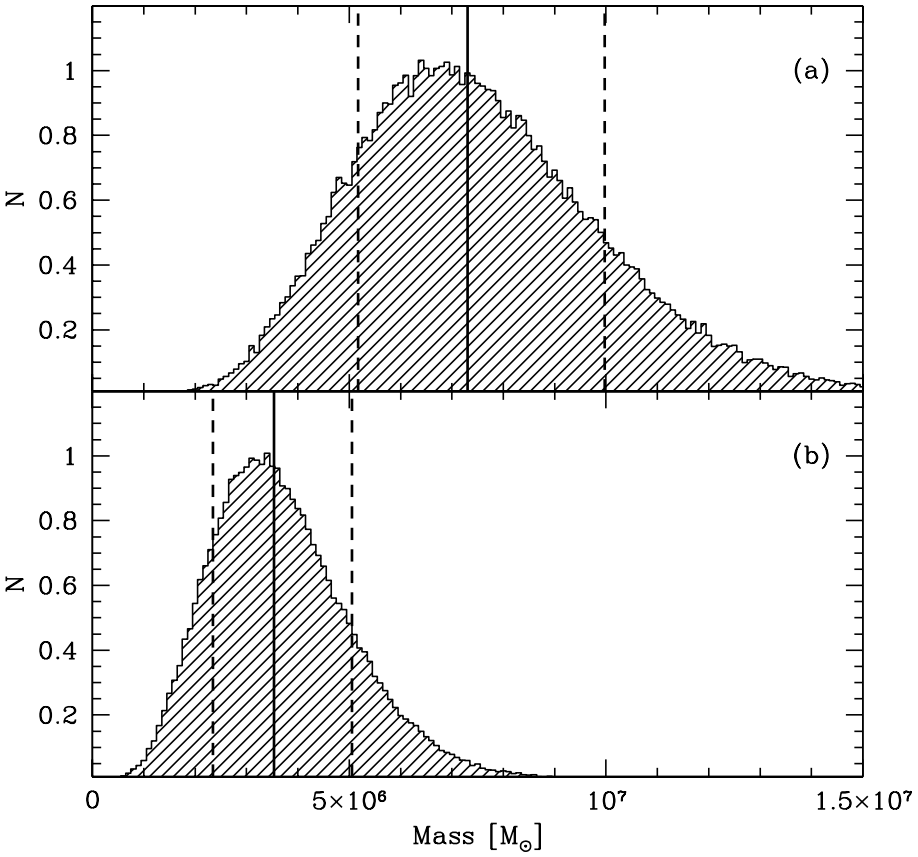

Figure 4.1: Probability distribution of the total mass, within the central 300 pc, for the Hercules dSph galaxy. Solid lines indicate the median and the dashed lines indicate the 1σ limits. **(a)** Based on a velocity dispersion for a sample of stars contaminated with foreground dwarf stars. **(b)** Based on a velocity dispersion for a sample of stars with Hercules RGB stars only.

Chapter 5

Summary and out-look

Given that the dSph galaxies are believed to play such an important role in the formation of large galaxies, the study of these galaxies has accelerated during the last decade. New telescopes and instruments are continuously pushing the boundary for the detection limit, and thus several new ultra-faint dSph galaxies have been discovered during the past few years and more will likely follow. The major concern to date regarding the dSph galaxies are the discrepancies between observations and theoretical predictions. With the advent of advanced cosmological simulations of galaxy formation, such as the ΛCDM simulations, the residuals between theory and observations can be studied in greater detail. For example, the missing satellite problem has been rapidly revised with the discovery of the ultra-faint dSph galaxies in the Milky Way. However, there are still a lot of missing satellites in the vicinity of the Milky Way. Future surveys that target the southern hemisphere will most likely detect additional dSph galaxies. Follow-up observations of these objects will benefit from the studies available to date of the ultra-faint and classical dSph galaxies in the northern hemisphere.

Knowledge of dSph galaxy masses is essential for comparison with cosmological simulations of galaxy formation. Good mass estimates help us to establish whether the missing satellite problem represents a fundamental failure of our cosmological model, or whether it is simply telling us that galaxy formation is inefficient on small scales. Additionally, given that the dSph galaxies are being considered as test beds for direct studies of dark matter, accurate determinations of the properties of dSph galaxies are more important than ever. However, determining the mass for an object that is barely visible is difficult. For robust mass estimates, several stars with radial velocity measurements are required and the structural parameters of the dSphs have to be determined. Given the uncertainty to date on the properties of the ultra-faint dSph galaxies, and the low number of member stars identified, mass estimates for these objects will most likely be revised as new and

improved observations are carried out.

Determining the metallicity for stars has improved significantly over the past few decades. Even though measuring the equivalent widths of the iron lines is the most reliable method, competing methods are still being developed. The Ca II IR triplet lines are among the strongest features in a near-infrared spectrum. Thus, estimating [Fe/H] based on these lines is favourable given that it requires less exposure time than if iron lines are measured. The Strömgren m_1 index is a measure of the total intensity of metal lines at about $\lambda \sim 4110$ Å. Thus, a photometric observation with the Strömgren filters may provide an estimate of [Fe/H] for thousands of stars. However, as discussed in this thesis. Estimating [Fe/H] from anything other than the iron lines requires a calibration. Future detailed elemental abundance analysis of dSph galaxy stars will assist in providing calibrations of higher accuracy and precisions than the calibrations applied today. Indeed, studies of the dSph galaxies will most likely yield additional very metal-poor stars that will expand the metallicity range for which new calibrations are valid.

Chapter 6

The Papers

This chapter provides a brief description of the four papers on which this thesis is based. In addition to describing the paper content, I describe my contribution to each of the papers, both in doing the research and the analysis and in writing the papers.

Paper I: A photometric and spectroscopic study of the new dwarf spheroidal galaxy in Hercules. Metallicity, velocities, and a clean list of RGB members.

D. Adén, S. Feltzing, A. Koch, M. I. Wilkinson, E. K. Grebel, I. Lundström, G. F. Gilmore, D. B. Zucker, V. Belokurov, N. W. Evans, D. Faria
Astronomy & Astrophysics, 2009, 506, 1147

In Paper I we combine Strömgren photometry and FLAMES multi-fibre spectroscopy to provide information about the evolutionary stage of the stars and their radial velocities. Based on this information, we provide a clean sample of RGB stars in the Hercules dSph galaxy. With this clean sample, we derive the velocity dispersion and the metallicity for the Hercules. We find that it is of the outmost importance to get rid of the foreground contamination of Milky Way dwarf stars for the derivation of the velocity dispersion. We show that it is difficult to achieve this without the knowledge of the evolutionary stage of the stars.

The photometric observational data, and subsequent analysis, was obtained and performed by me. Mark Wilkinson supplied the spectroscopic data. However, I analysed it. The interpretation of the analysis was carried out by me in collaboration with the co-authors. All of the text was written by me with the co-authors as advisors, except for the introduction that was mainly written by Eva Grebel.

Paper II: A New Low Mass for the Hercules dSph: The End of a Common Mass Scale for the Dwarfs.

D. Adén, M. I. Wilkinson, J. I. Read, S. Feltzing, A. Koch, G. F. Gilmore, E. K. Grebel, I. Lundström
Astrophysical Journal, 2009, 706, L150

In Paper II we explored the consequence of the low velocity dispersion determined in Paper I. We found that the total mass of the Hercules dSph galaxy, within the central 300 pc, was lower than as determined in a previous study. Our mass estimate calls into question the recent claim of a "common mass scale" for the dSph galaxies orbiting the Milky Way.

The bulk of the analysis was carried out by me. However, the mass estimate, in Sect. 4.1, based on the tidal radius of the Hercules was carried out by Justin Read. The text was written by me with the co-authors as advisors, except for Sect. 4.1 that was mainly written by Justin Read.

Paper III: An abundance study of red-giant-branch stars in the Hercules dwarf spheroidal galaxy

D. Adén, K. Eriksson, S. Feltzing, E. K. Grebel, A. Koch, M. I. Wilkinson
Astronomy & Astrophysics, 2011, 525, 153

Given our clean sample of stars discovered in Paper I, and subsequent analysis that gave interesting results, we were able to obtain additional observation time using the VLT telescope at paranal, Chile. In Paper III we describe the analysis of the follow-up observation. Using high-resolution spectroscopy of RGB stars in the Hercules dSph galaxy, we are able to determine [Fe/H] and [Ca/H] based on the iron and calcium lines. This is interesting since our previous determination of [Fe/H] relied on calibrations that translates Strömgren photometry or low-resolution spectroscopy to an estimate of [Fe/H].

We found that the RGB stars of the Hercules dSph galaxy was more metal-poor than we previously thought. Additionally, we found an abundance trend such that [Ca/H] is higher for more metal-poor stars, and lower for more metal-rich stars. The [Ca/Fe] trend suggests an early rapid chemical enrichment through supernovae of type II, followed by a phase of slow star formation dominated by enrichment through supernovae of type Ia.

The majority of the work was carried out by me and Kjell Eriksson. I measured the equivalent widths of the spectra and determined the stellar parameters. Kjell Eriksson handled the model atmospheres and the computation of the radiative transfer equations using Eqwi/Bsyn. The text was written by me with the co-authors as advisors

Paper IV: An analysis of classical and ultra-faint dSph galaxies using Strömgren photometry

D. Adén, S. Feltzing, G. F. Gilmore, M. I. Wilkinson
Astronomy & Astrophysics, in preparation.

In Paper IV we repeat a lot of the analysis from Paper I. However, instead of focusing on the Hercules dSph galaxy, we include the Draco, Sextans and UMaII dSph galaxies. Given our determination of [Fe/H] from Paper III, and available similar studies in the literature, we are able to provide a new metallicity calibration for Strömgren photometry. To further enhance our analysis, we combine our Strömgren photometry with SDSS photometry. We find evidence for metallicity gradients in all of the dSph galaxies included in the study, and provide updated metallicity distribution functions. Additionally, although at a much lower success rate than the Strömgren photometry, we find that the SDSS photometric system is able to separate RGB stars from dwarf stars.

All of the analysis and text writing for Paper IV have been carried out by me.

Popular Summary (In Swedish)

Särtryck från Populär Astronomi, nummer 4, December 2010

6.1 Kosmologi

Universums energifördelning består av ungefär 70 procent mörk energi, 25 procent mörk materia och de resterande 5 procent är det som vi uppfattar som vanlig materia. Mörk energi introducerades i astrofysiken då man upptäckte att universums expansion är accelererande. Idag finns det ingen accepterad modell som beskriver vad mörk energi skulle kunna vara, men den motverkar gravitationen. Begreppet mörk materia myntades vid studier av hur stjärnor rör sig i galaxers närhet. Man upptäckte att galaxerna måste bestå av betydligt mer materia än den detekterad med teleskop. Idag tror forskarna att mörk materia består av en special typ av partiklar, och man hoppas kunna detektera den inom en snart framtid. Energifördelningen i universum är en del av den moderna kosmologiska modellen, och det är i ett universum med denna energifördelning astronomer tror att galaxerna har utvecklats.

6.2 Galaxer

En galax är ett gravitationellt bundet system bestående av gas, mörk materia, stoft och stjärnor. De stora galaxerna, som tex. Vintergatan, kan även ett supertungt svart hål i sina centrum. Vintergatan kan delas upp i komponenter; en central bulb, en skiva där det förekommer mycket stjärnbildning och en mycket stor sfärisk halo. Halon har en mycket låg densitet av stjärnor och dess radie tros vara flera hundra gånger större än skivans radie. En av de stora frågorna i modern astronomi är hur galaxer bildas. Idag vet forskare att stora galaxer till viss del bildas genom en sammanslagning av mindre objekt i ett mörkmateria Universum dominerat av mörk energi, men många frågetecken kvarstår.

Dvärgsfäroid (dSph)-galaxer är den vanligaste typen av galaxer och de är ofta följeslagare till större galaxer. I Vintergatans halo har det än så länge upptäckts ett trettiotal dSph-galaxer. Med framtida teleskop och instrument kommer med stor sannolikhet fler att upptäckas, inte bara i Vintergatan utan även i mer avlägsna galaxer. En dSph-galax karaktäriseras av att den är mycket ljussvag, extremt gammal, har en liten massa, är dominerad av mörk materia och är fattig på tyngre grundämnen. Dessa galaxer är till och med de mest mörk-materiadominerade objekten vi känner till i universum. En stor galax, likt Vintergatan, väger ungefär hundra tusen gånger mer än en typisk dSph-galax. även om egenskaperna för en dSph-galax kan tyckas ointressanta att studera, har de en mycket betydelsefull roll i bildandet av stora galaxer. dSph-galaxer tros vara ett av byggblocken som slås samman och bildar delar av de stora galaxerna, speciellt deras yttre delar där rester av dSph-galaxer kan existera relativt ostörda. För att förstå hur de stora galaxerna har bildats, måste man i detalj studera egenskaper för de minsta galaxerna.

6.3 En kort historik

Historiskt sett har bildandet av galaxer delats in i två teorier. Den första introducerades i en klassisk artikel av Eggen, Lynden-Bell och Sandage (1962). Den beskriver bildandet av en galax som en ”proto-galax” som kollapsar från ett intergalaktiskt gasmoln. Kollapsen bromsas sedan av den rotation som uppstår då materian komprimeras, och kvar blir en skivliknande eller sfärisk roterande struktur. Denna model är idag känd som den monolitiska modellen. Idag vet vi att stora galaxer som Vintergatan inte bildats på detta sätt.

Den andra modellen presenterades först av Searle & Zinn (1978) och är känd som den hierarkiska modellen. Genom att studera mängden tunga grundämnen i sjärnhopar som en funktion av deras avstånd till Vintergatans centrum, fann dessa forskare bevis som ifrågasatte den monolitiska modellen. Istället föreslog de ett betydligt mer kaotiskt ursprung för galaxerna. I deras sammanfattning skriver de ”Dessa stjärnhopar kan ha bildats i mindre objekt som successivt slogs samman för att bilda Vintergatans yttre delar”. Detta indikerar att de dSph-galaxer och strömmar av stjärnor vi observerar i Vintergatan idag skulle vara rester av en mycket kaotisk epok i Vintergatans historia.

Den hierarkiska modellen är idag en del av den moderna kosmologiska modellen som baseras på ett universum som är domineras av mörk materia. Denna modell har varit mycket framgångsrik för att beskriva storskaliga strukturer i universum. Genom att observera mycket avlägsna galaxer studeras universum från ett tidsperspektiv. Desto längre bort ett observerat objekt befinner sig, desto längre bak i tiden ser man. Astronomer har till exempel sett ordnade filament i rymden där materia har ansamlats. Dessa filament syns även i simuleringar, och det är via dessa filament som mindre galaxer faller på en central ansamling av materia. Resultatet blir en stor central galax, och i vissa fall

uppstår spiralgalaxer. Simuleringar har även indikerat att vi idag ska kunna se signaturer från den hierarkiska sammanslagningen i form av dSph-galaxer och strömmar av stjärnor. Strömmar har observerats i många galaxer, och de kan i Vintergatan studeras i detalj. Ett bra exempel är Sagittarius-strömmen som sträcker sig som en orm genom Vintergatan. Denna ström av stjärnor tros ha bildats då dSph-galaxen Sagittaruis kolliderade med Vintergatan. Ytterligare ett exempel är strömmen av stjärnor kring galaxen NGC 5907 som upptäcktes med hjälp av ett amatörteleskop i New Mexico.

6.4 Problem med modellen

Trots att den moderna kosmologiska modellen är mycket framgångsrik för att förklara bildandet av galaxer, har den även sina problem. Simuleringar av universums utveckling förutsäger att det i Vintergatans närhet ska existera hundratals mörk-materia-dominerade system, likt dSph-galaxer, som är reliker från den era då galaxen bildades. Tills för några år sedan var endast en handfull kända i Vintergatans närhet. Detta statistiska dilemma har kommit att bli känt som ”The missing satellite problem”. Under de senaste åren har dock antalet kända dSph-galaxer i Vintergatans närhet mer än fördubblats. Antalet kända dSph-galaxer som tillhör Vintergatan är nu uppe i ett trettiotal tack vare utvecklingen av bättre instrument och metoder för att finna mycket ljussvaga objekt i Vintergatans närhet. Det är onekligen fantastiskt att vi än idag upptäcker galaxer nära vår egen galax Vintergatan. Med dessa nyupptäckta ultraljussvaga dSph-galaxer har man börjat att tänkta om vad gäller ”The missing satellite problem”. Flertalet teorier existerar för att förklara problemet, som trots de senaste upptäckterna kvarstår. En av de populäraste förklaringarna baseras på att astrofysikaliska processer har hindrat dSph-galaxer från att ansamla tillräckligt med gas för att starta en effektiv födelseplats för stjärnor. Exempelvis skulle energirika fotoner kunna ha hettat upp de små dSph-galaxerna, och gasen som i normal fall bildar stjärnor flyr galaxen. Om detta scenario är sant existerar idag de dSph-galaxer vi inte kan se i form av mörk materia, men utan tillräckligt med stjärnor för att vi ska upptäcka dem med hjälp av optiska instrument. Denna teori stöds av att de ultraljussvaga dSph-galaxer man upptäckt de senaste åren är mycket fattiga på stjärnor. Metoder för att upptäcka dessa extremt ljusfattiga föremål är under utveckling. Eftersom de inte kan upptäckas med hjälp av optiskt ljus hoppas de kunna upptäckas i granngalaxer med hjälp av så kallad gravitationell linsning. Detta eftersom den höga halten av mörk materia böjer ljuset från bakomliggande föremål. Gravitationell linsning förutsades av Einstein och har idag bekräftats med hjälp av större ljusstarka galaxer.

Eftersom dSph-galaxer tros vara byggstenar till Vintergatan, speciellt dess yttre komponent halon, är det av intresse att jämföra mängden tunga grundämnen hos dSph-galaxer med halterna hos stjärnorna i Vintergatans halo. Om stjärnorna skapades i dSph-galaxerna innan de slogs samman med Vintergatan, borde andelen stjärnor med låg respektive hög andel tunga grundämnen stämma överens.

Med hjälp av spektroskopi har man uppskattat mängden tunga grundämnen hos stjärnorna i många av dSph-galaxerna, men de stjärnor med mycket låg halt som observerats i Vintergatans halo fanns det inte många av i dSph-galaxerna. Problemet formulerades av Amina Helmi, vid Kapteyn Astronomical Institue i Holland, i en studie från 2006 och mycket forskning har sedan dess ägnats åt problemet. En vändning kom 2008 då en forskargrupp vid University of California, ledd av Evan Kirby, lyckades identifiera en mängd stjärnor med låg halt tunga grundämnen i de nyupptäckta ultraljussvaga dSph-galaxerna. Baserat på dessa stjärnor visade de att mängden tunga grundämnen för dSph-galaxer och Vintergatan stämmer ganska bra överens. Parallellt med studierna av dSph-galaxer förbättrades även uppskattningen av halterna för Vintergatans halo. Denna förbättring föreslog också att skillnaden kanske inte är så stor som man tidigare trott.

6.5 Dvärgsfäroidgalaxer och stjärnhopar

dSph-galaxer och stjärnhopar i Vintergatans närhet har mycket gemensamt. De har en jämförbar ljusstyrka och stjärnmassa, och de kan vara mycket gamla och fattiga på tunga grundämnen. Då man upptäcker ett nytt stjärnsystem kan det därför vara svårt att avgöra om det är en stjärnhop eller en dSph-galax. Men, det är några få egenskaper som skiljer dem åt. Stjärnhopar har oftast endast en enda stjärnpopulation, dvs. att stjärnorna i galaxen skapades ungefär samtidigt, medan dSph-galaxer kan bestå av flera stjärnpopulationer. även om de har en total ljusstyrka som överlappar, är ljusstyrkan för dSph-galaxerna fördelad över en mycket större yta. dSph-galaxerna är också betydligt större. Som nämnts tidigare, dSph-galaxerna är de mest mörk-materiadominerade objekten man känner till. Stjärnhopar å andra sidan visar inga tecken på att innehålla stora mängder av mörk materia.

6.6 Dvärgsfäroidgalaxer i Lund

Sedan upptäckten av de ultraljussvaga dSph-galaxerna har forskningen kring dessa objekt accelererat. Vid institutionen för astronomi och teoretisk fysik i Lund har dSph-galaxer studerats under en längre tid. Med hjälp av fotometri tagen med teleskop på La Palma, Kanarieöarna, har astronomer i Lund i ett flertal studier analyserat såväl de klassiska som de nyupptäckta ultraljussvaga dSph-galaxerna. Ett av de stora problemen vid vetenskapliga studier av dessa galaxer är att exponeringarna ofta lider av mycket kontaminerande stjärnor från Vintergatan, men med hjälp av ett smart filtersystem kan stjärnor som tillhör dSph-galaxerna isoleras. Stjärnorna som tillhör Vintergatan måste sållas bort för att man ska kunna studera egenskaper hos dSph-galaxerna. Ett fåtal kontaminerande stjärnor från Vintergatan kan påverka ett resultat mycket. I en nyligen publicerad studie ledd av Daniel Adén, där de även inkluderade observationer tagna med VLT-teleskopet på Paranal i Chile,

fann man bland annat att den ultraljussvaga dSph-galaxen Hercules kan vara mycket lättare än tidigare studier föreslagit. En lättare vikt för Hercules har bidragit till teorin om hur dSph-galaxerna skapades i ett mycket ungt universum. Man har också med hjälp av ytterligare observationer med VLT-teleskopet på Paranal funnit en mängd stjärnor med mycket låg mängd tunga grundämnen i Hercules, vilket kan bidra till en lösning för problemet med de försvunna tunga-grundämnesfattiga stjärnorna. Eftersom dSph-galaxerna tros vara bland de första objekten som skapades i universum, är de också viktiga att studera för att förstå hur stjärnor har fötts och utvecklats i ett mycket ungt universum. dSph-galaxen Hercules upptäcktes så sent som 2007 av ett forskarlag vid Cambridge University lett av Vasily Belokurov, och den befinner sig på ett avstånd av ungefär 500 000 ljusår från Vintergatans centrum. Trots att detta är ett enormt avstånd relativt storleken på Vintergatans disk av stjärnor befinner den sig fortfarande i Vintergatans halo. Inom de närmsta åren kommer med stor säkerhet fler dSph-galaxer att upptäckas i Vintergatan. Detaljerade studier av dessa objekt kommer att öka vår förståelse om hur galaxer bildas, och egenskaper för mörk materia.

References

Adén, D., Eriksson, K., Feltzing, S., et al. 2011, A&A, 525, A153+

Adén, D., Feltzing, S., Koch, A., et al. 2009a, A&A, 506, 1147

Adén, D., Wilkinson, M. I., Read, J. I., et al. 2009b, ApJ, 706, L150

Alloin, D. & Bica, E. 1989, A&A, 217, 57

Árnadóttir, A. S., Feltzing, S., & Lundström, I. 2010, A&A, 521, A40+

Battaglia, G., Tolstoy, E., Helmi, A., et al. 2010, MNRAS, 1817

Beers, T. C., Drilling, J. S., Rossi, S., et al. 2002, AJ, 124, 931

Bell, R. A. & Gustafsson, B. 1978, A&AS, 34, 229

Belokurov, V., Zucker, D. B., Evans, N. W., et al. 2007, ApJ, 654, 897

Benson, A. J., Frenk, C. S., Lacey, C. G., Baugh, C. M., & Cole, S. 2002, MNRAS, 333, 177

Binney, J. & Tremaine, S. 2008, Galactic Dynamics: Second Edition, ed. Binney, J. & Tremaine, S. (Princeton University Press)

Bond, H. E. 1980, ApJS, 44, 517

Brasseur, C. M., Martin, N. F., Rix, H., et al. 2011, ApJ, 729, 23

Calamida, A., Bono, G., Stetson, P. B., et al. 2007, ApJ, 670, 400

Calamida, A., Bono, G., Stetson, P. B., et al. 2009, ApJ, 706, 1277

Carretta, E. & Gratton, R. G. 1997, A&AS, 121, 95

Cayrel, R., Depagne, E., Spite, M., et al. 2004, A&A, 416, 1117

Clem, J. L., VandenBerg, D. A., Grundahl, F., & Bell, R. A. 2004, AJ, 127, 1227

Cohen, J. G. & Huang, W. 2009, ApJ, 701, 1053

Eggen, O. J. 1978, ApJS, 37, 251

Eggen, O. J., Lynden-Bell, D., & Sandage, A. R. 1962, ApJ, 136, 748

Faria, D., Feltzing, S., Lundström, I., et al. 2007, A&A, 465, 357

Ferrara, A. & Tolstoy, E. 2000, MNRAS, 313, 291

Ferrarese, L. & Ford, H. 2005, Space Sci. Rev., 116, 523

Frebel, A., Simon, J. D., Geha, M., & Willman, B. 2010, ApJ, 708, 560

Gallagher, III, J. S. & Wyse, R. F. G. 1994, PASP, 106, 1225

Gott, J. R. I., Juri , M., Schlegel, D., et al. 2005, ApJ, 624, 463

Gratton, R. G., Sneden, C., Carretta, E., & Bragaglia, A. 1999, VizieR Online Data Catalog, 335, 40169

Gray, D. F. 2005, The Observation and Analysis of Stellar Photospheres, ed. Gray, D. F.

Grebel, E. K., Gallagher, III, J. S., & Harbeck, D. 2003, AJ, 125, 1926

Grebel, E. K. & Richtler, T. 1992, A&A, 253, 359

Helmi, A., Irwin, M. J., Tolstoy, E., et al. 2006, ApJ, 651, L121

Hilker, M. 2000, A&A, 355, 994

Hubble, E. P. 1929, ApJ, 69, 103

Ibata, R., Lewis, G. F., Irwin, M., Totten, E., & Quinn, T. 2001, ApJ, 551, 294

Keller, S. C., Schmidt, B. P., Bessell, M. S., et al. 2007, Publications of the Astronomical Society of Australia, 24, 1

Kirby, E. N., Guhathakurta, P., Bolte, M., Sneden, C., & Geha, M. C. 2009, ApJ, 705, 328

Kirby, E. N., Lanfranchi, G. A., Simon, J. D., Cohen, J. G., & Guhathakurta, P. 2011, ApJ, 727, 78

Kirby, E. N., Simon, J. D., Geha, M., Guhathakurta, P., & Frebel, A. 2008, ApJ, 685, L43

Kleyna, J., Wilkinson, M. I., Evans, N. W., Gilmore, G., & Frayn, C. 2002, MNRAS, 330, 792

Klypin, A., Kravtsov, A. V., Valenzuela, O., & Prada, F. 1999, ApJ, 522, 82

Koch, A. 2009, Astronomische Nachrichten, 330, 675

Lehnert, M. D., Nesvadba, N. P. H., Cuby, J., et al. 2010, Nature, 467, 940

Lind, K., Charbonnel, C., Decressin, T., et al. 2010, ArXiv e-prints

Martin, N. F., de Jong, J. T. A., & Rix, H. 2008, ApJ, 684, 1075

Martin, N. F., Ibata, R. A., Chapman, S. C., Irwin, M., & Lewis, G. F. 2007, MNRAS, 380, 281

Martínez-Delgado, D., Peñarrubia, J., Gabany, R. J., et al. 2008, ApJ, 689, 184

Mateo, M., Olszewski, E. W., Pryor, C., Welch, D. L., & Fischer, P. 1993, AJ, 105, 510

Mateo, M. L. 1998, ARA&A, 36, 435

Moore, B., Ghigna, S., Governato, F., et al. 1999, ApJ, 524, L19

Perryman, M. A. C., Lindegren, L., Kovalevsky, J., et al. 1997, A&A, 323, L49

Ramírez, I. & Meléndez, J. 2004, A&A, 417, 301

Read, J. I., Pontzen, A. P., & Viel, M. 2006, MNRAS, 371, 885

Rutledge, G. A., Hesser, J. E., & Stetson, P. B. 1997a, PASP, 109, 907

Rutledge, G. A., Hesser, J. E., Stetson, P. B., et al. 1997b, PASP, 109, 883

Schlegel, D. J., Finkbeiner, D. P., & Davis, M. 1998, ApJ, 500, 525

Schörck, T., Christlieb, N., Cohen, J. G., et al. 2009, A&A, 507, 817

Schuster, W. J., Beers, T. C., Michel, R., Nissen, P. E., & García, G. 2004, A&A, 422, 527

Searle, L. & Zinn, R. 1978, ApJ, 225, 357

Shetrone, M. D., Côté, P., & Sargent, W. L. W. 2001, ApJ, 548, 592

Simon, J. D. & Geha, M. 2007, ApJ, 670, 313

Springel, V., White, S. D. M., Jenkins, A., et al. 2005, Nature, 435, 629

Starkenburg, E., Hill, V., Tolstoy, E., et al. 2010, A&A, 513, A34+

Strigari, L. E., Bullock, J. S., Kaplinghat, M., et al. 2008, Nature, 454, 1096

Strömgren, B. 1963, QJRAS, 4, 8

Tollerud, E. J., Bullock, J. S., Strigari, L. E., & Willman, B. 2008, ApJ, 688, 277

VandenBerg, D. A., Bergbusch, P. A., & Dowler, P. D. 2006, ApJS, 162, 375

Walker, M. G., Mateo, M., Olszewski, E. W., et al. 2006, AJ, 131, 2114

Walker, M. G., Mateo, M., Olszewski, E. W., et al. 2007, ApJ, 667, L53

Walker, M. G., Mateo, M., Olszewski, E. W., et al. 2009, ApJ, 704, 1274

Walsh, S. M., Willman, B., & Jerjen, H. 2009, AJ, 137, 450

Zucker, D. B., Belokurov, V., Evans, N. W., et al. 2006, ApJ, 650, L41

Acknowledgements

I would like to thank my supervisor, Sofia Feltzing, for all the time and effort that she has spent on my education and scientific work. Without her constant whipping, my scientific achievements would have been negligible in comparison.

I also thank my co-supervisors, Ingemar Lundström and Thomas Bensby, for their help when required. They have both spent time with me on observations, La Palma and Las Campanas, and guided me on how to observe as a proper astronomer.

A special thanks goes to Lennart Lindegren who has helped me with mathematical statistics. With his aid, I have been able to utilise more advanced analytical methods for my scientific work.

To everyone at Lund Observatory: Thank you. You have all contributed in making the Ph.D studies at Lund Observatory a pleasant one. Especially, I want to thank Daniel Malmberg. We shared office for three and a half years. Even though he had no idea of what my thesis work was about, he contributed significantly to my education as a stand-alone scientist.

To my family, Yvonne, Linda, Curt and Noah, I send my warmest thanks. I know that you are more proud of this thesis than I am.

Additionally, and most obvious, thank you Mari. Your support has been the one of greatest value since I started my Ph.D studies. My greatest achievement to date is our engagement.

Paper I

A&A 506, 1147–1168 (2009)
DOI: 10.1051/0004-6361/200912718

Astronomy & Astrophysics

A photometric and spectroscopic study of the new dwarf spheroidal galaxy in Hercules⋆,⋆⋆

Metallicity, velocities, and a clean list of RGB members

D. Adén[1], S. Feltzing[1], A. Koch[2], M. I. Wilkinson[2], E. K. Grebel[3], I. Lundström[1], G. F. Gilmore[4], D. B. Zucker[5,6], V. Belokurov[4], N. W. Evans[4], and D. Faria[4]

[1] Lund Observatory, Box 43, 22100 Lund, Sweden
e-mail: daniel.aden@astro.lu.se
[2] Department of Physics and Astronomy, University of Leicester, University Road, Leicester LE1 7RH, UK
[3] Astronomisches Rechen-Institut, Zentrum für Astronomie der Universität Heidelberg, Mönchhofstr. 12-14, 69120 Heidelberg, Germany
[4] Institute of Astronomy, Madingley Road, Cambridge, CB3 0HA, UK
[5] Department of Physics, Macquarie University, North Ryde, NSW 2109, Australia
[6] Anglo-Australian Observatory, PO Box 296, Epping, NSW 1710, Australia

Received 18 June 2009 / Accepted 13 August 2009

ABSTRACT

Context. Dwarf spheroidal (dSph) galaxies are the least luminous, least massive galaxies known. Recently, the number of observed galaxies in this class has greatly increased thanks to large surveys. Determining their properties, such as mass, luminosity and metallicity, provides key information in our understanding of galaxy formation and evolution.
Aims. Our aim is to provide as clean and as complete a sample as possible of red giant branch stars that are members of the Hercules dSph galaxy. With this sample we explore the velocity dispersion and the metallicity of the system.
Methods. Strömgren photometry and multi-fibre spectroscopy are combined to provide information about the evolutionary state of the stars (via the Strömgren c_1 index) and their radial velocities. Based on this information we have selected a clean sample of red giant branch stars, and show that foreground contamination by Milky Way dwarf stars can greatly distort the results.
Results. Our final sample consists of 28 red giant branch stars in the Hercules dSph galaxy. Based on these stars we find a mean photometric metallicity of -2.35 ± 0.31 dex which is consistent with previous studies. We find evidence for an abundance spread. Using those stars for which we have determined radial velocities we find a systemic velocity of 45.20 ± 1.09 km s^{-1} with a dispersion of 3.72 km s^{-1}, this is lower than values found in the literature. Furthermore we identify the horizontal branch and estimate the mean magnitude of the horizontal branch of the Hercules dSph galaxy to be $V_0 = 21.17 \pm 0.05$, which corresponds to a distance of 147^{+8}_{-7} kpc.
Conclusions. When studying sparsely populated and/or heavily foreground contaminated dSph galaxies it is necessary to include knowledge about the evolutionary stage of the stars. This can be done in several ways. Here we have explored the power of the c_1 index in Strömgren photometry. This index is able to clearly identify red giant branch stars redder than the horizontal branch, enabling a separation of red giant branch dSph stars and foreground dwarf stars. Additionally, this index is also capable of correctly identifying both red and blue horizontal branch stars. We have shown that a proper cleaning of the sample results in a smaller value for the velocity dispersion of the system. This has implications for galaxy properties derived from such velocity dispersions.

Key words. galaxies: dwarf – galaxies: fundamental parameters – galaxies: individual: Hercules – galaxies: kinematics and dynamics – galaxies: photometry

1. Introduction

In the past few years the number of known Milky Way satellites has increased considerably. Our Galaxy has gained at least ten newly recognized companions, and additional ones await confirmation (e.g. Zucker et al. 2006a,b; Walsh et al. 2007; Belokurov et al. 2006, 2007, 2008, 2009). These recently discovered satellites resemble the previously known dwarf spheroidal (dSph) galaxies in many of their characteristics (see Grebel et al. 2003, for a detailed discussion of the properties of the classical dSph galaxies), but most of the new satellites are several magnitudes fainter than any dwarf galaxy known before. Hence these objects are now often referred to as "ultra-faint dwarf spheroidal galaxies". Since most of the new discoveries were made using deep CCD sky surveys such as the Sloan Digital Sky Survey, which cover primarily the northern hemisphere, it seems highly likely that additional objects will be added once the southern sky is scanned in a similar manner (e.g. Keller et al. 2007; Walsh et al. 2009).

One of the new discoveries is the Hercules dwarf spheroidal galaxy (Belokurov et al. 2007). Hercules lies at a distance of 132 ± 12 kpc from us, has an absolute V-band magnitude of

⋆ Based on observations made with the INT telescope operated on the island of La Palma by the Isaac Newton Group in the Spanish Observatorio del Roque de los Muchachos of the Instituto de Astrofisica de Canarias.
⋆⋆ Based on spectra obtained with the VLT-U2 telescope ESO Proposal number 079.B-0447(A).

about −6.6 ± 0.3, a V-band surface brightness of only 27.2 ± 0.6 mag arcsec^{-2}, and appears highly elongated (Coleman et al. 2007; Martin et al. 2008). Its stellar mass is estimated to be in the range of several $\times 10^4$ $M_\odot$. The mass of the Hercules dSph galaxy, as inferred from line-of-sight radial velocity measurements, is of the order of 10^7 $M_\odot$ within the central 300 pc (Strigari et al. 2008). This value is in good agreement with the seemingly ubiquitous, common mass scale of the other Galactic satellites (e.g. Gilmore et al. 2007; Walker et al. 2007; Strigari et al. 2008, and references therein).

As would be expected from its low luminosity and low surface brightness, Hercules is a metal-poor dSph galaxy. From measurements of the Ca II IR triplet lines in red giant stars, Simon & Geha (2007) inferred a mean metallicity of [Fe/H] = −2.27 ± 0.07 on the metallicity scale of Carretta & Gratton (1997). Using spectrum synthesis of Fe I lines, Kirby et al. (2008b) derived a mean metallicity of −2.58 ± 0.51 dex. Both studies found a wide range of metallicities among the red giant stars in Hercules, confirming the trend known from brighter dSph galaxies that often exhibit spreads of 1 dex and more (e.g. Shetrone et al. 2001; Koch et al. 2006, 2007a,b).

A detailed, high-resolution abundance analysis of two red giants in the Hercules dSph galaxy revealed that the enrichment in heavy elements proceeded inhomogeneously and that core-collapse supernovae were the primary contributors to the enrichment of Hercules (Koch et al. 2008b). Evidence for such chemical inhomogeneities on small scales has also been found in the more luminous dSph galaxies (Koch et al. 2008a) and in more massive dIrr galaxies (Kniazev et al. 2005).

In our current study we explore the potential of Strömgren photometry for the study of the stellar content of ultra-faint dSph galaxies, such as the one in Hercules. In contrast to the usual broadband photometry, Strömgren photometry offers several advantages. It provides us with gravity-sensitive multi-colour indices useful for distinguishing different evolutionary stages including giant-dwarf discrimination. This is a very valuable option when trying to eliminate foreground dwarfs from a giant candidate sample to be used for subsequent spectroscopy, particularly when dealing with sparse, extended, ultra-faint dSph galaxies that tend to suffer from substantial Galactic foreground contamination. Moreover, Strömgren indices offer the possibility to estimate metallicities for red giant stars. This method has been considerably refined since the early calibration attempts by Grebel & Richtler (1992). As compared to other photometric estimates, it has the added advantage of providing age-independent metallicity estimates (e.g. Faria et al. 2007). In terms of telescope time, intermediate-band photometry is a lot cheaper than spectroscopic surveys of faint giants.

We have obtained both Strömgren photometry as well as spectroscopic observations of the Ca II IR triplet lines for stars in the field of the Hercules dSph galaxy. These observations enable a full analysis both of evolutionary stage as well as radial velocities for these stars. It turns out that knowledge about the evolutionary stage of the stars is crucial for the construction of a clean sample of red giant branch (RGB) stars in the Hercules dSph galaxy.

The paper is organized as follows: in Sect. 2 we describe the observations and data reductions for both the photometric and the spectroscopic observations. In Sect. 3 we present the colour–magnitude diagram as well as the measured radial velocities. In Sect. 4 we show how the gravity sensitive Strömgren c_1 index can be used to disentangle the Hercules dSph galaxy members from the foreground contamination, and Sect. 5 deals with membership determination based on radial velocities. Section 6 summarizes how we define a Hercules member star. Section 7 provides a comparison with previous velocity determinations. In Sect. 8 we derive metallicities for the stars identified as members of the Hercules dSph galaxy using the Strömgren m_1 index as well as from the measurements of the Ca II IR triplet lines, and compare the results with previous studies of the metallicity of the Hercules dSph galaxy. In Sect. 9 our results are discussed and they are summarized in Sect. 10.

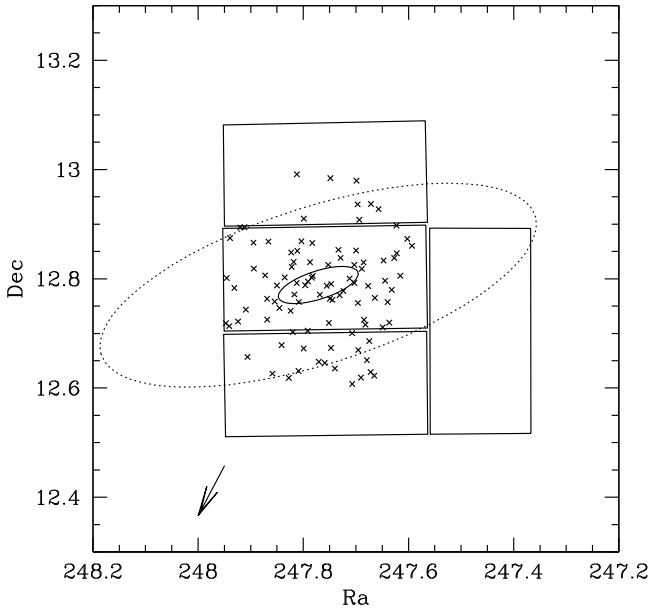

Fig. 1. Position on the sky of our observations. The coordinates are given in decimal degrees, epoch J2000. Central coordinates for the galaxy are from Martin et al. (2008). The solid ellipse represents the core radius and the dotted ellipse the King profile limiting radius of the Hercules dSph galaxy as determined by Coleman et al. (2007). Solid rectangles outline the four CCD chips in the WFC used for the photometric observations. × marks the fibre positions for the FLAMES observations. Here we show the fibres positioned on the stars only. The arrow in the bottom left hand corner indicates the direction to the centre of the Milky Way.

2. Observations and data reductions

In this section we detail the observations as well as the data reduction for both photometric and spectroscopic observations.

2.1. Photometry

Intermediate-band Strömgren u, v, b and y photometry was obtained during six nights with the Wide Field Camera (WFC) on the 2.5-m Isaac Newton Telescope (INT) on La Palma. Of the six nights only three provided useful data due to bad weather conditions. The WFC consists of 4 2k × 4k CCDs. The CCDs have a pixel size of 13.5 microns corresponding to 0.33″ per pixel. Figure 1 shows the location and dimensions of the galaxy on the sky and the positions of the CCD chips of the WFC.

The observations are summarised in Table 1 and all observations were centered at RA = $16^h31^m05^s$ and Dec = +12°47′18″ (Martin et al. 2008). Typical seeing during the three good nights was about 1.3 arcsec.

Multiple standard and extinction stars were observed each night. During the observations of the Hercules dSph galaxy, we observed 12 Strömgren standard stars chosen from the list in Schuster & Nissen (1988) plus one star from Olsen (1993), see

Table 1. Summary of the photometric observations obtained with the Isaac Newton Telescope.

Filter	13 April 2007 [min]	14 April 2007 [min]	15 April 2007 [min]	Total [min]
y	1×30	1×30	1×30	90
b	1×30	1×30	1×30	90
v	1×30	1×30	1×30	90
u	1×30	2×30	2×30	150

Column 1 lists the filter. Columns 2–4 list the number of 30 min exposures obtained for each filter during each of the three useful nights. Column 5 lists the total exposure time for each filter.

Table 2. Standard stars from Schuster & Nissen (1988), except HD107853 (Olsen 1993).

ID	Hip	V	$(b-y)$	m_1	c_1
HD 100363	56327	8.648	0.191	0.139	0.760
HD 107853	...	9.100	0.321	0.157	0.472
HD 108754	60956	9.006	0.435	0.217	0.254
HD 120467	67487	8.147	0.728	0.757	0.088
HD 134439	74235	9.058	0.484	0.224	0.165
HD 138648	76203	8.137	0.504	0.358	0.290
HD 149996	81461	8.495	0.396	0.164	0.305
HD 158226	85378	8.494	0.386	0.146	0.316
DM -05 3063	51127	9.734	0.568	0.461	0.182
DM -08 4501	87062	10.591	0.452	0.032	0.274
DM -12 2669	43099	10.230	0.229	0.094	0.490
DM -13 3834	69232	10.685	0.415	0.098	0.183
DM -14 4454	81294	10.332	0.565	0.469	0.192

Columns 1 and 2 list the star ID and Hipparcos number, respectively. Column 3 lists the standard values adopted for the magnitude (note $y \equiv V$) and Cols. 4 to 6 the standard values adopted for the $(b-y)$, m_1 and c_1 indices, respectively.

Table 2. Two stars from the list of standard stars were observed several times during each night in order to sample the extinction for a large range of airmass. These stars will henceforth be referred to as extinction stars.

The observations of standard and extinction stars are used to find the zeropoint, extinction coefficients and colour terms, see Sect. 2.1.2.

2.1.1. Reduction of the photometric observations

The images for the Hercules dSph galaxy and the standard stars were reduced with the Wide Field Survey Pipeline provided by the Cambridge Astronomical Survey Unit (Irwin & Lewis 2001). The processing operations applied to the images were de-biasing, trimming, flatfielding, astrometry and correction for non-linearity.

2.1.2. Standard star photometry and establishing the photometric calibration

We obtained aperture photometry for the standard and extinction stars using the task PHOT within the IRAF[1] APPHOT package. The size of the aperture was determined individually for each star by plotting the measured flux as a function of increasing aperture size. The aperture at which the flux no longer increased was chosen as the aperture for that star (typically 4–5 $\times FWHM$ of the stellar psf). This curve-of-growth is used in order to maximise the signal-to-noise ratio (S/N) while measuring as much flux as possible from the star (Howell 1989).

The measurements of the standard and extinction stars were used to establish the transformations needed to put our observations on the standard system of Olsen (1993). Note that the Schuster & Nissen (1988) stars are secondary standards in this system. See Olsen (1995) for a discussion about the Olsen system as compared to the system established by Bond (1980) and Anthony-Twarog & Twarog (1994).

The first night out of the three useful nights did not give us reliable photometry for the standard stars (i.e. there was no well defined linear relation for the transformation to the standard system for that night), and this night was thus excluded from the calibration.

First, we derived preliminary extinction coefficients, k_i, and zeropoints, z_i, for each filter i by solving the following equation with a least-square fit

$$m_s = m_0 + k_i \cdot X + z_i \quad (1)$$

where m is the magnitude of the star and X is the airmass. The subscripts s, 0 and i designates the standard magnitude, the observed magnitude and the filter, respectively. With preliminary zeropoints and extinction coefficients we then solved for the colour term, a_i, using a least-square fit

$$m_s = m_0 + a_i \cdot (v-y)_s + z_i' \quad (2)$$

where z_i' is the residual from the linear fit. Note that here we use the data for both nights in order to make use of the colours for all standard stars. With preliminary colour terms we can now solve the full equation to obtain better estimates of z_i and k_i

$$m_s = m_0 + a_i \cdot (v-y)_s + k_i'' \cdot X + z_i'' \quad (3)$$

with these better estimates, Eq. (2) is again solved and Eqs. (2) and (3) are then iterated until convergence in a, z and k is achieved. Typically convergence is reached within 6 to 7 iterations. The final zeropoint is given by z'' in Eq. (3) plus the residual zeropoint from Eq. (2) from the last iteration. The extinction coefficients, colour terms, zeropoints and correlation coefficients between the uncertainty in z and k, ρ_{zk}, for each filter and night are listed in Table 3. We note that the uncertainty in zeropoint and extinction coefficient are strongly anti-correlated.

The z, k and a obtained were used to transform our observations onto the standard system of Olsen (1993). The uncertainty for z, k and a, and the correlation coefficient ρ_{zk} were used to calculate the errors in the magnitudes, Sect. 2.1.4.

In Fig. 2 we show the residuals between our photometry and the standard values from Schuster & Nissen (1988) and Olsen (1993) as a function of our calibrated $(v-y)$ colour. We note that there are no trends with colour.

2.1.3. Photometry of the stars in the science images

Instead of co-adding the science images, we did aperture photometry on each of the images separately. Co-adding the images would be difficult since the seeing varied from night to night and because of the necessity to apply the extinction correction for each night separately. As described later in this section the final flux for each star in each filter was calculated using a weighted-mean of the individual measurements. This enables us to do a more detailed study of the night to night quality. As a quality

[1] IRAF is distributed by the National Optical Astronomy Observatories, which are operated by the Association of Universities for Research in Astronomy, Inc., under cooperative agreement with the National Science Foundation.

Table 3. Coefficients for Eq. (3).

Night	k_y	z_y	a_y	ρ_{zk}
14 April 2007	–0.155 ± 0.021	23.009 ± 0.031	0.016 ± 0.005	–0.92
15 April 2007	–0.142 ± 0.016	22.989 ± 0.023	0.016 ± 0.005	–0.96
Night	k_b	z_b	a_b	ρ_{zk}
14 April 2007	–0.240 ± 0.031	23.337 ± 0.043	0.009 ± 0.005	–0.97
15 April 2007	–0.210 ± 0.036	23.297 ± 0.050	0.009 ± 0.005	–0.96
Night	k_v	z_v	a_v	ρ_{zk}
14 April 2007	–0.349 ± 0.023	23.051 ± 0.034	0.050 ± 0.006	–0.98
15 April 2007	–0.353 ± 0.023	23.048 ± 0.032	0.050 ± 0.006	–0.96
Night	k_u	z_u	a_u	ρ_{zk}
14 April 2007	–0.582 ± 0.036	23.131 ± 0.052	0.065 ± 0.007	–0.98
15 April 2007	–0.569 ± 0.013	23.117 ± 0.021	0.065 ± 0.007	–0.96

Columns 2 to 4 list the airmass extinction coefficients, k_i, zeropoints, z_i and colour coefficients, a_i, for each filter as indicated with uncertainties σ_k, σ_z and σ_a respectively. Column 5 lists the correlation coefficient between the uncertainty in extinction coefficient, σ_k, and uncertainty in zeropoint, σ_z. This coefficient is denoted by ρ_{zk}.

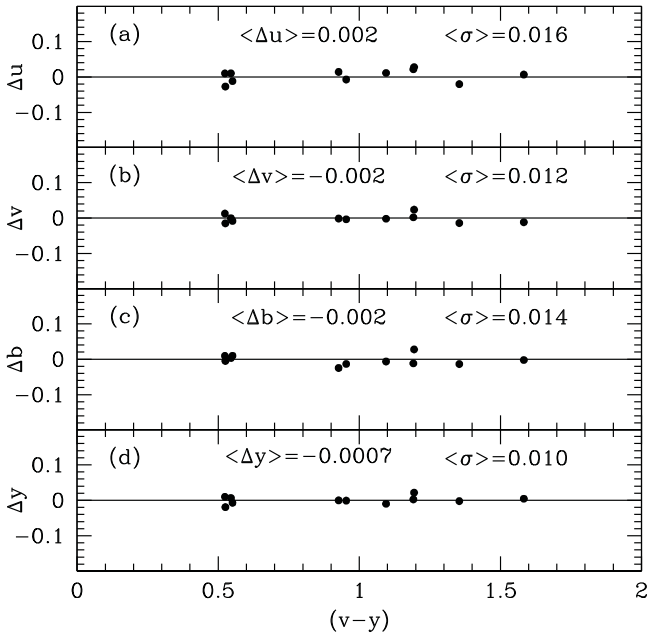

Fig. 2. The residuals for the standard stars as a function of our final $(v-y)$ colour. The residuals are given in the sense "our observed value" – "the standard value". Mean differences and σ as indicated.

check we compared the flux for the brightest targets for each night with a mean flux, calculated for each object for all nights, to see if any of the images deviated in flux. None of the images deviated. From this we draw the conclusion that the calibration was consistent throughout the entire observing run.

Coordinate lists for the images were created using the task DAOFIND in the APPHOT package in IRAF. To establish the coordinate lists we used the best y image, since the stars are brightest in this filter. We then used this catalogue of coordinates for all the other images. We used the aperture photometry task PHOT, within the APPHOT package, to measure the flux for all objects on the images.

Aperture correction. When doing photometry on the science images we used a fixed aperture of 5 pixels. Applying a curve-of-growth we obtained, for each individual image, the aperture correction out to $4 \times FWHM$ of the psf. The aperture corrections were based on measurements of many bright isolated stars, typically 20 stars per CCD. The aperture corrections were done in flux-space and are listed in Table 4.

Table 4. Aperture corrections.

File name	Filter	CCD chip	Aperture correction
r556732	y	1/2/3/4	1.265/1.266/1.278/1.266
r556737	b	1/2/3/4	1.273/1.262/1.274/1.256
r556748	v	1/2/3/4	1.195/1.191/1.164/1.168
r556754	u	1/2/3/4	1.171/1.161/1.135/1.148
r556882	b	1/2/3/4	1.269/1.264/1.259/1.240
r556887	y	1/2/3/4	1.162/1.166/1.162/1.155
r556893	v	1/2/3/4	1.268/1.264/1.223/1.238
r556898	u	1/2/3/4	1.378/1.366/1.312/1.343
r556899	u	1/2/3/4	1.384/1.362/1.316/1.352
r556997	y	1/2/3/4	1.254/1.261/1.254/1.244
r557004	b	1/2/3/4	1.212/1.203/1.204/1.188
r557009	v	1/2/3/4	1.382/1.382/1.336/1.356
r557018	u	1/2/3/4	1.209/1.198/1.160/1.185
r557019	u	1/2/3/4	1.335/1.322/1.282/1.308

Column 1 lists the file name for the image as named by the observing and archiving system on the Isaac Newton Telescope. Column 2 lists the filter. Column 3 lists the CCD chip number and Col. 4 the aperture correction for each CCD in the same order as in Col. 3.

Table 5. Summary of the spectroscopic observations with FLAMES.

Date	Exp. time [min]
15 April 2007	45
15 April 2007	45
10 May 2007	45
17 May 2007	40
21 June 2007	40
21 June 2007	40
21 June 2007	40
Total Exp. Time	295

Column 1 lists the date of observation and Col. 2 the exposure time.

Final magnitudes. Initial magnitudes were calculated for each object and night for every image and calibrated for the airmass extinction and zeropoint using Eq. (2), but this time with subscript s as our calibrated magnitude and, as before, 0 as the observed magnitude, with coefficients from Table 3. Since the first night did not give us reliable standard star photometry, and we thus have no calibration for that night, we normalized the

magnitudes from that night to the mean of the magnitudes for the two following nights.

For all three nights, erroneous measurements returned from PHOT for the individual exposures were removed from the data set (i.e. the measurements for which `sier, cier` and `pier`≠0, which are the error in sky fitting, centering algorithm and photometry, respectively). The flux was then calculated for each star. The final flux, $\overline{F}$, was obtained by using a weighted-mean flux where the photometric errors returned from PHOT (`merr`) were used as weights. The expression for the final flux is thus

$$\overline{F} = \frac{\sum_{j=1}^{n} f_j/\sigma_j^2}{\sum_{j=1}^{n} 1/\sigma_j^2} \tag{4}$$

where the subscript j is the exposure, n is the total number of exposures, f_j is the flux of the individual exposure and σ_j the error (`merr`). These mean fluxes were then converted back to magnitudes and the colour terms were applied to get the final magnitudes. By definition, $y \equiv V$ (e.g. Olsen 1983), and we will henceforth use V instead of y in figures and discussions.

2.1.4. Photometric errors

The errors in magnitude for the Strömgren photometry were calculated using a Monte Carlo Simulation, taking into account `merr`, the uncertainty in zeropoint, extinction coefficient and colour term and the strong anti-correlation between the uncertainty in zeropoint and extinction coefficient.

We did this in the following way. For each object, a new magnitude was calculated

$$m_i = m_{0,i} + \Delta m \tag{5}$$

where m_0 is the observed magnitude in filter i and Δm is a random number, drawn from a normal distribution with a mean of 0 and a variance of σ_m^2, where σ_m is the error in the magnitude as returned from the PHOT task (`merr`). Additionally, for each object, a new zeropoint and extinction coefficient were calculated

$$z_i = z_{0,i} + \Delta z \tag{6}$$

$$k_i = k_{0,i} + \Delta k \tag{7}$$

where $z_{0,i}$ and $k_{0,i}$ are the zeropoint and extinction coefficient for filter i used in the calibration (see Sect. 2.1.2) and Δz is a random number, drawn from a normal distribution with a mean of 0 and a variance of σ_z^2, see Table 3. Since σ_z and σ_k are strongly anti-correlated, we take into account the correlation coefficient from the calibration when calculating the random number Δk (see Sect. 2.1.2 and Table 3). Finally, a new colour term was calculated

$$a_i = a_{0,i} + \Delta a \tag{8}$$

where $a_{0,i}$ is the calculated colour term for filter i and Δa is a random number, drawn from a normal distribution with a mean of 0 and a variance of σ_a^2.

This process was then repeated 2000 times, generating a new set of u, v, b and y magnitudes in each iteration. As the final error for each magnitude we adopt the standard deviation of the magnitudes from the Monte Carlo simulation. This is calculated as follows

$$\sigma_{\overline{m}} = \sqrt{\frac{1}{n-1}\sum_{j=1}^{n}\left(m_j - \overline{m}\right)^2} \tag{9}$$

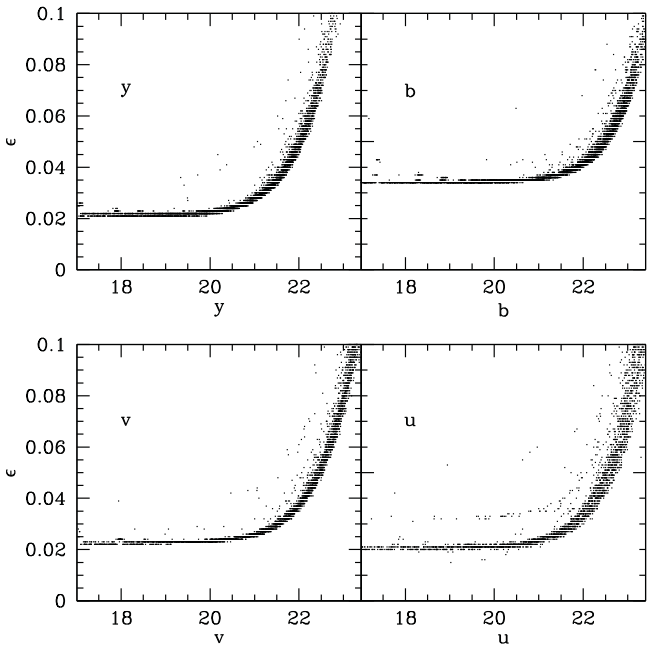

Fig. 3. Errors in the photometry for y, b, v and u, as indicated. The calculation of the errors is described in Sect. 2.1.4. The few stars with anomalously high errors at a given magnitude are also discussed there.

where the subscript j is the Monte Carlo iteration number, and $\overline{m}$ the mean magnitude of the distribution.

Figure 3 presents our final photometric errors, ϵ. The base-level error of ~0.02 mag (0.035 for the b filter) is due mainly to the errors in the photometric calibration, see Table 3 and the discussion above. The profile of the errors, i.e. increasing error with decreasing magnitude, is dominated by `merr` (i.e. photon statistics). Some stars show a larger ϵ than the majority of stars at that magnitude. This is most obvious in the u filter and is a statistical feature caused by the number of exposures that are included for that star. The u filter suffers most from this since stars are generally a lot fainter in this filter, and therefore more measurements are rejected due to errors in sky fitting, centering and photometry. For example, the stars in u with a larger ϵ for a given magnitude have three or fewer individual measurements while the stars in the main trend all have five measurements. The higher error in b is caused by the higher uncertainty for the zeropoint in b (compare Table 3).

2.1.5. Stellar classification using SExtractor

Contamination by background galaxies is a concern for our observations. As our images are uncrowded we can reach faint magnitudes with relative ease using aperture photometry. However, by using aperture photometry we have no information about the shape of the objects. In order to sort the stars from background galaxies we used SExtractor v2.5. SExtractor uses a tunable neural network trained on realistic simulated images to separate galaxies from stars in moderately crowded images (Bertin & Arnouts 1996). The SExtractor output, which is of interest to us, is the stellarity index, *sclass*; *sclass* takes on values between 0 and 1, where 0 indicates a galaxy and 1 a star. Following Bertin & Arnouts (1996), objects with a stellarity index greater than or equal to 0.5 were identified as stars.

As can be seen in Fig. 4, SExtactor clearly removes galaxies at bright magnitudes but its ability to distinguish stars from

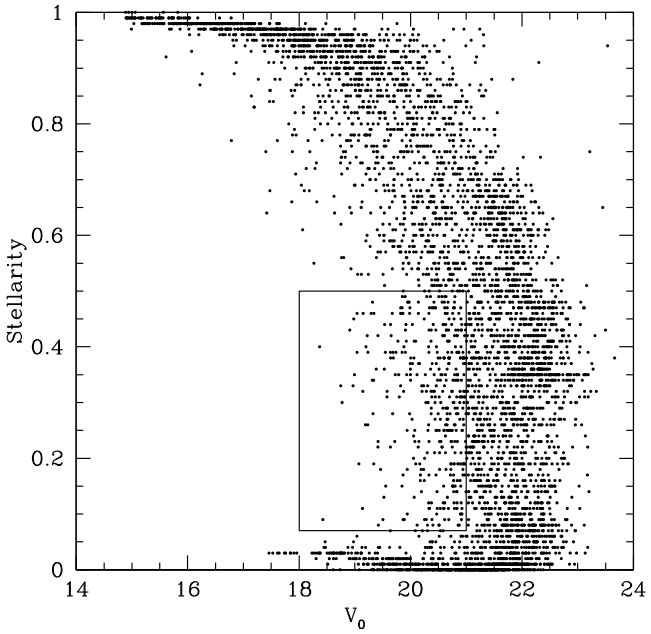

Fig. 4. SExtractor stellarity index (*sclass*) as a function of V_0. A star takes on values close to 1 and galaxies values close to 0. The rectangle indicates the area where we investigated each object individually (see Sect. 2.1.5).

galaxies diminishes at fainter magnitudes where the S/N is lower. During our membership analysis (see Sect. 4.2) we investigated objects in a stellarity index range $0.07 < sclass < 0.5$ and magnitude range $18 < V_0 < 21$ in order to make sure that we did not exclude any objects of interest based on the stellarity index alone. This area is marked with a solid line in Fig. 4. We found two objects of interest, INT 34489 and INT43290 (see Sect. 4.2 for a discussion of these two objects).

2.2. Spectroscopy

Our spectroscopy was carried out using the multiobject spectrograph Fibre Large Array Multi Element Spectrograph (FLAMES) at the Very Large Telescope (VLT) on Paranal. Operated in Medusa fibre mode, this instrument allows for the observation of up to 130 targets at the same time (Pasquini et al. 2002). Figure 1 shows the fibre positions on the sky for the stellar targets. 21 additional fibres were dedicated to observing blank sky. We used the GIRAFFE/L8 grating, which provides a nominal spectral resolution of $R \sim 6500$ and a wavelength coverage from 821 nm to 940 nm, centred on the Ca II IR triplet lines in the spectral region around 860 nm.

2.2.1. Reduction of spectroscopic observations

Initially, the FLAMES observations were reduced with the standard GIRAFFE pipeline version 2.2 (Blecha et al. 2000). This version of the pipeline, however, was not able to reduce a persistent glow on the CCD (Lind et al. 2008). This glow then created an extra background that increases towards the red. The effect was very large and would have affected the equivalent width measurements. Fortunately, during our work with these spectra a beta-version of the next version of the pipeline became available. The data were thus re-reduced with the GIRAFFE pipeline, version 2.5. This pipeline provides bias subtraction, flat fielding, dark-current subtraction, and accurate wavelength calibration from a ThAr lamp. It also solved the issue of the CCD glow.

2.2.2. Spectroscopic measurements

The 21 sky spectra were combined and subtracted from the object spectra with the task SKYSUB in the SPECRED package in IRAF. Figure 5 gives an example of the sky-subtraction process.

Finally, the object spectra from the individual frames were Doppler-shifted to the heliocentric rest frame and median-combined into the final one-dimensional spectrum. When combining the object spectra we used an average sigma clipping algorithm, rejecting measurements deviating by more than 3σ, in order to remove cosmic rays.

Radial velocities were determined by a Fourier cross-correlation of the combined spectra against a synthetic template spectrum using the IRAF task FXCOR. The template consisted of three Gaussian absorption lines at the positions of the Ca II IR triplet lines, with equivalent widths (W) representative for red giant stars. The radial velocities were determined from a Gaussian fit to the strongest correlation peak within a 300 km s^{-1} window. The uncertainty in the measurement of the radial velocity was returned by FXCOR and is based on the Tonry-Davis R-value (Tonry & Davis 1979, see Figs. 7a and b).

During the Fourier cross-correlation process we performed an ocular inspection of the quality of the spectra. Spectra of objects fainter than $V_0 \sim 21.3$ showed no clearly visible Ca II IR triplet lines and were thus removed from the sample. The S/N for these spectra was typically ~4 or less.

The equivalent widths, W, for the Ca II IR triplet lines were measured by fitting a Gaussian profile (Cole et al. 2004) to each of the three lines using the IRAF task SPLOT. From an ocular inspection of the spectra we found that the Gaussian profile fitted the Ca II triplet lines better than a Voigt profile.

2.3. Interstellar reddening

We corrected the photometric magnitudes for interstellar extinction using the dust maps by Schlegel et al. (1998). This gives $E(B-V) = 0.062$, in agreement with Koch et al. (2008b).

Coleman et al. (2007) used a reddening of $E(B-V) = 0.055$ with an uncertainty of 0.005 that represents the variation in reddening over the Large Binocular Telescope $23' \times 23'$ field. In Sect. 8.1 we investigate how different values of $E(B-V)$ affect the estimated metallicities for the stars.

We used the Schlegel et al. (1998) relations to translate these extinction values into the Strömgren system. De-reddened magnitudes, colours and Strömgren indices will henceforth have the subscript 0.

3. Results

3.1. Colour–magnitude diagram in the direction of the Hercules dSph galaxy

Figure 6 presents our colour–magnitude diagrams in the direction towards the Hercules dSph galaxy. The horizontal branch (HB) is seen at $V_0 \approx 21.2$ in Fig. 6a. A large population of foreground stars can also be seen with a cut-off at $(b-y)_0 \approx 0.3$, associated with the blue limit of the turnoff stars in the Milky Way disk and halo. The RGB of the Hercules dSph galaxy cannot easily be seen due to the heavy contamination by foreground dwarf stars.

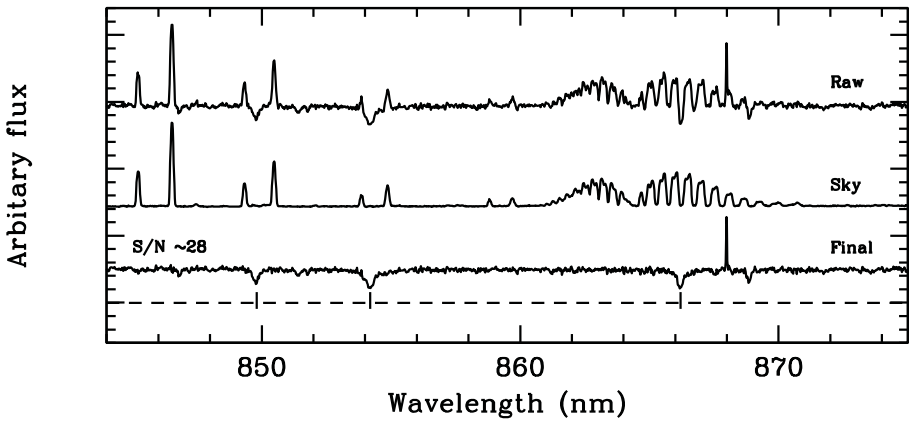

Fig. 5. Example showing the subtraction of sky-emission lines from the stellar spectra. At the top we show a raw, one-dimensional, spectrum for one of the brightest stars in our sample, $V = 18.4$. Below that spectrum is the final spectrum of the sky constructed through the combination of all 21 sky fibres. At the bottom we show the stellar spectrum once the sky has been removed. The S/N for the final stellar spectrum is 28. The rms in the sky spectrum is ~1.1 counts and ~9.8 counts in the stellar spectrum. The three Ca II IR triplet lines are indicated by vertical lines in the bottom spectrum. The dashed line indicates the position of zero intensity for the final spectrum.

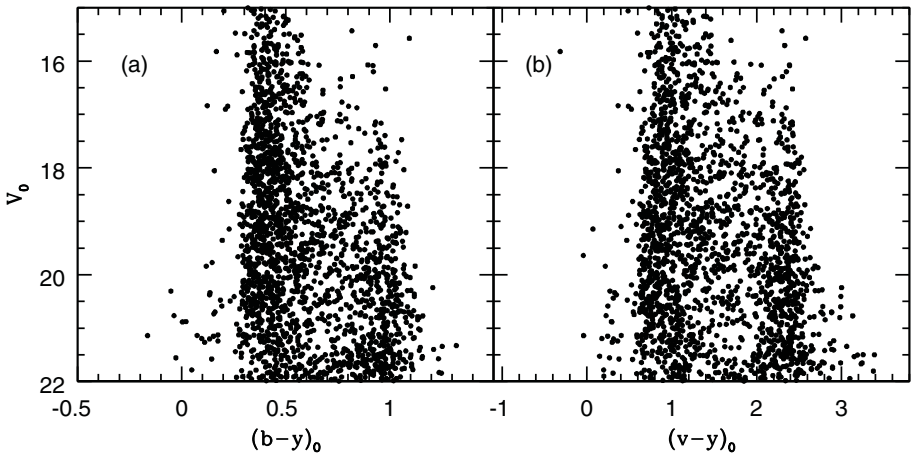

Fig. 6. Colour–magnitude diagram centred on the Hercules dSph galaxy. **a)** V_0 vs. $(b-y)_0$. **b)** V_0 vs. $(v-y)_0$. Only objects with a stellarity index $sclass \geq 0.5$ are shown (see Sect. 2.1.5).

3.2. Radial velocities

Figure 7a shows the stellarity index as a function of the derived radial velocity for the objects observed with FLAMES. Objects with a stellarity index less than 0.5 are excluded from the sample (see Sect. 2.1.5). We investigated the objects with a stellarity index less than 0.5 and a velocity close to the systemic velocity and found that all of these objects are fainter than $V_0 = 21$ except three objects, INT 43290, INT 40586 and INT 41659. INT 43290 lies on top of a background galaxy and is therefore contaminated. INT 40586 and INT 41659 have a questionable surface distribution on the CCD. We flag them as blends and possible double-star systems and identify them in Fig. 7b.

Figure 7b shows the magnitude of the stars vs. the derived radial velocities. The error-bars on the radial velocities are from the Tonry-Davis R-value (Tonry & Davis 1979) estimates. As expected, errors in the velocities correlate with magnitude such that fainter stars have larger errors.

In Fig. 8 we compare the distribution of our radial velocities in the direction of the Hercules dSph galaxy with the predictions of the Besançon model (Robin et al. 2003) with the same area on the sky as that covered by our observations. The colour and magnitude range for the distribution of stars from the Besançon model is the same as spanned by the FLAMES targets. As can be seen, also in this respect the Hercules dSph galaxy suffers from heavy foreground contamination. We note that the observed velocity distribution is not centred on the field star distribution predicted by the model, but is shifted by about -25 km s^{-1}. Moreover, disregarding the peak created by the Hercules members, the observed distribution is narrower than the model prediction. This may point to some problem with the model; however, a full investigation of the origin of this difference is beyond the scope of the present study.

4. Finding the giant and horizontal branch stars in the Hercules dSph galaxy

4.1. The ability of the Strömgren c_1 index to identify RGB stars

As Figs. 6 and 8 show, the line of sight towards the Hercules dSph galaxy is heavily contaminated with foreground stars, making it impossible to determine membership from the Colour–magnitude diagram alone. Even when radial velocities are added the selection remains uncertain, because the mean velocity of the Hercules dSph galaxy coincides with the velocity of the (thick) disk.

The c_1 index in the Strömgren system gives us the ability to disentangle the RGB and HB stars in a dSph galaxy from the foreground dwarf stars. The c_1 index is a measure of the Balmer discontinuity in a stellar spectrum and is defined as

$$c_1 = (u - v) - (v - b). \quad (10)$$

The strength of the Balmer discontinuity depends on the evolutionary stage of the star. Stars in a plot of $c_{1,0}$ vs. $(b-y)_0$ will therefore occupy different regions depending on their evolutionary stage. Figure 9 shows which regions are occupied by stars at different evolutionary stages. This classification is adopted from Schuster et al. (2004). We also show the region occupied by the RGB stars in the Draco dSph galaxy (Faria et al. 2007).

Schuster et al. (2004) were mainly concerned with high velocity dwarf stars and to a lesser extent interested in the redder

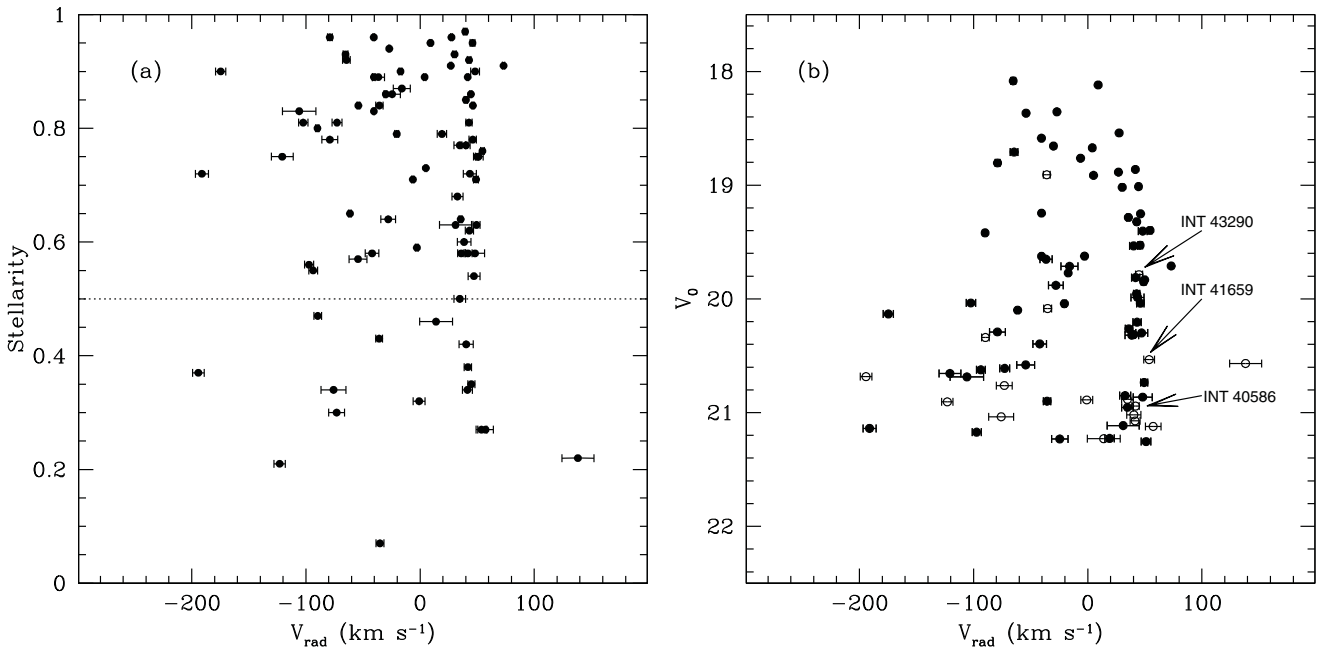

Fig. 7. a) SExtractor stellarity index vs. radial velocity for the objects observed with FLAMES. The error-bars represent the error in V_{rad} as returned by the task FXCOR. The dotted line indicates stellarity index 0.5. **b)** V_0 vs. radial velocity. • indicates objects with a stellarity index greater than 0.5. The error-bars represent the error in V_{rad} as returned by the task FXCOR. ∘ indicates objects with a stellarity index lower than 0.5. Three stars are identified with their INT numbers. These stars are discussed in Sects. 3.2 and 4.2.

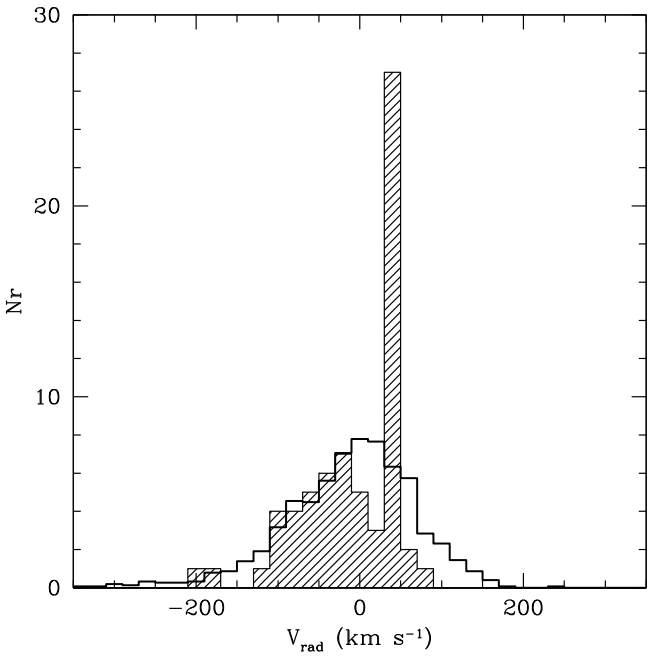

Fig. 8. Distributions of radial velocities. The solid histogram shows the distribution of velocities from a Besançon model in the direction of the Hercules dSph galaxy. The shaded histogram shows the distribution of radial velocities for our FLAMES observations. Only objects with *sclass* > 0.5 are included (see Sect. 2.1.5). Note that the area of the histogram based on the Besançon model has been normalized to cover the same area as the FLAMES histogram.

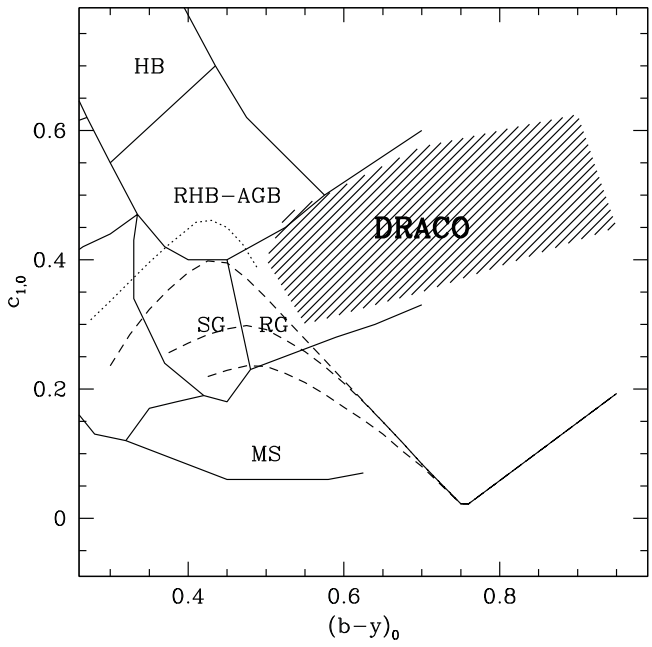

Fig. 9. $c_{1,0}$ vs. $(b-y)_0$ diagram with regions occupied by stars at various evolutionary stages as defined in Schuster et al. (2004). MS: the main sequence; SG: sub-giant stars; RG: red giant stars; RHB-AGB: the red horizontal-branch-asymptotic-giant-branch transition; HB: the horizontal branch. The shaded region marked DRACO indicates the region occupied by the RGB stars in the Draco dSph galaxy (Faria et al. 2007). The dashed lines indicate dwarf star sequences for different metallicities, [Fe/H] = 0.45, −0.05 and −1 from top to bottom and the dotted line marks the upper envelope for dwarf stars (all lines from Árnadóttir et al., in preparation).

dwarf and RGB stars. As the high-velocity halo stars that they studied tend to be fairly blue we will use tracings for dwarf stars from Árnadóttir et al. (in preparation), and isochrones for RGB stars by VandenBerg et al. (2006) with colour transformations by Clem et al. (2004), in the $c_{1,0}$ vs. $(b-y)_0$ diagram to define the dwarf and giant star regions also in the red. The dwarf sequences in Árnadóttir et al. (in preparation) provide an extension of the preliminary dwarf relation from Olsen (1984). The major

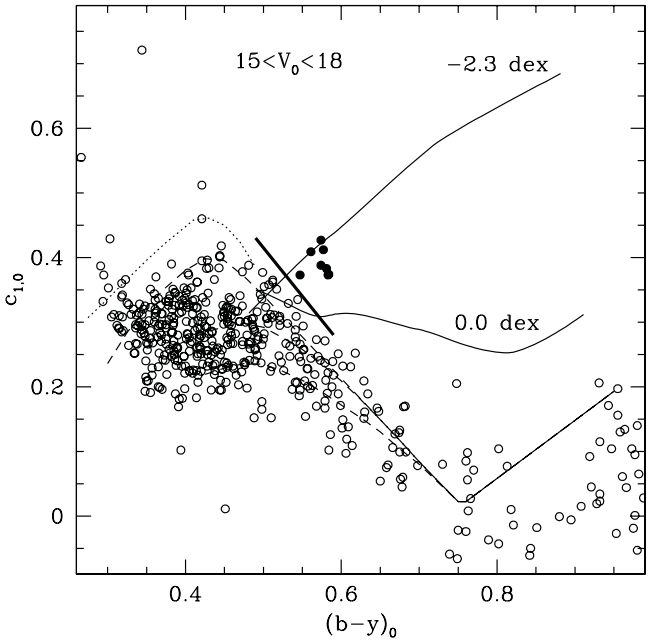

Fig. 10. $c_{1,0}$ vs. $(b-y)_0$ for stars, ∘, in the direction of the Hercules dSph galaxy. Only stars in the magnitude range $15 < V_0 < 18$ are shown. • mark stars that fall within the RGB region as defined by the isochrones by VandenBerg et al. (2006) with colour transformations by Clem et al. (2004). Metallicities as indicated. The thin dashed lines indicates dwarf star sequences for different metallicities, [Fe/H] = 0.45, −0.05 and −1 top to bottom and the dotted line marks the upper envelope for dwarf stars (all lines from Árnadóttir et al., in preparation). The thick line marks the empirically determined limit for the foreground contamination (see Sect. 4.1).

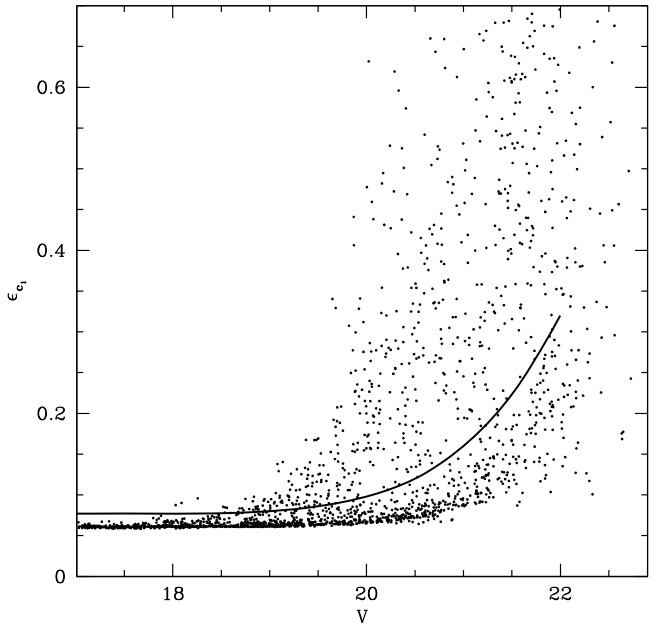

Fig. 11. Errors in the Strömgren colour index c_1 (see Sect. 4.1). The solid line indicates a spline function fitted to fall just above the trend with smaller errors. This line is used in Sect. 4.2 and Figs. 12 and 13 where we define the RGB stars.

difference between the preliminary relation by Olsen (1984) and the new relations is that the new relations are functions of metallicity. In Fig. 9 we show dwarf sequences for three different metallicities. These sequences, in accordance with Olsen (1984), trace the lower envelope for the dwarf stars (for $(b-y)_0$ less than about 0.55). Note that for redder colours ($(b-y)_0$ larger than about 0.55) all dwarf sequences merge and form a single line that traces the mean values of the colours. By studying dwarf stars from Olsen (1993, 1994a,b) in a $c_{1,0}$ vs. $(b-y)_0$ diagram it is possible to define an upper envelope for the region occupied by foreground dwarf stars. Árnadóttir et al. (in preparation) define such an upper envelope. We include this in our plots henceforth.

To define the RGB region we use two isochrones with [Fe/H] = −2.3 and [Fe/H] = 0.0 by VandenBerg et al. (2006) and colour transformations by Clem et al. (2004), see Fig. 10.

As can be seen from Fig. 10, for giant stars, the c_1 index has a clear metallicity dependence. This is more prononounced for the reddest colours (i.e. the tip of the RGB). However, in spite of this, this index still provides a strong discriminant between giant and dwarf stars for cooler stars. Note that the dwarf sequence is not metallicity dependent at these colours.

The blue limit for membership determination. Since in the $c_{1,0}$ vs. $(b-y)_0$ plane the dwarf and RGB stellar sequences converge around $(b-y)_0 \sim 0.5$ we need to identify a blue limit for stars that we identify as RGB stars. In Fig. 10 we show the $c_{1,0}$ vs. $(b-y)_0$ for stars in the magnitude range $15 < V_0 < 18$. Stars fainter than $V_0 = 15$ are not saturated on the images and, based on our membership-determination in the next section, this magnitude range is bright enough not to contain any RGB stars in the Hercules dSph galaxy. We define a line that follows the upper envelope of observed dwarf stars to separate the RGB stars from the dwarf stars in order to safely exclude any dwarf stars. This line is somewhat higher in $c_{1,0}$ at a given $(b-y)_0$ than the tracing from Árnadóttir et al. (in preparation). Our selection of RGB stars thus has a blue limit that is somewhat colour-dependent. No object bluer than this limit will be considered as an RGB star since they have a high probability of belonging to the foreground dwarf contamination.

In Fig. 10 we see 8 stars within the RGB region. A Besançon model in the direction of the Hercules dSph galaxy gives 15 RGB stars in the given magnitude and colour range. The conclusion is therefore that these stars are most likely foreground RGB stars belonging to the thick disc of the Milky Way.

4.2. Membership based on Strömgren photometry.

We study the $c_{1,0}$ vs. $(b-y)_0$ in magnitude bins rather than the entire sample of all stars all at once. With this approach the RGB region is easier to track. Figure 11 shows the errors in $c_{1,0}$ as a function of magnitude. We note the large errors in c_1 for fainter stars. These errors are due to the higher errors in u at any given magnitude. Note that in terms of errors (see Fig. 3), $V = 20$ corresponds to $u \sim 22.5$ for our RGB stars. In order to exclude stars with large errors, we reject all stars with errors higher than the median error, plus 0.015 mag, at a given magnitude (as indicated by the solid line in Fig. 11). We will now use this function in our classification of members and potential members of the Hercules dSph galaxy.

Figure 12a shows a clear and simple separation between the foreground dwarf stars and the four stars that fall in the RGB region. These four RGB stars all have errors in $c_{1,0}$ less than the line fitted in Fig. 11. Figures 12b–d show the three remaining magnitude bins. We also note that 9 stars fall within the RHB-AGB region, they are discussed in Sect. 4.3.

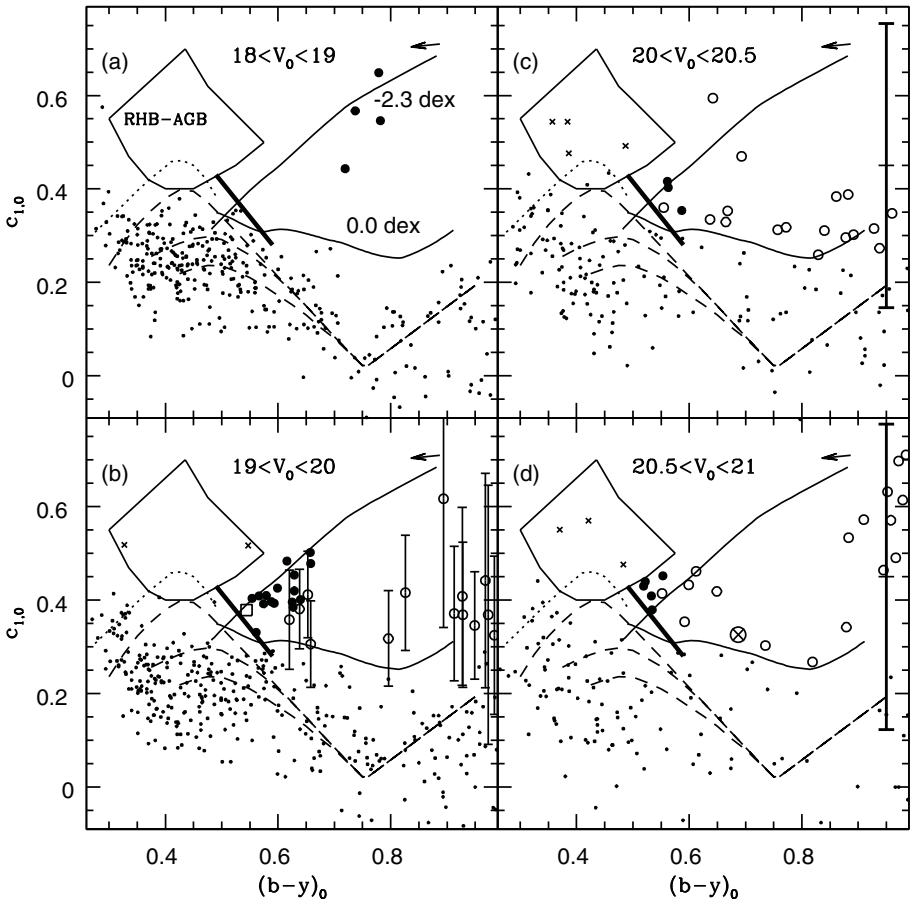

Fig. 12. $c_{1,0}$ vs. $(b-y)_0$ for stars in the direction of the Hercules dSph galaxy. The range of magnitude is indicated at the top of each panel. Dots are stars within the given magnitude range. • are stars that fall within the RGB region and have errors less than the line defined in Fig. 11. These are members based on their evolutionary stage. ∘ are stars that fall within the RGB and have errors larger than the line defined in Fig. 11. The star marked with ⊗ in **d**) is flagged as a non-member due to its position in the ϵ_{c_1} vs. $(b-y)_0$ plane, see Fig. 13. The star marked with a □ in **c**) is a foreground RGB star (see Sect. 4.2). The error-bars in **b**) represent the error in c_1 and are only displayed for stars that fall above the line defined in Fig. 11. The thick error-bars to the right in **c**) and **d**) represent the mean error in c_1 for stars that fall above the line defined in Fig. 11 (∘). × marks stars that fall in the RHB-AGB region (see Sect. 4.3). The arrow in the top right corner in each panel indicates the magnitude and direction of the de-reddening applied to the data (see Sect. 2.3). The solid lines indicate isochrones for RGB stars by VandenBerg et al. (2006) with colour transformations by Clem et al. (2004). Their metallicities are indicated in **a**). The dashed lines indicate dwarf star sequences for different metallicities, [Fe/H] = 0.45, −0.05 and −1 from top to bottom and the dotted line marks the upper envelope for dwarf stars (all lines from Árnadóttir et al., in preparation). The thick line marks the empirically determined limit for the foreground contamination (see Sect. 4.1).

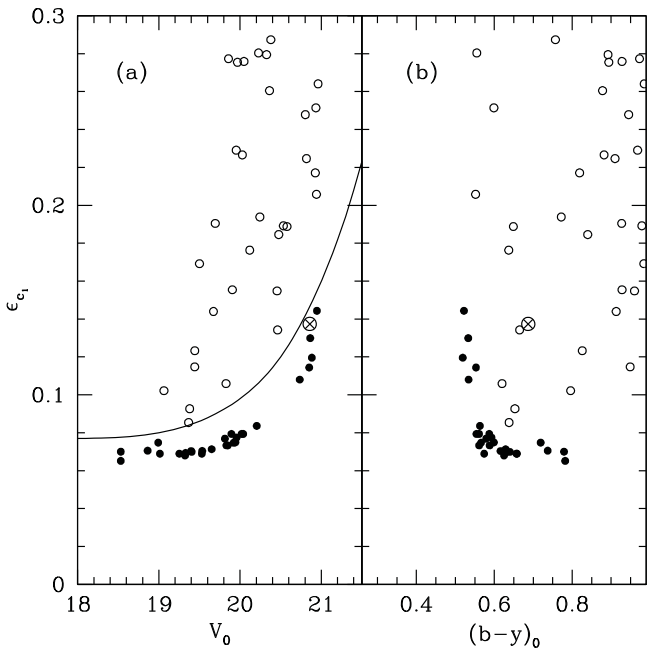

Fig. 13. ϵ_{c_1} vs. V_0 and $(b-y)_0$ for the stars in the RGB region identified in Fig. 12. Symbols are the same as in Fig. 12 and the line in **a)** is the same as in Fig. 11.

In Fig. 13 we show ϵ_{c_1} vs. V_0 and $(b-y)_0$ for all the stars falling in the RGB region.

In total we find 29 member stars in the RGB region, and 9 in the RHB-AGB region. They are listed in Table 9.

Table 6. Objects with a stellarity index lower than 0.5, a radial velocity much lower than the mean velocity of the galaxy or $V_0 > 21$.

ID	RA(2000)	Dec(2000)	V_0	$V_{\rm rad}$
34489	247.66907	13.07061	20.27 ± 0.02	...
43290[a]	247.63172	12.77969	19.79 ± 0.02	44.9 ± 3.1
42668	247.69964	12.85175	19.62 ± 0.02	−2.8 ± 1.3

[a] On top of a galaxy.
Column 1 lists the INT ID. Columns 2 and 3 list the coordinates. Column 4 lists the V_0 magnitude and its associated error. Column 5 lists the radial velocity and its associated error, both in km s^{-1}.

Objects with a stellarity index lower than 0.5. As mentioned in Sect. 2.1.5 we found two objects of interest, based on their position in the $c_{1,0}$ vs. $(b-y)_0$ diagram, with a stellarity index lower than 0.5. INT 34489 at $V_0 = 20.27$ has *sclass* = 0.3 and is located right at the edge of the blue limit. An ocular inspection of the object indicates that it may be a star, but it is slightly elongated on the CCD. INT 43290 at $V_0 = 19.79$ has *sclass* = 0.35. In Sect. 3.2 we found that this object lies on top of a galaxy and is therefore contaminated. Given the higher uncertainty of these two objects we do not include them in further analysis. The stars are listed in Table 6.

A possible foreground RGB star. In Fig. 12b we found one star, INT 42668, that fall within the RGB region but it has a radial velocity of $V_{\rm rad} = -2.8\,{\rm km\,s^{-1}}$ (see Sect. 5) and $[{\rm Fe/H}]_{\rm Cal} = -0.5$ (see Sect. 8.1). Since it has a radial velocity much lower than the mean velocity of the Hercules dSph galaxy, we identify

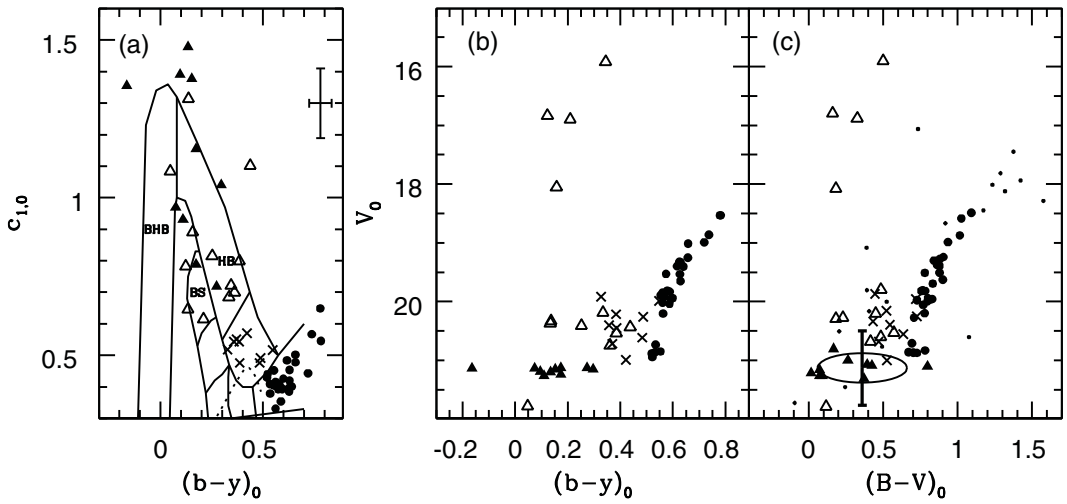

Fig. 14. a) $c_{1,0}$ vs. $(b-y)_0$ for the stars in the direction of the Hercules dSph galaxy. BHB: the blue horizontal branch; HB: the remainder of the horizontal branch; BS: the blue stragglers (Schuster et al. 2004). The dotted line marks the upper envelope for dwarf stars. • are stars identified as RGB members and × are stars identified as RHB-AGB stars based on their evolutionary stage (compare Figs. 9 and 12). △ are stars that fall on or are near the HB region but with a large offset to the expected HB magnitude. Filled triangles are stars that fall on or near the HB region and with the expected HB magnitude, they are thus identified as HB member stars. Error-bars in the top right corner are the mean $\epsilon_{c_{1,0}}$ and $\epsilon_{(b-y)_0}$ for the stars identified as HB stars. **b)** Colour–magnitude diagram in the Strömgren system for the stars identified in **a)**. **c)** Colour–magnitude diagram in the Johson-Cousin UBVRI system for the stars identified in **a)**. The solid ellipse outlines the distribution of variable stars in the Draco dSph galaxy from Bonanos et al. (2004), normalized in V_0 to fit our HB and · marks variable stars from Bonanos et al. (2004) that fall outside the ellipse. The error bar on the ellipse corresponds to the mean amplitude of the variable stars used to define the ellipse.

this star as a likely foreground RGB star, thus removing it from the sample of member RGB stars. The star is listed in Table 6.

4.3. Finding the HB and AGB of the Hercules dSph galaxy

In Fig. 12 we identified RGB members of the Hercules dSph galaxy. Additionally, we found 9 RHB-AGB stars. However, it is possible to use the Strömgren photometry to further explore the RHB-AGB and blue HB stars (BHB). Figure 14a shows the BHB, HB and blue straggler (BS) regions in the c_1 vs. $(b-y)$ plane using the areas defined in Schuster et al. (2004).

In Fig. 14a and b we show the previously identified RGB and RHB-AGB stars. In addition we show all stars bluewards of $(b-y)_0 = 0.5$ with an ϵ_{c_1} less than the function in Fig. 11. We further divide these stars into two sets according to their V magnitude. The HB of the Hercules dSph galaxy is roughly at $V_0 = 21.2$ (compare Fig. 6 and Coleman et al. 2007). We therefore define a box with $21 < V_0 < 21.4$ and $-0.2 < (b-y)_0 < 0.5$ for the potential BHB stars. The second region is given by the magnitude range above and below the first box, i.e. $15 < V_0 < 21$ and $21.4 < V_0 < 22$ with $-0.2 < (b-y)_0 < 0.5$.

Figure 14a and b then show these stars both in the c_1 vs. $(b-y)$ and in the Colour–magnitude diagram. The stars selected in the magnitude range of the HB are all narrowly spaced in magnitude and they all fall close to the BHB-RHB sequences. Hence we take all 10 of these stars to represent the HB of the Hercules dSph galaxy. We find a mean magnitude for the HB of $V_0 = 21.17 \pm 0.05$ and $V = 21.36 \pm 0.05$.

4.4. A new distance determination to the Hercules dSph galaxy

We used the relation between the absolute magnitude of the HB and metallicity (−2.35 dex as derived in Sect. 8), based on globular clusters, as defined in Carretta et al. (2000) to determine the absolute magnitude for the HB, $M_{\rm HB}$, in the Hercules dSph galaxy. Using an apparent magnitude for the Hercules HB of $m_{\rm HB} = 21.17 \pm 0.05$ we solve for the distance, d

$$m_{\rm HB} - M_{\rm HB} = -5 + 5 \cdot \log(d). \quad (11)$$

The errors in the distance determination were calculated using a Monte Carlo simulation. For each parameter with an associated error (apparent HB magnitude, metallicity and constants in the relation between the absolute magnitude and HB and metallicity), a new random apparent HB magnitude, metallicity and constants were calculated, and a new distance based on these parameters was found. This process was repeated 100 000 times. In Fig. 15 we show the distribution of the Monte Carlo simulation. As the final errors for the distance, we adopt the lower and the upper sextile of the distribution of simulated distances; the lower sextile cuts off the lowest 16.67 per cent of the data and the upper sextile cuts off the highest 16.67 per cent of the data. We find that Hercules is at a distance of 147^{+8}_{-7} kpc from us.

4.5. Variable stars in the Hercules dSph galaxy

In Fig. 14b we see some scatter in the Colour–magnitude diagram above the HB. In agreement with a Besançon model, some of these objects are likely HB stars that belong to the Milky Way. However, the Besançon model can not explain the overabundance of stars seen at $V \sim 20.4$ and $(b-y)_0 \sim 0.35$. We now investigate if these stars are variable stars that, due to variation in magnitude, position themselves above the HB. Since we do not have more than 3 exposures in the bright filters, y and b, it is difficult to determine the variability of these stars as a function of time.

We investigated the variance between the individual exposures in the y, b, v and u filter, but given the small number of exposures we found no strong indication of variability for these stars.

Siegel (2006) report the finding of 15 RR Lyrae variable stars in the Boötes dSph galaxy with periods from ~0.3 to ~0.9 days.

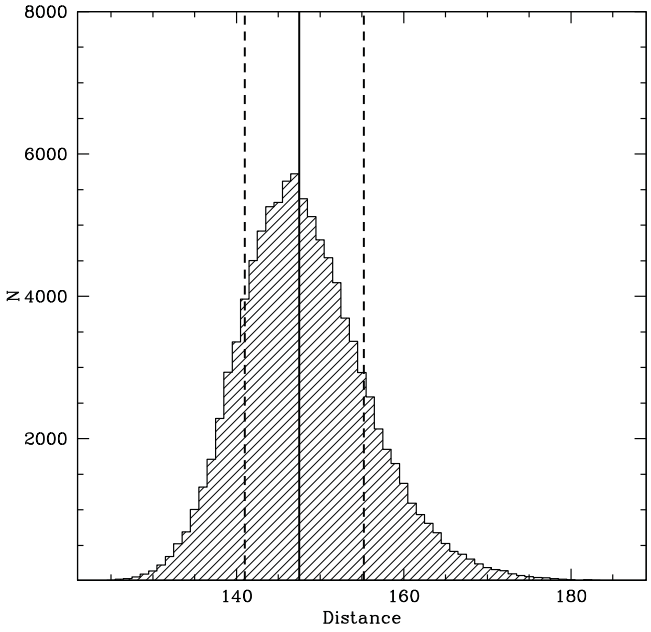

Fig. 15. Determination of the distance to the Hercules dSph galaxy, see Sect. 4.4. Solid line indicates the median distance to the Hercules dSph galaxy. Dashed vertical lines indicate the upper and lower sextile.

Since Boötes, with $M_V = -5.8$ (Belokurov et al. 2006), is fainter than the Hercules dSph galaxy, finding a similar number of RR Lyrae stars in our sample is a plausible scenario.

To further investigate the possible presence of variable stars we cross-correlated our photometry with the SDSS photometry in order to obtain *ugriz* photometry for our stars. We then transformed the *ugriz* magnitudes on to the Johnson-Cousins *UBVRI* system using the colour transformations in Jordi et al. (2006). Bonanos et al. (2004) found 163 variable stars in the Draco dSph galaxy. Mean magnitudes in V, I and B and amplitudes in V for these stars are available on-line. We de-reddened the Draco photometry using $E(B-V) = 0.027$ (Bonanos et al. 2004) and constructed an ellipse encircling the distribution of the variable stars from Bonanos et al. (2004) in the V_0 vs. $(B-V)_0$ Colour–magnitude diagram (see Fig. 14c).

Using isochrones by Marigo et al. (2008) we find that the HB for two metal-poor, old populations (−2.3 and −2.0 dex) coincide in V. We therefore normalized the positions of the Draco variable stars in V_0 so that the ellipse is aligned with the mean magnitude of our HB in the Hercules dSph galaxy, Fig. 14c. We also include the variable stars in Draco from Bonanos et al. (2004) that fall outside the ellipse. We see that the positions of the variable stars in the Colour–magnitude diagram for the Draco dSph galaxy are similar to the positions of our open triangles: 1) they have a similar colour range; 2) they are more likely to fall above the HB than below; 3) the spread in V_0 at $(B-V)_0 \sim 0.5$ is similar for both data sets.

Our conclusion from this analysis is that the 8 stars, fainter than $V_0 = 19$, likely are variable stars in the Hercules dSph galaxy. These stars are listed in Table 7.

5. Determining the systemic velocity of the Hercules dSph galaxy

Using radial velocity measurements to separate the stars belonging to a dSph galaxy from foreground stars has proven to be an efficient method for membership determination. However, for the Hercules dSph galaxy this method is complicated since this galaxy has a systemic velocity that falls within the velocity distribution of the foreground dwarf stars in the Milky Way.

Table 7. Possible variable stars in the Hercules dSph galaxy identified in Sect. 4.5.

ID	RA(2000)	Dec(2000)	V_0	$(b-y)_0$
11718	247.84445	12.60114	20.44 ± 0.02	0.44 ± 0.04
22960	247.45022	12.59089	20.19 ± 0.02	0.33 ± 0.04
33388	247.74828	12.96788	20.38 ± 0.04	0.13 ± 0.06
41701	247.78819	12.78892	20.74 ± 0.03	0.36 ± 0.04
41807	247.77753	12.76208	20.34 ± 0.02	0.14 ± 0.04
42113	247.74934	12.76745	20.41 ± 0.02	0.25 ± 0.04
42503	247.71592	12.77974	21.78 ± 0.04	0.05 ± 0.06
43193	247.64148	12.79060	20.54 ± 0.03	0.39 ± 0.04

Column 1 lists the INT ID. Columns 2 and 3 list their coordinates. Columns 4 and 5 list the Strömgren magnitude V_0 and colour $(b-y)_0$ and their associated errors, respectively.

In Fig. 8 we show the velocity distribution for our observations together with a Besançon model in the direction of the Hercules dSph galaxy. As can be seen, the velocity peak of the Hercules dSph galaxy lies within the velocity distribution of the Milky Way galaxy. A sample of member stars, identified as members based only on radial velocity will therefore contain a non-negligible number of foreground stars. However, adding knowledge about the evolutionary stage of the stars means that we can eliminate the foreground dwarf stars (compare Sect. 4.2) and obtain a clean sample which can be used to determine the systemic velocity and velocity dispersion for the dSph galaxy.

In order to illustrate the importance of knowing the evolutionary stage of the star we will first consider only the radial velocities as a means to define a sample of stars belonging to the dSph galaxy. After that we will add knowledge about the evolutionary stage to clean the sample further.

5.1. Using only radial velocities to select RGB members

We used the maximum likelihood method described in Walker et al. (2006) to determine the mean heliocentric velocity and internal velocity dispersion for stars in the direction of the Hercules dSph galaxy.

The natural logarithm of the probability function defined in Walker et al. (2006) was maximized

$$\ln(p) = -\frac{1}{2}\sum_{i=1}^{N}\ln(\sigma_i^2+\sigma_p^2) - \frac{1}{2}\sum_{i=1}^{N}\frac{(v_i-u)^2}{(\sigma_i^2+\sigma_p^2)} - \frac{N}{2}\ln(2\pi). \quad (12)$$

In each iteration we rejected stars deviating by more than 3σ as they are likely not members. As can be seen in Fig. 8, the objects targeted with FLAMES span a broad range of velocities. For the first pass through the maximum likelihood iteration we selected stars with $10\,\mathrm{km\,s^{-1}} < V_{\rm rad} < 70\,\mathrm{km\,s^{-1}}$. The maximization converged after 1 iteration. This method gives us a mean velocity of $40.87 \pm 1.42\,\mathrm{km\,s^{-1}}$ with a dispersion of $7.33 \pm 1.08\,\mathrm{km\,s^{-1}}$. Stars deviating by less than 3σ from the velocity could be considered as possible Hercules dSph galaxy members. We find 32 stars in this velocity range.

5.2. Weeding out foreground dwarf stars with the same velocity as the Hercules dSph galaxy

One of the 32 stars found in Sect. 5.1 (excluding the three stars with *sclass* < 0.5), INT 42568, lies on the edge of the WFC

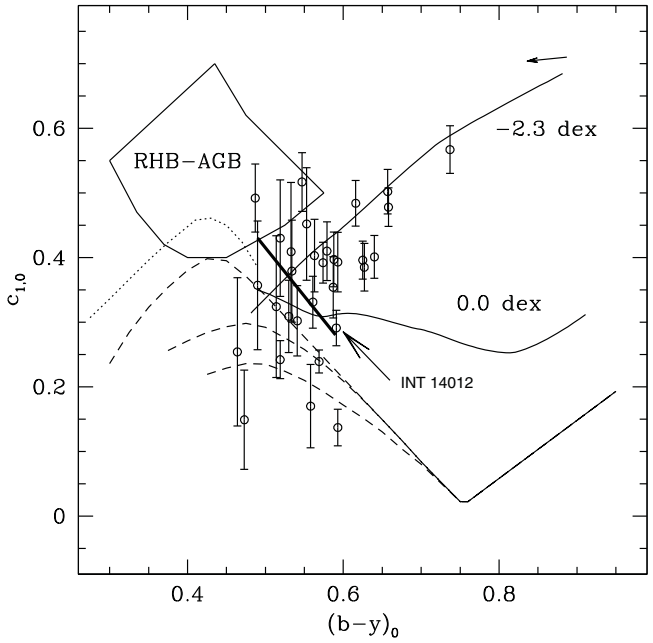

Fig. 16. $c_{1,0}$ vs. $(b-y)_0$ diagram for stars considered as members from the radial velocity measurement alone (see Sect. 5.1). The thin solid lines indicate the isochrones for RGB stars by VandenBerg et al. (2006) with colour transformations by Clem et al. (2004). The thin dashed lines indicate dwarf star sequences for different metallicities, [Fe/H] = 0.45, −0.05 and −1 top to bottom and the dotted line marks the upper envelope for dwarf stars (all lines from Árnadóttir et al., in preparation). The thick solid line is our lower limit for identification of RGB stars (see Sect. 4). The arrow in the top right corner indicates the magnitude and direction of the de-reddening applied to the data (see Sect. 2.3).

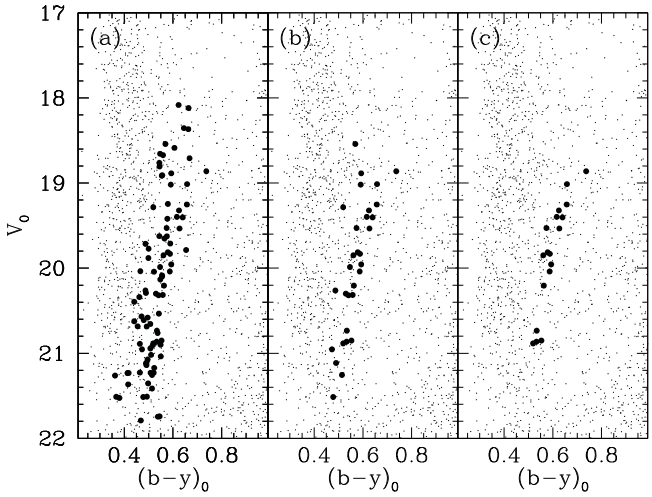

Fig. 17. Colour–magnitude diagrams. **a)** Objects targeted with FLAMES are shown as large •. Small dots indicate stars from Fig. 6a. **b)** Stars that have radial velocities within 3σ of the systemic velocity. **c)** Stars that are members based on the evolutionary stage and have measured velocities within 3σ of the systemic velocity (see Sect. 5.2).

CCD #4 and does not have any photometry available and is hence excluded from the following discussions. In Fig. 16 we plot $c_{1,0}$ vs. $(b-y)_0$ for the 31 stars considered as possible members based on the radial velocities. We find the following

- out of the 31 stars 10 fall on or below the dwarf sequences and are therefore excluded;
- of the remaining 21 stars, 18 are RGB members, 2 fall in the RHB-AGB region;
- the last star falls below the RGB solar isochrone but is redder than the blue limit (compare Figs. 12 and 16). This star is marked in Fig. 16 (INT 14012). We consider this star as a member (but see discussion below).

Hence, we find about 30 per cent contamination by foreground stars in our sample. For the 19 RGB stars with the right evolutionary stage, we re-derive the mean velocity and dispersion using the maxiumum likelihood method. We note that star INT 14012 was rejected during the iteration due to the 3σ limit. This star is not included in the final sample of RGB stars. We note that one of the remaining 18 stars, INT 42170, has a velocity just outside the re-derived more narrow 3σ limit. Since it falls short of this limit by only 1.32 km s^{-1} and the error in the velocity for the star is 4.77 km s^{-1}, we keep it in the final sample. This star could also be a binary, which would explain its deviating velocity. We found no stars that are likely members based on the Strömgren photometry, but non-members based on the radial velocity measurement.

We find a mean final systemic velocity of 45.20 ± 1.09 km s^{-1} with a dispersion of 3.72 ± 0.91 km s^{-1}. Our conclusion is that all stars, except INT 14012, with the right evolutionary stage fall within 3σ of the systemic velocity.

Figures 17a to c show the Colour–magnitude diagrams for objects targeted with FLAMES, stars identified as members from the radial velocity measurement only and, finally, stars identified as members from the radial velocity measurement and using photometry to weed out foreground dwarf stars.

6. Final sample

Our final sample of RGB, AGB and HB Hercules member stars was defined as follows: 1) first we select the RGB stars with the right evolutionary stage and a radial velocity within $\sim 3\sigma$ of the systemic velocity (compare Sect. 5.2 and Fig. 17c); 2) to these stars we add stars without spectroscopic measurements, which were selected as RGB, AGB, or HB stars as determined from photometry (compare Sect. 4.2). These stars are listed in Table 9. Figures 18a and b show the Colour–magnitude diagrams for the final sample.

7. A comparison with previous velocity determinations

Simon & Geha (2007) have obtained radial velocities for 86 stars in the direction of the Hercules dSph galaxy. In order to avoid including foreground dwarf stars they used measurements of the strength of the Na I lines at 818.3 and 819.5 nm to distinguish between dwarf and giant stars. As discussed in Schiavon et al. (1997) the strength of these lines depend on the gravity of the star. Hence, it enables a distinction between dwarf and giant stars. Out of the 86 stars 29 were identified as members based on the measurements of the strength of the Na I lines.

There are 21 stars in common, including field dwarf stars, between our spectroscopic study and Simon & Geha (2007)[2]. In Fig. 19 we show the difference, in units of Gaussian σ, in stellar velocity for these stars (see Kleyna et al. 2002, for a similar study of the Draco dSph galaxy). We note that the velocity measurements are in agreement, and that there are no obvious outliers, hence there is no evidence for binaries in this sample.

[2] J. Simon and M. Geha have kindly provided the relevant data so that we could do this analysis.

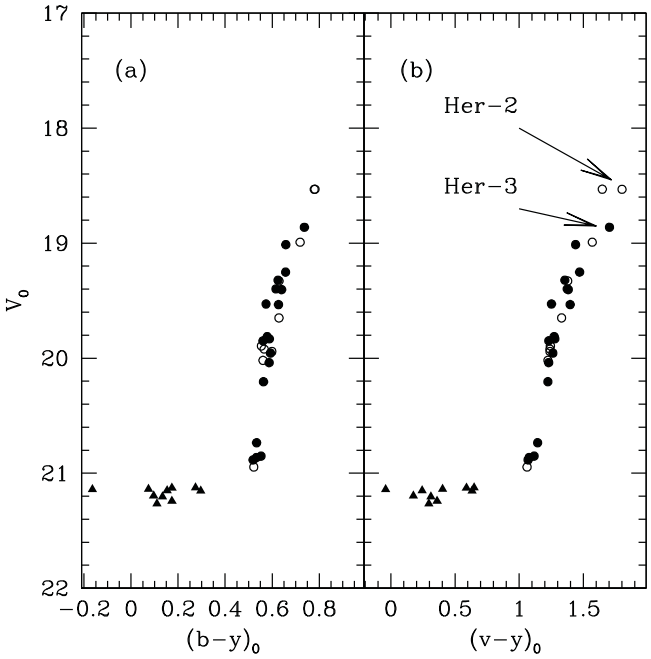

Fig. 18. Final Colour–magnitude diagrams for the Hercules dSph galaxy. **a)** V_0 vs. $(b-y)_0$. **b)** V_0 vs. $(v-y)_0$. • are members based on the evolutionary stage and have measured velocities within 3σ of the systemic velocity (see Sect. 5.2). ◦ are stars that do not have radial velocity measurements but are members according to their evolutionary stage (see Sect. 4.2). The filled triangles are stars identified as HB stars (see Sect. 4.3). Her-2 and Her-3 are discussed in Sect. 8.3. Note that there are two stars in **a)** at $V_0 \sim 18.5$ that split in **b)**.

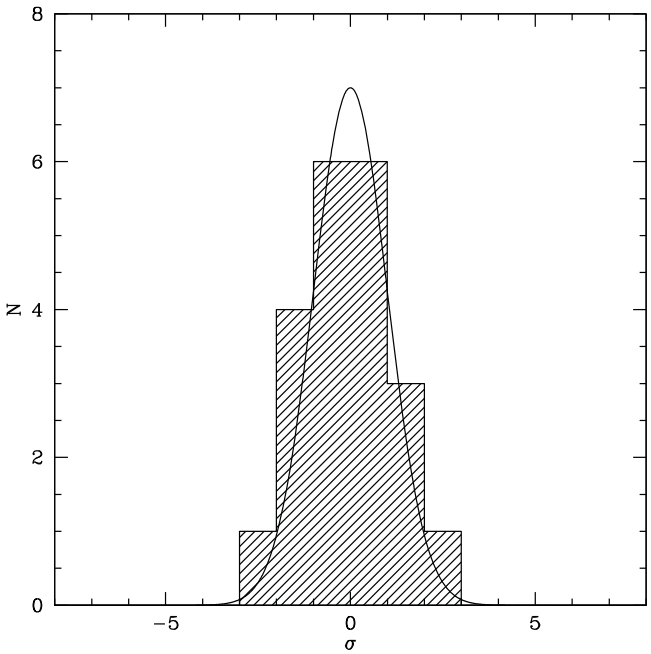

Fig. 19. Difference, in units of Gaussian σ (see Sect. 7), between our measured stellar velocities and the velocities from Simon & Geha (2007). Note that this histogram includes both members and non-members. The solid line indicates a Gaussian with $\sigma = 1$.

However, given the limited time sampling of the combined spectroscopy, and the fact that there are stars in our spectroscopic study for which there are no velocity measurement in Simon & Geha (2007), we cannot rule out the presence of binaries in our

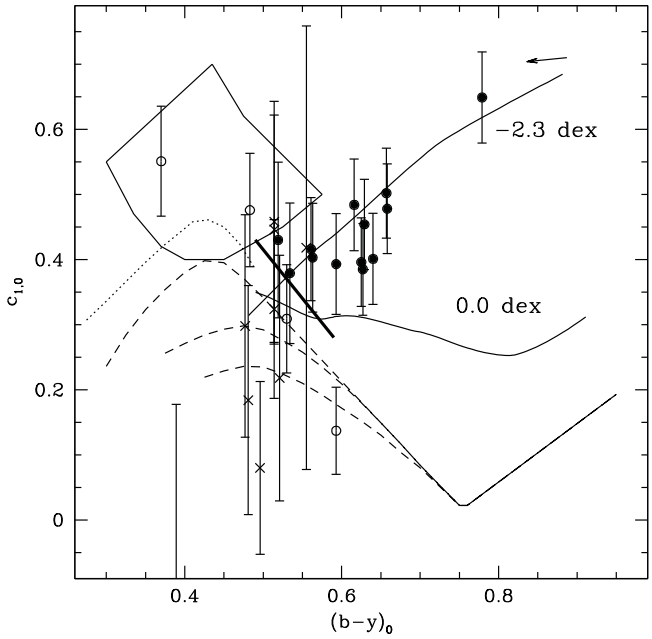

Fig. 20. Strömgren $c_{1,0}$ vs. $(b-y)_0$ diagram for the stars from Simon & Geha (2007). • are stars considered as RGB members and ◦ are stars identified as non-RGB members based on our Strömgren photometry (see Sect. 4.2). × are stars that have $V_0 > 21$, hence we have not considered their evolutionary stage as they are too faint. The thin solid lines indicates the isochrones for RGB stars by VandenBerg et al. (2006) with colour transformations by Clem et al. (2004). The thin dashed lines indicates dwarf star sequences for different metallicities, [Fe/H] = 0.45, −0.05 and −1 top to bottom and the dotted line marks the upper envelope for dwarf stars (all lines from Árnadóttir et al., in preparation). The thick solid line is our lower limit for identification of RGB stars. The arrow in the top right corner indicates the magnitude and direction of the de-reddening applied to the data (see Sect. 2.3).

study. The presence of binaries could inflate the observed velocity dispersion by a small amount (e.g. Olszewski et al. 1996).

For the stars in common between our photometric study and Simon & Geha (2007) we show a c_1 vs. $(b-y)$ diagram in Fig. 20. From this comparison we find the following

- out of the 29 stars considered as members in Simon & Geha (2007), 2 fall in the RHB-AGB region and are therefore excluded as RGB members;
- of the remaining 27 stars, 12 have $V_0 > 21$, hence we have not considered their evolutionary stage as they are too faint. 4 out of the 12 stars with $V_0 > 21$ fall outside the limits of Fig. 20;
- 2 of the remaining stars fall on or below the dwarf sequences and are therefor excluded as members of the Hercules dSph galaxy;
- thus 13 stars remain that are considered as RGB members based on Strömgren photometry.

For the 13 RGB members in common between us and Simon & Geha (2007), using the velocities from Simon & Geha (2007), we find a mean systemic velocity of 46.10 ± 1.30 km s^{-1} with a dispersion of 4.01 ± 1.08 km s^{-1}.

For 10 of the 13 RGB members we have determined radial velocities (see Sect. 2.2.2). Given the small offset in velocity determination between our study and Simon & Geha (2007), see Fig. 19, it is possible to include the velocities of the 3 stars for which we have not obtained a velocity measurement into our calculation of the mean velocity. We find a mean systemic velocity

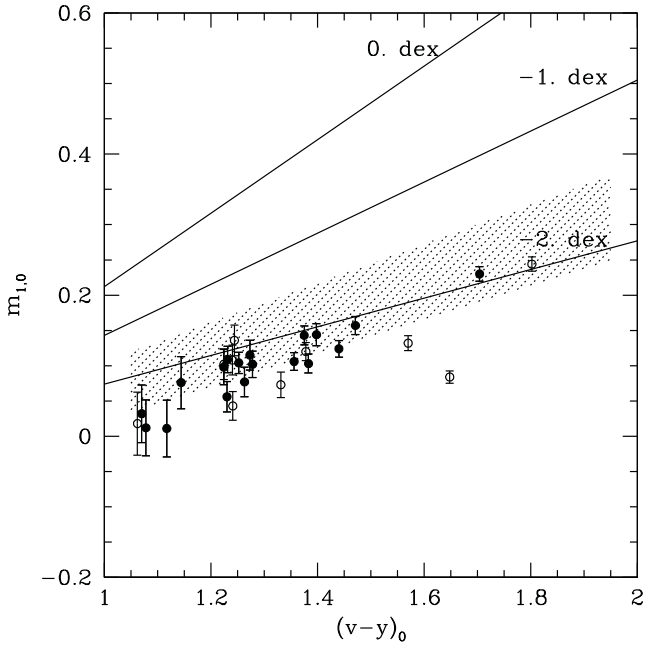

Fig. 21. $m_{1,0}$ vs. $(v-y)_0$ for the Hercules dSph galaxy. • are members based on the evolutionary stage as derived from photometry and they have radial velocities within 3σ of the systemic velocity for the Hercules dSph galaxy (see Sect. 5.2). The ◦ are stars that do not have radial velocity measurements but are members according to our photometric criteria as developed in Sect. 4.2. The solid lines are isometallicity lines based on Eq. (14) with metallicities as indicated. The shaded area indicates the distribution of RGB stars from Faria et al. (2007) for the Draco dSph galaxy, adopted from their Fig. 19.

of $44.95 \pm 1.02\,\mathrm{km\,s^{-1}}$ with a dispersion of $3.84 \pm 0.85\,\mathrm{km\,s^{-1}}$ which is in agreement with our result from Sect. 5.2.

There are 15 stars in our final sample of RGB members (based on the evolutionary stage) that do not have radial velocities measured in Simon & Geha (2007).

Measuring the strength of the Na I to exclude foreground dwarf stars is valid for $(V-I) > 1$ (Gilbert et al. 2006; Koch et al. 2008c). This corresponds to $(b-y) > 0.55$ and is confirmed by our comparison where the 16 stars that are bluer than this limit are identified as either foreground dwarf stars or HB stars by the Strömgren c_1 index.

8. Metallicities

8.1. Metallicities based on Strömgren photometry

8.1.1. Determination of metallicities

The Strömgren filters have proven useful to estimate stellar metallicities for RGB stars via the m_1 index (e.g. Richtler 1989),

$$m_1 = (v-b) - (b-y). \tag{13}$$

A review of the Strömgren metallicity calibrations for RGB stars, available at the time, is provided by Faria et al. (2007). They adopt the Hilker (2000) calibration for their RGB stars in the Draco dSph galaxy. Since the Hilker (2000) calibration is not valid for [Fe/H] < -2.0 dex and the newly found ultra-faint dSph galaxies such as Hercules are metal-poor, we adopt the semi-empirical calibration by Calamida et al. (2007) onto the metallicity scale of Zinn & West (1984) as this calibration is valid at least down to −2.4 dex.

Figure 21 shows the $m_{1,0}$ vs. $(v-y)_0$ plane for the stars identified as RGB stars in the Hercules dSph galaxy.

Equation (14), adopted from Calamida et al. (2007), is used to convert $m_{1,0}$ and $(v-y)_0$ to $[\mathrm{Fe/H}]_{\mathrm{Cal}}$ for the RGB stars.

$$[\mathrm{Fe/H}]_{\mathrm{Cal}} = \frac{(m_1 + b_1(v-y) + b_2)}{(b_3(v-y) + b_4)} \tag{14}$$

where $b_1 = -0.521 \pm 0.001$, $b_2 = 0.309$, $b_3 = 0.159 \pm 0.001$ and $b_4 = -0.09 \pm 0.002$ (note that b_2 does not have an error estimate in Calamida et al. 2007).

For comparison we re-calculated the stellar metallicities for the Draco RGB sample from Faria et al. (2007) using the calibration by Calamida et al. (2007, see Fig. 21). We found that the Draco dSph galaxy has a mean metallicity of −2.0 dex instead of −1.74 dex as calculated by Faria et al. (2007). A comparison between the metallicities derived using the older Hilker (2000) calibration and $[\mathrm{Fe/H}]_{\mathrm{Cal}}$ shows an offset of ∼0.3 dex, where $[\mathrm{Fe/H}]_{\mathrm{Cal}}$ is more metal-poor.

In Sect. 2.3 we described how we correct the photometric magnitudes for interstellar extinction using $E(B-V) = 0.062$. As a test we re-calculated $[\mathrm{Fe/H}]_{\mathrm{Cal}}$ using $E(B-V) = 0.032$ and $E(B-V) = 0.092$, which correspond to an uncertainty of ±0.03 mag. We found that $E(B-V) = 0.032$ increased and $E(B-V) = 0.092$ decreased the metallicity by ∼0.1 dex and ∼0.12 dex, respectively.

8.1.2. Error estimates

Following Faria et al. (2007), the errors in $[\mathrm{Fe/H}]_{\mathrm{Cal}}$ were calculated using a Monte Carlo simulation.

The simplest version of this approach would be to calculate the errors in metallicities taking into account only the measurement errors from PHOT (`merr`) and propagate those errors through Eq. (14) (this is the approach used in Faria et al. 2007). A more involved approach would be to include also the uncertainties in zeropoints, extinction coefficients and colour terms. For comparison we have calculated the errors using both approaches.

In both cases we used the following approach to calculate the errors. For every star identified as an RGB member of the Hercules dSph galaxy, new random magnitudes (v, b and y) were calculated from Gaussian probability distributions with standard deviations equal to that of the photometric error for each filter using a Box-Muller transformation. $m_{1,0}$ and $(v-y)_0$ were re-calculated from these new magnitudes and used to derive a new metallicity for the star. This process was then repeated 10^5 times for each star and since the distributions of the new metallicities are not Gaussian around the original [Fe/H], a standard deviation based on the sextiles (which is equivalent to 1σ in the case of a Gaussian distribution) was calculated for each star from the distribution of simulated [Fe/H]. This sextile standard deviation is our error in $[\mathrm{Fe/H}]_{\mathrm{Cal}}$ (compare Faria et al. 2007).

In Fig. 22a we show the errors in $[\mathrm{Fe/H}]_{\mathrm{Cal}}$ as a function of V_0. Note that the five faintest stars have significantly larger errors. Also note that the errors are much larger when the uncertainties in zeropoints, extinction coefficients and colour terms are taken into account. We find that it is the errors in the b filter that is the largest contributor to the error in $[\mathrm{Fe/H}]_{\mathrm{Cal}}$ when the uncertainties in zeropoints, extinction coefficients and colour terms are taken into account (compare Table 3). The errors in the b filter account for almost 50 per cent of the total error.

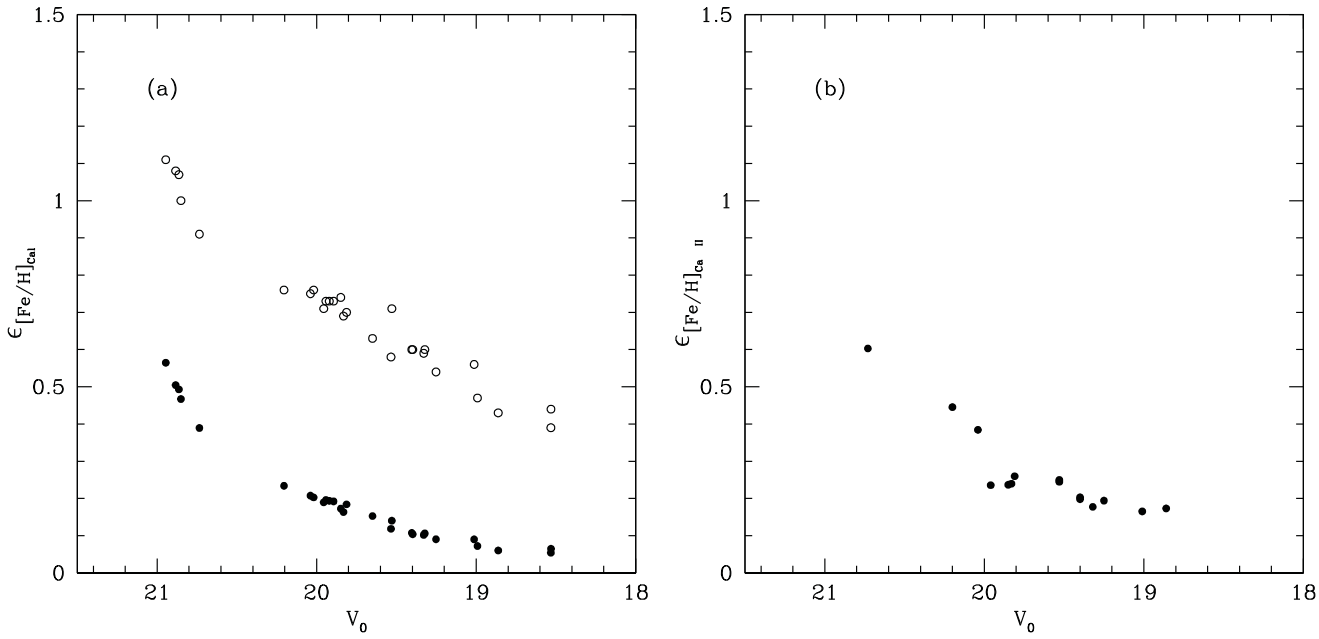

Fig. 22. **a)** Errors in the $[Fe/H]_{CaI}$ for all stars identified as RGB members of the Hercules dSph galaxy in Sect. 8.1.2. • indicates the errors if only `merr` and the uncertainties in the coefficients of Eq. (14) are included. ◦ indicates the errors if `merr`, the uncertainties in the coefficients of Eq. (14), and the uncertainties in zeropoints, extinction coefficients and colour terms are included. **b)** Errors in the $[Fe/H]_{CaII}$ as derived in Sect. 8.2.2 for stars identified as RGB members.

8.2. Metallicities based on Ca II IR triplet lines

8.2.1. Determination of metallicities

For those RGB stars for which we have FLAMES observations we also determined metallicities ($[Fe/H]_{CaII}$) from measurements of the equivalent width of the Ca II IR triplet lines at λ = 849.8, 854.2 and 866.2 nm. We follow Rutledge et al. (1997b) in defining the line strength of the Ca II IR triplet lines as the weighted sum of the W, with lower weights for the weaker lines

$$\sum W = 0.5 \cdot W_1 + W_2 + 0.6 \cdot W_3 \quad (15)$$

where W_1, W_2 and W_3 are the widths of the individual Ca II IR triplet lines in the order of increasing wavelength.

As discussed e.g. in Rutledge et al. (1997a), the strength of the Ca II IR triplet lines depend not only on metallicity but also on the surface gravity and effective temperature of the star. It is possible to remove the effect of gravity and temperature to first order by taking into account the position of the star on the RGB. This is done by defining the reduced W as

$$W' = \sum W + 0.64(\pm 0.02)(V - V_{HB}) \quad (16)$$

where $(V - V_{HB})$ is the difference between the V magnitude of the star and the V magnitude of the horizontal branch (V_{HB}). The final $[Fe/H]_{CaII}$ were calculated using the calibration by Rutledge et al. (1997a) onto the metallicity scale of Carretta & Gratton (1997). The Rutledge et al. (1997a) calibration reads as follows

$$[Fe/H]_{CaII} = -2.66(\pm 0.08) + 0.42(\pm 0.02)W'. \quad (17)$$

Of the 18 RGB stars considered as members based on the evolutionary stage and which have measured velocities within 3σ of the systemic velocity, 3 have too low S/N for measurements of the W and are therefore excluded from this metallicity determination.

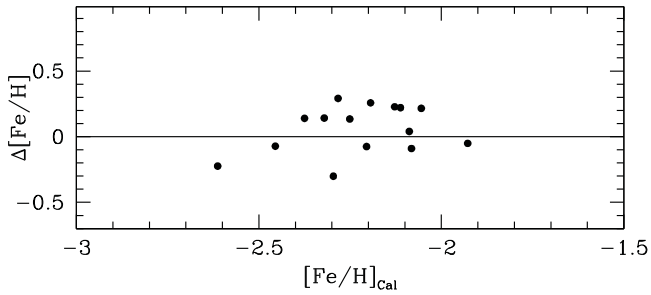

Fig. 23. A comparison between metallicities derived from the m_1 index and those derived from Ca II IR triplet line measurements. $\Delta[Fe/H] = [Fe/H]_{CaI} - [Fe/H]_{CaII}$. The offset is 0.06 dex with a scatter of 0.18 dex.

Figure 23 shows a comparison between our two metallicity estimates. We find that $[Fe/H]_{CaI}$ is on average 0.06 dex larger than $[Fe/H]_{CaII}$ with a scatter of 0.18 dex. This scatter is consistent with the typical measurement uncertainty of $[Fe/H]_{CaII}$ (see below). In conclusion, the agreement between the photometric and spectroscopic metallicities is very good. Since the calibration by Calamida et al. (2007) is valid to at least [Fe/H] = −2.4, we conclude that the extrapolation for the $[Fe/H]_{CaII}$ to [Fe/H] ∼ −2.4 is valid (compare Battaglia et al. 2008). We note that the abundance scale of Zinn & West (1984), as used by Calamida et al. (2007), in general has ∼0.2 dex lower metallicities at around −2.0 dex than the abundance scale of Carretta & Gratton (1997) as used by Rutledge et al. (1997a).

8.2.2. Error estimates

Following Battaglia et al. (2008), we define the error due to random noise in the measurement of the W as

$$\Delta W = \frac{\sqrt{1.5 \cdot FWHM}}{S/N} \quad (18)$$

where *FWHM* is the Gaussian full-width-half maximum. The S/N varies from ∼24 for the brightest star to ∼5 for the faintest star. The errors in $[Fe/H]_{Ca\,II}$ were calculated following a Monte Carlo simulation procedure similar to the one used in Sect. 8.1.2. The process was repeated 100 000 times. As the final error for $[Fe/H]_{Ca\,II}$, we adopt the standard deviation calculated from the distribution of simulated $[Fe/H]_{Ca\,II}$. In Fig. 22b we show the errors in $[Fe/H]_{Ca\,II}$ as a function of V_0.

8.3. A comparison with metallicities determined in other studies

Koch et al. (2008b) obtained high resolution spectroscopy of two stars in the Hercules dSph galaxy, Her-2 and Her-3. These stars correspond to our stars INT 42241 (V_0 = 18.53) and INT 41082 (V_0 = 18.86). The stars are marked in Fig. 18. Koch et al. (2008b) find [Fe/H] = −2.02 and −2.04 for Her-2 and Her-3, respectively.

In Sect. 4.2 we identify both of these stars as RGB stars and members of the Hercules dSph galaxy. We only have a radial velocity for one of the stars, INT 41082 (Her-3). The velocity of this star falls within 3σ of our final systemic velocity (see Sect. 5.2). For this star we find $[Fe/H]_{Cal}$ = −1.93 and $[Fe/H]_{Ca\,II}$ = −1.88. For INT 42241 (Her-2) we derive $[Fe/H]_{Cal}$ = −1.96.

Hence, there is a difference of 0.11 and 0.06 dex, respectively, when high resolution spectroscopy Fe abundances and metallicities derived from Strömgren photometry are compared. This must be regarded as excellent agreement given the complexities in analysing spectra of such cool, evolved giant stars and the general simplifications made when using calibrations of photometric measurements to obtain estimates of stellar metallicities. It should also be noted that an overestimate in the reddening of a few hundredths would easily account for this difference (compare Sect. 8.1).

Kirby et al. (2008b) studied 20 stars in the direction of the Hercules dSph galaxy. Their metallicities are based on a recently developed automated spectrum synthesis method that takes the information in the whole spectrum into account (Kirby et al. 2008a). The method was originally developed for globular clusters in the Milky Way and was then applied to ultra-faint dSph galaxies in Kirby et al. (2008b). [Fe/H] from Kirby et al. (2008b) will henceforth be referred to as $[Fe/H]_{Kirby}$. We have cross-correlated our photometry with their 20 stars and found the following (see Fig. 24)[3]

- out of the 20 stars considered as members by Kirby et al. (2008b), 2 fall in the RHB-AGB region and are therefore excluded as RGB members;
- of the remaining 18 stars, 4 have $V_0 > 21$, hence we have not considered their evolutionary stage but all indications are that at least three of them are foreground dwarf stars, compare Fig. 24;
- 2 of the 14 remaining stars fall on or below the dwarf sequences and are therefore foreground dwarf stars.

For the remaining 12 stars we find a mean metallicity of $[Fe/H]_{Cal}$ = −2.25 ± 0.20 dex (Sect. 8.1) and a mean metallicity based on the values from Kirby et al. (2008b) $[Fe/H]_{Kir}$ = −2.70 ± 0.47 dex. Figure 25 shows the difference between $[Fe/H]_{Cal}$ and $[Fe/H]_{Kirby}$. We find that the median offset is 0.67 dex, where $[Fe/H]_{Cal}$ is more metal-rich. We have investigated Δ[Fe/H] as a function of both magnitude and radial velocity but found no trend.

[3] E. Kirby has kindly provided the relevant data so that we could do this analysis.

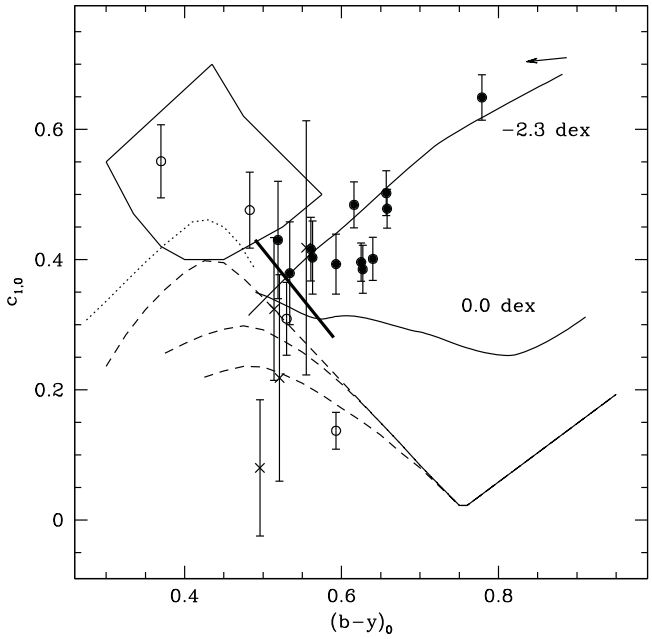

Fig. 24. Strömgren $c_{1,0}$ vs. $(b-y)_0$ diagram for the stars from Kirby et al. (2008b). • are stars considered as RGB members and ◦ are stars identified as non-RGB members based on our Strömgren photometry (see Sect. 4.2). × are stars that have $V_0 > 21$, hence we have not considered their evolutionary stage as they are too faint for our membership determination based on Strömgren photometry. The thin solid lines indicates isochrones for RGB stars by VandenBerg et al. (2006) with colour transformations by Clem et al. (2004). The thin dashed lines indicates dwarf star sequences for different metallicities, [Fe/H] = 0.45, −0.05 and −1 top to bottom and the dotted line marks the upper envelope for dwarf stars (all lines from Árnadóttir et al., in preparation). The thick solid line is our lower limit for the identification of RGB stars. The arrow in the top right corner indicates the magnitude and direction of the de-reddening applied to the data (see Sect. 2.3).

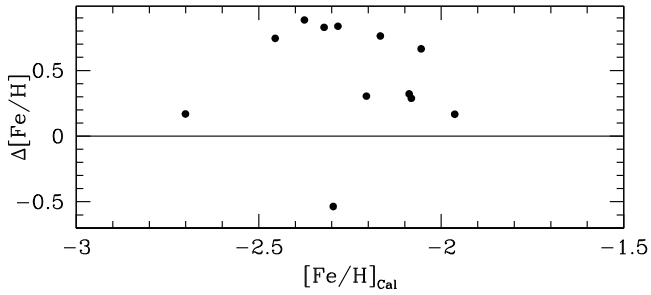

Fig. 25. A comparison between our metallicities derived from m_1 and metallicities from Kirby et al. (2008b). $\Delta[Fe/H] = [Fe/H]_{Cal} - [Fe/H]_{Kirby}$.

Simon & Geha (2007) obtained metallicities from the Ca II IR triplet lines and found a mean metallicity of [Fe/H] = −2.27 dex. Finally, Coleman et al. (2007) report a metallicity of [Fe/H] = −2.26 dex based on fitting an isochrone to a Colour–magnitude diagram.

In summary, we have five different determinations of the mean metallicity for the Hercules dSph galaxy. These determinations range from about −2.25 dex (Simon & Geha 2007;

Table 8. Summary of determination of systemic velocities, velocity dispersions and metallicities for the Hercules dSph galaxy.

	Number of stars	v_{sys} [km s^{-1}]	σ [km s^{-1}]	⟨[Fe/H]⟩ dex	[Fe/H]$_{Median}$ dex
This study	28 [RGB stars, c_1 sel.]	...	...	-2.35 ± 0.31	$-2.25^{+0.14}_{-0.31}$
This study	32 [Only V_{rad} sel.]	40.87 ± 1.42	7.33 ± 1.08	...	...
This study	18 [RGB stars with V_{rad}]	45.20 ± 1.09	3.72 ± 0.91	-2.34 ± 0.30	$-2.25^{+0.14}_{-0.20}$
S&G	29 [Their calculation]	$45.0^a \pm 1.1$	$5.1^a \pm 0.9$	...	...
S&G+c_1	13 [c_1 sel. sample]	46.10 ± 1.30	4.01 ± 1.08	...	...
Kirby et al.	20 [Their sample]	...	...	$-2.58^b \pm 0.51$	...
Kirby et al.+c_1	12 [c_1 sel. sample]	...	...	-2.70 ± 0.47	$-2.72^{+0.35}_{-0.40}$

[a] Value from Simon & Geha (2007). [b] Value from Kirby et al. (2008b).
Columns 1 and 2 list the number of stars for each study and a short description of how the stars were selected. Note: S&G indicates the sample of 29 stars from Simon & Geha (2007). Columns 3 and 4 list the systemic velocities and velocity dispersions and their errors. Column 5 lists the mean metallicities. Column 6 lists the median metallicities. Errors for the median metallicity are the upper and lower quartile. For the calculations we use our metallicites based on Strömgren photometry, but for the Kirby et al. (2008b) sample we use their metallicities.

Coleman et al. 2007, this study) to –2.7 dex (Kirby et al. 2008b). All determinations based on measurements of the Ca II IR triplet lines and the m_1-index agree on a mean metallicity of about −2.3 dex. These determinations also agree with the high-resolution analysis by Koch et al. (2008b). The determinations by Kirby et al. (2008b) are ∼0.5 dex more metal-poor (Table 8). This discrepancy is not-negligible. However, future high-resolution studies of additional Hercules stars (as in Koch et al. 2008b, which essentially is in agreement with our method) will determine which methods tend to over- or underestimate the [Fe/H]. This has important implications for our understanding of the origin of the metal poor halo stars (e.g. Helmi et al. 2006; Koch 2009).

8.4. Metallicity for the Hercules dSph galaxy

We find a metallicity range of $-2.99 < [Fe/H]_{Ca\,II} < -1.88$ with a mean metallicity of $\langle[Fe/H]_{Cal}\rangle = -2.35$ dex with $\sigma = 0.31$ dex, and a median [Fe/H] of −2.25 dex with an upper and lower quartile of −2.11 dex and −2.56 dex, respectively. If we exclude stars fainter than $V_0 = 20.5$ (compare Fig. 22a) we find a mean metallicity of $\langle[Fe/H]_{Cal}\rangle = -2.26$ dex with $\sigma = 0.24$ dex. We do not detect any significant spatial metallicity gradient in our data.

9. Discussion

9.1. Spatial distribution

The new, faint dSph galaxies are in general found to be quite elongated (Martin et al. 2008). The dSph galaxy in Hercules is no exception, in fact it is one of the new galaxies with the largest ellipticity ($e = 0.68$). The large ellipticity of these objects might be attributable to tidal distortions but could also be due to poor sampling statistics. Each galaxy is only represented by a limited number of RGB stars in most of the cases (Martin et al. 2008). Martin et al. (2008) and Ural & Wilkinson (2008) conclude that it is entirely possible that the shape determinations for these the faintest of galaxies are entirely dominated by shot-noise. This does not exclude tidal disruption as an explanation for their, in general, very elongated shapes.

With our Strömgren observations we have searched about 2/3 of the area on the sky inside the King profile limiting radius, as defined by Coleman et al. (2007), for members of the Hercules dSph galaxy. Additionally, we have searched about the same area on the sky outside the King profile limiting radius (see Figs. 1 and 26). Through this search we have found in total 28 stars that are RGB members of the Hercules dSph galaxy. These stars are spatially confined to a fairly small, elongated area falling inside the core radius from Coleman et al. (2007; see Fig. 26a). The RGB members show a slight distortion such that there appear to be a few stars trailing the ellipsoid in the direction of the Milky Way. These stars are few and none have had their radial velocities measured.

The distribution of the HB, RHB, and potential variable stars are shown in Fig. 26b. These stars confirm the central concentration and general shape of the Hercules dSph galaxy. There are some HB, RHB and variable stars scattered outside the ellipsoid defining the King profile limiting radius. It can not be excluded that some of these stars are foreground contaminators. The presence of such stars might distort the determination of the shape parameters for the galaxy. Measurements of radial velocities for these stars would confirm their membership. To our knowledge the HB of the Hercules dSph galaxy has not yet been targeted for such observations.

In conclusion we find that for a well-defined sample of RGB stars (free from contaminating foreground dwarf stars) the Hercules dSph galaxy appears to still have a fairly elongated structure, confirming previous studies.

9.2. Measured velocity dispersion

As discussed in Sect. 5, the velocity peak of the Hercules dSph galaxy lies within the bulk of the velocity distribution of the Milky Way galaxy, thus contaminating it. We have shown that relying on radial velocites for membership determination yields a velocity dispersion of 7.33 ± 1.08 km s^{-1}, whilst excluding stars that are not members (i.e. they are foreground dwarf stars) yields a velocity dispersion of 3.72 ± 0.91 km s^{-1}.

It is clear that the velocity dispersion is over-estimated when only considering the radial velocity for membership identification. This is expected since the foreground contaminating stars in the direction of the Hercules dSph galaxy have a much broader velocity distribution than that for the dSph galaxy (compare Fig. 8).

In Fig. 27 we show the velocity distribution for our observations in the velocity range $0 < V_{rad} < 100$ km s^{-1}, highlighting the objects that are members based on the evolutionary stage as derived in Sect. 4.2. As can be seen, objects with a lower velocity than the systemic velocity of the Hercules dSph galaxy are more likely to be excluded as foreground contaminating dwarf

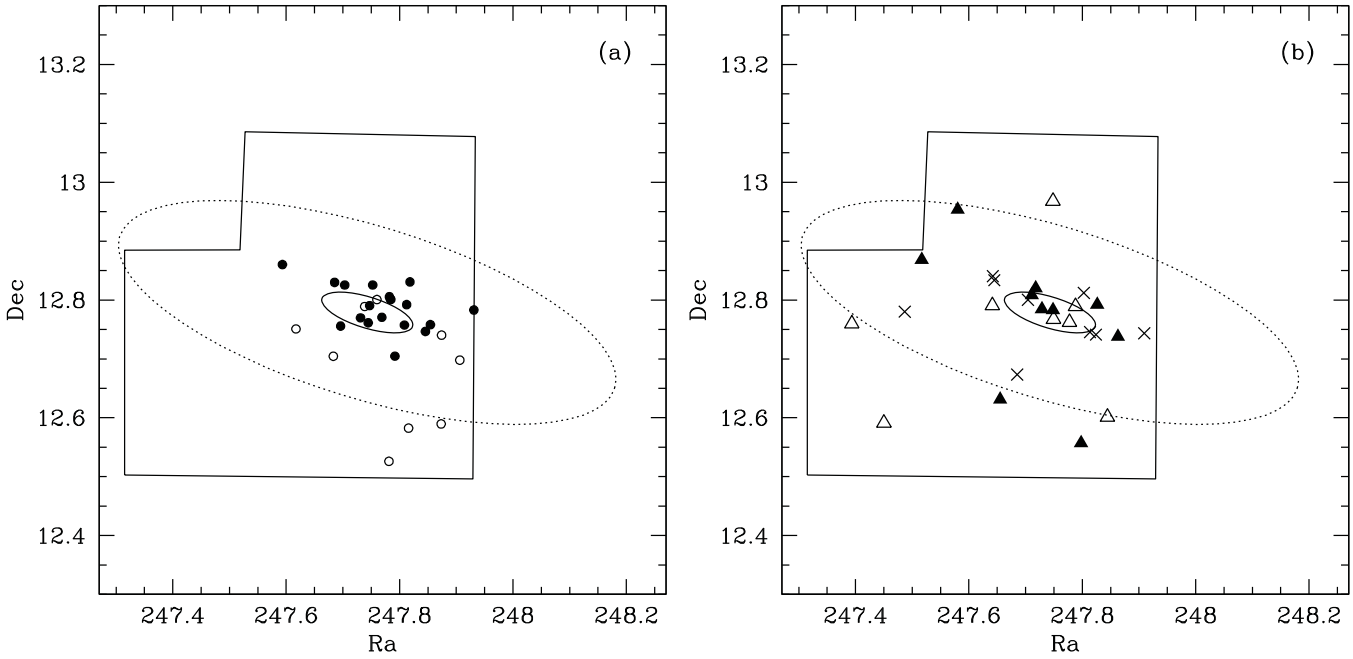

Fig. 26. Spatial distribution of the stars identified as members from both spectroscopy and photometry. **a)** • are members based on the evolutionary stage as derived from photometry and they have radial velocities within 3σ of the systemic velocity for the Hercules dSph galaxy (see Sect. 5.2). The ○ are stars that do not have radial velocity measurements but are members according to our photometric criteria (see Sect. 4.2). **b)** Filled triangles are HB members. △ are probable variable stars and × are stars identified as RHB-AGB based on the evolutionary stage as derived from photometry (see Sects. 4.5 and 4.3, respectively). The solid ellipse represents the core radius and the dotted ellipse the King profile limiting radius of the Hercules dSph galaxy as determined by Coleman et al. (2007). Solid lines outline the footprint of the WFC. Central coordinates for the galaxy are from Martin et al. (2008).

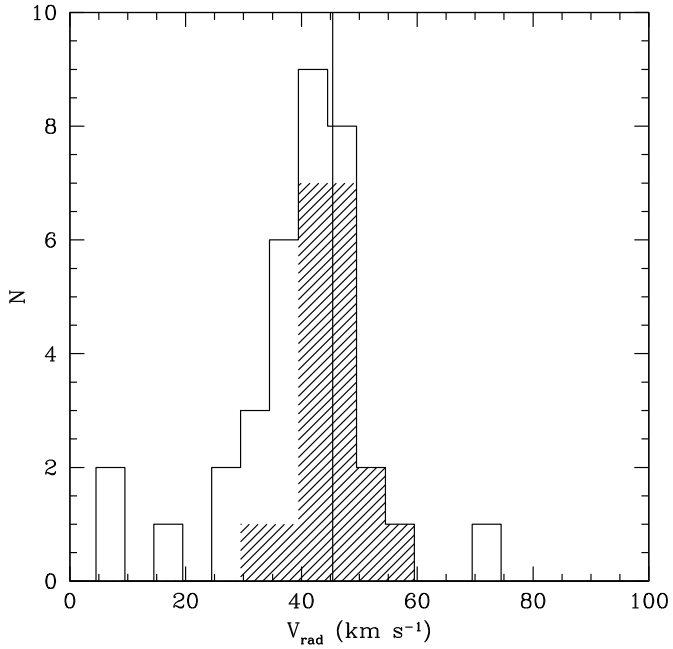

Fig. 27. Distributions of radial velocities. The solid histogram shows the distribution of velocities for objects in the direction of the Hercules dSph galaxy. The shaded histogram shows the distribution of radial velocities for stars identified as RGB members based on the evolutionary stage as derived from photometry. The solid-vertical line indicates the systemic velocity as derived from the RGB members.

stars. Comparing with Fig. 8 verifies that the majority of the velocities from a Besançon model in the direction of the Hercules dSph galaxy have a velocity lower than the systemic velocity for dSph galaxy.

In conclusion we find that when deriving the velocity dispersion for dSph galaxies it is important to have a well defined sample of member stars representing the velocity distribution of the dSph galaxy.

9.3. Kinematic sub-structure in Hercules.

Simon & Geha (2007) detected possible evidence of kinematic sub-structure in the Hercules dSph galaxy. They found nine stars clumped together between 41 and 43 km s^{-1} in a sample of 30 stars distributed between 30 and 60 km s^{-1}.

However, for our final sample of RGB stars in the Hercules dSph galaxy a one-sample Kolmogorov-Smirnov test yields a significance level of 74% for the null hypothesis that the radial velocity distribution is drawn from a Gaussian distribution. The conclusion is therefore that we do not see any kinematic sub-structure in our sample.

9.4. Metallicity

Figure 28a shows the metallicity distribution for the Hercules dSph galaxy based on the m_1-index for our final sample of RGB members (see Sects. 6 and 8.1). Figure 28b shows the corresponding normal probability function. The data points only deviate slightly from a linear fit which suggests that the metallicity distribution is drawn from a single normal distribution. The slight deviation from the linear fit is noticeable at low metallicities where the cut-off is less sharp than at high metallicities. These features is predicted by models and indicate the occurrence of strong galactic winds (Lanfranchi & Matteucci 2007).

Table 9. Hercules dSph galaxy members.

ID	RA(2000)	Dec(2000)	V	b	v	u	Chip		$[Fe/H]_{Cal}$	V_{rad}[km s^{-1}]
11239	247.87333	12.58958	19.92 ± 0.02	20.49 ± 0.04	21.16 ± 0.03	22.24 ± 0.04	1	RGB	–2.14 ± 0.73	...
12175	247.81591	12.58238	18.53 ± 0.02	19.31 ± 0.03	20.18 ± 0.02	21.59 ± 0.03	1	RGB	–2.71 ± 0.44	...
12729	247.78123	12.52606	19.65 ± 0.02	20.28 ± 0.03	20.98 ± 0.03	22.10 ± 0.04	1	RGB	–2.56 ± 0.63	...
40222	247.93108	12.78307	19.81 ± 0.02	20.39 ± 0.04	21.09 ± 0.03	22.19 ± 0.04	4	RGB	–2.13 ± 0.70	41.90 ± 3.65
40457	247.90631	12.69785	20.95 ± 0.03	21.47 ± 0.04	22.01 ± 0.04	22.99 ± 0.12	4	RGB	–2.87 ± 1.11	...
40789	247.87404	12.74030	19.33 ± 0.02	19.96 ± 0.03	20.71 ± 0.03	21.91 ± 0.03	4	RGB	–2.24 ± 0.59	...
40993	247.85432	12.75811	19.53 ± 0.02	20.16 ± 0.03	20.93 ± 0.03	22.09 ± 0.04	4	RGB	–2.08 ± 0.58	40.22 ± 3.58
41082	247.84564	12.74666	18.86 ± 0.02	19.60 ± 0.04	20.57 ± 0.02	22.10 ± 0.04	4	RGB	–1.93 ± 0.43	41.73 ± 0.67
41371	247.81831	12.83070	20.04 ± 0.02	20.63 ± 0.04	21.27 ± 0.03	22.27 ± 0.04	4	RGB	–2.61 ± 0.75	46.11 ± 3.22
41423	247.81247	12.79209	20.88 ± 0.03	21.40 ± 0.04	21.95 ± 0.04	22.93 ± 0.09	4	RGB	–2.70 ± 1.08	34.79 ± 5.06
41460	247.80860	12.75741	19.40 ± 0.02	20.04 ± 0.04	20.79 ± 0.03	21.93 ± 0.03	4	RGB	–2.38 ± 0.60	48.20 ± 3.91
41642	247.79179	12.70463	20.86 ± 0.03	21.40 ± 0.04	21.94 ± 0.04	22.90 ± 0.10	4	RGB	–2.96 ± 1.07	48.09 ± 8.30
41737	247.78436	12.80075	19.94 ± 0.02	20.54 ± 0.04	21.18 ± 0.03	22.25 ± 0.04	4	RGB	–2.75 ± 0.73	...
41743	247.78386	12.80170	19.25 ± 0.02	19.91 ± 0.04	20.72 ± 0.02	22.04 ± 0.04	4	RGB	–2.09 ± 0.54	46.29 ± 0.95
41758	247.78206	12.80545	20.20 ± 0.02	20.77 ± 0.04	21.43 ± 0.03	22.49 ± 0.05	4	RGB	–2.21 ± 0.76	43.18 ± 3.51
41912	247.76877	12.77069	19.96 ± 0.02	20.55 ± 0.04	21.22 ± 0.03	22.28 ± 0.04	4	RGB	–2.46 ± 0.71	42.81 ± 2.78
42008	247.76005	12.80071	20.02 ± 0.02	20.58 ± 0.04	21.24 ± 0.03	22.32 ± 0.04	4	RGB	–2.17 ± 0.76	...
42096	247.75261	12.82550	19.40 ± 0.02	20.01 ± 0.04	20.77 ± 0.03	22.02 ± 0.04	4	RGB	–2.06 ± 0.60	54.61 ± 1.62
42149	247.74718	12.79045	19.01 ± 0.02	19.67 ± 0.04	20.45 ± 0.02	21.71 ± 0.04	4	RGB	–2.28 ± 0.56	44.48 ± 0.87
42170	247.74480	12.76128	20.85 ± 0.03	21.40 ± 0.04	21.97 ± 0.04	22.98 ± 0.08	4	RGB	–2.99 ± 1.00	32.72 ± 4.77
42241	247.73849	12.78898	18.53 ± 0.02	19.31 ± 0.04	20.33 ± 0.02	22.01 ± 0.04	4	RGB	–1.96 ± 0.39	...
42324	247.73111	12.76968	19.53 ± 0.02	20.10 ± 0.04	20.78 ± 0.03	21.85 ± 0.03	4	RGB	–2.19 ± 0.71	45.94 ± 2.18
42637	247.70322	12.82538	20.73 ± 0.03	21.27 ± 0.04	21.88 ± 0.04	22.87 ± 0.07	4	RGB	–2.30 ± 0.91	49.41 ± 3.16
42692	247.69607	12.75570	19.83 ± 0.02	20.42 ± 0.04	21.11 ± 0.03	22.20 ± 0.04	4	RGB	–2.25 ± 0.69	49.90 ± 1.45
42795	247.68541	12.82996	19.32 ± 0.02	19.95 ± 0.03	20.68 ± 0.03	21.80 ± 0.03	4	RGB	–2.32 ± 0.60	42.90 ± 1.57
42799	247.68313	12.70449	18.99 ± 0.02	19.71 ± 0.03	20.56 ± 0.03	21.86 ± 0.04	4	RGB	–2.36 ± 0.47	...
43428	247.61721	12.75078	19.89 ± 0.02	20.45 ± 0.04	21.14 ± 0.03	22.23 ± 0.04	4	RGB	–1.88 ± 0.73	...
43688	247.59341	12.86022	19.85 ± 0.02	20.41 ± 0.04	21.08 ± 0.03	22.08 ± 0.04	4	RGB	–2.11 ± 0.74	48.96 ± 2.14
12453	247.79788	12.55701	21.20 ± 0.03	21.29 ± 0.04	21.37 ± 0.03	22.84 ± 0.06	1	HB	...	...
14592	247.65505	12.63128	21.15 ± 0.03	21.30 ± 0.04	21.39 ± 0.03	22.86 ± 0.07	1	HB	...	...
20190	247.51674	12.86830	21.14 ± 0.03	20.98 ± 0.04	21.10 ± 0.04	22.58 ± 0.07	2	HB	...	...
35570	247.58018	12.95372	21.14 ± 0.03	21.21 ± 0.04	21.54 ± 0.03	22.84 ± 0.07	3	HB	...	...
40911	247.86293	12.73797	21.15 ± 0.03	21.45 ± 0.04	21.79 ± 0.04	23.16 ± 0.10	4	HB	...	...
41298	247.82626	12.79214	21.24 ± 0.03	21.41 ± 0.04	21.60 ± 0.03	22.94 ± 0.08	4	HB	...	...
42134	247.74830	12.78317	21.20 ± 0.03	21.34 ± 0.04	21.52 ± 0.03	23.17 ± 0.12	4	HB	...	...
42355	247.72872	12.78445	21.13 ± 0.04	21.30 ± 0.04	21.72 ± 0.04	22.92 ± 0.08	4	HB	...	...
42484	247.71764	12.81998	21.27 ± 0.03	21.38 ± 0.04	21.56 ± 0.03	22.68 ± 0.06	4	HB	...	...
42550	247.71108	12.80838	21.13 ± 0.03	21.40 ± 0.04	21.78 ± 0.03	22.87 ± 0.07	4	HB	...	...
14151	247.68517	12.67333	20.99 ± 0.03	21.41 ± 0.04	21.77 ± 0.03	22.70 ± 0.05	1	RHB-AGB	...	...
21089	247.48689	12.78015	20.41 ± 0.02	20.76 ± 0.04	21.13 ± 0.03	22.05 ± 0.04	2	RHB-AGB	...	...
40435	247.90930	12.74345	20.26 ± 0.02	20.75 ± 0.04	21.30 ± 0.03	22.35 ± 0.05	4	RHB-AGB	...	36.07 ± 3.27
41310	247.82408	12.74113	19.99 ± 0.02	20.53 ± 0.04	21.13 ± 0.03	22.25 ± 0.04	4	RHB-AGB	...	43.63 ± 5.72
41401	247.81359	12.74562	20.22 ± 0.02	20.60 ± 0.04	21.03 ± 0.03	22.00 ± 0.04	4	RHB-AGB	...	...
41532	247.80268	12.81217	20.45 ± 0.02	20.84 ± 0.04	21.24 ± 0.03	22.13 ± 0.04	4	RHB-AGB	...	...
42621	247.70415	12.80033	20.61 ± 0.03	21.10 ± 0.04	21.56 ± 0.03	22.50 ± 0.05	4	RHB-AGB	...	...
43167	247.64480	12.83356	19.92 ± 0.02	20.25 ± 0.04	20.54 ± 0.03	21.35 ± 0.03	4	RHB-AGB	...	...
43194	247.64213	12.84056	20.72 ± 0.03	21.09 ± 0.04	21.48 ± 0.03	22.41 ± 0.05	4	RHB-AGB	...	...

Column 1 lists the ID. Columns 2 and 3 list the coordinates. Columns 4 to 7 list the Strömgren magnitudes V, b, v and u. Column 8 lists on what CCD chip the star is located. Column 9 lists the evolutionary stage of the star. Column 10 lists the photometric metallicity as derived from the Calamida et al. (2007) calibration. Column 11 list the radial velocity, if available.

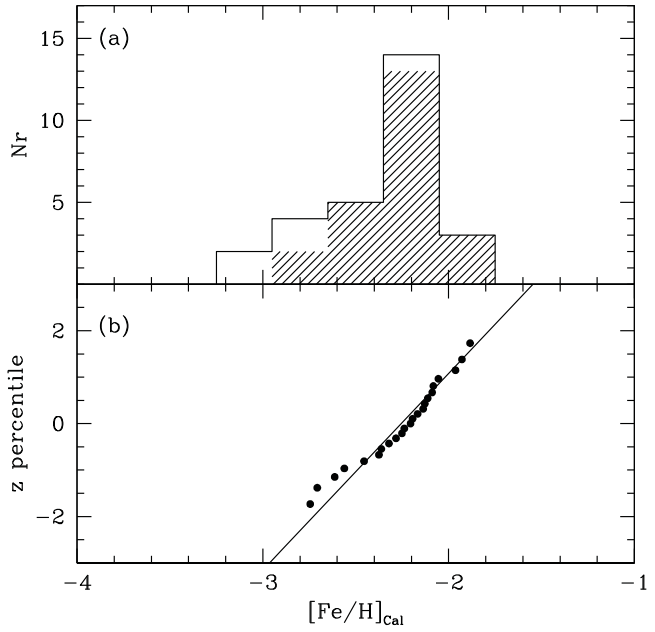

Fig. 28. a) Metallicity histogram for RGB stars in the Hercules dSph galaxy. The solid histogram shows the distribution for all stars in our final sample. The shaded histogram shows the distribution for stars in our final sample with $V_0 < 20.5$ (compare Fig. 22a). **b)** Corresponding normal probability plot, for stars in our final sample with $V_0 < 20.5$, assuming a normal distribution. The solid line indicates a linear fit to the data with a mean metallicity of [Fe/H] = −2.26 dex and $\sigma = 0.24$ dex.

In Sect. 8.1.2 we calculated the errors in $[Fe/H]_{Cal}$. When we take into account the uncertainties in zeropoints, extinction coefficients and colour terms we note that the errors are in general much larger than the σ of the metallicity distribution (compare Fig. 22a where we show the error in $[Fe/H]_{Cal}$). However, since the uncertainties in zeropoints, extinction coefficients and colour terms propagate as a magnitude offset, equal for all stars, we re-calculate the errors in metallicities excluding the uncertainties in zeropoints, extinction coefficients and colour terms (see Fig. 22a). We find that these errors in metallicity, for stars brighter than $V_0 = 20.5$, are smaller than the metallicity spread of 0.24 dex. This enables us to study the star-to-star scatter in $[Fe/H]_{Cal}$, making the profile of the distribution in Fig. 28 significant. We conclude that there is an abundance spread in the metallicity distribution for the RGB members of up to 1 dex.

10. Summary

We have, for the first time, presented a list of Hercules dSph galaxy members based on an analysis of radial velocity, evolutionary stage obtained from photometry, and stellar classification using SExtractor. In detail we provide the following inventory of the Hercules dSph galaxy

- 28 stars as RGB members based on their evolutionary stage, see Sect. 4.2. Of these, 19 have measured radial velocities (see Sect. 5.2).
- 9 stars as RHB-AGB members based on their evolutionary stage (see Sect. 4.2). Of these, 2 have radial velocities (see Sect. 5.2).
- 10 stars as BHB members based on their evolutionary stage, see Sect. 4.2.
- 8 stars that are possible variable stars based on their evolutionary stage, see Sect. 4.5.

Our best determination of the systemic velocity is 45.20 ± 1.09 km s^{-1} with a dispersion of 3.72 ± 0.91 km s^{-1}. We have shown that membership based on radial velocity alone is not a good method for the Hercules dSph galaxy, since it has a systemic velocity that falls well within the velocity distribution of the foreground dwarf stars belonging to the Milky Way.

Stellar metallicities have been determined using the Strömgren m_1 index with a calibration that translates $m_{1,0}$ to [Fe/H] for RGB stars. We found a mean metallicity of −2.35 dex. We also derived metallicities for our stars observed with FLAMES from measurements of the equivalent width of the Ca II IR triplet lines. The agreement between the two determinations was very good, with an offset of only 0.06 dex.

Finally, we have estimated the mean magnitude of the HB of the Hercules dSph galaxy to $V_0 = 21.17 \pm 0.05$ based on the 10 stars identified as BHB members. This gives a distance of 147^{+8}_{-7} kpc.

Acknowledgements. We would like to thank Andreas Korn for putting us on the right track to understand the erroneous spectra created by the CCD-glow. D.A. thanks Simon Hodgkin at the Wide Field Survey unit at IoA, Cambridge, for help with the INT data reduction. D.A. thanks Lennart Lindegren at Lund Observatory for his help in problems of mathematical nature. S.F. is a Royal Swedish Academy of Sciences Research Fellow supported by a grant from the Knut and Alice Wallenberg Foundation. M.I.W. is supported by a Royal Society University Research Fellowship.
Funding for the SDSS and SDSS-II has been provided by the Alfred P. Sloan Foundation, the Participating Institutions, the National Science Foundation, the US Department of Energy, the National Aeronautics and Space Administration, the Japanese Monbukagakusho, the Max Planck Society, and the Higher Education Funding Council for England. The SDSS Web Site is http://www.sdss.org/. The SDSS is managed by the Astrophysical Research Consortium for the Participating Institutions. The Participating Institutions are the American Museum of Natural History, Astrophysical Institute Potsdam, University of Basel, University of Cambridge, Case Western Reserve University, University of Chicago, Drexel University, Fermilab, the Institute for Advanced Study, the Japan Participation Group, Johns Hopkins University, the Joint Institute for Nuclear Astrophysics, the Kavli Institute for Particle Astrophysics and Cosmology, the Korean Scientist Group, the Chinese Academy of Sciences (LAMOST), Los Alamos National Laboratory, the Max-Planck-Institute for Astronomy (MPIA), the Max-Planck-Institute for Astrophysics (MPA), New Mexico State University, Ohio State University, University of Pittsburgh, University of Portsmouth, Princeton University, the United States Naval Observatory, and the University of Washington.

References

Anthony-Twarog, B. J., & Twarog, B. A. 1994, AJ, 107, 1577
Battaglia, G., Irwin, M., Tolstoy, E., et al. 2008, MNRAS, 383, 183
Belokurov, V., Zucker, D. B., Evans, N. W., et al. 2006, ApJ, 647, L111
Belokurov, V., Zucker, D. B., Evans, N. W., et al. 2007, ApJ, 654, 897
Belokurov, V., Walker, M. G., Evans, N. W., et al. 2008, ApJ, 686, L83
Belokurov, V., Walker, M. G., Evans, N. W., et al. 2009, MNRAS, 397, 1748
Bertin, E., & Arnouts, S. 1996, A&AS, 117, 393
Blecha, A., Cayatte, V., North, P., Royer, F., & Simond, G. 2000, in Optical and IR Telescope Instrumentation and Detectors, ed. M. Iye, & A. F. Moorwood, Proc. SPIE, 4008, 467
Bonanos, A. Z., Stanek, K. Z., Szentgyorgyi, A. H., Sasselov, D. D., & Bakos, G. Á. 2004, AJ, 127, 861
Bond, H. E. 1980, ApJS, 44, 517
Calamida, A., Bono, G., Stetson, P. B., et al. 2007, ApJ, 670, 400
Carretta, E., & Gratton, R. G. 1997, A&AS, 121, 95
Carretta, E., Gratton, R. G., Clementini, G., & Fusi Pecci, F. 2000, ApJ, 533, 215
Clem, J. L., VandenBerg, D. A., Grundahl, F., & Bell, R. A. 2004, AJ, 127, 1227
Cole, A. A., Smecker-Hane, T. A., Tolstoy, E., Bosler, T. L., & Gallagher, J. S. 2004, MNRAS, 347, 367
Coleman, M. G., de Jong, J. T. A., Martin, N. F., et al. 2007, ApJ, 668, L43
Faria, D., Feltzing, S., Lundström, I., et al. 2007, A&A, 465, 357
Gilbert, K. M., Guhathakurta, P., Kalirai, J. S., et al. 2006, ApJ, 652, 1188
Gilmore, G., Wilkinson, M. I., Wyse, R. F. G., et al. 2007, ApJ, 663, 948
Grebel, E. K., & Richtler, T. 1992, A&A, 253, 359
Grebel, E. K., Gallagher, III, J. S., & Harbeck, D. 2003, AJ, 125, 1926
Helmi, A., Irwin, M. J., Tolstoy, E., et al. 2006, ApJ, 651, L121

Hilker, M. 2000, A&A, 355, 994
Howell, S. B. 1989, PASP, 101, 616
Irwin, M., & Lewis, J. 2001, New Astron. Rev., 45, 105
Jordi, K., Grebel, E. K., & Ammon, K. 2006, A&A, 460, 339
Keller, S. C., Schmidt, B. P., Bessell, M. S., et al. 2007, Publications of the Astronomical Society of Australia, 24, 1
Kirby, E. N., Guhathakurta, P., & Sneden, C. 2008a, ApJ, 682, 1217
Kirby, E. N., Simon, J. D., Geha, M., Guhathakurta, P., & Frebel, A. 2008b, ApJ, 685, L43
Kleyna, J., Wilkinson, M. I., Evans, N. W., Gilmore, G., & Frayn, C. 2002, MNRAS, 330, 792
Kniazev, A. Y., Grebel, E. K., Pustilnik, S. A., Pramskij, A. G., & Zucker, D. B. 2005, AJ, 130, 1558
Koch, A. 2009, ArXiv e-prints
Koch, A., Grebel, E. K., Wyse, R. F. G., et al. 2006, AJ, 131, 895
Koch, A., Grebel, E. K., Kleyna, J. T., et al. 2007a, AJ, 133, 270
Koch, A., Wilkinson, M. I., Kleyna, J. T., et al. 2007b, ApJ, 657, 241
Koch, A., Grebel, E. K., Gilmore, G. F., et al. 2008a, AJ, 135, 1580
Koch, A., McWilliam, A., Grebel, E. K., Zucker, D. B., & Belokurov, V. 2008b, ApJ, 688, L13
Koch, A., Rich, R. M., Reitzel, D. B., et al. 2008c, ApJ, 689, 958
Lanfranchi, G. A., & Matteucci, F. 2007, A&A, 468, 927
Lind, K., Korn, A. J., Barklem, P. S., & Grundahl, F. 2008, A&A, 490, 777
Marigo, P., Girardi, L., Bressan, A., et al. 2008, A&A, 482, 883
Martin, N. F., de Jong, J. T. A., & Rix, H.-W. 2008, ApJ, 684, 1075
Olsen, E. H. 1983, A&AS, 54, 55
Olsen, E. H. 1984, A&AS, 57, 443
Olsen, E. H. 1993, A&AS, 102, 89
Olsen, E. H. 1994a, A&AS, 104, 429
Olsen, E. H. 1994b, A&AS, 106, 257
Olsen, E. H. 1995, A&A, 295, 710
Olszewski, E. W., Pryor, C., & Armandroff, T. E. 1996, AJ, 111, 750
Pasquini, L., Avila, G., Blecha, A., et al. 2002, The Messenger, 110, 1
Richtler, T. 1989, A&A, 211, 199
Robin, A. C., Reylé, C., Derrière, S., & Picaud, S. 2003, A&A, 409, 523
Rutledge, G. A., Hesser, J. E., & Stetson, P. B. 1997a, PASP, 109, 907
Rutledge, G. A., Hesser, J. E., Stetson, P. B., et al. 1997b, PASP, 109, 883
Schiavon, R. P., Barbuy, B., Rossi, S. C. F., & Milone, A. 1997, ApJ, 479, 902
Schlegel, D. J., Finkbeiner, D. P., & Davis, M. 1998, ApJ, 500, 525
Schuster, W. J., & Nissen, P. E. 1988, A&AS, 73, 225
Schuster, W. J., Beers, T. C., Michel, R., Nissen, P. E., & García, G. 2004, A&A, 422, 527
Shetrone, M. D., Côté, P., & Sargent, W. L. W. 2001, ApJ, 548, 592
Siegel, M. H. 2006, ApJ, 649, L83
Simon, J. D., & Geha, M. 2007, ApJ, 670, 313
Strigari, L. E., Bullock, J. S., Kaplinghat, M., et al. 2008, Nature, 454, 1096
Tonry, J., & Davis, M. 1979, AJ, 84, 1511
Ural, U., & Wilkinson, M. 2008, Astron. Nachr., 329, 1040
VandenBerg, D. A., Bergbusch, P. A., & Dowler, P. D. 2006, ApJS, 162, 375
Walker, M. G., Mateo, M., Olszewski, E. W., et al. 2006, AJ, 131, 2114
Walker, M. G., Mateo, M., Olszewski, E. W., et al. 2007, ApJ, 667, L53
Walsh, S. M., Jerjen, H., & Willman, B. 2007, ApJ, 662, L83
Walsh, S. M., Willman, B., & Jerjen, H. 2009, AJ, 137, 450
Zinn, R., & West, M. J. 1984, ApJS, 55, 45
Zucker, D. B., Belokurov, V., Evans, N. W., et al. 2006a, ApJ, 650, L41
Zucker, D. B., Belokurov, V., Evans, N. W., et al. 2006b, ApJ, 643, L103

Paper II

The Astrophysical Journal, 706:L150–L154, 2009 November 20 doi:10.1088/0004-637X/706/1/L150

A NEW LOW MASS FOR THE HERCULES dSph: THE END OF A COMMON MASS SCALE FOR THE DWARFS?

D. Adén[1], M. I. Wilkinson[2], J. I. Read[2,3], S. Feltzing[1], A. Koch[2], G. F. Gilmore[4], E. K. Grebel[5], and I. Lundström[1]
[1] Lund Observatory, Box 43, SE-22100 Lund, Sweden
[2] Department of Physics and Astronomy, University of Leicester, University Road, Leicester LE1 7RH, UK
[3] Institute for Theoretical Physics, University of Zurich, Winterthurerstrasse 190 8047, Switzerland
[4] Institute of Astronomy, Madingley Road, Cambridge CB3 0HA, UK
[5] Astronomisches Rechen-Institut, Zentrum für Astronomie der Universität Heidelberg, Mönchhofstr. 12-14, 69120 Heidelberg, Germany
Received 2009 June 26; accepted 2009 October 6; published 2009 November 4

ABSTRACT

We present a new mass estimate for the Hercules dwarf spheroidal (dSph) galaxy, based on the revised velocity dispersion obtained by Adén et al. The removal of a significant foreground contamination using newly acquired Strömgren photometry has resulted in a reduced velocity dispersion. Using this new velocity dispersion of 3.72 ± 0.91 km s^{-1}, we find a mass of $M_{300} = 1.9^{+1.1}_{-0.8} \times 10^6\, M_\odot$ within the central 300 pc, which is also the half-light radius, and a mass of $M_{433} = 3.7^{+2.2}_{-1.6} \times 10^6\, M_\odot$ within the reach of our data to 433 pc, significantly lower than previous estimates. We derive an overall mass-to-light ratio of $M_{433}/L = 103^{+83}_{-48}[M_\odot/L_\odot]$. Our mass estimate calls into question recent claims of a common mass scale for dSph galaxies. Additionally, we find tentative evidence for a velocity gradient in our kinematic data of 16 ± 3 km s^{-1} kpc^{-1}, and evidence of an asymmetric extension in the light distribution at ∼0.5 kpc. We explore the possibility that these features are due to tidal interactions with the Milky Way. We show that there is a self-consistent model in which Hercules has an assumed tidal radius of $r_t = 485$ pc, an orbital pericenter of $r_p = 18.5 \pm 5$ kpc, and a mass within r_t of $M_{\mathrm{tid},r_t} = 5.2^{+2.7}_{-2.7} \times 10^6\, M_\odot$. Proper motions are required to test this model. Although we cannot exclude models in which Hercules contains no dark matter, we argue that Hercules is more likely to be a dark-matter-dominated system that is currently experiencing some tidal disturbance of its outer parts.

Key words: galaxies: dwarf – galaxies: formation – galaxies: fundamental parameters – galaxies: individual (Hercules) – galaxies: kinematics and dynamics

1. INTRODUCTION

Dwarf spheroidal (dSph) galaxies are believed to play an important role in the formation and evolution of much more luminous galaxies (e.g., Gallagher & Wyse 1994). dSphs are characterized by their low surface brightness, low total luminosity, and spheroidal shapes that are consistent with their pressure-supported stellar kinematics (e.g., Grebel et al. 2003).

Knowledge of dSph masses is essential for comparison with cosmological simulations of galaxy formation. Good mass estimates help us to establish whether the paucity in the number of observed systems (a few tens) to the number of predicted satellite halos (several thousands) represents a fundamental failure of our cosmological model (e.g., Moore et al. 1999), or whether it is simply telling us that galaxy formation is inefficient on small scales (e.g., Read et al. 2006a). Recent studies have suggested that the dSph galaxies share a common mass within a certain radius (Walker et al. 2007, 2009; Strigari et al. 2008). If confirmed, this would be an important clue to the processes that regulate the formation of the lowest luminosity galaxies.

All mass estimates implicitly assume that contamination of the kinematic sample by foreground stars or unbound tidal tails is negligible, and that the system is in (or close to) virial equilibrium. Since the mass of an equilibrium stellar system is proportional to its velocity dispersion squared, an overestimate of the velocity dispersion will result in an inflated mass estimate. The assumption of virial equilibrium may be called into question if the system is tidally disrupting (Oh et al. 1995; Kroupa 1997; Klimentowski et al. 2007; Muñoz et al. 2008).

The recently discovered Hercules dSph (Belokurov et al. 2007), with an ellipticity of $e \sim 0.5$ (Coleman et al. 2007), is an example of a galaxy in which assumptions of equilibrium may be incorrect. In Adén et al. (2009), we showed that the mean velocity of the Hercules dSph is embedded in the foreground dwarf star velocity distribution. We used the Strömgren c_1 index to weed out the foreground dwarf stars. This index is able to clearly identify red giant branch (RGB) stars redder than the horizontal branch, enabling a separation of RGB stars in the dSph galaxy and foreground dwarf stars. By weeding out the foreground contaminants, we found that the dispersion for Hercules is reduced from 7.33 ± 1.08 km s^{-1} to 3.72 ± 0.91 km s^{-1}. In this Letter, we explore the consequences of this finding.

In Section 2, we derive a new mass for Hercules and show that it is not consistent with a common mass scale for the dSphs. In Section 3, we investigate the possibility of a velocity gradient in the kinematic data of Hercules. In Section 4, we discuss the relative importance of tides and dark matter in Hercules. Section 5 summarizes our conclusions.

2. MASS ESTIMATE FROM THE SPHERICAL JEANS EQUATIONS

We use the velocity dispersion, $\sigma_v = 3.72 \pm 0.91$ km s^{-1} (Adén et al. 2009), to constrain the mass of the Hercules dSph. We assume that the system is in dynamical equilibrium, is spherically symmetric, has an isotropic velocity distribution, and a flat velocity dispersion profile.[6] With these assumptions, the Jeans equation for the mass distribution (Equation (4.215)

[6] Note that Wolf et al. (2009) and Walker et al. (2009) find that their mass estimates at the half-light radius are insensitive to a wide range of mass models and velocity anisotropy parameterizations, so our results should not be sensitive to these assumptions.

Table 1
Summary of Determination of Systemic Velocities, Velocity Dispersions, Masses, and Metallicities for the Hercules dSph

Study	Number of Stars	v_{sys} (km s^{-1})	σ (km s^{-1})	$M_{\rm Furthest\ star}$ ($M_\odot$)	$M_{300\,\rm pc}$ ($M_\odot$)	$\langle$[Fe/H]$\rangle$[a] dex
Adén et al. (2009)	28 [RGB stars, c_1 sel.]	...	...	...	...	-2.35 ± 0.31
This study	32 [Only $V_{\rm rad}$ sel.]	40.87 ± 1.42	7.33 ± 1.08	$1.4^{+0.5}_{-0.4} \times 10^7$	$7.4^{+2.7}_{-2.1} \times 10^6$	...
This study	18 [RGB stars with $V_{\rm rad}$]	45.20 ± 1.09	3.72 ± 0.91	$3.7^{+2.2}_{-1.6} \times 10^6$	$1.9^{+1.1}_{-0.8} \times 10^6$	...

Notes. Columns: (1,2) number of stars in each study and a short description of how the stars were selected; (3,4) systemic velocities and velocity dispersions; (5) mass within the radius defined by the outermost RGB star in our study; (6) mass within the inner 300 pc; (7) mean metallicity. See Adén et al. (2009) for a full discussion of metallicities.
[a] See Adén et al. (2009).

in Binney & Tremaine 2008) becomes

$$\sigma_v^2 \frac{d\,\nu(r)}{dr} = -\frac{\nu(r)\,G\,M(r)}{r^2}, \quad (1)$$

where r is the three-dimensional distance from the center of the galaxy, $\nu(r)$ is the de-projected stellar density profile, and $M(r)$ is the enclosed mass. We use the exponential profile from Martin et al. (2008) to describe the stellar density profile. The de-projected exponential profile is given by Klimentowski et al. (2007) as (setting $m = 1$ in their Equation (4))

$$\nu(r) = \nu_0 \left(\frac{r}{\alpha}\right)^{-0.445} e^{-r/\alpha}, \quad (2)$$

where α is the exponential scale radius, related to the half-light radius as $r_h = 1.68\,\alpha$, and ν_0 is the central stellar density. Solving Equation (1) for $M(r)$ using Equation (2) yields

$$M(r) = \frac{r(r + 0.445\,\alpha)\sigma_v^2}{\alpha\,G}. \quad (3)$$

Using a half-light radius of 330^{+75}_{-52} pc (Martin et al. 2008) we solve Equation (3) for $r = 433$ pc, which corresponds to the outermost member in our kinematic sample (Table 1).

We estimate the error in the mass using 10^5 Monte Carlo realizations of the half-light radius, distance, and velocity dispersion of Hercules drawn from within the individual error bars on each parameter. In this way, we obtain $M_{433} = 3.7^{+2.2}_{-1.6} \times 10^6\,M_\odot$ (Figure 1). The quoted errors are 1σ limits from the Monte Carlo sampling. Assuming a total luminosity of $L = (3.6 \pm 1.1) \times 10^4\ L_\odot$ (Martin et al. 2008), we find a median mass-to-light ratio of $M_{433}/L = 103^{+83}_{-48}\ [M_\odot/L_\odot]$.

Adén et al. (2009) emphasize the importance of weeding out foreground contaminating dwarf stars. This is particularly vital for the Hercules dSph as its systemic velocity coincides with the bulk motion of dwarf stars in the Milky Way disk in the direction of Hercules. Using the contaminated[7] velocity dispersion (Table 1), we would obtain a mass of $1.4^{+0.5}_{-0.4} \times 10^7\,M_\odot$, almost a factor of 4 larger than the uncontaminated estimate.

2.1. Hercules and the "Common Mass Scale"

Strigari et al. (2008) speculate that the mass within a fixed radius, 300 pc, is approximately the same ($\sim 10^7\,M_\odot$) in all the observed dSphs. Our revised velocity dispersion implies a mass within the inner 300 pc (M_{300}) of only $1.9^{+1.1}_{-0.8} \times 10^6\,M_\odot$. This indicates that Hercules falls considerably below this "common mass scale" for dSphs. Since 300 pc is also approximately the half-light radius, this implies that Hercules also lies significantly off the Walker et al. (2009) enclosed half-light mass scaling relation.

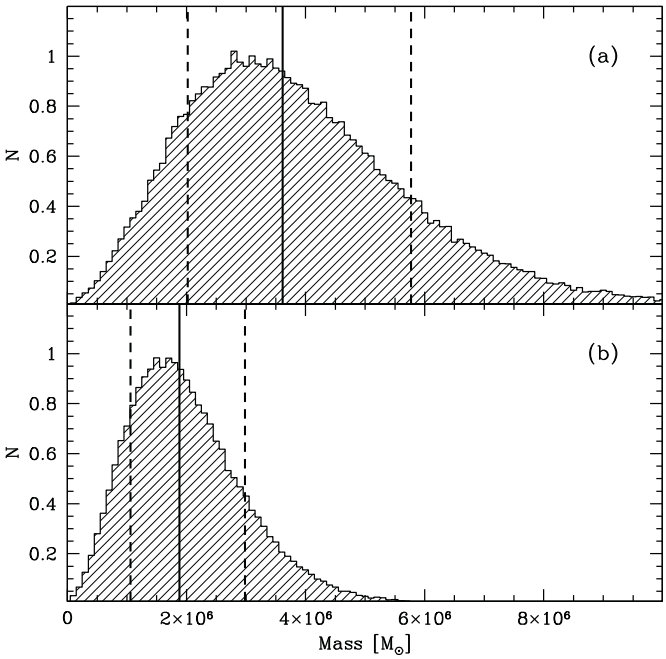

Figure 1. Distribution of Monte Carlo mass estimates for Hercules. Solid line indicates the median from the Monte Carlo sampling. Dashed lines indicate the 1σ limits from the Monte Carlo sampling. (a) Mass within the radius defined by the outermost RGB star in the kinematic sample, $r = 433$ pc. (b) Mass within the inner 300 pc.

To confirm that our result is not sensitive to our choice of surface brightness profile, we have repeated our calculation using a Plummer profile with scale radius $r_{\rm pl} = 321$pc (as used by Strigari et al. 2008). In this case, we find $M_{300} = 2.3 \times 10^6\,M_\odot$ in agreement with the mass calculated above. If instead we use our contaminated velocity dispersion and the exponential surface density profile, we obtain $M_{300} = 7.4^{+2.7}_{-2.1} \times 10^6\,M_\odot$ which agrees with the value presented in Strigari et al. (2008).

However, we note that Strigari et al. (2008) used a dispersion of 5.1 ± 0.9 km s^{-1} (taken from Simon & Geha 2007) to obtain their mass estimate. This is smaller than our contaminated value of 7.33 ± 1.08 km s^{-1}, yet they obtain a similar median mass to us. If we use a dispersion of 5.1 ± 0.9 km s^{-1} as they do, we

[7] Note that this "contaminated" dispersion has had its 3σ velocity outliers removed. Also, the initial candidate selection for the velocities was chosen using color–magnitude diagram cuts. Even so, a significant fraction of foreground stars remain in this sample and are detected only through the use of the Strömgren photometry.

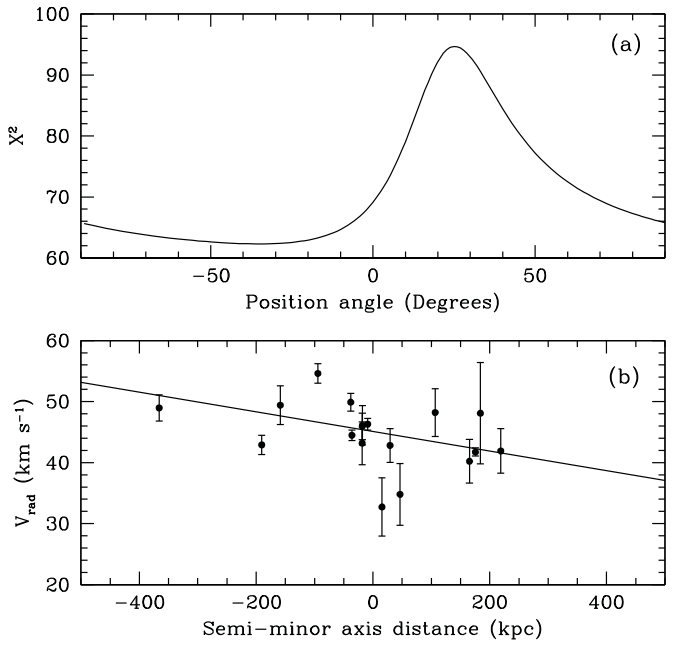

Figure 2. (a) χ^2 vs. the position angle. (b) $V_{\rm rad}$ vs. the semiminor axis distance. The solid line indicates the least-squares fit. "•" indicate members based on the Strömgren photometry (see Adén et al. 2009).

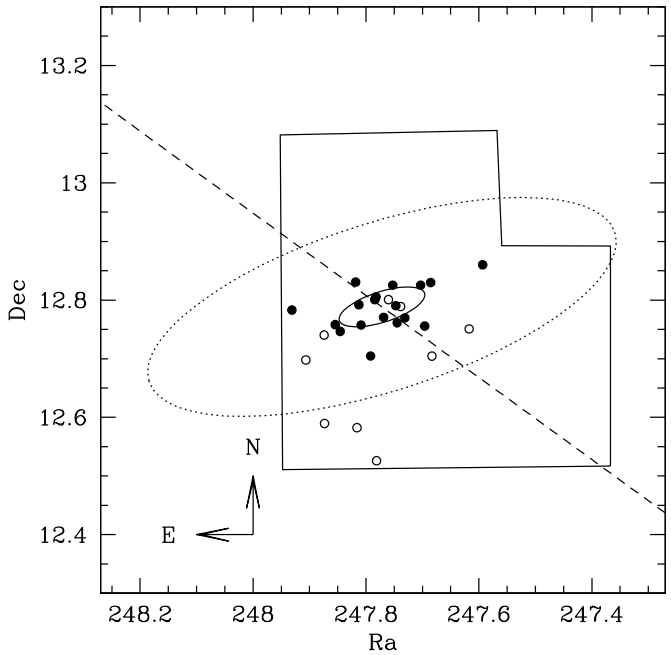

Figure 3. Spatial distribution on the sky of the stars identified as Hercules members from both spectroscopy and photometry. "○" indicate members based on the Strömgren photometry. "•" indicate members based on the Strömgren photometry for which there are radial velocity measurements. The dashed line indicates the semiminor axis for the position angle of our detected rotation axis. The solid ellipse represents the core radius and the dotted ellipse the inner border of the field region of the Hercules dSph (Coleman et al. 2007). Solid lines outline the footprint of the WFC used to obtain the Strömgren photometry.

obtain a mass $M_{300} = 3.6^{+1.5}_{-1.2} \times 10^6\ M_\odot$. This is just consistent with their determination within our mutual error bars. We note that the median M_{300} will depend on the details of the mass modeling procedure and so can be expected to differ between their study and ours (M. Walker 2009, private communication).

Additionally, we have repeated our calculation of the mass within 300 pc using a more recent estimate of the half-light radius, $r_h = 230$ pc, by Sand et al. (2009). This half-light radius is smaller and gives a mass that is ∼1.5 times more massive than the mass calculated using the half-light radius from Martin et al. (2008).

3. A VELOCITY GRADIENT IN HERCULES

The presence of a velocity gradient in a dSph could either be indicative of an intrinsic rotation, or a sign of tidal interaction with the Milky Way. In this section, we test for possible velocity gradients in Hercules.

Assuming that the rotation around the semiminor axis (in the ellipse that describes the orientation of the dSph) is more likely than around the semimajor axis, we can define the "semiminor axis distance" $d_{\rm mi}(\theta)$ as the distance, perpendicular to the semiminor axis, between the axis and the star. For each of the 18 RGB stars with radial velocities, we calculate this distance for different position angles θ. We then derive the gradient, $k_{\rm rot}$, and zeropoint, m_v, by solving the following equation with a least-squares fit for each position angle,

$$V_{\rm rad} = k_{\rm rot} \times d_{\rm mi}(\theta) + m_v, \quad (4)$$

where $V_{\rm rad}$ is the radial velocity measurement for each star. The least-squares fit to this function yields a χ^2 value for each θ (Figure 2(a)).

The distribution enclosed by $\chi^2_{\rm min} + 1$ corresponds to 1σ for a normal distribution (Press et al. 1992). We use this to obtain the error in the position angle which minimizes χ^2.

We find a position angle of -35^{+18}_{-23} degrees with a velocity gradient of 16 ± 3 km s^{-1} kpc^{-1}, and a zeropoint of 45.11 ± 0.38 km s^{-1}. We obtain a reduced χ^2 of 3.89 for our 18 stars with 2 degrees of freedom.

Following Walker et al. (2008), we estimate the significance of the velocity gradient using 10^5 Monte Carlo realizations. In each realization, we sample the velocity and spatial distributions independently. Thus, we scramble the correlation between velocity and position, while maintaining the original velocity distribution and spatial positions. This is valid as long as the phase space distribution function of the stars is separable (which implies that the velocity dispersion is independent of radius). We determine the significance of the velocity gradient by computing the fraction of realizations that fail to produce a χ^2 as low as the one calculated from the real data. We find a significance of the velocity gradient of 78% (1.23σ).

4. DISCUSSION

4.1. Galactic Tides in Hercules?

In the previous section, we found tentative evidence for a velocity gradient in the Hercules dSph. The peak-to-peak difference of ∼10 km s^{-1} within a radius of less than 1 kpc could be interpreted as the effect of Galactic tides (Read et al. 2006b). Interestingly, Martin (2009) recently estimated the orbit of Hercules based on the assumption that its elongation is tidally induced and predicted a velocity gradient of at least 7 km s^{-1} kpc^{-1} which is consistent with our observed gradient. Additionally, in Adén et al. (2009) we found that the spatial distribution of the Hercules stars is asymmetric at ∼0.5 kpc. There are three significant outlier stars to the south, but no corresponding members at this distance in either the northern or western fields (Figure 3). These three stars are unambiguously identified as RGB stars from the Strömgren photometry. We

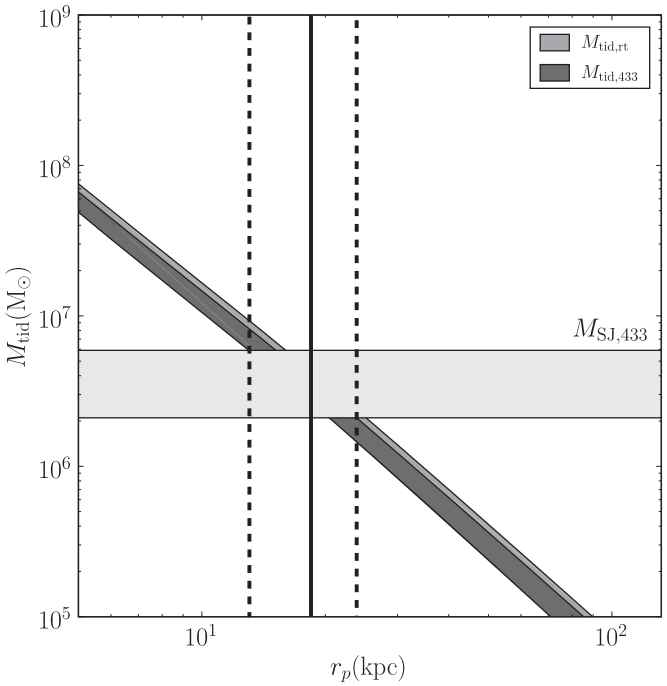

Figure 4. Tidally determined mass for Hercules as a function of orbital pericenter r_p. We assume a retrograde tidal radius of $r_t = 1$ kpc for this calculation. The horizontal gray band marks our mass estimate from the spherical Jeans equation $M_{\rm SJ,433}$ (see Section 2). The dark gray band marks our tidally determined mass within 433 pc $M_{\rm tid,433}$ for Hercules. The medium gray band shows $M_{{\rm tid},r_t}$, our tidally determined mass within r_t. The vertical solid and dashed lines mark the pericenters at which $M_{\rm tid,433} = M_{\rm SJ,433}$ (see Equation (6) for a formula giving the scaling of $M_{{\rm tid},r_t}$ with r_t).

now consider the possibility that the velocity gradient and the positional outliers are evidence that Hercules is being tidally disrupted, and use this information to obtain a second mass estimate for the system.

The tidal radius of a dSph depends on the potential of the host galaxy, the potential of the dSph, the orbit of the dSph within the host galaxy and the orbit of the stars within the dSph (e.g., Read et al. 2006c). We parameterize the Milky Way potential using the default model in Johnston et al. (2005), analyzed in the Galactic plane; and the Hercules potential using a generalized Hernquist profile (Hernquist 1990),

$$\rho(r) = \frac{M(3-\gamma)}{4\pi r_s^3}\left(\frac{r}{r_s}\right)^{-\gamma}\left(1+\frac{r}{r_s}\right)^{\gamma-4}, \quad (5)$$

where M is the total mass, r_s is the scale length, and γ is the central logarithmic cusp slope. We consider the ranges $0.3 < r_s < 3$ kpc and $0 < \gamma < 1$. Our results are not sensitive to these choices.

The orbit of the Hercules dSph is unknown but currently lies at a distance of 132 kpc from the galactic center and has a heliocentric velocity of 45.2 ± 1.09 km s^{-1}, which implies a galactocentric radial velocity of 145 ± 1.09 km s^{-1} (see Equation (5) in Courteau & van den Bergh 1999). Using the above potential model for the Milky Way and setting the tangential velocity component for Hercules to zero, this gives us a minimum apocenter for Hercules of $r_{a,\rm min} = 188.5$ kpc. Thus, we consider apocenter and pericenter ranges of $188.5 < r_a < 600$ kpc and $5 < r_p < 132$ kpc, respectively.

Read et al. (2006c) find that photometric features are typically seen beyond the retrograde tidal radius. To proceed, we make the assumption that the outliers in Figure 3 indicate the location of the retrograde tidal radius of Hercules, i.e., $r_t \sim 485$ pc. If we assume further that the tidal radius of Hercules is set at the pericenter of its orbit, we can solve Equation (7) of Read et al. (2006c) to calculate the mass, $M_{\rm tid}$, of Hercules as a function of its orbital pericenter, r_p, for our assumed ranges of r_s, γ, and r_a. We calculate both its mass within r_t ($M_{{\rm tid},r_t}$) and its mass within 433 pc ($M_{\rm tid,433}$) which can then be compared with our mass estimate based on the spherical Jeans equation ($M_{\rm SJ,433}$). The results of this calculation are given in Figure 4. The horizontal light gray band marks $M_{\rm SJ,433}$, the dark gray band marks $M_{\rm tid,433}$ and the medium gray band marks $M_{{\rm tid},r_t}$. The vertical solid and dashed lines mark the pericenters at which $M_{\rm tid,433} = M_{\rm SJ,433}$. The width of the tidal mass bands is due to the unknowns: r_s, γ, and r_a. However, to lowest order r_t depends only on the mean density enclosed within it, and so these bands are narrow. For this reason, we obtain an estimate of both the orbital pericenter of Hercules ($r_p = 18.5 \pm 5$ kpc) and its mass within the tidal radius ($M_{{\rm tid},r_t} = 5.2^{+2.7}_{-2.7} \times 10^6\, M_\odot$). The primary source of error on both of these quantities is our assumed tidal radius r_t. Empirically, we derive scalings of

$$r_p = 32\left(\frac{r_t}{1\ {\rm kpc}}\right)^{\beta}\ {\rm kpc}, \quad (6)$$

with $\beta = 0.76$ over the range $r_t = [0.4, 2]$ kpc, and

$$M_{{\rm tid},r_t} = 24 \times 10^6\left(\frac{r_t}{1\ {\rm kpc}}\right)^{\alpha} M_\odot, \quad (7)$$

with $\alpha = 2.1$ over the same range.

If we assume $r_{\rm t} = 485$ pc, we obtain a similar estimate of the pericentric distance as that obtained by Martin (2009).

4.2. Is Hercules a Dark-Matter-Free System?

We have shown that our Hercules data are consistent with the presence of dark matter. We now consider whether models without dark matter could also reproduce the data.

The most extreme scenario is that Hercules is disintegrating and its velocity dispersion arises solely due to the motion of its unbound member stars. If so, it will rapidly become unobservable (i.e., reach a lower surface brightness than the detection limit of the Sloan Digital Sky Survey (SDSS)). Hercules has a surface brightness of 27.2 ± 0.6 mag arcsec^{-2} (Martin et al. 2008). If the unbound stars are moving away from Hercules at a velocity equal to the velocity dispersion (3.72 ± 0.91 km s^{-1}), it would require only $\sim 200 \times 10^6$ years for the Hercules dSph to fall below the detection limit of SDSS ($\sim$30 mag arcsec^{-2}; Koposov et al. 2008). Given this short timescale, it is very unlikely that we would observe Hercules at this phase of its evolution.

Fellhauer et al. (2007) simulated the disruption of the UMa II dSph. Using a model that does not distinguish between luminous and dark matter they simulate the surface brightness, velocity dispersion, and the mean radial velocity for UMa II after 9 Gyr, 10 Gyr, and 11 Gyr (their Figure 9).

In the absence of dark matter, the equilibrium velocity dispersion (i.e., $\sigma^2 = G\,M/r$) for the Hercules dSph would be ~ 1 km s^{-1}, assuming a stellar mass of $5 \times 10^4\ M_\odot$ and a radius equal to the observed half-light radius (300 pc; Martin et al. 2008). This is much lower than the measured velocity dispersion of 3.72 ± 0.91 km s^{-1}. We conclude that the Hercules dSph can only be a dark-matter-free system if its velocity dispersion has

been inflated significantly, i.e., if it is in the advanced stages of tidal disruption.

However, in the simulations of Fellhauer et al. (2007), the evolutionary phase in which a tidal remnant exhibits both an inflated velocity dispersion and a velocity gradient, and remains centrally concentrated is very short. Within ∼1 Gyr the system goes from bound, with almost no signs of tidal disturbance, to complete disruption.

We note that Kroupa (1997) performed simulations of dSph galaxies without dark matter, and found that it is possible to obtain long-lived remnants whose properties are remarkably similar to those of Hercules in terms of velocity dispersion and velocity gradient (see his Figure 9). However, the remnants simulated by Kroupa (1997) are significantly more luminous than the Hercules dSph. Based on the simulations of Fellhauer et al. (2007), it seems unlikely that lower luminosity, purely stellar remnants with the correct properties could survive for a significant time.

It seems difficult to understand Hercules without dark matter. However, it could be dark matter dominated *and* experiencing significant tidal disturbance. In this case, our simple Jeans analysis may have overestimated its mass and Hercules might lie even further away from a possible common mass scale for the dSph galaxies.

5. CONCLUSIONS

We have calculated the mass of the Hercules dSph using the new velocity dispersion for the system obtained by Adén et al. (2009). We find that the mass within the volume enclosed by our observed stars is $3.7^{+2.2}_{-1.6} \times 10^6\ M_\odot$, leading to a mass-to-light ratio of $103^{+83}_{-48}[M_\odot/L_\odot]$. Interestingly, the mass within 300 pc is significantly lower than the "common mass scale" found by Strigari et al. (2008), suggesting that Hercules does not share the halo properties seen in other dSphs.

We found tentative evidence for a velocity gradient of 16 ± 3 km s^{-1} kpc^{-1}, and evidence of an asymmetric extension in the light distribution at ∼0.5 kpc. We explored the hypothesis that these features are due to tidal interactions with the Milky Way. Assuming a tidal radius of 485 pc, we show that a self-consistent model requires Hercules to be on an orbit with pericenter $r_p = 18.5 \pm 5$ kpc, and with a mass within r_t of $M_{\mathrm{tid},r_t} = 5.2^{+2.7}_{-2.7} \times 10^6\ M_\odot$.

We are very grateful to Matt Walker for useful discussions regarding the mass estimates in earlier works. We thank Pavel Kroupa for stimulating discussions. D.A. thanks Lennart Lindegren at Lund Observatory for help with statistics. S.F. is a Royal Swedish Academy of Sciences Research Fellow supported by a grant from the Knut and Alice Wallenberg Foundation. M.I.W. is supported by a Royal Society University Research Fellowship.

REFERENCES

Adén, D., et al. 2009, arXiv:0908.3489
Belokurov, V., et al. 2007, ApJ, 654, 897
Binney, J., & Tremaine, S. (ed.) 2008, in Galactic Dynamics (2nd ed.; Princeton, NJ: Princeton Univ. Press)
Coleman, M. G., et al. 2007, ApJ, 668, L43
Courteau, S., & van den Bergh, S. 1999, AJ, 118, 337
Fellhauer, M., et al. 2007, MNRAS, 375, 1171
Gallagher, J. S., III, & Wyse, R. F. G. 1994, PASP, 106, 1225
Grebel, E. K., Gallagher, J. S., III, & Harbeck, D. 2003, AJ, 125, 1926
Hernquist, L. 1990, ApJ, 356, 359
Johnston, K. V., Law, D. R., & Majewski, S. R. 2005, ApJ, 619, 800
Klimentowski, J., et al. 2007, MNRAS, 378, 353
Koposov, S., et al. 2008, ApJ, 686, 279
Kroupa, P. 1997, New Astron., 2, 139
Martin, N. 2009, MNRAS, submitted
Martin, N. F., de Jong, J. T. A., & Rix, H.-W. 2008, ApJ, 684, 1075
Moore, B., Ghigna, S., Governato, F., Lake, G., Quinn, T., Stadel, J., & Tozzi, P. 1999, ApJ, 524, L19
Muñoz, R. R., Majewski, S. R., & Johnston, K. V. 2008, ApJ, 679, 346
Oh, K. S., Lin, D. N. C., & Aarseth, S. J. 1995, ApJ, 442, 142
Press, W. H., Teukolsky, S. A., Vetterling, W. T., & Flannery, B. P. 1992, Numerical Recipes in FORTRAN: The Art of Scientific Computing (2nd ed.; Cambridge: Cambridge Univ. Press)
Read, J. I., Pontzen, A. P., & Viel, M. 2006a, MNRAS, 371, 885
Read, J. I., Wilkinson, M. I., Evans, N. W., Gilmore, G., & Kleyna, J. T. 2006b, MNRAS, 367, 387
Read, J. I., Wilkinson, M. I., Evans, N. W., Gilmore, G., & Kleyna, J. T. 2006c, MNRAS, 366, 429
Sand, D. J., Olszewski, E. W., Willman, B., Zaritsky, D., Seth, A., Harris, J., Piatek, S., & Saha, A. 2009, ApJ, 704, 898
Simon, J. D., & Geha, M. 2007, ApJ, 670, 313
Strigari, L. E., et al. 2008, Nature, 454, 1096
Walker, M. G., Mateo, M., & Olszewski, E. W. 2008, ApJ, 688, L75
Walker, M. G., Mateo, M., Olszewski, E. W., Peñarrubia, J., Wyn Evans, N., & Gilmore, G. 2009, ApJ, 704, 1274
Walker, M. G., et al. 2007, ApJ, 667, L53
Wolf, J., Martinez, G. D., Bullock, J. S., Kaplinghat, M., Geha, M., Munoz, R. R., Simon, J. D., & Avedo, F. F. 2009, arXiv:0908.2995

Paper III

A&A 525, A153 (2011)
DOI: 10.1051/0004-6361/201014963

Astronomy & Astrophysics

An abundance study of red-giant-branch stars in the Hercules dwarf spheroidal galaxy

D. Adén[1], K. Eriksson[2], S. Feltzing[1], E. K. Grebel[3], A. Koch[4], and M. I. Wilkinson[4]

[1] Lund Observatory, Box 43, 22100 Lund, Sweden
e-mail: daniel.aden@astro.lu.se
[2] Department of Physics and Astronomy, Uppsala University, Box 515, 751 20 Uppsala, Sweden
[3] Astronomisches Rechen-Institut, Zentrum für Astronomie der Universität Heidelberg, Mönchhofstr. 12-14, 69120 Heidelberg, Germany
[4] Department of Physics and Astronomy, University of Leicester, University Road, Leicester LE1 7RH, UK

Received 10 May 2010 / Accepted 24 October 2010

ABSTRACT

Context. Dwarf spheroidal galaxies are some of the most metal-poor, and least luminous objects known. Detailed elemental abundance analysis of stars in these faint objects is key to our understanding of star formation and chemical enrichment in the early universe, and may provide useful information on how larger galaxies form.
Aims. Our aim is to provide a determination of [Fe/H] and [Ca/H] for confirmed red-giant branch member stars of the Hercules dwarf spheroidal galaxy. Based on this we explore the ages of the prevailing stellar populations in Hercules, and the enrichment history from supernovae. Additionally, we aim to provide a new simple metallicity calibration for Strömgren photometry for metal-poor, red giant branch stars.
Methods. High-resolution, multi-fibre spectroscopy and Strömgren photometry are combined to provide as much information on the stars as possible. From this we derive abundances by solving the radiative transfer equations through MARCS model atmospheres.
Results. We find that the red-giant branch stars of the Hercules dSph galaxy are more metal-poor than estimated in our previous study that was based on photometry alone. From this, we derive a new metallicity calibration for the Strömgren photometry. Additionally, we find an abundance trend such that [Ca/Fe] is higher for more metal-poor stars, and lower for more metal-rich stars, with a spread of about 0.8 dex. The [Ca/Fe] trend suggests an early rapid chemical enrichment through supernovae of type II, followed by a phase of slow star formation dominated by enrichment through supernovae of type Ia. A comparison with isochrones indicates that the red giants in Hercules are older than 10 Gyr.

Key words. galaxies: dwarf – galaxies: evolution – galaxies: individual: Hercules – stars: abundances

1. Introduction

Over the past few years, the number of known dwarf spheroidal (dSph) galaxies orbiting the Milky Way has more than doubled through systematic searches in large photometric surveys such as the Sloan Digital Sky Survey (e.g., Zucker et al. 2006; Belokurov et al. 2007). These recently discovered dSph galaxies have much lower surface brightness than the previously known dSph galaxies. Typically, these systems have total luminosities $M_V > -6$ (e.g., Martin et al. 2008), so they are named ultra-faint (e.g., Koch 2009). Additionally, they are so faint that thus far they have only been detected around the Milky Way, but more sensitive surveys in the future may yield additional detections also at larger distances (Tollerud et al. 2008). These galaxies are also more metal-poor than the classical, more luminous dSph galaxies (e.g., Simon & Geha 2007; Kirby et al. 2008b)

Very metal-poor stars have been found in the Galactic halo (e.g., Schörck et al. 2009). However, studies of the more luminous dSph galaxies (e.g., Koch et al. 2006; Helmi et al. 2006) have found a significant lack of stars with [Fe/H] ≤ -3 when compared to the stars of the Milky Way halo. Since dSph galaxies may be the building blocks of parts of the Galactic halo (see Grebel & Gallagher 2004, for a discussion of the ages of stellar populations in the Galactic dSphs and halo), this result was considered a problem for our current understanding of the formation of large galaxies (Schörck et al. 2009). However, recent studies of the ultra-faint (e.g., Kirby et al. 2008b; Frebel et al. 2010b; Norris et al. 2010; Simon et al. 2010) and the classical (e.g., Starkenburg et al. 2010; Frebel et al. 2010a) dSph galaxies have discovered stars with [Fe/H] ≤ -3, thus reigniting the discussion of the origin of the Galactic halo. Whether the metallicity distribution functions of the halo and of the dSph galaxies agree still remain to be determined. Additional abundance studies are needed for both halo and dSph stars, in order to rule out selection biases due to low number statistics.

Studies of [α/Fe] in the stars in the more luminous dSph galaxies suggest that stars more metal-rich than [Fe/H] > -2 have lower [α/Fe] ratios, whilst more metal-poor stars (from now taken to be stars with [Fe/H] < -2) have about the same enhancement in the α-elements relative to iron as the stars in the halo and disk of the Milky Way (see, e.g., Shetrone et al. 2001; Geisler et al. 2007; Tolstoy et al. 2009). This could be interpreted as support for an early accretion of dSphs. The discrepancy is poorly constrained for the recently discovered ultra-faint dSph galaxies, with notable exceptions for a few stars in these ultra-faint objects (Feltzing et al. 2009; Frebel et al. 2010b).

The Hercules dSph galaxy lies at a distance of ~150 kpc from us (Adén et al. 2009a) and it has a V-band surface brightness of only 27.2 ± 0.6 mag arcsec^{-2} (Martin et al. 2008). Previous studies, based on photometry and the measurements of

Table 1. Properties of the Hercules dSph galaxy.

Parameter			Footnote
α_0	J2000	16 31 05.2 ± 2.5	[a]
δ_0	J2000	+ 12 47 18 ± 17	[a]
r_h	arcmin	$8.6^{+1.8}_{-1.1}$	[a]
M_V		−6.6 ± 0.3	[a]
D	kpc	147^{+8}_{-7}	[b]
$E(B-V)$		0.062	[b]
M_{300}	$M_\odot$	$1.9^{+1.1}_{-0.8} \times 10^6$	[c]

Notes. [(a)] The centroid, α_0 and δ_0, half-light radius, r_h, and absolute magnitude are taken from Martin et al. (2008). [(b)] The distance, D, and reddening, $E(B-V)$, are taken from Adén et al. (2009a). [(c)] The mass within the central 300 pc is taken from Adén et al. (2009b).

the near-infrared Ca II triplet lines in red giant branch (RGB) stars, have found a mean metallicity of [Fe/H] ∼ −2.3 (Simon & Geha 2007; Adén et al. 2009a). In Table 1 we provide a list with additional properties of the Hercules dSph galaxy.

A study using spectrum synthesis of Fe I lines (Kirby et al. 2008b) found a lower mean metallicity of −2.58 ± 0.51 dex. Koch et al. (2008b) found, using high-resolution spectroscopy of two Hercules RGB stars, that the hydrostatic burning α-elements (e.g., Mg, O) are strongly enhanced, while the heavy (mainly) s-process elements (e.g., Y, Sr, Ba, La) are largely depleted. The low [Fe/H] observed for the Hercules dSph galaxy suggests that star formation ceased relatively early after the formation of this galaxy. Thus, detailed elemental abundances for stars in the ultra-faint dSph galaxies are key to our understanding of star formation and chemical enrichment in the early universe.

In this study we will determine some of the elemental abundance trends in the ultra-faint Hercules dSph galaxy.

This paper is organised as follows: in Sect. 2 we describe the observations and the reduction of our spectra. In Sect. 3 we describe the determination of the stellar parameters for each star. Section 4 deals with the abundance analysis. In Sect. 5 we provide a comparison with abundances determined in other studies, in Sect. 6 we show and discuss our results and Sect. 7 concludes the article.

2. Observations, data reduction, and measurement of equivalent widths

2.1. Selection of targets

Some of the new ultra-faint dSph galaxies are seen through a significant portion of the Milky Way disk. Moreover, sometimes they have systemic velocities very similar to the bulk motion of the stars in the Milky Way disk. This is the case for the Hercules dSph galaxy (Adén et al. 2009a). Thus, when studying systems like Hercules it is very important that the stars are confirmed members of the galaxy, and not foreground contaminating stars that belong to the Milky Way. In Adén et al. (2009a) we showed that the mean velocity of the Hercules dSph is very similar to the velocity distribution of the foreground dwarf stars, making it difficult to disentangle the dSph galaxy stars from the foreground dwarf stars using radial velocity measurements alone. We used the Strömgren c_1 index to identify the RGB stars that belong to the dSph galaxy and showed that a proper cleaning of the sample results in a smaller value for the velocity dispersion of the system. This has implications for galaxy properties derived from such velocity dispersions, e.g., resulting in a lower mass

Table 2. Data for the RGB stars in the Hercules dSph galaxy observed with FLAMES.

ID	RA J2000.0	Dec J2000.	V	$(b-y)$	S/N	Used
12 175	247.81 591	12.58 238	18.72	0.83	35	*
42 241	247.73 849	12.78 898	18.72	0.82	36	*
41 082	247.84 564	12.74 666	19.05	0.78	23	
42 149	247.74 718	12.79 045	19.21	0.70	25	*
41 743	247.78 386	12.80 170	19.44	0.70	24	*
42 795	247.68 541	12.82 996	19.51	0.67	23	*
40 789	247.87 404	12.74 030	19.52	0.67	20	*
41 460	247.80 860	12.75 741	19.60	0.69	21	*
42 096	247.75 261	12.82 550	19.59	0.66	20	*
40 993	247.85 432	12.75 811	19.73	0.67	20	*
42 324	247.73 111	12.76 968	19.72	0.62	13	*
12 729	247.78 123	12.52 606	19.84	0.67	12	*
40 222	247.93 108	12.78 307	20.01	0.62	11	
42 692	247.69 607	12.75 570	20.02	0.63	12	
43 688	247.59 341	12.86 022	20.04	0.61	8	
43 428	247.61 721	12.75 078	20.09	0.60	11	
11 239	247.87 333	12.58 958	20.11	0.61	9	
41 912	247.76 877	12.77 069	20.15	0.64	8	
42 008	247.76 005	12.80 071	20.21	0.61	9	
41 371	247.81 831	12.83 070	20.23	0.63	10	

Notes. Column 1 lists the RGB star ID (Adén et al. 2009a). Columns 2 and 3 list the coordinates. Column 4 lists the V magnitude and column 5 lists the $(b-y)$ colour. Column 6 lists estimates of the S/N in the final spectra and Col. 7 indicates whether the star was analysed in this work, compare Sect. 4.

(Adén et al. 2009b; Walker et al. 2009). In this study, we revisit the previously identified RGB stars of the Hercules dSph galaxy with high-resolution spectroscopy.

The RGB stars for this study were taken from the list of Hercules dSph galaxy members in Adén et al. (2009a). We selected RGB stars brighter than $V_0 \sim 20$ (see Fig. 1). Stars fainter than $V_0 \sim 20$ were not considered since the signal-to-noise ratio, per pixel, (S/N) would be too low for equivalent width measurements. In total, 20 RGB stars were selected (see Table 2).

2.2. Observations

Our spectroscopy was carried out using the multiobject spectrograph Fibre Large Array Multi Element Spectrograph (FLAMES) at the Very Large Telescope (VLT) on Paranal. The observations, 18 observing blocks of 60 min each made in service mode, are summarised in Table 3. Operated in Medusa fibre mode, this instrument allows for the observation of up to 130 targets at the same time (Pasquini et al. 2002). 23 fibres were dedicated to observing blank sky. We used the GIRAFFE/HR13 grating, which provides a nominal spectral resolution of $R \sim 20\,000$ and a wavelength coverage from 6100 Å to 6400 Å. We verified the spectral resolution by measuring the full-width-half maximum of telluric emission lines in the combined sky spectrum.

2.3. Data reduction and measurement of equivalent widths

The FLAMES observations were reduced with the standard GIRAFFE pipeline, version 2.8.1 (Blecha et al. 2000). This pipeline provides bias subtraction, flat fielding, dark-current subtraction, and accurate wavelength calibration from a ThAr lamp.

Table 3. Summary of the spectroscopic observations with FLAMES.

Date	Exp. time [min]
17 May 2009	180
20 May 2009	120
22 May 2009	120
23 May 2009	120
24 May 2009	60
25 May 2009	180
26 May 2009	60
13 June 2009	180
18 June 2009	60
Total Exp. Time	1080

Notes. Column 1 lists the date of observation and Col. 2 the exposure time.

The 23 sky spectra were combined and subtracted from the object spectra with the task SKYSUB in the SPECRED package in IRAF[1].

Next, the object spectra from the individual frames were Doppler-shifted to the heliocentric rest frame and median-combined into the final one-dimensional spectrum. When combining the object spectra we used an average sigma clipping algorithm, rejecting measurements deviating by more than 3σ, in order to remove cosmic rays.

Finally, we normalised the spectra with the task CONTINUUM in the ONEDSPEC package in IRAF. We used a Spline1 function of the 1st order. We note that the nomalisation was not optimal over the entire wavelength range. To accomodate for this, we set the continuum for each line individually when measuring the equivalent widths, W_λ.

The W_λ for the absorption lines were measured by fitting a Gaussian profile to each of the lines using the IRAF task SPLOT. However, for some of the weak lines with low S/N it was better to determine the W_λ by integration of the pixel values using the "e" option in SPLOT. The W_λs are listed in Table 4.

We were not able to identify any absorption lines in the continuum for stars fainter than $V_0 = 19.80$. The S/N for the spectra for these stars are about 10. Thus, 8 stars were discarded from the abundance analysis (compare Table 2). Additionally, we were not able to remove the sky emission for RGB star 41082 to a satisfying level, and the S/N was lower than expected from the stars magnitude, indicating that something may have gone wrong with the positioning of the fibre. Therefore, the spectrum for this star was discarded also, leaving us with spectra for 11 usable RGB targets.

3. Stellar parameters

The effective temperature ($T_{\rm eff}$) is often determined by requiring that the abundances derived from individual Fe lines are independent of the excitation potential for the lines. This was not an option for us due to the small number of Fe I lines for each star. Instead, we calculated $T_{\rm eff}$ from Strömgren photometry using the calibration in Alonso et al. (1999). The photometry is from Adén et al. (2009a) and has been corrected for interstellar extinction using the dust maps by (Schlegel et al. 1998). These maps give a reddening of $E(B-V) = 0.062$. We estimated the errors in $T_{\rm eff}$ using the uncertainties for the Strömgren photometry. Since we are using deep photometry, and are only using stars at the brighter end of the luminosity function, the errors are essentially the same for the stars in the sample. We find a typical error of about 100 K for all stars.

Surface gravities, $\log g$, were estimated using an isochrone by VandenBerg et al. (2006) with [Fe/H] = −2.31 (most metal-poor isochrone available), an age of 12 Gyr, colour transformations by Clem et al. (2004), and no α-enhancement. Figure 1 shows the colour–magnitude diagram for the Hercules dSph galaxy with $\log g$ values indicated. The isochrone was shifted using the distance modulus derived in Adén et al. (2009a), $(m-M) = 20.85 \pm 0.11$.

To estimate how sensitive our value of $\log g$ is to the choice of the age for the isochrone, we repeated the above derivation for isochrones with an age of 8 and 18 Gyr, and [Fe/H] = −2.31. We find that the estimated value of $\log g$ deviated by a maximum of ∼0.1 dex from the initial $\log g$ when the age was changed. Additionally, for comparison with an isochrone based on a different stellar evolutionary model, we compared with values of $\log g$ derived using the Darthmouth isochrones (Dotter et al. 2008) with colour transformations by Clem et al. (2004), and similar age and metallicity as for the isochrone by VandenBerg et al. (2006). We find that the values of $\log g$ estimated using the two sets of isochrones differ by about 0.1 dex.

Finally, we estimated the contribution to the error in $\log g$ from the uncertainty in the distance modulus and magnitude using 10^6 Monte Carlo realisations of the distance modulus and magnitude drawn from within the individual error bars on each parameter. We find that the values of $\log g$ deviated by ∼0.1 dex from the initial $\log g$. Based on these three error estimates, we define an upper limit to the error in $\log g$ of 0.35 dex to make sure that the error is not under-estimated.

In Sect. 4 we investigate how different values of $\log g$ affect the abundance analysis.

We estimated the microturbulence, $\xi_{\rm t}$, using the $\xi_{\rm t}$ and $\log g$ for metal-poor halo stars from Andrievsky et al. (2010). These stars have about the same metallicity and $\log g$ as our Hercules RGB stars. A least-square fit to their data, in $\xi_{\rm t}$ vs. $\log g$ space (Fig. 2), of 35 giant stars yields

$$\xi_{\rm t} = -0.38(\pm0.06)\log g + 2.47(\pm0.1). \quad (1)$$

We estimated the errors in $\xi_{\rm t}$ using the uncertainties for the least-square fit (Eq. (1)) and an uncertainty in $\log g$ of 0.3 dex. We find a typical error in $\xi_{\rm t}$ of ~ 0.2 km s^{-1}.

The final stellar parameters used in the abundance analysis are summarised in Table 5.

4. Abundance analysis

Model atmospheres were calculated for the programme stars with the code MARCS according to the procedures described in Gustafsson et al. (2008), and using the fundamental parameters in Table 5. Next, a line list was compiled in the wavelength region 6120–6400 Å with spectral lines from neutral and singly ionised atoms from the VALD database (Piskunov et al. 1995; Ryabchikova et al. 1997; Kupka et al. 1999, 2000). Equivalent widths or synthetic spectra were then computed from radiative transfer calculations in spherical geometry in the model atmospheres using the Eqwi/Bsyn codes that share many subroutines and data files with MARCS making the analysis largely self-consistent.

For stars with at least two lines measurable, we adopt the mean of the abundances derived from the individual W_λ for each

[1] IRAF is distributed by the National Optical Astronomy Observatories, which are operated by the Association of Universities for Research in Astronomy, Inc., under cooperative agreement with the National Science Foundation.

Table 4. Equivalent width measurements.

			RGB	12 175	42 241	42 149	41 743	42 795	40 789	41 460	42 096	40 993	42 324	12 729
Ion	λ	$\log gf$	EP	W_λ	W_λ	W_λ	W_λ	W_λ	W_λ	W_λ	W_λ	W_λ	W_λ	W_λ
	(Å)	(dex)	eV	(mÅ)	(mÅ)	(mÅ)	(mÅ)	(mÅ)	(mÅ)	(mÅ)	(mÅ)	(mÅ)	(mÅ)	(mÅ)
Ca I	6122.22	−0.386	1.886	46	89	44	66	...	24	49	89	52	57	...
Ca I	6162.17	−0.167	1.899	72	122	35	96	...	43	...	70	...	61	69
Fe I	6137.69	−1.403	2.588	41	148	48	65	...	43	...	...	66	...	86
Fe I	6151.62	−3.299	2.176	...	62	...	...	...	...	...	...	...	...	...
Fe I	6173.34	−2.880	2.223	...	96	...	52	...	...	...	...	65	...	...
Fe I	6180.20	−2.586	2.727	...	38	...	13	...	...	...	...	30	...	...
Fe I	6200.31	−2.437	2.608	...	75	...		...	14	...	...	...	...	...
Fe I	6213.43	−2.482	2.223	...	92	25	35	...	...	...	...	49	...	65
Fe I	6219.28	−2.433	2.198	...	111	...	58	...	...	...	...	40	...	...
Fe I	6232.64	−1.223	3.654	...	59	...	...	...	...	...	...	...	...	...
Fe I	6246.32	−0.733	3.602	...	87	...	...	...	...	...	...	...	...	...
Fe I	6252.56	−1.687	2.404	50	149	...	81	...	...	...	71	...	...	98
Fe I	6265.13	−2.550	2.176	...	124	...	83	...	...	...	43	...	...	...
Fe I	6270.23	−2.464	2.858	...	42	...	...	...	...	...	...	...	...	...
Fe I	6301.50	−0.718	3.654	...	119	...	42	...	...	...	...	...	...	...
Fe I	6302.49	−0.973	3.686	...	57	...	...	...	...	...	...	...	...	...
Fe I	6322.69	−2.426	2.588	...	97	...	40	...	...	...	...	...	...	...
Fe I	6335.33	−2.177	2.198	36	121	...	91	27	...	...	58	51	...	50
Fe I	6336.82	−0.856	3.686	...	83	...	...	...	...	...	...	33	...	...
Fe I	6355.03	−2.350	2.845	...	55	...	...	...	...	...	...	...	...	...
Fe I	6393.60	−1.432	2.433	69	138	...	109	35	39	...	65	68	...	85
Fe II	6149.26	−2.841	3.899	...	30	...	...	...	...	...	...	...	...	...
Fe II	6247.56	−2.435	3.892	...	40	...	...	...	...	...	...	...	...	...

Table 5. Photometry and model parameters used in the abundance analysis of the stars.

ID	Other ID	V_0	$(b-y)_0$	[Fe/H]	$T_{\rm eff}$	$\log g$	$\xi_{\rm t}$	S/N
				dex	K	dex	km s^{-1}	
12 175	...	18.53	0.78	−3.17	4370	0.78	2.17	35
42 241	Her−2	18.53	0.78	−2.03	4270	0.78	2.17	36
41 082	Her−3	18.86	0.74	...	4340	0.97	2.10	23
42 149	...	19.01	0.66	−2.95	4540	1.06	2.07	25
41 743	...	19.25	0.66	−2.42	4520	1.19	2.02	24
42 795	...	19.32	0.63	−3.17	4620	1.22	2.01	23
40 789	...	19.33	0.63	−2.88	4600	1.24	2.00	20
41 460	...	19.40	0.64	−3.10	4590	1.27	1.99	21
42 096	...	19.40	0.62	−2.60	4620	1.27	1.99	20
40 993	...	19.53	0.63	−2.38	4600	1.33	1.97	20
42 324	...	19.53	0.57	−2.70	4740	1.33	1.97	13
12 729	...	19.65	0.63	−2.35	4640	1.40	1.94	12

Notes. Column 1 lists the RGB star ID (Adén et al. 2009a). Column 2 lists the ID from Koch et al. (2008b). Column 3 lists the V_0 magnitude and Col. 4 lists the $(b-y)_0$ colour. Column 5 lists the metallicity as determined in Sect. 4.2. Columns 6 to 8 list the stellar parameters as determined in Sect. 3. Column 9 lists an estimate of the S/N.

element as the final elemental abundances. For stars more difficult, in terms of identifying absorption lines, the final elemental abundances are determined using a χ^2-test (see Sect. 4.2.3)

4.1. Elemental abundance errors

For elements with more than four lines measured, the random errors in the elemental abundance ratios were calculated as

$$\epsilon_{\rm rand,[X/H]} = \frac{\sigma_{\rm X}}{\sqrt{N}} \quad (2)$$

where X is the element, σ is the standard deviation of the abundances derived from the individual W_λ, and N the number of lines for that element. For elements with two to four lines measured, the uncertainty in the measurement of W_λ, ϵ_{W_λ}, was estimated using the relation in Cayrel (1988). The random errors in the elemental abundances were then estimated using 10^5 Monte Carlo realisations of W_λ, drawn from within the probability distribution of W_λ given ϵ_{W_λ}. For each value of W_λ, we recalculate an elemental abundance using the relation $\log(A) \propto \log(W_\lambda)$ where A is the elemental abundance. We note that the probability

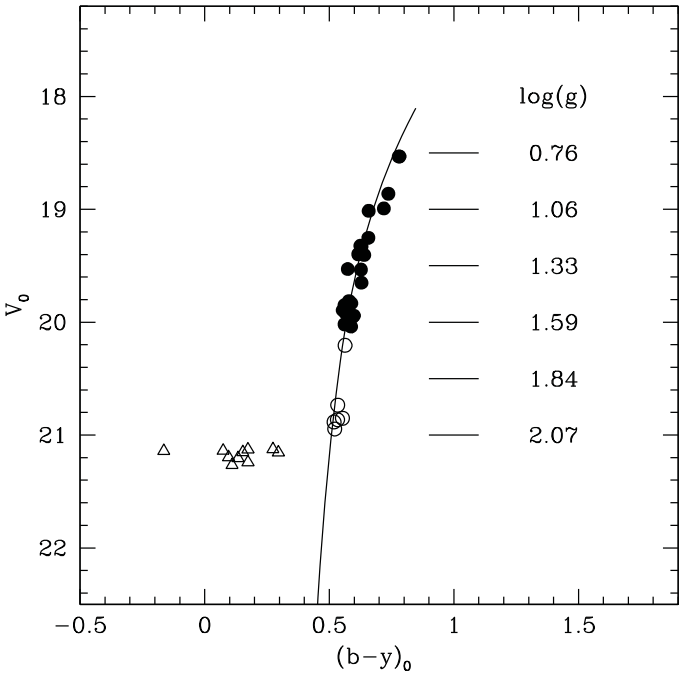

Fig. 1. Colour–magnitude diagram for the Hercules dSph galaxy (Adén et al. 2009a). • are RGB stars selected for this study. ∘ indicate RGB stars too faint for this study and open triangles are horizontal-branch stars. The solid line indicates the isochrone by VandenBerg et al. (2006) with colour transformations by Clem et al. (2004). $\log g$ values for different magnitudes as indicated. Note that there are two stars at $V_0 \sim 18.5$ superimposed on each other.

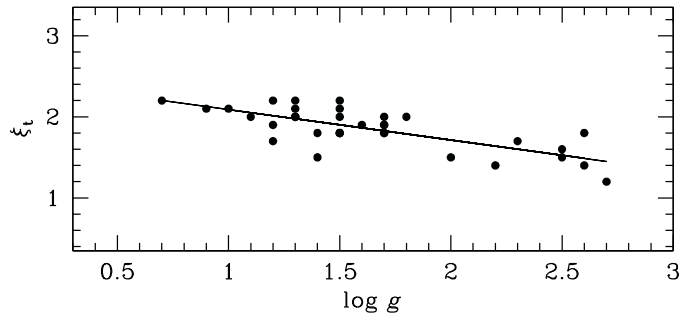

Fig. 2. ξ_t vs. $\log g$ for metal-poor giant stars from Andrievsky et al. (2010). The solid line indicates a least-square fit to the data.

distribution of $\log(A)$ is asymmetric. Thus, we adopt the standard deviation based on the sextiles (which is equivalent to 1σ in the case of a Gaussian distribution) as our final random error. For elements with less than two lines measured we performed a χ^2-test between the stellar spectrum and a grid of synthetic spectra, to estimate the random errors in the elemental abundances (see Sects. 4.2 and 4.3). Note that none of the Ca abundances are estimated using more than two lines. Thus, the errors in [Ca/H] are derived using either a χ^2-test or by propagating ϵ_{W_λ} as derived using the relation in Cayrel (1988).

The systematic errors, $\epsilon_{\mathrm{sys,[X/H]}}$, were estimated from the errors in the stellar parameters (Sect. 3) as follows: two stars were selected randomly, RGB star 40 789 and 42 241. For these two stars, we study the final elemental abundances for several model atmospheres. The model atmospheres were chosen so that we had two values of $\log g$, separated by 0.5 dex, three values of T_{eff}, separated by 100 K, and three values of ξ_t, separated by 0.2 km s^{-1}. The separation between the T_{eff} and ξ_t values corresponds to the estimated errors in the parameters (see Sect. 3). The centre value for T_{eff} and ξ_t corresponds to the values as determined in Sect. 3. Since the error in $\log g$ was more difficult to determine (see Sect. 3), we chose a separation in $\log g$ of 0.5 dex to make sure that we got an upper limit of the contribution from this stellar parameter. The elemental abundances varies with less than 0.05 dex when the value of $\log g$ is separated by 0.5 dex. However, we note that this is based on Fe I lines. Fe II lines are more sensitive to changes in $\log g$.

Thus, we have 18 model atmospheres for which we determine the final elemental abundances of iron and calcium. The standard deviation of the 18 final elemental abundances, for iron and calcium, is then adopted as $\epsilon_{\mathrm{sys,[X/H]}}$. We find a typical $\epsilon_{\mathrm{sys,[X/H]}}$ of ∼0.12 dex.

The total errors in the elemental abundance ratios were calculated as

$$\epsilon_{\mathrm{[X/H]}} = \sqrt{\epsilon^2_{\mathrm{rand,[X/H]}} + \epsilon^2_{\mathrm{sys,[X/H]}}}. \quad (3)$$

The final total errors are summarised in Table 6.

4.2. Iron

The mean [Fe/H] is determined on the scale where $\log \epsilon_{\mathrm{H}} = 12.00$. The solar iron abundance of 7.45 is adopted from Grevesse et al. (2007).

Due to the variation in the S/N, and the number of measurable lines in the spectra, we analyse these stars individually or as groups with spectra of similar quality (Sects. 4.2.1, 4.2.2 and 4.2.3). The result from the analysis is summarised in Table 6.

4.2.1. Highest S/N spectra

RGB star 12 175, with $V_0 = 18.5$, is one of the two brightest RGB stars discovered in the Hercules dSph galaxy. However, due to its low metallicity, only 4 Fe I lines were distinguishable from the continuum in the spectral range covered by our observation. These four iron lines give [Fe/H] = −3.17 ± 0.14. Figure 3b shows the spectrum of 12 175 around two of the four Fe I lines. Close to these two lines there are two additional Fe I lines that we could not measure quantitatively, but that we were able to identify with the help of a synthetic spectrum. The synthetic spectrum shown in Fig. 3b supports the result that this is a very metal-poor star with [Fe/H] = −3.2.

RGB star 42 241 has about the same magnitude and S/N as 12 175. However, due to its higher iron abundance, about four times as many lines were measurable in this spectrum (compare Table 4). We find an [Fe/H] of −2.03 ± 0.14 dex. Additionally, for this star, we were able to measure two Fe II lines. These lines give an iron abundance of −1.40 ± 0.20 dex. Thus, the [Fe/H] as derived from Fe I lines do not agree within the error bars with [Fe/H] as derived from Fe II lines. This discrepancy in the determination of the iron abundance could partially be caused by over-ionisation in Fe I. Ivans et al. (2001) argue that over-ionisation could cause an under-estimate of about 0.1 dex for RGB stars if Fe I lines are used.

Figure 3d shows the stellar spectrum of 42 241 around four of the measured Fe I lines. As can be seen, [Fe/H] derived from the W_λ agrees well with a synthetic spectrum with an iron abundance close to the –2 dex value derived from the W_λs.

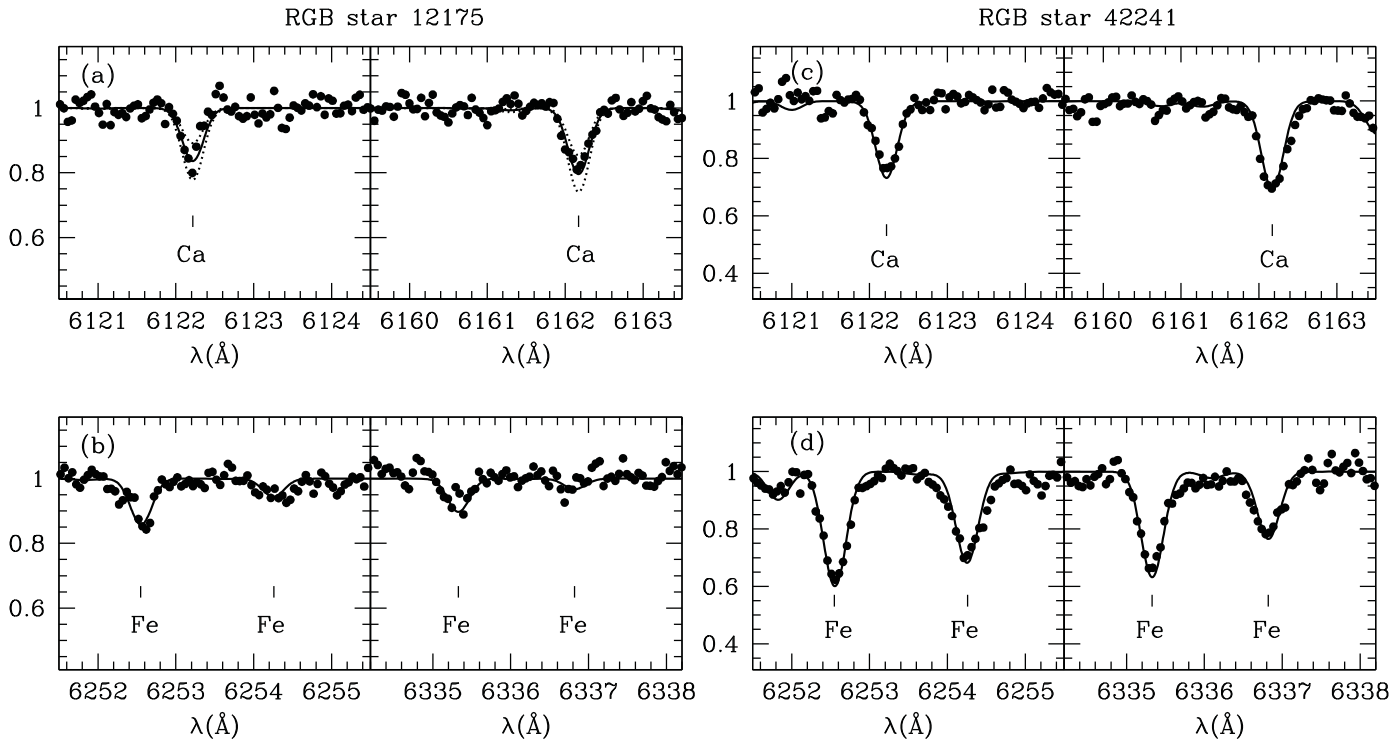

Fig. 3. *Left panels*: portions of stellar spectra around four Fe I **b)** and two Ca I **a)** lines for RGB star 12175. • indicate the observed spectrum. The solid line indicates a synthetic spectrum with [Fe/H] = −3.1 and [Ca/H] = −2.8. The dotted lines in **a)** indicate synthetic spectra with [Ca/H] ± 0.3 relative to the solid-line-synthetic spectrum. *Right panels*: Portions of stellar spectra around four Fe I **d)** and two Ca I **c)** lines for star 42 241. • indicate the observed spectrum. The solid line indicates a synthetic spectrum with [Fe/H] = −2.0 and [Ca/H] = −2.6.

4.2.2. Low S/N spectra

RGB stars 42 149, 41 743, 42 795, 40 789, 42 096, 40 993 and 12 729 have a lower S/N than 12 175 and 42 241. However, at least two Fe I lines were measurable for each of the stars.

Since the S/N is much lower for these stars, we did the following test to ensure that the [Fe/H] derived from the equivalent widths are reasonable. For each of the stars, we generated a set of synthetic spectra with five different [Fe/H] values, separated by 0.2 dex, centred on the [Fe/H] derived from the equivalent widths. A plot of the stellar spectrum, with the synthetic spectra over-plotted, enabled us to verify that the [Fe/H] derived from the W_λs is a good estimate of the iron abundance of the star. We found that none of the stellar spectra deviated significantly from a synthetic spectrum with a similar [Fe/H] abundance.

Figure 4 shows an example, for 41 743. As can be seen, an [Fe/H] of ∼−2.4 dex is a reasonable estimate of the iron abundance for this star.

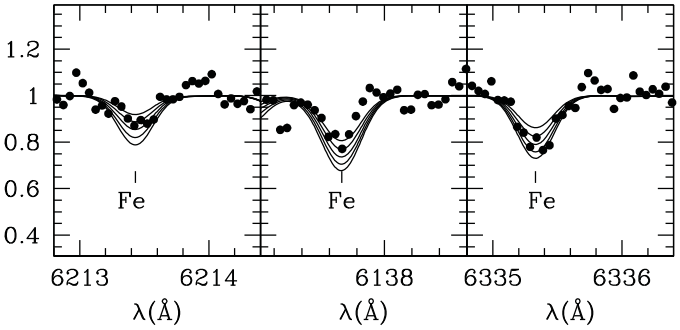

Fig. 4. Portions of stellar spectra around three Fe I lines for RGB star 41 743. • indicate the observed spectra. The solid lines indicate synthetic spectra with [Fe/H] from −2.85 to −2.05 dex, *top to bottom*, separated by 0.2 dex each.

4.2.3. Difficult spectra

RGB stars 41 460 and 42 324 have low S/N (21 and 13, respectively) and are very metal-poor. Thus, it was difficult to identify the Fe I absorption lines in the spectra. However, we did see faint absorption signatures but the low S/N made it virtually impossible to measure the lines. Instead, we performed a χ^2-test between the observed spectrum and a grid of synthetic spectra with 17 different [Fe/H] values, separated by 0.05 dex. Each synthetic spectrum yields a χ^2 value, and the best fit is found when χ^2 is minimised ($\chi^2_{\rm min}$). We used a width of 3σ, which covers about 99.7 per cent of the absorption feature, for each iron line in the line list (see Table 4). We investigated the sensitivity of the χ^2-test region by varying it between 2σ and 4σ and found that it had negligible impact on the result. The continuum for each line was adjusted, as the average of the signal on each side of the absorption feature over 0.6 Å, to accommodate for the local deviations from the continuum normalisation in Sect. 2.3. The error for each pixel in the observed spectrum was approximated by the variance in the spectrum. The distribution enclosed by $\chi^2_{\rm min} + 1$ corresponds to 1σ for a normal distribution (Press et al. 1992). We used this as the measurement error.

4.3. Calcium

The mean [Ca/H] is determined on the scale where $\log \epsilon_{\rm H} = 12.00$ The solar calcium abundance of 6.34 is adopted from Asplund et al. (2009). There are two Ca I lines, at 6122.22 Å and 6162.17 Å in the wavelength region covered by our spectra,

that were possible to measure in the majority of the stars. The results from the analysis are summarised in Table 6. Individual stars are, in similar manner as done for Fe, discussed in the following sections.

4.3.1. Highest S/N spectra

For RGB star 12 175 both Ca I lines were measured and they give [Ca/H] = −2.9 ± 0.1. Figure 3a shows the stellar spectrum around the Ca I lines. As can be seen, [Ca/H] as measured from the W_λ agree well with a synthetic spectrum with similar [Ca/H]. Additionally, Fig. 3a shows an example of two synthetic spectra with [Ca/H] ±0.3.

For RGB star 42 241 we find a [Ca/H] of −2.5 ± 0.2. This is significantly higher than [Ca/H] for RGB star 12 175. Figure 3c shows the stellar spectrum of 42 241 around the two Ca I lines. As can be seen, [Ca/H] as derived from the W_λ agree well with a synthetic spectrum with a similar abundance.

4.3.2. Low S/N spectra

RGB stars 42 149, 41 743, 40 789, 42 096 and 42 324 have a lower S/N than RGB stars 12 175 and 42 241. However, both of the Ca I lines were measurable in all four stars.

Since the S/N is lower we repeated the same test done for the iron abundance analysis (compare Sect. 4.2.2), generating a grid of synthetic spectra for each star, to see if the [Ca/H] as derived from the W_λ were reasonable. We found that the synthetic spectrum of RGB star 40 789, in comparison with the observed spectrum, indicates that the [Ca/H] determined from the measurements of the W_λ was slightly, about 0.1 dex, over-estimated. Thus, we estimated the Ca I abundance for RGB star 40 789 using the same method as for the spectra identified as difficult for the measurement of the Fe I lines (see Sect. 4.2.3). For all other stars in this category, the abundances from the measured W_λ and those from the χ^2-comparison of synthetic spectra showed good agreement.

4.3.3. Difficult spectra

For RGB star 42 795, 41 460, and 40 993 only one or none of the Ca I lines were measurable. However we did see a general decrease in the continuum at the wavelengths for the Ca I lines indicating the presence of Ca in the atmospheres of these metal-poor stars. Thus, we estimated the Ca I abundance using the same method as for the spectra identified as difficult for the measurement of the Fe I lines (see Sect. 4.2.3). The results from the analysis are summarised in Table 6.

We were not able to identify any Ca I absorption features for RGB star 12 729. Thus, [Ca/H] remains unknown for this star.

5. A comparison with abundances determined in other studies

5.1. A comparison with a high S/N RGB star

Lind et al. (2009) obtained high S/N spectroscopy of several bright RGB stars in the Milky Way. They used the same instrument and grating (GIRAFFE/HR13) as in this study. Through private communication they provided us with a spectrum of one of their bright targets, star 17691, that has a S/N of about 300. We measured the W_λ for the lines in Table 4 and performed an abundance analysis for this star as described in Sects. 2.3 and 4.

Table 6. Derived elemental abundances for the RGB stars in the Hercules dSph galaxy.

Star	[Fe/H]	N	[Ca/H]	N	[Ca/Fe]
12 175	−3.17 ± 0.14	4	−2.89 ± 0.15	2	0.28 ± 0.21
42 241	−2.03 ± 0.14	20	−2.54 ± 0.15	2	−0.51 ± 0.21
42 149	−2.95 ± 0.15	2	−3.08 ± 0.16	2	−0.13 ± 0.22
41 743	−2.42 ± 0.15	11	−2.51 ± 0.16	2	−0.09 ± 0.22
42 795	−3.17 ± 0.15	2	−3.11 ± 0.17	χ^2	0.06 ± 0.23
40 789	−2.88 ± 0.17	3	−3.06 ± 0.16	χ^2	−0.18 ± 0.23
41 460	−3.10 ± 0.16	χ^2	−2.78 ± 0.15	χ^2	0.32 ± 0.22
42 096	−2.60 ± 0.17	4	−2.40 ± 0.18	2	0.20 ± 0.25
40 993	−2.38 ± 0.19	8	−2.68 ± 0.15	χ^2	−0.3 ± 0.24
42 324	−2.70 ± 0.14	χ^2	−2.60 ± 0.28	2	0.10 ± 0.31
12 729	−2.35 ± 0.17	5	...	...	

Notes. Column 1 lists the RGB star ID. Columns 2 and 4 list the [Fe/H] and [Ca/H], respectively, with total errors in the abundances as indicated. N indicates the number of lines measured for the determination of [Fe/H] and [Ca/H], as indicated. χ^2 indicates that the corresponding abundance was determined through a χ2-test using a grid of synthetic spectra (see Sects. 4.2.3 and 4.3.3). Column 6 lists [Ca/Fe].

The stellar parameters was adopted from Lind et al. (2009). We find an Fe abundance that is 0.01 dex more metal poor, and a Ca abundance 0.04 dex lower than given in Lind et al. (2009). Thus, our determinations of the abundances of Ca and Fe in star 17691 are in agreement with Lind et al. (2009). Additionally, we find that none of the elemental abundances as derived from individual measurements of the W_λ deviate significantly. This suggests that the effect of atomic parameters should not contribute to our elemental abundance errors.

5.2. A comparison with earlier spectroscopic results

Koch et al. (2008b) obtained high resolution spectroscopy ($R \sim 20\,000$), with similar S/N and resolution as in this study, of two stars in the Hercules dSph galaxy, Her-2 and Her-3. These stars correspond to our RGB stars 42 241 and 41 082. However, RGB star 41 082 was discarded from our sample (see Sect. 4). Koch et al. (2008b) find [Fe/H] = −2.02 ± 0.20 and [Ca/Fe] = −0.13 ± 0.05 for RGB star 42 241. Note, however, that Koch et al. (2008b) measured W_λ values of lines over a broader wavelength range from 5500–8900 Å. Our estimates of [Fe/H] are in very good agreement, but [Ca/Fe] as derived by Koch et al. (2008b) is 0.4 dex higher.

Figure 5 shows our spectrum and the spectrum from Koch et al. (2008b) for RGB star 42 241. In Table 7 we provide a comparison between W_λs as measured from our observed spectrum, and W_λs as measured by us from the spectrum obtained by Koch et al. (2008b). We note that, for the Ca I lines, the spectrum from Koch et al. (2008b) has deeper absorption. However, the overall absorption for the Fe I and blended lines are in good agreement, except for one weak Fe I line at λ = 6200.31 Å that is more prominent in our observed spectrum. We note that the S/N at this line in the spectrum from Koch et al. (2008b) is low, making it difficult to distinguish such a weak line in the spectrum. There is a much brighter star, SDSS J163056.63+124737.5, located only ∼12 arcsec from 42 241. Thus, we investigate the possibility that the fibre allocated for 42241 has collected a significant amount of flux from SDSS J163056.63+124737.5. SDSS J163056.63+124737.5 is 6.7 mag brighter in the SDDS r-filter, which is centred on our wavelength region of interest. The seeing for our observations was ∼1 arcsec. Based on this,

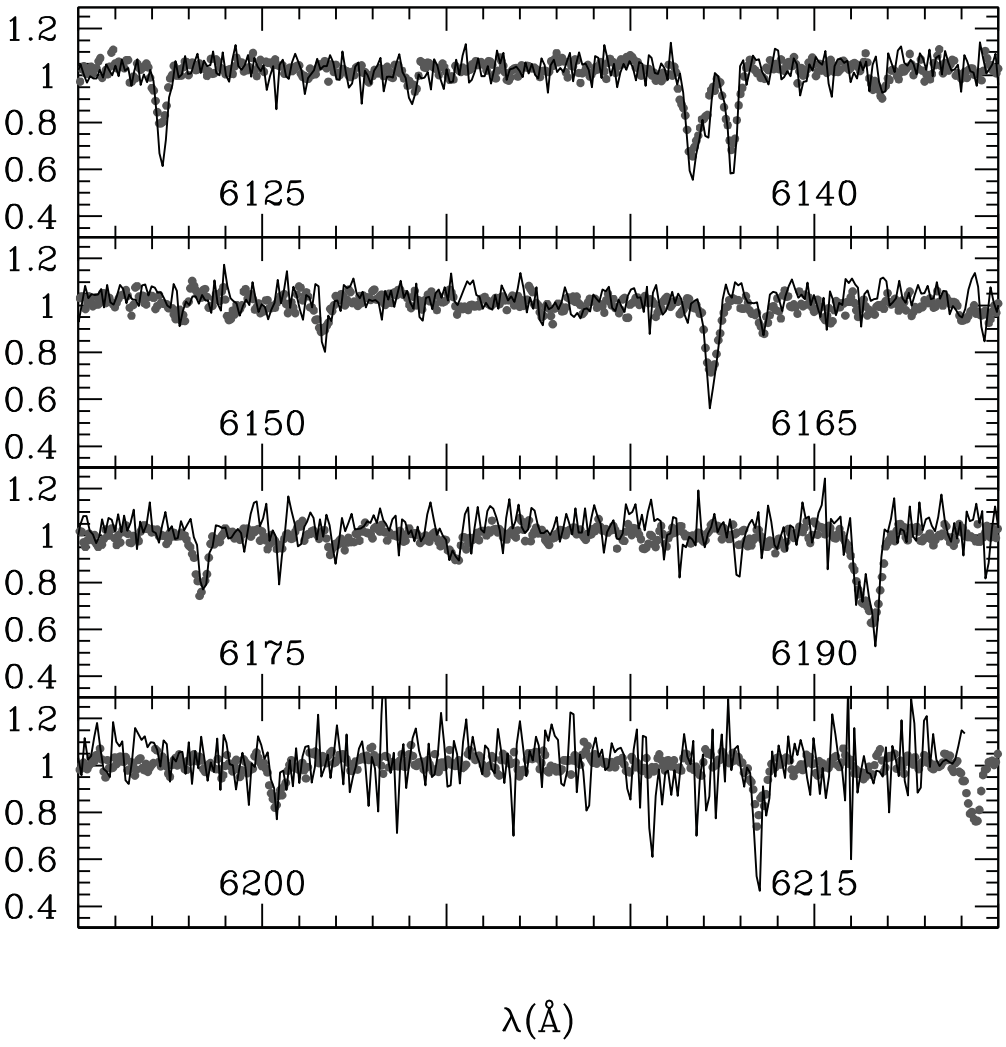

Fig. 5. A comparison between our spectrum and the spectrum from Koch et al. (2008b) , in the region where they overlap, for RGB star 42 241. • indicate our stellar spectrum. The solid line indicates the spectrum from Koch et al. (2008b).

Table 7. Equivalent width measurements for RGB star 42 241/Her-2.

Ion	λ (Å)	$W_{\lambda,A}$ (mÅ)	$W_{\lambda,K}$ (mÅ)	$\frac{W_{\lambda,A}}{W_{\lambda,K}}$
Ca I	6122.22	89	124	0.72
Ca I	6162.17	122	153	0.79
Fe I	6137.69	148	141	1.05
Fe I	6151.62	62	49	1.26
Fe I	6173.34	96	98	0.98
Fe I	6180.20	38	40	0.94
Fe I	6200.31	75	40	1.87
Fe I	6213.43	92	111	0.83
Blend	6128.96	35	33	1.06
Blend	~6136.6	239	241	0.99
Blend	6163.54	36	33	1.10
Blend	~6191.5	265	262	1.01

Notes. Columns 1 and 2 list the Ion and wavelength, respectively. Columns 3 and 4 list W_λ as measured from our observed spectrum and the spectrum obtained by Koch et al. (2008b), respectively. Column 5 lists the ratio between the measurements.

we constructed a model of two Gaussian flux distributions with a full-width half-maximum of 1.5 arcsec and magnitudes that represent the brightness of the stars. We found that the amount of flux from SDSS J163056.63+124737.5 at the position of the fibre is negligible. A similar investigation was carried out for the spectrum obtained by Koch et al. (2008b), yielding the same conclusion. Thus, the origin of this discrepancy can not be due to a contamination by light from this nearby star. A more thorough investigation than this goes beyond the scope of this study. However, one could speculate that there is an unresolved binary present that was overlapped in one observation and out of phase in the other observation, or that it may be due to some differences in the reduction procedure.

Kirby et al. (2008b) studied 20 stars in the direction of the Hercules dSph galaxy. Their metallicities are based on a recently developed automated spectrum synthesis method that takes the information in the whole spectrum into account (Kirby et al. 2008a). The method was originally developed for globular clusters in the Milky Way and was then applied to ultra-faint dSph galaxies in Kirby et al. (2008b). We have 7 stars in common between our samples. Figure 6b shows the difference between our respective determinations of [Fe/H]. We find that our [Fe/H] is on average 0.07 dex more metal-rich, with a scatter of 0.09 dex. In conclusion, the agreement between the [Fe/H] determinations is very good.

5.3. A comparison with earlier photometric results

In a previous study of the Hercules dSph galaxy (Adén et al. 2009a) we estimated [Fe/H] using the Strömgren m_1 index using the calibration from Calamida et al. (2007). Figure 6a shows

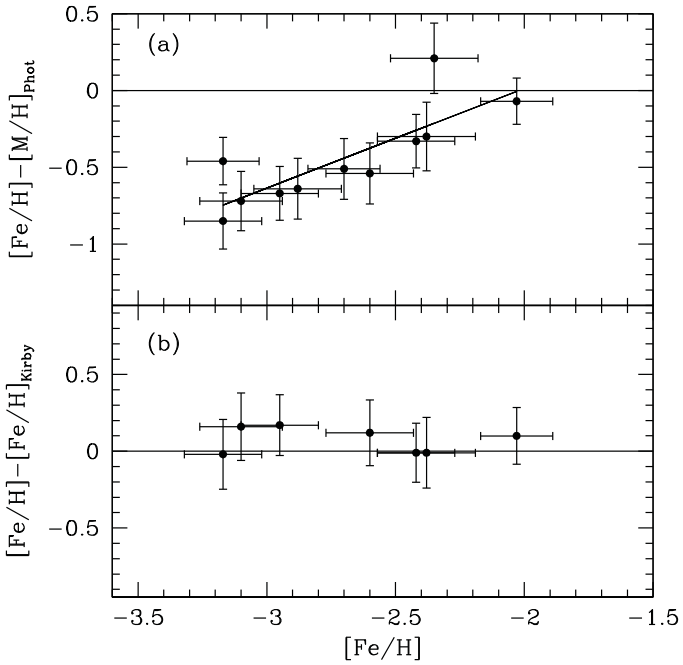

Fig. 6. a) A comparison between our [Fe/H] and [M/H] from Adén et al. (2009a) ($[M/H]_{Phot}$). The error-bars represent the error in [Fe/H] – $[M/H]_{Phot}$ and [Fe/H], respectively. **b)** A comparison between our [Fe/H] and [Fe/H] from Kirby et al. (2008b) ($[Fe/H]_{Kirby}$). The error-bars represent the error in [Fe/H] – $[Fe/H]_{Kirby}$ and [Fe/H], respectively.

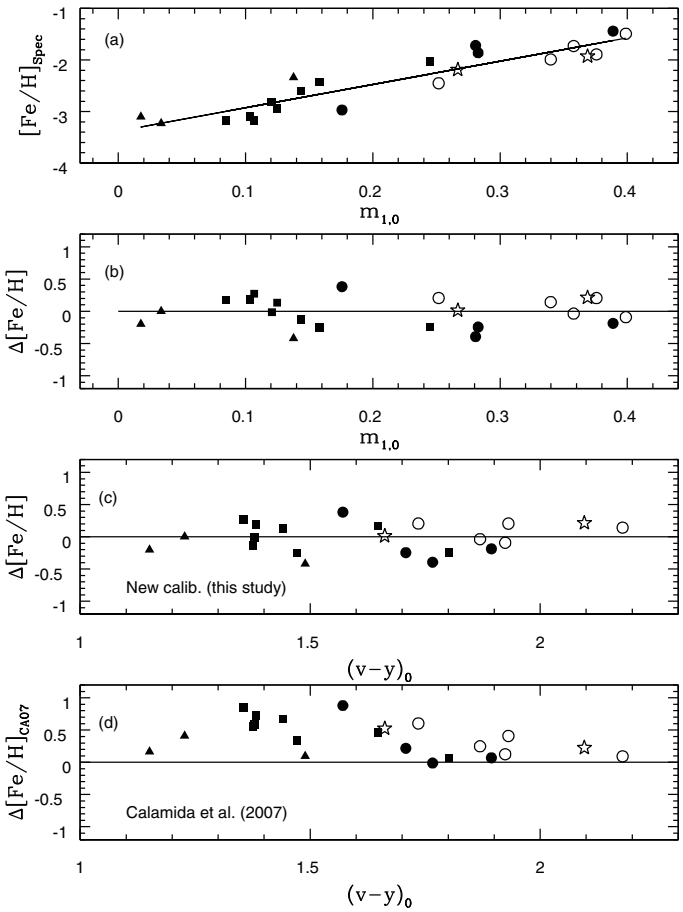

Fig. 7. a) Spectroscopic [Fe/H] vs. $m_{1,0}$ for Draco (• and ◦), Sextans (open stars), UMaII (filled triangles) and Hercules (filled squares). **b)**, $[M/H]_{phot,new}$ – [Fe/H] vs. $m_{1,0}$ using Eq. (4) to derive [M/H]. **c)**, $[M/H]_{phot,new}$ – [Fe/H] vs. $(v-y)_0$ using Eq. (4) to derive [M/H]. **d)** $[M/H]_{CA07}$ – [Fe/H] vs. $(v-y)_0$ using the calibration by Calamida et al. (2007) to derive [M/H].

a comparison between the photometric [Fe/H] as estimated in Adén et al. (2009a), $[M/H]_{phot}$, and [Fe/H] as determined from high-resolution spectroscopy in this study. We note that there is a strong trend such that [M/H] appears to be over-estimated in Adén et al. (2009a) for metal-poor stars.

5.4. A new metallicity calibration for Strömgren photometry for metal-poor red giant stars

Given the excellent agreement between all three spectroscopic studies it must be concluded that the metallicity calibration by Calamida et al. (2007) over-estimates the metallicity for very metal-poor stars. This result is expected, since the calibration by Calamida et al. (2007) is valid only for [Fe/H] > −2.4 This is an unfortunate situation since the photometry allows us in principle to determine the metallicity of RGB stars with good accuracy also for the fainter stars (compare errors in Adén et al. 2009a) and thus allowing the study of much more complete stellar samples in the ultra-faint dSph galaxies.

Here we present an attempt to deal with the situation. So far this is a very simplistic relation and *only* formally valid for stars with $0.02 < m_{1,0} < 0.40$, $-3.29 <$ [Fe/H] < 1.58 and $1.15 < (v-y)_0 < 2.18$.

We have collected all spectroscopic [Fe/H] derived from high-resolution spectra available for stars in Draco (Cohen & Huang 2009; Shetrone et al. 2001), Sextans (Shetrone et al. 2001), UMaII (Frebel et al. 2010b) and Hercules (this study), and combined these data with our own Strömgren photometry where available. Figure 7a shows the spectroscopic [Fe/H] as a function of $m_{1,0}$ for the stars. A least-squares fit yields

$$[M/H]_{phot,new} = 4.51(\pm0.41)\, m_{1,0} - 3.38(\pm0.10). \quad (4)$$

Figures 7b,c show $[M/H]_{phot,new}$ – [Fe/H] as a function of $m_{1,0}$ and $(v-y)_0$, respectively. No strong trends are seen. For comparison Fig. 7d shows $[M/H]_{CA07}$ – [Fe/H] vs. $(v-y)_0$, where $[M/H]_{CA07}$ is [Fe/H] as determined using the calibration in Calamida et al. (2007). Here we can note a significant difference of both metallicity scales such that $[M/H]_{CA07} > [Fe/H]_{spec}$. Taking into account the uncertainties of the least-squares fit and the correlation between the fitting parameters (Eq. (4)), and the error in $m_{1,0}$ from Adén et al. (2009a) we find a typical error in $[M/H]_{phot,new}$ of 0.17 dex.

6. Results and discussion

6.1. Iron abundance and ages for the RGB stars in Hercules

The RGB stars analysed in this paper span a large range of iron abundances, from about –3.2 dex to –2 dex, indicating an extended period of chemical enrichment. It is somewhat fortuitous that the two brightest stars in our sample, RGB stars 12 175 and 42 241, bracket the full range of metallicities. Thus, there is no doubt that the range of metallicities derived from high-resolution spectroscopy is real.

In Sect. 5.4 we provide a new Strömgren metallicity calibration. This calibration is valid for stars with $0.02 < m_{1,0} < 0.40$ and $-3.29 <$ [Fe/H] < 1.58. Two of the 28 RGB stars from

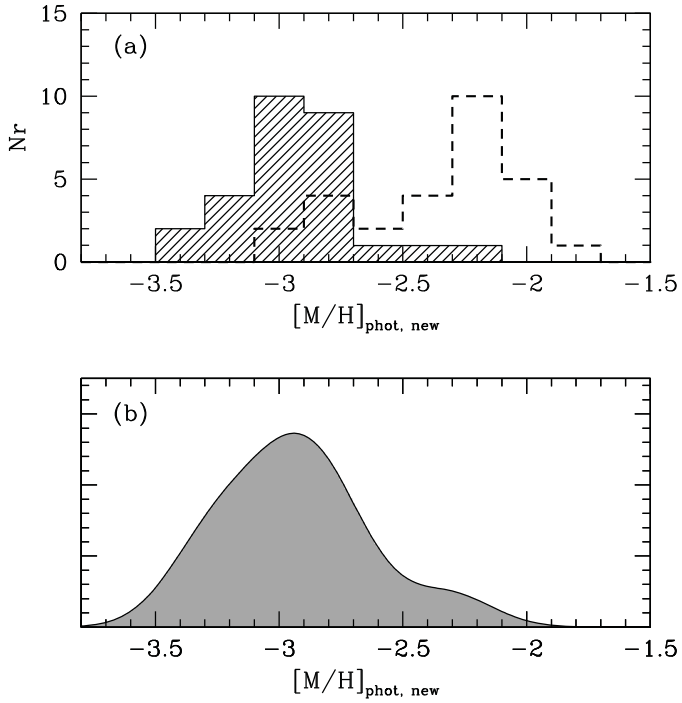

Fig. 8. a) Metallicity histogram for RGB stars in the Hercules dSph galaxy. The shaded histogram shows the distribution of $[M/H]_{phot,\,new}$. For comparison, the dashed histogram shows the distribution of $[M/H]_{phot}$ (Adén et al. 2009a). **b)** Corresponding error-weighted metallicity distribution.

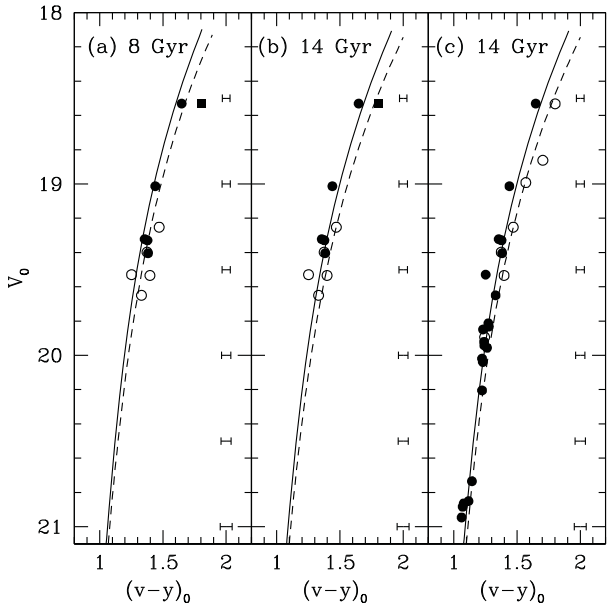

Fig. 9. a) and **b)** Colour–magnitude diagrams for RGB stars with high–resolution spectroscopy of the Hercules dSph galaxy. • indicate RGB stars more metal-poor than [Fe/H] = −2.7. ◦ represents RGB stars more metal-rich than, or equal to, [Fe/H] = −2.7. The filled square indicates the most metal-rich RGB star at [Fe/H] = −2.0. The solid and dashed lines represent isochrones with [Fe/H] = −2.31 and −2.14 dex, respectively, by VandenBerg et al. (2006) with colour transformations by Clem et al. (2004). **c)** Colour–magnitude diagram for the RGB stars in Adén et al. (2009a) with $[M/H]_{phot,\,new}$ as determined in Sect. 5.4. • indicate RGB stars more metal-poor than [M/H] = −2.8. ◦ indicate RGB stars more metal-rich than [M/H] = −2.8. Isochrones as in **b**). The error bars on the right hand side in each figure represent the typical error in $(v - y)_0$.

Adén et al. (2009a) have an $m_{1,0}$ less than the range for which the new metallicity calibration is valid. However, with an $m_{1,0}$ of 0.01, these stars are included in the sample as a slight extrapolation. In Fig. 8a we show the resulting histogram of $[M/H]_{phot,\,new}$ for all the 28 RGB stars identified in (Adén et al. 2009a). The bin size of 0.2 dex represents the typical error in $[M/H]_{phot,\,new}$ (see Sect. 5.4). Figure 8b shows the corresponding error-weighted metallicity distribution. For this plot, each stars was assigned a Gaussian distribution with a mean of $[M/H]_{phot,\,new}$ and a dispersion equal to the typical error in $[M/H]_{phot,\,new}$ (0.17 dex). The Gaussians, one for each star, were then added to create the metallicity distribution function. We note that the distribution of $[M/H]_{phot,\,new}$ is shifted towards lower metallicities when the new calibration is applied, and that there is an abundance spread in the metallicity distribution for the RGB stars of at least 1.0 dex. Additionally, we note a more concentrated distribution.

Figure 9a,b show V_0 vs. $(v - y)_0$ for the stars with [Fe/H] derived from high resolution spectroscopy. Additionally, in these plots, we show two isochrones with [Fe/H] = −2.31 (most metal-poor isochrone available) and −2.14 dex. As can be seen, the isochrones of a given metallicity become redder with increasing age. Since the isochrone with [Fe/H] = −2.31 is too metal-rich, compared to [Fe/H] as derived from the spectroscopy, an even more metal-poor isochrone at the age of 8 Gyr would be even bluer, excluding an age of about 10 Gyr or younger. At an age of 14 Gyr, the isochrone with [Fe/H] = −2.31 is slightly redder than most of the stars more metal-poor than [Fe/H] = −2.7. Hence a more metal-poor isochrone would presumably represent the locus of these stars very well, arguing for an age older than about 10 Gyr for the Hercules dSph galaxy.

Figure 9c shows V_0 vs. $(v - y)_0$ for all the 28 RGB stars identified in (Adén et al. 2009a).

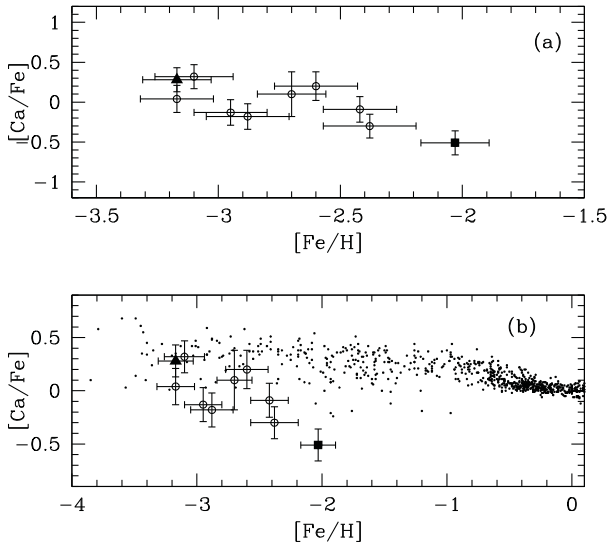

Fig. 10. a) [Ca/Fe] as a function of [Fe/H]. Filled triangle and filled square indicate our two brightest RGB stars, RGB stars 12 175 and 42 241, respectively. The error-bars represent the error in [Ca/Fe] and [Fe/H], respectively. **b)** Same as **a)** but with a compilation of the Milky Way disk and halo stars abundances from Venn et al. (2004), as indicated by small dots.

6.2. [Ca/Fe]

Figure 10 shows [Ca/Fe] as a function of [Fe/H]. We find a trend such that [Ca/Fe] is higher for more metal-poor stars, and

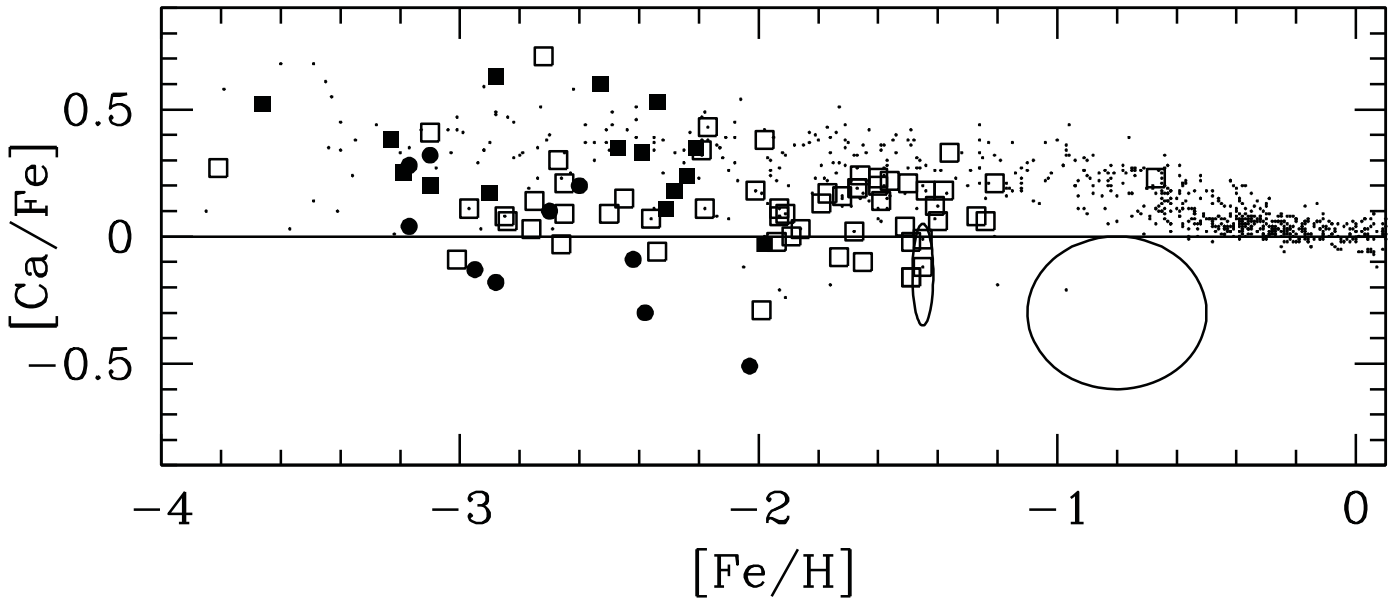

Fig. 11. A comparison of [Ca/Fe] as a function of [Fe/H] for stars in several dSph galaxies. • indicate Hercules (this study). Filled squares represent the ultra-faint dSph galaxies Ursa Major II, Coma Berenices, Boötes I and Leo IV (Feltzing et al. 2009; Frebel et al. 2010b; Norris et al. 2010; Simon et al. 2010). Open squares represent the classical dSph galaxies Draco, Sextans, Ursa Minor, Fornax, Carina and Sculptor (Shetrone et al. 2001, 2003; Sadakane et al. 2004; Koch et al. 2008a; Cohen & Huang 2009; Aoki et al. 2009; Frebel et al. 2010a). The solid ellipses outline RGB stars in the classical dSph galaxy Fornax from Letarte et al. (2007).

lower for more metal-rich stars. Fortuitously, the most metal-rich and the most metal-poor star in the sample are both bright and have spectra with high S/N (see discussion in Sect. 4 and also Table 2). Thus we can be certain that the trend actually has this shape and we are not misinterpreting spectra of lower quality.

The production of alpha (α)-elements, such as Ca, Si, Ti, Mg, and O, is correlated with the end stage of massive stars. Mg and O are created during the hydrostatic He burning in massive stars, and Si, Ca, and Ti are primarily produced during core-collapse supernovae (Woosley & Weaver 1995). On the other hand, less massive stars are able to produce significant amounts of Fe in SNe Ia. Thus, the ratio of α-elements to iron is used to trace the time scale of the star formation in a stellar system. If the star formation rate is high, then the gas will be able to reach a higher [Fe/H] before the first SNe Ia occur. This can be observed in a plot of [Ca/Fe] vs. [Fe/H] as a "knee", where [Ca/Fe] decrease as [Fe/H] increase (McWilliam 1997). The fraction of stars at [Fe/H] less than the "knee" gives information on the star formation timescale.

The observed continuous downward trend, without a "knee", for [Ca/Fe] vs. [Fe/H] in Hercules can thus be interpreted as a brief initial burst of short-lived SNe II that enhanced the production of α-elements. Since there are no stars at [Fe/H] less than the "knee", the star formation rate was very low. The subsequent continuous decline would be expected if contributions from long-lived SNe Ia were the dominant factor, decreasing [α/Fe] while increasing [Fe/H]. This means that essentially no massive stars formed after the initial burst. Additionally, we interpret the relatively short range in [Fe/H] (no stars with [Fe/H] > -2 are seen in our sample) as a tentative evidence for a short duration of this low-efficiency star formation (for a discussion of continuous and bursty star formation histories and the role of SNe Ia see, e.g., Gilmore & Wyse 1991; Matteucci 2009). The classical dSph galaxies, such as Carina, Sculptor and Fornax, also show these types of trends for the α-elements (e.g., Venn et al. 2004; Koch et al. 2008a; Tolstoy et al. 2009; Kirby et al. 2009). However, these dSph galaxies are more metal-rich and more massive than, e.g., Hercules. Only a few other ultra-faint dSphs have chemical element abundances published for only a handful of stars each.

Frebel et al. (2010b), Feltzing et al. (2009), Norris et al. (2010) and Simon et al. (2010) studied Coma Berenices, Ursa Major II, Boötes I, and Leo IV, all recently discovered ultra-faint and metal-poor systems. Figure 11 summarises our data and their data. Additionally, recent studies have analysed very metal-poor stars in the classical systems Draco, Sextans and Sculptor (Cohen & Huang 2009; Aoki et al. 2009; Frebel et al. 2010a). We add these new data to the plot in addition to the abundances from other studies of Fornax, Carina, Sculptor, Sextans, Ursa Minor and Draco (Shetrone et al. 2001, 2003; Sadakane et al. 2004; Letarte et al. 2007; Koch et al. 2008a).

Overall, there is a faster declining [Ca/Fe] with [Fe/H] for the dSph galaxies as compared with the halo stars in the solar neighbourhood (from the compilation by Venn et al. 2004, including data from Fulbright (2002, 2000); Stephens & Boesgaard (2002); Bensby et al. (2003); Nissen & Schuster (1997); Hanson et al. (1998); Prochaska et al. (2000); Reddy et al. (2003); Edvardsson et al. (1993); McWilliam (1998); McWilliam et al. (1995); Johnson (2002); Burris et al. (2000); Ivans et al. (2003); Ryan et al. (1996); Gratton & Sneden (1991, 1994, 1988)). Thus, for example, the trend seen from our data in Hercules is the same as the overall trend seen for Draco. This is interesting and could be interpreted as that the Fe contribution from SNe Ia were the dominant factor for both Hercules and Draco. However, since Draco has many more stars with [Fe/H] > -2 it must have had a more integrated star formation than the Hercules dSph galaxy, as may be expected given its higher baryon content.

7. Conclusions

We have studied confirmed RGB stars in the ultra-faint Hercules dSph galaxy with FLAMES high-resolution spectroscopy.

Abundances were determined by solving the radiative transfer calculations using the codes Eqwi/Bsyn in MARCS model atmospheres.

We find that the RGB stars of the Hercules dSph galaxy included in this study are more metal-poor than estimated in Adén et al. (2009a), however in good agreement with Kirby et al. (2008b), with a metallicity spread of at least 1 dex. Based on the position of the RGB stars in colour–magnitude diagrams, in comparison with isochrones, we conclude that there is no clear indication of a population younger than about 10 Gyr.

Additionally, we provide a first attempt at a new metallicity calibration for Strömgren photometry based on high-resolution spectroscopy for several dSph galaxies. With this new calibration, we find several RGB stars in the Hercules dSph galaxy that are more metal-poor than [Fe/H] = −3.0 dex.

Finally, we have determined the [Ca/Fe] for the RGB stars in this study. We found a trend such that [Ca/Fe] is higher for more metal-poor stars, and lower for more metal-rich stars. This trend is supported by our two brightest stars in the sample and is interpreted as a brief initial burst of SNe II during a very low star formation rate, followed by the enrichment of [Fe/H] by SNe Ia.

Acknowledgements. We acknowledge Karin Lind for providing us with a spectrum of one of their RGB stars. S.F. is a Royal Swedish Academy of Sciences Research Fellow supported by a grant from the Knut and Alice Wallenberg Foundation. K.E. is gratefully acknowledging support from the Swedish research council. M.I.W. is supported by a Royal Society University Research Fellowship. AK acknowledges support by an STFC postdoctoral fellowship.

References

Adén, D., Feltzing, S., Koch, A., et al. 2009a, A&A, 506, 1147
Adén, D., Wilkinson, M. I., Read, J. I., et al. 2009b, ApJ, 706, L150
Alonso, A., Arribas, S., & Martínez-Roger, C. 1999, A&AS, 140, 261
Andrievsky, S. M., Spite, M., Korotin, S. A., et al. 2010, A&A, 509, A88
Aoki, W., Arimoto, N., Sadakane, K., et al. 2009, A&A, 502, 569
Asplund, M., Grevesse, N., Sauval, A. J., & Scott, P. 2009, ARA&A, 47, 481
Belokurov, V., Zucker, D. B., Evans, N. W., et al. 2007, ApJ, 654, 897
Bensby, T., Feltzing, S., & Lundström, I. 2003, A&A, 410, 527
Blecha, A., Cayatte, V., North, P., Royer, F., & Simond, G. 2000, in Optical and IR Telescope Instrumentation and Detectors, ed. M. Iye, & A. F. Moorwood, SPIE Conf., 4008, 467
Burris, D. L., Pilachowski, C. A., Armandroff, T. E., et al. 2000, ApJ, 544, 302
Calamida, A., Bono, G., Stetson, P. B., et al. 2007, ApJ, 670, 400
Calamida, A., Bono, G., Stetson, P. B., et al. 2009, ApJ, 706, 1277
Cayrel, R. 1988, in The Impact of Very High S/N Spectroscopy on Stellar Physics, ed. G. Cayrel de Strobel & M. Spite, IAU Symp., 132, 345
Clem, J. L., VandenBerg, D. A., Grundahl, F., & Bell, R. A. 2004, AJ, 127, 1227
Cohen, J. G., & Huang, W. 2009, ApJ, 701, 1053
Dotter, A., Chaboyer, B., Jevremović, D., et al. 2008, ApJS, 178, 89
Edvardsson, B., Andersen, J., Gustafsson, B., et al. 1993, A&A, 275, 101
Feltzing, S., Eriksson, K., Kleyna, J., & Wilkinson, M. I. 2009, A&A, 508, L1
Frebel, A., Kirby, E. N., & Simon, J. D. 2010a, Nature, 464, 72
Frebel, A., Simon, J. D., Geha, M., & Willman, B. 2010b, ApJ, 708, 560
Fulbright, J. P. 2000, AJ, 120, 1841
Fulbright, J. P. 2002, AJ, 123, 404
Geisler, D., Wallerstein, G., Smith, V. V., & Casetti-Dinescu, D. I. 2007, PASP, 119, 939
Gilmore, G., & Wyse, R. F. G. 1991, ApJ, 367, L55
Gratton, R. G., & Sneden, C. 1988, A&A, 204, 193
Gratton, R. G., & Sneden, C. 1991, A&A, 241, 501
Gratton, R. G., & Sneden, C. 1994, A&A, 287, 927
Grebel, E. K., & Gallagher, III, J. S. 2004, ApJ, 610, L89
Grevesse, N., Asplund, M., & Sauval, A. J. 2007, Space Sci. Rev., 130, 105
Gustafsson, B., Edvardsson, B., Eriksson, K., et al. 2008, A&A, 486, 951
Hanson, R. B., Sneden, C., Kraft, R. P., & Fulbright, J. 1998, AJ, 116, 1286
Helmi, A., Irwin, M. J., Tolstoy, E., et al. 2006, ApJ, 651, L121
Ivans, I. I., Kraft, R. P., Sneden, C., et al. 2001, AJ, 122, 1438
Ivans, I. I., Sneden, C., James, C. R., et al. 2003, ApJ, 592, 906
Johnson, J. A. 2002, ApJS, 139, 219
Kirby, E. N., Guhathakurta, P., & Sneden, C. 2008a, ApJ, 682, 1217
Kirby, E. N., Simon, J. D., Geha, M., Guhathakurta, P., & Frebel, A. 2008b, ApJ, 685, L43
Kirby, E. N., Guhathakurta, P., Bolte, M., Sneden, C., & Geha, M. C. 2009, ApJ, 705, 328
Koch, A. 2009, Astron. Nach., 330, 675
Koch, A., Grebel, E. K., Wyse, R. F. G., et al. 2006, AJ, 131, 895
Koch, A., Grebel, E. K., Gilmore, G. F., et al. 2008a, AJ, 135, 1580
Koch, A., McWilliam, A., Grebel, E. K., Zucker, D. B., & Belokurov, V. 2008b, ApJ, 688, L13
Kupka, F., Piskunov, N., Ryabchikova, T. A., Stempels, H. C., & Weiss, W. W. 1999, A&AS, 138, 119
Kupka, F. G., Ryabchikova, T. A., Piskunov, N. E., Stempels, H. C., & Weiss, W. W. 2000, Baltic Astron., 9, 590
Letarte, B., Hill, V., & Tolstoy, E. 2007, in EAS Publications Series, ed. E. Emsellem, H. Wozniak, G. Massacrier, J.-F. Gonzalez, J. Devriendt, & N. Champavert, EAS Publ. Ser., 24, 33
Lind, K., Primas, F., Charbonnel, C., Grundahl, F., & Asplund, M. 2009, A&A, 503, 545
Martin, N. F., de Jong, J. T. A., & Rix, H. 2008, ApJ, 684, 1075
Matteucci, F. 2009, Mem. Soc. Astron. Ital., 80, 83
McWilliam, A. 1997, ARA&A, 35, 503
McWilliam, A. 1998, AJ, 115, 1640
McWilliam, A., Preston, G. W., Sneden, C., & Shectman, S. 1995, AJ, 109, 2736
Nissen, P. E., & Schuster, W. J. 1997, A&A, 326, 751
Norris, J. E., Yong, D., Gilmore, G., & Wyse, R. F. G. 2010, ApJ, 711, 350
Pasquini, L., Avila, G., Blecha, A., et al. 2002, The Messenger, 110, 1
Piskunov, N. E., Kupka, F., Ryabchikova, T. A., Weiss, W. W., & Jeffery, C. S. 1995, A&AS, 112, 525
Press, W. H., Teukolsky, S. A., Vetterling, W. T., & Flannery, B. P. 1992, Numerical recipes in FORTRAN. The art of scientific computing, ed. W. H., Press, S. A., Teukolsky, W. T., Vetterling, & B. P., Flannery
Prochaska, J. X., Naumov, S. O., Carney, B. W., McWilliam, A., & Wolfe, A. M. 2000, AJ, 120, 2513
Reddy, B. E., Tomkin, J., Lambert, D. L., & Allende Prieto, C. 2003, MNRAS, 340, 304
Ryabchikova, T. A., Piskunov, N. E., Kupka, F., & Weiss, W. W. 1997, Baltic Astron., 6, 244
Ryan, S. G., Norris, J. E., & Beers, T. C. 1996, ApJ, 471, 254
Sadakane, K., Arimoto, N., Ikuta, C., et al. 2004, PASJ, 56, 1041
Schlegel, D. J., Finkbeiner, D. P., & Davis, M. 1998, ApJ, 500, 525
Schörck, T., Christlieb, N., Cohen, J. G., et al. 2009, A&A, 507, 817
Shetrone, M. D., Côté, P., & Sargent, W. L. W. 2001, ApJ, 548, 592
Shetrone, M., Venn, K. A., Tolstoy, E., et al. 2003, AJ, 125, 684
Simon, J. D. & Geha, M. 2007, ApJ, 670, 313
Simon, J. D., Frebel, A., McWilliam, A., Kirby, E. N., & Thompson, I. B. 2010, ApJ, 716, 446
Starkenburg, E., Hill, V., Tolstoy, E., et al. 2010, A&A, 513, A34
Stephens, A., & Boesgaard, A. M. 2002, AJ, 123, 1647
Tollerud, E. J., Bullock, J. S., Strigari, L. E., & Willman, B. 2008, ApJ, 688, 277
Tolstoy, E., Hill, V., & Tosi, M. 2009, ARA&A, 47, 371
VandenBerg, D. A., Bergbusch, P. A., & Dowler, P. D. 2006, ApJS, 162, 375
Venn, K. A., Irwin, M., Shetrone, M. D., et al. 2004, AJ, 128, 1177
Walker, M. G., Mateo, M., Olszewski, E. W., et al. 2009, ApJ, 704, 1274
Woosley, S. E., & Weaver, T. A. 1995, ApJS, 101, 181
Zucker, D. B., Belokurov, V., Evans, N. W., et al. 2006, ApJ, 650, L41

Paper IV

Astronomy & Astrophysics manuscript no. dsph˙pro
February 24, 2011

An analysis of classical and ultra-faint dSph galaxies using Strömgren photometry

A study of Ursa Major II, a new metallicity calibration for metal poor stars, and the ability of SDDS *ugriz* filters to identify red giants

D. Adén[1], S. Feltzing[1], G.F. Gilmore[3], and M.I. Wilkinson[2]

[1] Lund Observatory, Box 43, SE-22100 Lund, Sweden
[2] Deptartment of Physics and Astronomy, University of Leicester, University Road, Leicester LE1 7RH, UK
[3] Institute of Astronomy, Madingley Road, Cambridge, CB3 0HA, UK

In preparation

ABSTRACT

Context. Dwarf spheroidal (dSph) galaxies are believed to be the remnants of a chaotic merging era in which large galaxies, such as the Milky Way and Andromeda galaxies, formed by the accretion of dwarf galaxies. Thus, determining the properties of the dSph galaxies, especially the recently discovered ultra-faint ones, is key to our understanding of galaxy formation and evolution, and may provide a window into the conditions during the star formation in the early universe.
Aims. To provide an inventory of bona fide member stars in the Draco, Sextans, Hercules and UMa II dSph galaxies and study the properties of these galaxies based on these member stars. A particular aim is to study the metallicity distribution function and the spatial distributions of the member stars as a function of metallicity.
Methods. We use Strömgren photometry towards the Draco, Sextans, Hercules and UMa II dSph galaxies to identify RGB and HB stars that belong to the dSph galaxies and thus weed out any contaminating foreground dwarf stars that belong to the Milky Way. This enables us to create a clean sample of member stars for each dSph galaxy. For Ursa Major II it is also possible to identify the turn-off region. To further enhance our analysis, we combine our Strömgren photometry with SDSS photometry. Additionally, we search the literature for [Fe/H] estimates based on high-resolution spectroscopy for dSph galaxy stars. These stars are included in our sample from which we determine a new metallicity calibration which turns the Strömgren photometry into metallicities.
Results. We provide an inventory of member stars on the RGB for the Draco and Sextans dSph galaxies that supersedes previous catalogues of stars. Additionally, we find new UMa II members. Furthermore we are able to establish a new metallicity calibration, based on [Fe/H] determined from high-resolution spectroscopy, from which we derive metallicity distribution functions for the Draco, Sextans and Hercules dSph galaxies. Additionally, we find evidence for metallicity gradients, ~ -1.5 [M/H]/kpc, for the Draco and Sextans dSph galaxies.

Key words. Galaxies:dwarf – Galaxies: evolution –

1. Introduction

Parts of large spiral galaxies, such as the Milky Way and Andromeda, are believed to have formed from the accretion of several smaller galaxies (as initially suggested by Searle & Zinn 1978). This is known as the hierarchical merging scenario, and large-scale simulations, based on the cold dark matter model, supports this theory for galaxy formation (Springel et al. 2005). Remnants of this chaotic merging era, such as dwarf-spheroidal (dSph) galaxies and stellar streams, are visible in the outskirts of large galaxies, since the dynamical timescale is long enough to allow for the remnants to remain gravitationally bound. To date, about 20 dSph galaxies have been discovered in the Local Group (e.g. Zucker et al. 2006a,b; Walsh et al. 2007; Belokurov et al. 2006, 2007, 2008, 2009), and additional ones will most likely be detected within the next few years (Tollerud et al. 2008). dSph galaxies, as compared to larger galaxies, are characterised by their low total luminosity, low surface brightness, and low abundance of heavy elements (see Grebel et al. 2003, for a discussion of the properties of dSph galaxies in general). Given this, they have more in common with globular clusters than the typical large galaxy. However, they separate in one significant aspect from globular clusters since the dSph galaxies are the most dark matter dominated objects known (e.g., Mateo 1998).

Given that many of the dSph galaxies span a large area on the sky, observations in the direction to these objects are often contaminated with a large fraction of dwarf stars the belong to the Milky Way disk, many of which may have luminosities that coincide with the luminosity of the red-giant branch (RGB) stars in the dSph galaxies (e.g., Adén et al. 2009). Thus, it is often difficult to identify stars that belong to the dSph galaxy, and not the Milky Way. A common method is to use radial velocity measurements to determine if the stars have the same velocity as the systemic velocity as the dSph galaxy (see, e.g., Walker et al. 2006; Adén et al. 2009). dSph galaxies have typical velocity dispersions of about 5 km/s. However, this requires a spectroscopic observation for each star in the study. Additionally, in some cases, the systemic velocity of the dSph galaxy may overlap with the velocity distribution of the Milky Way disk, making it difficult to separate the RGB stars in the dSph galaxy from the Milky Way dwarf stars. Indeed, in Adén et al. (2009) we showed that radial

Send offprint requests to: D. Adén daniel.aden@astro.lu.se

velocity measurements were not enough to identify members in the Hercules dSph galaxy. Instead, we relied on Strömgren photometry to provide information on the evolutionary stage of the stars. This enabled us to separate the Hercules RGB stars from the Milky Way dwarf stars, which gave us a clean sample of Hercules RGB member stars. In fact, ∼ 30 per cent of radial velocity selected stars were foreground dwarf stars. In this study, we apply the same method for membership determination on the Draco, Sextans and UMa II dSph galaxies.

The metallicity distribution function (MDF) for dSph galaxies reflect their star formation histories. The mean metallicity for a dSph galaxy increases with increasing galaxy mass, since a deeper gravitational potential is able to sustain a larger amount of gas for star formation, as predicted by theory (e.g., Ferrara & Tolstoy 2000). Estimating [Fe/H] for stars in dSph galaxies has improved significantly during the past few years. With the advent of multi-fibre spectrographs, it is now possible to cover hundreds of stars for detailed elemental abundance analysis in a reasonably short time span. The most reliable method to estimate [Fe/H] for stars is to measure the equivalent width of iron absorption lines. However, given that the Ca II triplet lines are among the strongest features in the near-infrared spectra of most late-type stars, the use of the Ca II triplet lines as an indicator for the metallicity is widely used (see, e.g., Rutledge et al. 1997; Adén et al. 2009; Starkenburg et al. 2010; Battaglia et al. 2010). However, given that wide-field photometry covers a large area of the sky, and therefore many stars, it is still beneficial to rely on a calibration that translates photometric magnitudes and colours to an estimate of [Fe/H]. The Strömgren *uvby* filter system has proven to be very suited for this.

The paper is organised as follows: in Sect. 2 we show how the gravity sensitive Strömgren c_1 index can be used to disentangle the dSph galaxy member stars from the foreground contamination. In Sect. 3 we describe the observations and data reductions for the photometric observations. In Sect. 4 we present our results. Section 5 shows our selection of RGB and HB stars for the Draco, Sextans, Hercules and UMa II dSph galaxies. In Sect. 6 we explore the ability of SDSS photometry to distinguish between RGB and dwarf stars. Section 7 deals with metallicity and our new metallicity calibration based on Strömgren photometry.

2. Finding the evolutionary stages of stars using Strömgren photometry

It is possible for RGB stars that belong to a dSph galaxy to have the same colours and magnitudes as foreground dwarf stars that belongs to the Milky Way disks. As Fig. 5 shows, the line of sight towards all of the dSph galaxies is heavily contaminated with foreground stars, making it impossible to identify the RGB stars in dSph galaxies from the colour-magnitude diagram alone. Thus, knowledge of the evolutionary stage of the stars is needed to disentangle the RGB member stars from the foreground contaminating dwarf stars that belong to the Milky Way disk and halo. The c_1 index in the Strömgren system gives us the ability to disentangle the RGB and HB stars in a dSph galaxy from the foreground dwarf stars. The c_1 index is a measure of the Balmer discontinuity in a stellar spectrum (Strömgren 1963) and is defined as

$$c_1 = (u - v) - (v - b) \quad (1)$$

The strength of the Balmer discontinuity depends on the evolutionary stage of the star. Stars in a plot of $c_{1,0}$ vs. $(b - y)_0$ will therefore occupy different regions depending on their evolutionary stage.

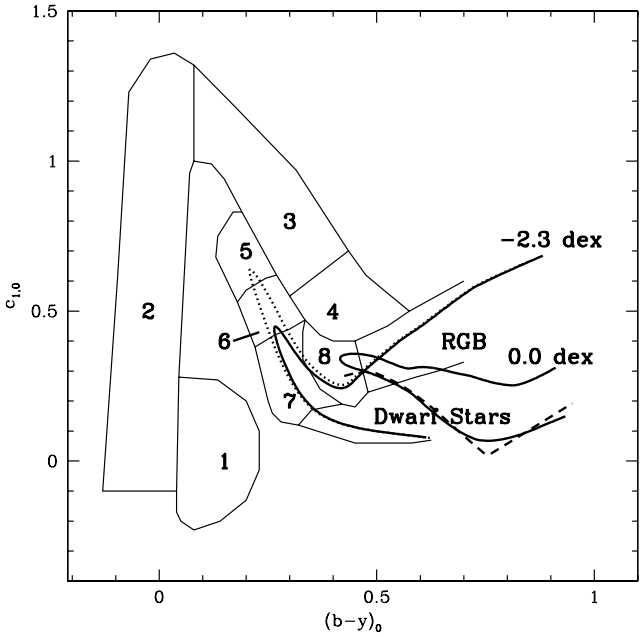

Fig. 1. $c_{1,0}$ vs. $(b - y)_0$ diagram with evolutionary regions as defined by Schuster et al. (2004). 1: the sub-luminous-blue-horizontal branch transition; 2: blue horizontal branch; 3: horizontal branch; 4: red-horizontal-branch-asymptotic-giant-branch transition; 5: blue stragglers; 6: blue-straggler-turnoff transition; 7: turnoff stars; 8: subgiant stars. The upper and lower thick solid lines indicate isochrones for RGB stars by VandenBerg et al. (2006) with colour transformations by Clem et al. (2004). Their metallicities are –2.3 and 0.0 dex, respectively, and the age is 12 Gyr. The dotted line indicates a stellar isochrone with a metallicity of –2.3 dex and an age of 12 Gyr. The dashed line indicates a dwarf star sequence with [Fe/H]=0.0 (Árnadóttir et al. 2010).

Figure 1 shows which regions are occupied by stars at different evolutionary stages. This classification is adopted from Schuster et al. (2004) and is based on metal-poor stars.

Schuster et al. (2004) were mainly concerned with high velocity dwarf stars and to a lesser extent interested in the redder dwarf and RGB stars. As the high-velocity halo stars that they studied tend to be fairly blue we will use a tracing for dwarf stars from Árnadóttir et al. (2010), and isochrones for RGB stars by VandenBerg et al. (2006) with colour transformations by Clem et al. (2004), in the $c_{1,0}$ vs. $(b - y)_0$ diagram to define part of the dwarf and all of giant star regions also in the red. The dwarf sequences in Árnadóttir et al. (2010) provide an extension of the preliminary dwarf relation from Olsen (1984). The major difference between the preliminary relation by Olsen (1984) and the new relations is that the new relations are functions of metallicity. In Fig. 1 we show a dwarf sequence for stars with [Fe/H]=0.0. This sequence, in accordance with Olsen (1984), traces the lower envelope for the dwarf stars for $(b - y)_0$ less than about 0.55. Beyond $(b - y)_0 = 0.55$ dwarf sequences for all metallicities are degenerate (Árnadóttir et al. 2010).

To define the RGB region we use two isochrones, for a 12 Gyr old system, with [Fe/H]= −2.3 and [Fe/H]= 0.0 by VandenBerg et al. (2006) and colour transformations by Clem et al. (2004), see Fig. 1. For comparison, we also show an 8 Gyr old isochrone with [Fe/H]= −2.3. We note that it separates from the 12 Gyr old isochrone at the turn-off.

As can be seen from Fig. 1, for giant stars, the c_1 index has a clear metallicity dependence. This is more pronounced for the

Table 1. Summary of the photometric observations obtained with the Isaac Newton Telescope.

dSph	*y*	*b*	*v*	*u*	Run
	[Min]	[Min]	[Min]	[Min]	
Draco field 0	120	120	120	200	2001
Draco field B	120	120	100	180	2006
Sextans	140	160	100	40	2001
Hercules	90	90	90	150	2007
UMaII	90	90	60	60	2007

Column 1 lists the dSph galaxy. Columns 2 to 5 list the exposure time for each filter. Column 6 lists the year of observation.

reddest colours (i.e. the tip of the RGB). However, in spite of this, this index still provides a strong discriminant between giant and dwarf stars for cooler stars. Additionally, we note that the isochrone with [Fe/H]= 0.0 and dwarf sequence with [Fe/H]= 0.0 are in agreement.

3. Photometric observations, data reduction, SDSS cross-correlation and de-reddening

The photometry was obtained using the Wide Field Camera (WFC) on the 2.5m Isaac Newton Telescope (INT) on La Palma. The WFC consists of 4 CCDs that cover about 0.5×0.5 degrees on the sky. We used the intermediate-band Strömgren u, v, b and y filters. Draco field 0 and Sextans were observed in March 2001, Draco field B in May 2006, and Hercules and UMaII in April 2007. During the run in 2006, an additional field towards the Draco dSph galaxy was observed (Draco field A). However, due to bad weather, it was not possible to obtain photometric data for this field. Table 1 summarises our observations of scientific targets, and Fig. 2 shows the positions of the CCD chips of the WFC for each observation.

During all our observing runs, multiple Strömgren standard stars from Schuster & Nissen (1988) and Olsen (1993) were observed. A few of these stars, typically two or three, were observed several times during each night in order to sample a wide range in airmass. The observations of these standard stars are used to calibrate the observations on to the standard system of Olsen (1993) (see Sect. 3.1).

The images for all fields were reduced with the Wide Field Survey Pipeline provided by the Cambridge Astronomical Survey Unit (Irwin & Lewis 2001). The processing operations applied to the images were de-biasing, trimming, flatfielding, astrometry and correction for non-linearity.

3.1. Photometric calibration

We obtained aperture photometry for the standard stars using the task PHOT within the IRAF [1] APPHOT package. The size of the aperture was determined individually for each star by plotting the measured flux as a function of increasing aperture size. The aperture at which the flux no longer increased was chosen as the aperture for that star (typically $4-5\times$FWHM of the stellar psf). This curve-of-growth is used in order to maximise the signal-to-noise ratio (S/N) while measuring as much flux as possible

[1] IRAF is distributed by the National Optical Astronomy Observatories, which are operated by the Association of Universities for Research in Astronomy, Inc., under cooperative agreement with the National Science Foundation.

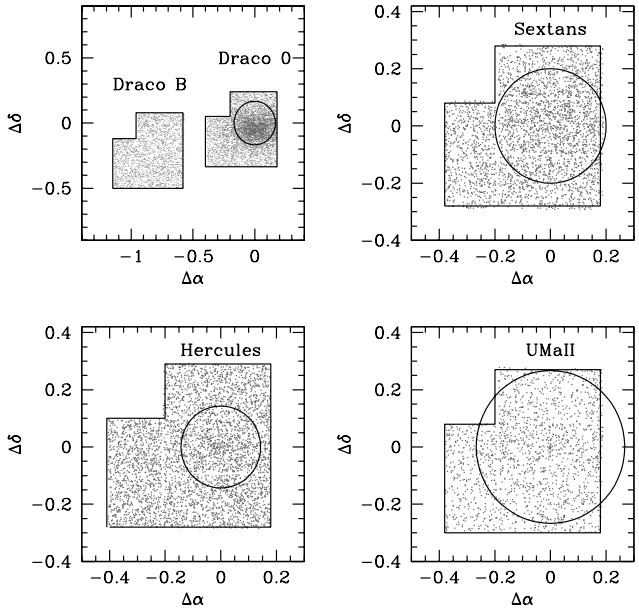

Fig. 2. Positions on the sky of our observations. The coordinates are given in Δ decimal degrees, relative to the centre of the dSph galaxy, epoch J2000. Central coordinates for the galaxies and the half-light radius (solid circles) are listed in Table 1. Solid rectangles outline the four CCD chips in the WFC used for the photometric observations. Grey dots marks the objects observed. Note the different scale for Draco for which we obtained data in two fields.

from the star (Howell 1989). The measurements of the standard and extinction stars were used to establish the transformations needed to put our observations on the standard system of Olsen (1993). See Olsen (1995) for a discussion about the Olsen system as compared to the system established by Bond (1980) and Anthony-Twarog & Twarog (1994).

We derived the parameters needed for the transformation, extinction coefficients (k) zeropoints (z) and the colour terms (a) for each of the observations following the iterative method applied in Adén et al. (2009). In short, we solved the equation

$$m_s = m_o + a_i \cdot (v-y)_s + k_i \cdot X + z_i \quad (2)$$

for a_i, k_i and z_i, where m is the magnitude of the star and X is the airmass. The subscripts s, o and i designates the standard magnitude, the observed magnitude and the filter, respectively. The extinction coefficients, colour terms and zeropoints for each filter, night and observing run are listed in Table 3. The z, k and a obtained were used to transform our observations onto the standard system of Olsen (1993). The uncertainty for z, k and a were used to calculate the typical zero point error in the magnitudes, Sect. 3.3.

3.2. Photometry of the science images

Instead of co-adding the science images, we did aperture photometry on each of the images separately. Co-adding the images would be difficult since the seeing varied from night to night and because of the necessity to apply the extinction correction for each night separately. Coordinate lists for the images were created using the task DAOFIND in the APPHOT package in IRAF. To establish the coordinate lists we used the best y image towards

Table 2. Properties of the dSph galaxies in this study.

	Draco0	DracoB	Sextans	Hercules	UMaII
α_0 (J2000)	17 20 14	17 14 30	10 13 02	16 31 05	08 51 30
δ_0 (J2000)	+57 57 54	+57 45 25	–01 36 53	+12 47 18	+63 08 18
D (kpc)	76 ± 5	...	86	132 ± 12	30 ± 5
$L_V(L_\odot)$	$2.7 \pm 0.4 \cdot 10^5$	...	$4.37 \pm 1.69 \cdot 10^5$	$3.6 \pm 1.1 \cdot 10^4$	$4.0^{+1.8}_{-1.9} \cdot 10^3$
$E(B-V)$	0.027	0.043	0.048	0.063	0.094
r_h (arcmin)	10	...	11.7	8.6	16

For Draco, Hercules and UMaII, the centroid, α_0 and δ_0, distance, D, half-light radius, r_h, and Luminosity, L_V, are adopted from Martin et al. (2008). For Sextans, these values are adopted from Walker et al. (2009); Battaglia et al. (2010). The reddening, $E(B-V)$, is given as estimated in Sect. 3.5.

each dSph galaxy, since the stars are brightest in this filter. We then used this catalogue of coordinates for all the other images. We did not put any constraints on sharpness or roundness for the detected objects. Instead, we utilised the SDSS cross-correlation, described in Sect. 3.4, to disentangle the stars from background galaxies and artefacts in the images.

We used the aperture photometry task PHOT, within the APPHOT package, to measure the flux for all objects on the images.

As a quality check we compared the flux for the brightest targets for each night with a mean flux, calculated for each object for all nights, to see if any of the images deviated in flux. None of the images deviated. From this we draw the conclusion that the calibration was consistent for each observing run.

Aperture correction. When doing photometry on the science images we used a fixed aperture of 5 pixels. Applying a curve-of-growth we obtained, for each individual image, the aperture correction out to $4 \times$ FWHM of the psf. The aperture corrections were based on measurements of many bright isolated stars, typically 20 stars per CCD. The aperture corrections were done in flux-space.

Final magnitudes. Initial magnitudes were calculated for each object and night for every image and calibrated for the airmass extinction and zeropoint using Eq. (2), but this time with subscript s as our calibrated magnitude and, as before, 0 as the observed magnitude, with coefficients from Table 3.

Since the first night for the run in 2007 (Hercules and UMaII dSph galaxies) did not give us reliable standard star photometry, and we thus have no calibration for that night, we normalized the magnitudes from that night to the mean of the magnitudes for the two following nights.

For all exposures, erroneous measurements returned from PHOT for the individual exposures were removed from the data set (i.e. the measurements for which `sier, cier` and `pier`$\neq 0$, which are the error in sky fitting, centering algorithm and photometry, respectively). The flux was then calculated for each star. The final flux, $\overline{F}$, was obtained by using a weighted-mean flux where the photometric errors returned from PHOT (`merr`) were used as weights. The expression for the final flux is thus

$$\overline{F} = \frac{\sum_{j=1}^{n} f_j/\sigma_j^2}{\sum_{j=1}^{n} 1/\sigma_j^2} \tag{3}$$

where the subscript j is the exposure, n is the total number of exposures, f_j is the flux of the individual exposure and σ_j the error (`merr`). These mean fluxes were then converted back to magnitudes and the colour terms were applied to get the final magnitudes. By definition, $y \equiv V$ (e.g., Olsen 1983).

3.3. Photometric errors

The errors in magnitudes, y, b, v and u, were calculated based on `merr` and the total number of exposures, n, for each star and filter. The final errors were calculated as

$$\epsilon = \sqrt{\frac{1}{\sum_{j=1}^{n} 1/\mathtt{merr_j}^2}} \tag{4}$$

where subscript j is the exposure. Note that if `merr` is the same for each exposure, this expression reduces to $\epsilon = \mathtt{merr}/\sqrt{n}$ which is defined as the error in the mean.

This error is suitable for a star by star quality comparison in the data, but it does not reflect the uncertainty introduced from the standard star calibration parameters, z, k and a. The errors in z, k and a translate to an uncertainty in the zero-level of the photometry.

In Adén et al. (2009) we calculated the errors in magnitude for each star using a Monte Carlo Simulation, taking into account `merr` and the uncertainty in zeropoint, extinction coefficient and colour term. We found that the uncertainty introduced from the calibration could be approximated by the uncertainty in zeropoint only. Thus, in this study, we define our total error as

$$\epsilon_{tot} = \sqrt{\epsilon_{phot}^2 + \epsilon_z^2} \tag{5}$$

where ϵ_{phot} is the final errors as derived above, and ϵ_z is the uncertainty in zeropoint as given in Table. 3. However, this error will only be discussed when it is required to consider the uncertainty in the zero-level of the photometry.

Figure 3 shows our final photometric errors for the Strömgren c_1 and $(b-y)_0$ colour indices. We denote the errors with $\epsilon_{c_{1,0}}$ and $\epsilon_{(b-y)_0}$, respectively. We note that $\epsilon_{c_{1,0}}$ is much larger than $\epsilon_{(b-y)_0}$ for a given magnitude brighter than $y_0 \sim 17$. This is because $\epsilon_{c_{1,0}}$ includes ϵ_u that in general is much larger since the u filter has the lowest transmission.

3.4. SDSS cross-correlation

In order to obtain *ugriz* photometry of our stars, and to verify that our objects observed with the Strömgren photometry are stars and not background galaxies, we cross-correlated our photometry with SDSS photometry. The SDSS photometry provide us with a stellar classification parameter. Since there exists a small difference in the astrometric solution between the Strömgren and

Table 3. Calibration coefficients.

Run 2001, Draco0 / Sextans			
Night	k_y	z_y	a_y
22 March 2001	–0.103 ± 0.015	22.704 ± 0.020	0.020 ± 0.006
24 March 2001	–0.125 ± 0.007	22.726 ± 0.012	0.020 ± 0.006
25 March 2001	–0.123 ± 0.010	22.742 ± 0.015	0.020 ± 0.006
28 March 2001	–0.142 ± 0.022	22.742 ± 0.028	0.020 ± 0.006
Night	k_b	z_b	a_b
22 March 2001	–0.157 ± 0.011	23.158 ± 0.011	0.004 ± 0.006
23 March 2001	–0.178 ± 0.005	23.175 ± 0.009	0.004 ± 0.006
24 March 2001	–0.179 ± 0.005	23.171 ± 0.009	0.004 ± 0.006
25 March 2001	–0.183 ± 0.008	23.196 ± 0.013	0.004 ± 0.006
28 March 2001	–0.193 ± 0.019	23.183 ± 0.025	0.004 ± 0.006
Night	k_v	z_v	a_v
23 March 2001	–0.293 ± 0.005	23.078 ± 0.010	0.044 ± 0.005
25 March 2001	–0.303 ± 0.013	23.100 ± 0.018	0.044 ± 0.005
28 March 2001	–0.295 ± 0.024	23.065 ± 0.031	0.044 ± 0.005
Night	k_u	z_u	a_u
24 March 2001	–0.532 ± 0.008	22.975 ± 0.014	0.068 ± 0.007
25 March 2001	–0.539 ± 0.022	23.001 ± 0.022	0.068 ± 0.007
28 March 2001	–0.521 ± 0.020	22.942 ± 0.027	0.068 ± 0.007
Run 2006, DracoB			
Night	k_y	z_y	a_y
03 May 2006	–0.140 ± 0.012	22.937 ± 0.017	0.023 ± 0.004
04 May 2006	–0.121 ± 0.015	22.472 ± 0.016	0.023 ± 0.004
05 May 2006	–0.148 ± 0.016	22.953 ± 0.023	0.023 ± 0.004
Night	k_b	z_b	a_b
03 May 2006	–0.189 ± 0.010	23.210 ± 0.015	0.013 ± 0.006
04 May 2006	–0.177 ± 0.010	22.759 ± 0.018	0.013 ± 0.006
05 May 2006	–0.199 ± 0.008	23.225 ± 0.013	0.013 ± 0.006
Night	k_v	z_v	a_v
03 May 2006	–0.289 ± 0.016	22.957 ± 0.021	0.040 ± 0.004
04 May 2006	–0.317 ± 0.017	22.565 ± 0.027	0.040 ± 0.004
05 May 2006	–0.297 ± 0.030	22.967 ± 0.030	0.040 ± 0.004
Night	k_u	z_u	a_u
03 May 2006	–0.542 ± 0.046	23.101 ± 0.046	0.063 ± 0.006
04 May 2006	–0.548 ± 0.012	22.660 ± 0.019	0.063 ± 0.006
05 May 2006	–0.560 ± 0.033	23.110 ± 0.044	0.063 ± 0.006
Run 2007, Hercules / UMaII			
Night	k_y	z_y	a_y
14 April 2007	–0.155 ± 0.021	23.009 ± 0.031	0.016 ± 0.005
15 April 2007	–0.142 ± 0.016	22.989 ± 0.023	0.016 ± 0.005
Night	k_b	z_b	a_b
14 April 2007	–0.240 ± 0.031	23.337 ± 0.043	0.009 ± 0.005
15 April 2007	–0.210 ± 0.036	23.297 ± 0.050	0.009 ± 0.005
Night	k_v	z_v	a_v
14 April 2007	–0.349 ± 0.023	23.051 ± 0.034	0.050 ± 0.006
15 April 2007	–0.353 ± 0.023	23.048 ± 0.032	0.050 ± 0.006
Night	k_u	z_u	a_u
14 April 2007	–0.582 ± 0.036	23.131 ± 0.052	0.065 ± 0.007
15 April 2007	–0.569 ± 0.013	23.117 ± 0.021	0.065 ± 0.007

Column 1 lists the field of observation and date. Columns 2 to 4 list the airmass extinction coefficients, k_i, zeropoints, z_i and colour coefficients, a_i, for each filter as indicated with uncertainties σ_k, σ_z and σ_a respectively.

the SDSS photometry, we estimated a search radius to find the matching objects, as the maximum allowed angular radius in a circle enclosing an object detected in the Strömgren photometry using a curve of growth. For each field, we increased the search radius and counted the number of objects that were found in both samples. We defined the final search radius as the radius where the number of cross-correlated objects flattened out significantly. We note that the number of cross-correlated objects do not increase significantly beyond a specific radius. Thus, this angular distance is chosen as our search radius. This procedure was repeated for all the dSph galaxy fields. The search radius was set to 4 arcsec for the Draco (field 0 and B), Sextans and Hercules fields, and 2 arcsec for the UMaII field.

However, even though the radius for the search window for the cross-correlation is small, there is still a possibility that an object is misidentified. Especially in the more crowded parts of the fields i.e., the Draco and Hercules fields. The Strömgren *b* filter and the SDSS *g* filter are positioned at the same central wavelength. Thus, to a first approximation, the difference between these two filters should be a constant. In Fig. 4 we show the dif-

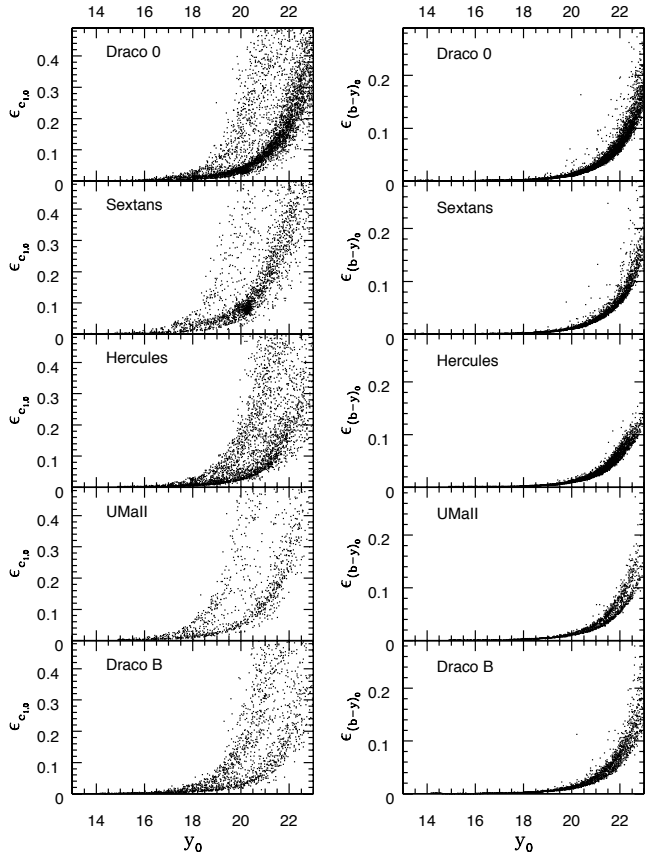

Fig. 3. Errors in the photometry for $c_{1,0}$ and $(b-y)_0$, as indicated for all our fields. Left and right columns show $\epsilon_{c_{1,0}}$ vs. y_0 and $\epsilon_{(b-y)_0}$ vs. y_0, respectively. Note the difference between $\epsilon_{c_{1,0}}$ and $\epsilon_{(b-y)_0}$ in scale.

ference between b and g as a function of b for all of our observed fields. We find that b is on average ~ 0.1 larger than g with a few outliers. These outliers could be misidentified stars and they are flagged as dubious targets. If any of these stars appear in our final sample, they will be discussed separately. Additionally, in Fig. 4, we highlight the RGB member stars as identified in 5.1. We note that the RGB stars position themselves at higher values of $(b-g)_0$, relative to the other stars in the field which essentially are the blue foreground stars. This indicates that there is a small dependence on colour in $(b-g)_0$.

3.5. De-reddening

We corrected the photometry towards the dSph galaxies for interstellar extinction using the dust maps, and relations to translate these extinction values into the Strömgren system, by Schlegel et al. (1998). The colour-excess, $E(B-V)$, found towards each dSph galaxy is given in Table 2. De-reddened magnitudes, colours and indices will henceforth have the subscript 0.

We note that several studies indicate that the dust maps by Schlegel et al. (1998) may over-estimate the reddening if $E(B-V)$ is greater than 0.15 (see, e.g., Arce & Goodman 1999; Beers et al. 2002; Yasuda et al. 2007). However, since none of our observations suffer from such high values of $E(B-V)$, we do not pursue this further.

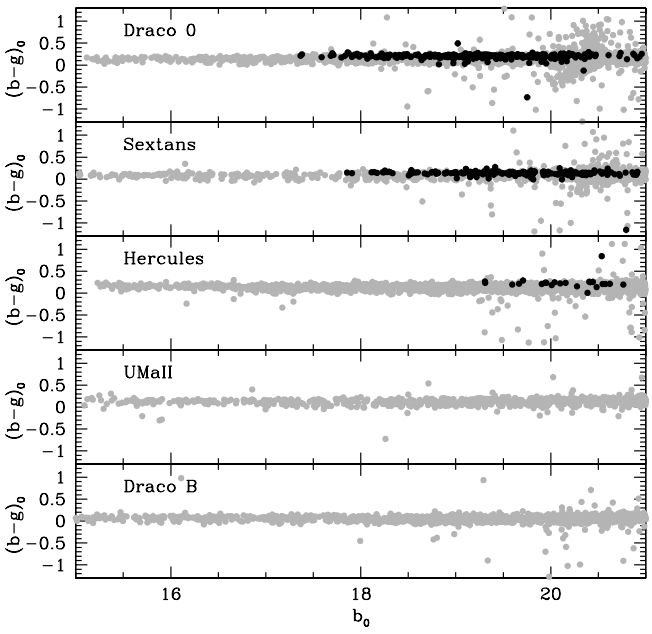

Fig. 4. $(b-g)_0$ vs. b_0 for the fields as indicated. Grey dots indicate all stars towards the indicated field. • indicate stars identified as RGB member stars for the Draco, Sextans and Hercules dSph galaxies.

4. Results

Figure 5 presents our colour magnitude diagrams in the direction towards the dSph galaxies. The horizontal branch (HB) and RGB are easily seen for the Draco and Sextans dSph galaxies. A large population of foreground stars can also be seen in all fields with a cut-off at $(b-y)_0 \approx 0.3$, associated with the blue limit of the turnoff stars in the Milky Way disk and halo. The RGB of the Hercules and UMaII dSph galaxies cannot easily be seen due to the heavy contamination by foreground dwarf stars. Additionally, the HB and RGB can not be seen in the DracoB field since it is in the extreme outer regions of the dSph galaxy.

Given that the colour $(v-y)_0$ is more metallicity sensitive than $(b-y)_0$, it is also displayed in Fig. 5 (right side panel).

For the UMaII dSph galaxy, we see an over-density of stars at the bottom left of the CMD, both in $(b-y)_0$ and $(v-y)_0$. Thus, for this field, we over-plot an isochrone for a 12 Gyr old system, by VandenBerg et al. (2006) with colour transformations by Clem et al. (2004), with [Fe/H]=–2.31 and Age=12 Gyr. We find that the over-density of stars are the turn off stars of the UMaII dSph galaxy. The isochrone was shifted with a distance modulus representative of the distance to the UMaII as given in Table 2. Given that the other dSph galaxies in this study are more distant than UMaII (compare Table 2), we do not see any turn-off stars for the other dSph galaxies. UMaII is further discussed in Sect. 9.

5. Identifying RGB and HB members of the dSph galaxies

Since the dwarf and RGB stellar sequences converge at around $(b-y)_0 \sim 0.5$ in the $c_{1,0}$ vs. $(b-y)_0$ plane, we need to identify a blue limit for stars that we identify as RGB stars. In Fig. 6 we show $c_{1,0}$ vs. $(b-y)_0$ for stars in the magnitude range $15.5 < V_0 < 17.5$ towards the Draco dSph galaxy. Stars fainter than $V_0 = 15.5$ are not saturated on the images and, given

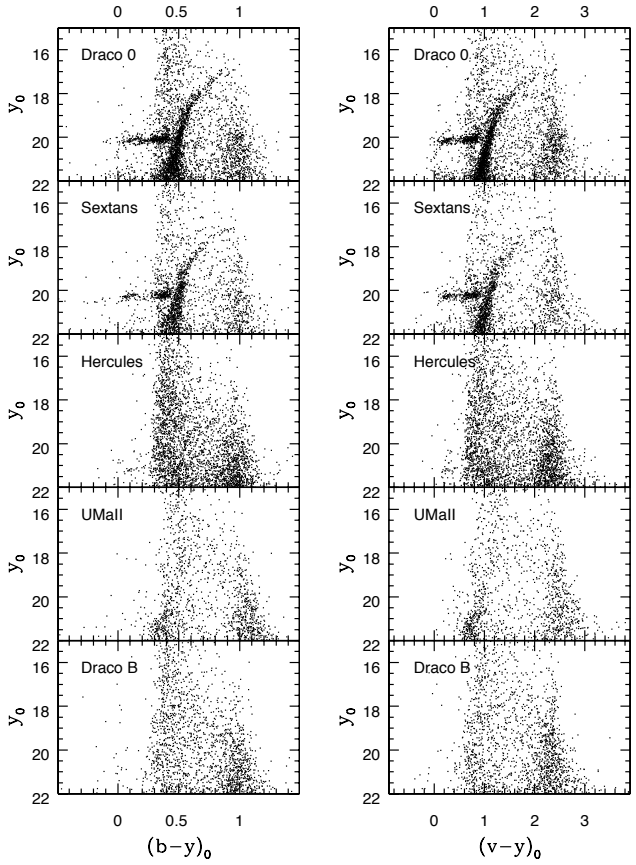

Fig. 5. Colour-magnitude diagrams centred on the dSph galaxies, as indicated. Left and right columns show y_0 vs. $(b-y)_0$ and y_0 vs. $(v-y)_0$, respectively.

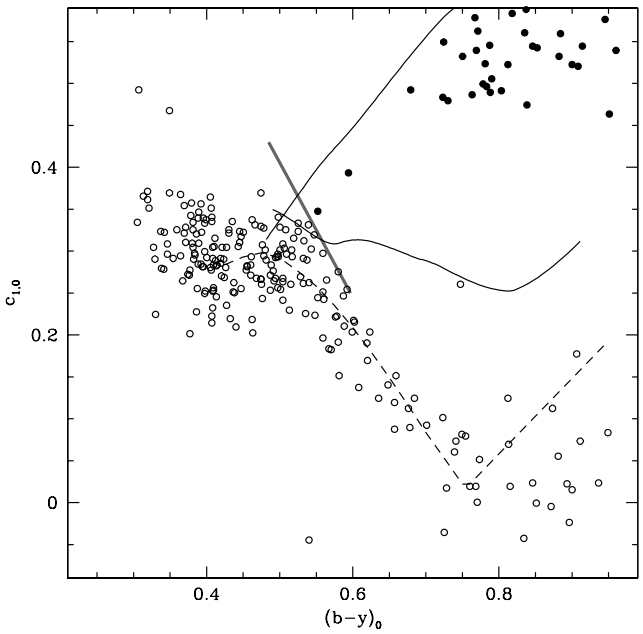

Fig. 6. $c_{1,0}$ vs. $(b-y)_0$ diagram for stars in the direction of the Draco dSph galaxy. Only stars in the magnitude range $15.5 < y_0 < 17.5$ are shown. ○ are stars within the given magnitude range. • are stars that fall within the RGB region. The upper and lower solid lines indicate isochrones for RGB stars by VandenBerg et al. (2006) with colour transformations by Clem et al. (2004). Their metallicities are, from top to bottom, -2.3 and 0.0 dex, respectively. The dashed line indicates a dwarf star sequence with [Fe/H]=0.0 Árnadóttir et al. (2010). The thick grey line marks the empirically determined blue limit for the foreground contamination.

that the distance to Draco is about 76 kpc, this magnitude range is bright enough not to contain any RGB stars in the Draco dSph galaxy that are blue enough to overlap with the dwarf sequences. Following Adén et al. (2009) and Árnadóttir et al. (2010), we define a line that follows the upper envelope of observed dwarf stars to separate the RGB stars from the dwarf stars in order to safely exclude any foreground dwarf stars. Our line is somewhat higher in $c_{1,0}$ at a given $(b-y)_0$ than the tracing from Árnadóttir et al. (2010). Our selection of RGB stars thus has a blue limit that is somewhat colour-dependent. Stars bluer than this limit will be considered as a low-probability member RGB star since they have a high probability of belonging to the foreground dwarf contamination. We applied this limit to the other fields and found that it is a good limit for them as well. Note how well the foreground dwarf stars fall along the dwarf sequence beyond $(b-y)_0 > 0.50$.

5.1. RGB members based on Strömgren photometry

Following Adén et al. (2009), we study the $c_{1,0}$ vs. $(b-y)_0$ diagram in magnitude bins. This enables a more careful selection than if the entire sample is considered at once, since we are tracing the RGB stars as they progresses towards fainter magnitudes. Additionally, this method reduces the level of foreground contamination since fewer foreground stars are considered in the region where the RGB stars are situated. See Fig. A.1, A.2, A.3, A.4 and A.5 for plots of the member selection procedure for each dSph galaxy field. For each magnitude bin and galaxy field we define the following identification system: stars that fall in the RGB region in the $c_{1,0}$ vs. $(b-y)_0$ diagram, as defined by the two isochrones, are flagged as RGB members. Stars that fall in the RGB region, but with high errors in $c_{1,0}$, relative to the majority of the stars identified as RGB stars, are removed from the member sample. We note that the majority of these stars with high errors deviate significantly from the RGB in the CMD as well. Stars that fall in the RGB region, but with a large deviation in the $c_{1,0}$ vs. $(b-y)_0$ diagram from the bulk of the RGB stars in that magnitude bin are removed from the sample. Stars that fall in the RHB-AGB region are flagged as RHB-AGB stars. Finally, stars that fall in the RGB region, but below the blue limit, as described in Sect. 2, are flagged as RGB members but with a lower membership probability since foreground dwarf stars occupy that region as well. In Table 4 we summarise the number of RGB members in each dSph galaxy.

5.1.1. Notes on individual dSph galaxy fields

Draco field 0. At a distance of about 80 kpc, the RGB stars of the Draco dSph galaxy start to appear around $y_0 = 16.5$. In Fig. A.1a, b, c and d we note that it is easy to track the bulk of the RGB as it progresses towards the blue limit in the $c_{1,0}$ vs. $(b-y)_0$ diagram. Of our fields, Draco has the highest amount of RGB stars. Additionally, we note that our criteria on the error in $c_{1,0}$ works well since the stars with a large error, marked with a

Table 4. Summary of the identified RGB and HB stars.

dSph	RGB	RGB2	HB
Draco field 0	304	186	214
Draco field B	6	5	9
Sextans	188	39	146
Hercules	28	0	10
UMaII	20	5	6

Column 1 lists the dSph galaxy. Column 2 lists the number of RGB members. Column 3 lists the number of RGB members with a lower membership probability, i.e., blue-wards of the blue limit defined in Sect. 5. Finally, column 4 lists the number of HB members.

×, deviate from the bulk of the RGB not only in error space but also in both CMD and $c_{1,0}$ vs. $(b-y)_0$ space.

Sextans. With a comparable distance to the Draco dSph galaxy, the RGB stars are expected to appear at about the same magnitudes as for the Draco dSph galaxy. Again, we note that the RGB stars clump together as we progress towards lower magnitudes. In general, the field of the Sextans dSph galaxy has fewer RGB stars than the field centred on the Draco dSph galaxy. The main reason for this is that Sextans has a much larger half-light radius (compare Fig. 2 and Table 2).

Hercules. The selection of RGB and HB stars is described in detail in Adén et al. (2009). This dSph galaxy has a much lower surface density of RGB stars, when compared to the Draco and Sextans dSph galaxies. Indeed, as explained in Adén et al. (2009), without the strength of the Strömgren photometric $c_{1,0}$ index it is very difficult to disentangle the RGB from the foreground contamination for this dSph galaxy (compare Fig. 5). We note that at a distance of about 130 kpc, the RGB stars are in general much fainter for this dSph galaxy, than for the Draco and Sextans dSph galaxies, and the tip of the RGB is at $V \sim 18.5$.

UMaII. This is by far the least populated dSph galaxy in this study. With a nominal distance of about 30 kpc (Martin et al. 2008), the RGB stars are expected to be bright. This dSph galaxy field is discussed in detail in Sect. 9

5.2. HB members based on Strömgren photometry

Apart from the identified RGB members of the dSph galaxies included in this study, we found RHB-AGB stars for the Draco, Sextans and UMaII dSph galaxies (Sect. 5.1). However, it is possible to use the Strömgren photometry to further explore the red-horisontal brach (RHB) and the blue-horizontal branch (BHB). Figures 8a, 9a and 10a show the BHB and RHB regions, for the Draco, Sextans and UMaII dSph galaxies, in the c_1 vs. $(b-y)$ plane as defined in Schuster et al. (2004). We limit our analysis of HB stars to $19.5 < y_0 < 21.0$ for the Draco and Sextans fields, and $17.5 < y_0 < 20.0$ for the UMaII field, since no HB stars are expected outside these magnitude regions. Stars that fall on or near the RHB or BHB region are identified as HB stars. We note that, for both the Draco and Sextans dSph galaxies, there are a lot of stars that fall in these regions. However, there are also a lot of stars that fall above the RHB region. To investigate this further, we cross-correlated our photometry for Draco with the photometry for variable stars in Bonanos et al. (2004). In Fig. 7a and 7b we show c_1 vs. $(b-y)$ and y_0 vs. $(b-y)$ for variable stars in the Draco dSph, as identified in Bonanos et al. (2004). We note that many of the variable stars fall above the RHB region, just as for our stars in the Draco and Sextans dSph galaxies. Thus, our stars that fall in this region, above the RHB region, are likely variable stars and are henceforth included in our sample of stars identified as HB stars.

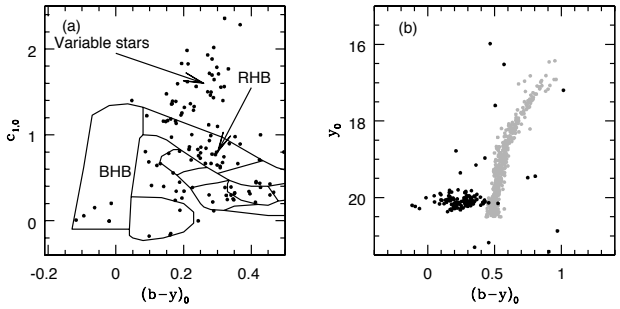

Fig. 7. (a) $c_{1,0}$ vs. $(b-y)_0$ for variable stars in the Draco dSph galaxy, as identified in Bonanos et al. (2004). The solid lines outline the identification scheme for metal-poor stars developed by Schuster et al. (2004), see also Sect. 2. BHB: the blue horizontal branch; RHB: the red horizontal branch. • indicate the variable stars. **(b)** Colour-magnitude diagram in the Strömgren system for the stars in (a). • indicate the variable stars, and grey dots mark the stars identified as RGB stars (see Sect. 5.1)

In Fig. 8b,c, 9b,c and 10b,c we show y_0 vs. $(b-y)$ and ϵ_{c_1} vs. $(b-y)$ for the stars in the Draco, Sextans and UMaII dSph galaxies, respectively. Note that Fig. 8 includes both Draco 0, (field centred on the dSph galaxy) and Draco B (outskirts), compare Fig. 2. Given that all of our stars identified as HB stars have relatively small errors, we do not exclude any stars from the sample based on error cuts.

For the Draco dSph galaxy we note that there is a peculiar feature for the HB stars. At $(b-y)_0 \sim 0$, we see a small dip that extends to fainter magnitudes. For comparison, in Fig. 8d, we show SDSS i_0 vs. $(g-i)_0$ for the HB stars identified in the Draco dSph galaxies. We see a similar feature for the HB stars in the SDSS CMD. Thus the sudden dip in magnitude is most likely not caused by a systematic error in our INT photometry but is a real feature. The same feature is seen for the outer Draco field (field B).

The selection of HB stars in the Hercules dSph galaxy was carried out in Adén et al. (2009).

In Table 4 we summarise the number of HB members in each dSph galaxy.

6. Identifying red giants with SDSS *ugriz* filters

Using the photometry from SDSS, the SEGUE survey designed a series of colour, magnitude, and other criteria to identify the evolutionary stages for stars. In Fig. 11a we show SDSS colours $(u-g)_0$ vs. $(g-r)_0$ for the Draco dSph galaxy. The region highlighted with solid lines marks the region where late K giants are assumed to fall, as defined by the SEGUE target selection[2]. We find 21 stars in this region. In Fig. 11b we show $c_{1,0}$ vs. $(b-y)_0$ for the stars in Fig. 11a (compare Fig. 1). We find that 6 of the

[2] The criteria for different evolutionary stages can be found at `http://www.sdss3.org/dr8/algorithms/segueii/segue_target_selection.php`

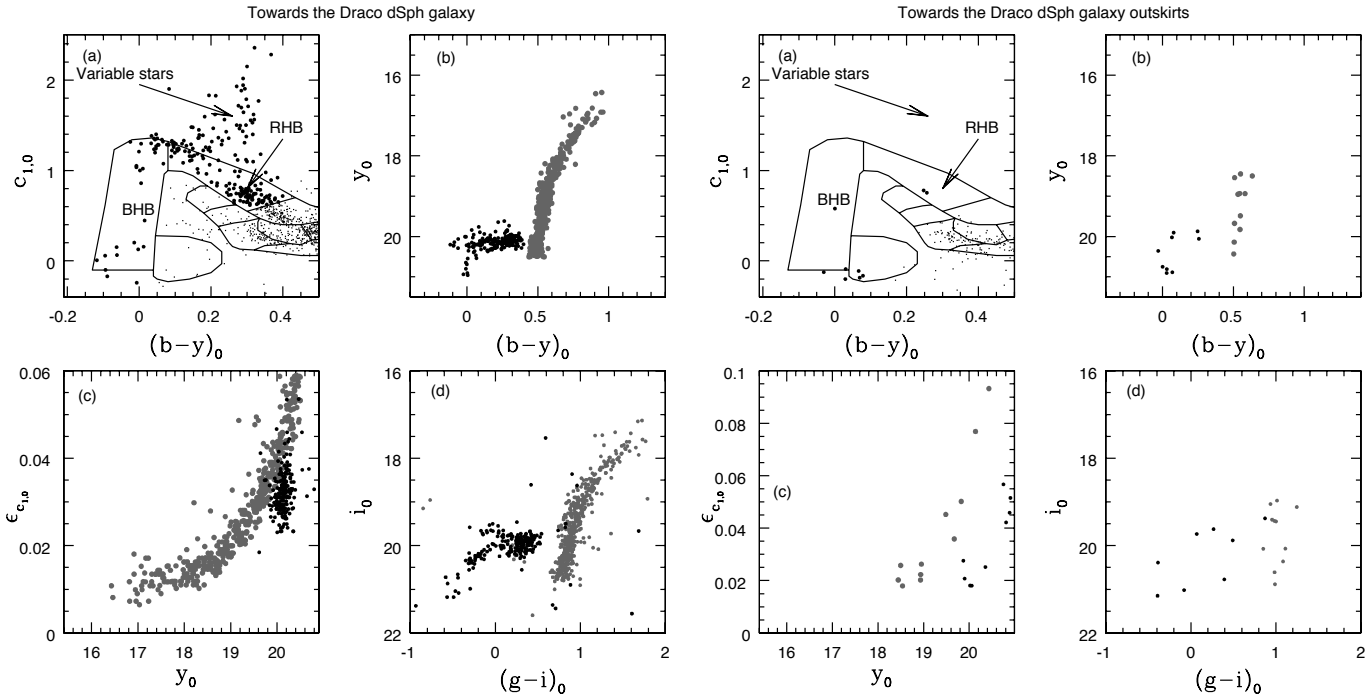

Fig. 8. (a) $c_{1,0}$ vs. $(b-y)_0$ for the stars in the direction of the Draco dSph galaxy. The solid lines outline the identification scheme for metal-poor stars developed by Schuster et al. (2004), see also Sect. 2. BHB: the blue horizontal branch; RHB: the red horizontal branch. • are stars that fall on or near the HB region, they are thus identified as HB member stars. Small dots are all stars within the magnitude range $19.5 < y_0 < 21.0$. **(b)** Colour-magnitude diagram in the Strömgren system. • indicate HB stars. Grey dots are identified RGB stars. **(c)** $\epsilon_{c_{1,0}}$ index vs. y_0 for the stars in (b), with the same coding. SDSS i_0 vs. $(g-i)_0$ for the stars in (b), with the same coding.

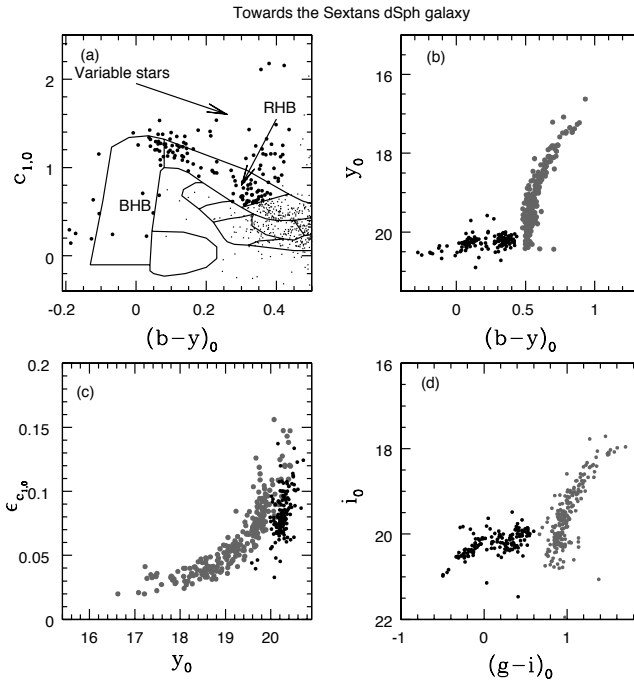

Fig. 9. Same as Fig. 8, but for the Sextans dSph galaxy.

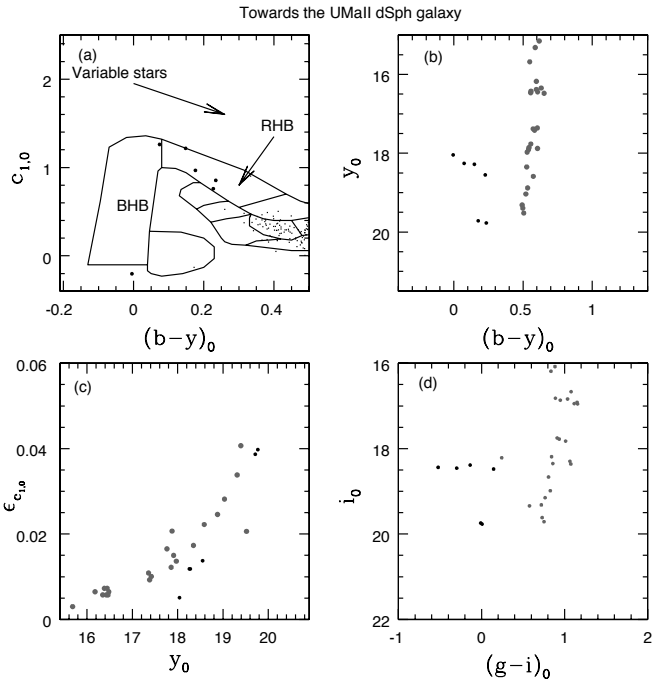

Fig. 10. Same as Fig. 8, but for the UMaII dSph galaxy.

stars are RGB stars, 11 are dwarf stars, and 4 of the stars occupy a region with $c_{1,0} \sim -0.5$ and $(b-y)_0 \sim 1$. These 4 stars are highlighted in Fig. 11 with ⊗. In Faria et al. (2007) it was concluded that carbon giant stars in the Draco dSph galaxy occupy this region. We flag these stars as likely giant carbon stars. Thus, about 10 of the 21 stars are likely giant stars. Figure 11c and 11d show SDSS and Strömgren colour-magnitude diagrams, respectively, for the stars in 11a and 11b. Given that all of the stars considered in this Sect. are bright, we do not apply any error cuts to the data. In 11a, b, c and d we repeat the procedure for the Sextans dSph galaxy. We find 4 stars in the late K giants region, of which 2 are dwarf stars and 2 are RGB stars.

We conclude that the SEGUE target selection is able to identify giant stars at a ∼ 50 per cent success rate.

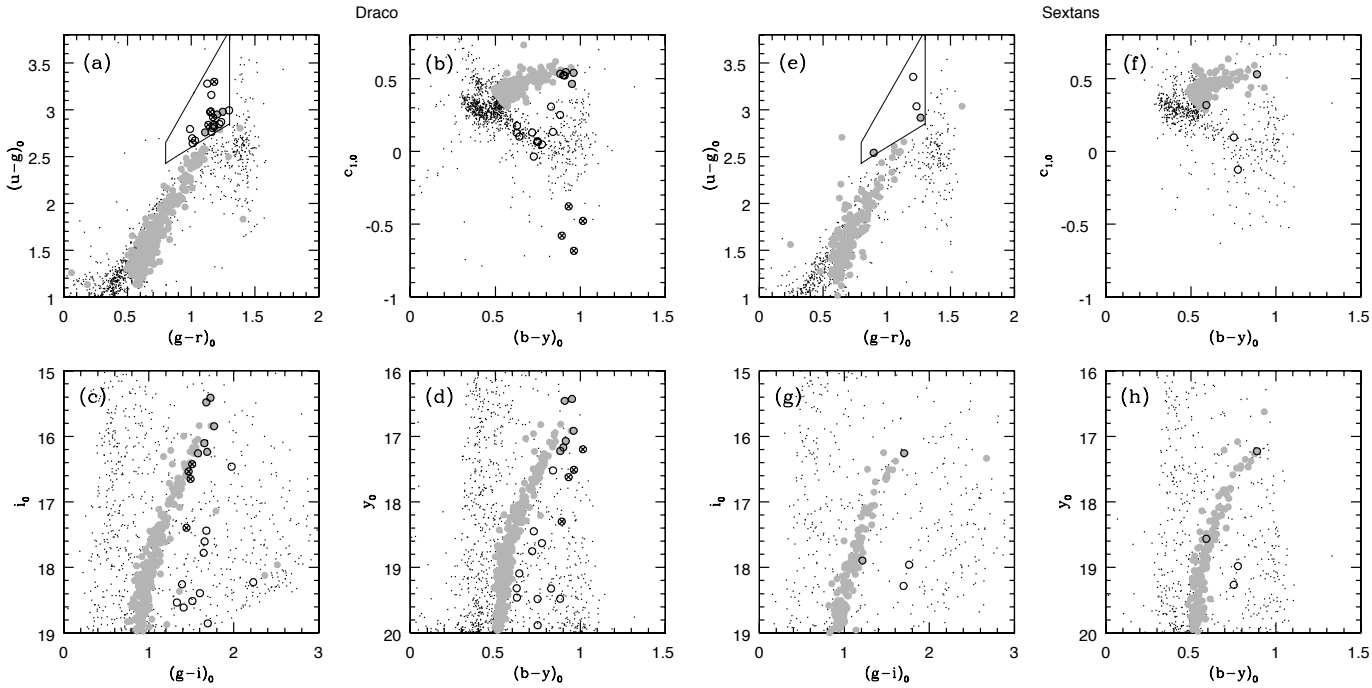

Fig. 11. Left-hand side: (a) $(u-g)_0$ vs. $(g-r)_0$ for stars in the direction of the Draco dSph galaxy. Grey solid circles indicate stars identified as RGB stars (see Sect. 5.1). Black circles mark stars that fall in the region for K giants, outlined by solid lines, as defined by the SEGUE target selection. ⊗ show likely carbon stars. **(b)** $c_{1,0}$ vs. $(b-y)_0$ for the stars in (a). **(c)** and **(d)** show SDSS and Strömgren colour-magnitude diagrams, respectively, as indicated. **Right-hand side:** Same as the left-hand side for the Sextans dSph galaxy.

7. Metallicities

Estimating the metallicity for stars in coherent stellar systems is key for our understanding of the origin and evolution of the system. Obviously, the most reliable method for the determination of [Fe/H] is to measure the equivalent widths of the iron lines themselves. However, this method relies on the collection of large amounts of light from the individual stars. This is a time consuming procedure, especially if one wishes to probe to faint magnitudes. A competing method for the determination of [Fe/H] is to measure the equivalent width of Ca II IR triplet lines. These absorption lines are, relative to iron lines, intrinsically strong and easily accessible. However, determining [Fe/H] based on the Ca II IR triplet lines is difficult for metal-poor stars since the equivalent widths are weak. Additionally, the production of Ca is associated with the end-stage of massive stars which indicates that the Ca abundance do not trace the over all metallicity for a star. i.e., stars formed early in the star formation history generally have a higher [Ca/Fe] than stars formed subsequently.

With the advent of multi-fibre spectrographs, it has become more common to measure the [Fe/H] for many stars in dSph galaxies and globular clusters. However, the possibility of photometry to estimate metallicity has its advantages since it may cover a large area on the sky, and thus many stars at once can be analysed. Strömgren photometry offers an interesting possibility as it can provide good metallicity estimates (e.g., much better than broad band photometry, compare Árnadóttir et al. 2010).

One of the difficulties when deriving a new metallicity calibration is to define the sample on which the calibration is based on. This sample will not only define the accuracy of the calibration, but also define for which range that it is valid. Finding metal-poor field stars is challenging. Because of this, most calibrations utlizes globular clusters as sources of reasonably large samples of the most metal-poor stars. However, globular clusters do no contain stars much more metal-poor than ~ -2.2 dex and thus most calibrations to derive metallicities, both from photometry as well as from Ca II NIR triplet measurements, are not applicable at lower metallicities (e.g., Hilker 2000; Calamida et al. 2007). Our studies of dSph galaxies, using Strömgren photometry combined with our own and others high resolution spectroscopic studies, provide an entirely new data set that can be utilised to provide a new calibration.

7.1. A new metallicity calibration for RGB stars from *uvby*-photometry

In this section, for giant stars based on Strömgren photometry, we construct a new metallicity calibration. Following Grebel & Richtler (1992), we use the relation

$$m_1 = \alpha + \beta \cdot (b-y) + \gamma \cdot [\mathrm{Fe/H}] + \delta \cdot (b-y) \cdot [\mathrm{Fe/H}] \qquad (6)$$

to translate the Strömgren m_1 and $(b-y)$ index to an estimate of [Fe/H] based on photometry, [M/H]. The task now becomes to determine the constants α, β, γ and δ.

Sample of stars for the calibration. For the calibration, we have collected spectroscopic [Fe/H] derived from high-resolution spectra available for stars in Draco (Cohen & Huang 2009; Shetrone et al. 2001), Sextans (Shetrone et al. 2001), UMaII (Frebel et al. 2010) and Hercules (Koch et al. 2008; Adén et al. 2011), and combined these data with our own Strömgren photometry. In this way we will be able to push the calibration to lower metallicities than what is available for globular clusters (e.g., M92, with a metallicity of about -2.3 dex, is one of the most metal-poor globular clusters Sneden et al. 2000). Note that not all stars in the spectroscopic studies have Strömgren photometry as they may fall outside the field of view or, in a few

Table 6. Multilinear regression coefficients.

α	β	γ	δ
-0.168	0.878	0.005	0.149

$$m_1 = \alpha + \beta \cdot (b-y) + \gamma \cdot [\mathrm{Fe/H}] + \delta \cdot (b-y) \cdot [\mathrm{Fe/H}]$$

unfortunate cases, just in the regions between the four CCDs in the WFC mosaic.

In total, this gives us 29 dSph galaxy RGB stars for the calibration. Unfortunately, the recently published metal-poor stars in the Sextans dSph galaxy (Aoki et al. 2009; Tafelmeyer et al. 2010) were not possible to include in the sample, since they are all outside our field of view. Additionally, in order to increase the [Fe/H] calibration range and to increase the accuracy and precision of the multi-linear regression, we add Milky Way RGB field stars from Cayrel et al. (2004), 6 stars, and Gratton et al. (1999), 24 stars, to the sample. The photometry for these stars are adopted from Olsen (1993) and Olsen (1994). For 6 of the stars, Olsen photometry is not available. Instead, we adopt the Strömgren photometry from Hauck & Mermilliod (1998). [Fe/H] and photometry for theses stars are listed in Table 5.

De-reddening of the field stars. We corrected the photometry for the field stars for interstellar extinction using the dust maps by Schlegel et al. (1998). Since most of the field stars are inside the dust disk, we have to reduce the reddening according to their position in the galaxy. Following, e.g., Beers et al. (2002); Árnadóttir et al. (2010), we reduce the extinction using

$$E(B-V) = \left(1 - e^{-|d \sin b|/h}\right) \cdot E(B-V)_{LOS} \quad (7)$$

where $E(B-V)_{LOS}$ is the full extinction along the line of sight (LOS), as determined from Schlegel et al. (1998), d is the distance to the star, b is the galactic latitude and h is the scale height of the Milky Way disk. We adopt a scale height of 125 kpc from Beers et al. (2002), and the distances from the Hipparcos catalogue (Perryman et al. 1997).

Regression results. We use a multilinear regression to solve Eq. 6 for α, β, γ and δ. After the first fit with the full sample, we remove stars with [Fe/H]–[M/H]> 3σ, where [M/H] is the metallicity as derived using the new calibration. We iterate this process until no more 3σ outliers are found. In total, we removed 4 stars from the sample in this way. Thus, 55 stars remain in the final calibration sample. Our final multilinear regression coefficients are given in Table. 6, and in Fig. 12 we show the residuals, [Fe/H]-[M/H]. The standard deviation for the residuals is σ = 0.28 dex. We adopt this error as the uncertainty in [M/H] introduced by the calibration.

7.2. Testing our new metallicity calibration

Lind et al. (2010) studied the metal-poor globular cluster NGC6397. Using high-resolution spectra, obtained with the FLAMES/UVES spectrograph, they determined [Fe/H] based on measurements of the equivalent widths of iron lines for 21 RGB stars. In Fig. 13a we show the residuals, $[\mathrm{Fe/H}]_{\mathrm{Lind}} - [\mathrm{M/H}]$, vs. $[\mathrm{Fe/H}]_{\mathrm{Lind}}$ for their 21 RGB stars. In Fig. 13b we show $[\mathrm{Fe/H}]_{\mathrm{Lind}} - [\mathrm{M/H}]$ vs. $(b-y)_0$. [M/H] for these stars were determined using our new calibration, with the photometry from Lind et al. (2009). We find that the agreement

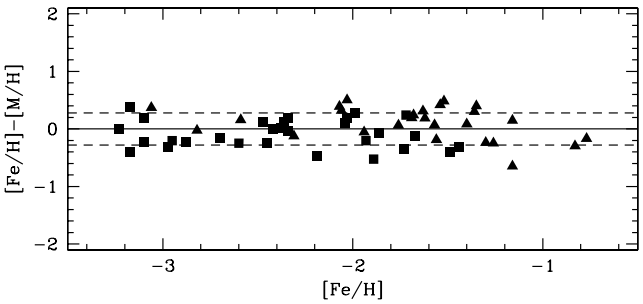

Fig. 12. The residuals, [Fe/H]-[M/H], vs. [Fe/H] for the stars in the metallicity calibration. Solid triangles indicates RGB field stars. Solid squares indicates dSph galaxy RGB stars. The upper and lower dashed lines indicate the 1σ limits.

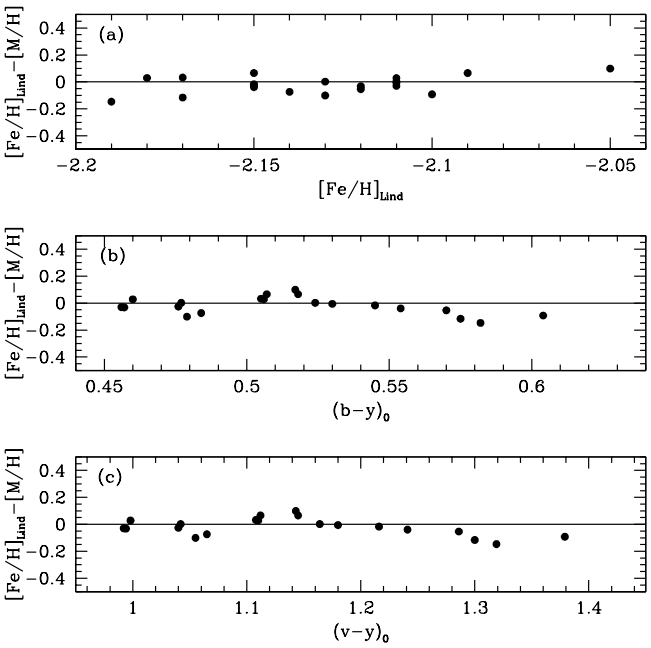

Fig. 13. The residuals, $[\mathrm{Fe/H}]_{\mathrm{Lind}} - [\mathrm{M/H}]$, vs. $[\mathrm{Fe/H}]_{\mathrm{Lind}}$ **(a)**, $(b-y)_0$ **(b)** and $(v-y)_0$ **(c)** for the stars in Lind et al. (2010).

is very good,with no significant trend in the colour $(b-y)_0$, and an offset of $[\mathrm{Fe/H}]_{\mathrm{Lind}} - [\mathrm{M/H}] = -0.02$. This is within our error-bars for the new metallicity calibration. Additionally, we note that the RGB stars in Lind et al. (2010) span a large range in colour (compare Fig. 1 in Lind et al. 2010). This indicates that our calibration is working as intended over a wide range of colours.

As an additional comparison, we apply our calibration to RGB stars in the M92 globular cluster (Strömgren photometry provided by Frank Grundahl, private communication). M92 has an average [Fe/H] of about –2.3 dex (Sneden et al. 2000). We select stars brighter than $y_0 < 15$. We find an average metallicity for these RGB stars of –2.4 dex with a σ of 0.16 dex. Thus, this comparison gives further evidence that the calibration performs well.

Table 5. Summary of the stars for the new metallicity calibration.

ID	RA(2000)	DEC(2000)	$(b-y)$	m_1	[Fe/H]	E(B-V)	REF
HD 2796	7.82047	-16.79467	0.54	0.07	-2.470	0.021	0
HD 122563	210.63269	9.68610	0.64	0.10	-2.820	0.022	0
HD 186478	296.30892	-17.49085	0.69	0.08	-2.590	0.106	0
BD +173248	262.06029	17.50996	0.50	0.05	-2.070	0.034	0
BD -185550	299.70724	-18.20310	0.69	-0.02	-3.060	0.161	0
CD -38245 [a]	11.65081	-37.65932	0.61	0.03	-4.190	0.012	0
HD 2665	7.68936	57.06490	0.55	0.07	-1.940	0.124	1
HD 7041	17.45612	-56.35602	0.50	0.22	-0.830	0.014	1
HD 9051	22.19376	-24.34040	0.54	0.16	-1.570	0.010	1
HD 21581	52.22702	-0.41753	0.56	0.13	-1.560	0.099	1
HD 23798	56.69051	-30.85370	0.74	0.18	-2.030	0.009	1
HD 26169	60.21849	-75.60318	0.51	0.06	-2.310	0.062	1
HD 26297	62.26424	-15.89085	0.74	0.24	-1.680	0.032	1
HD 36702	82.96763	-38.55668	0.82	0.23	-2.060	0.031	1
HD 41667	91.26519	-32.99409	0.61	0.29	-1.160	0.034	1
HD 74462	132.08605	67.44997	0.66	0.20	-1.360	0.051	1
HD 83212	144.08314	-20.88743	0.70	0.25	-1.400	0.046	1
HD 111721	192.85498	-13.49116	0.51	0.16	-1.260	0.044	1
HD 118055	203.66630	-16.32298	0.85	0.27	-1.760	0.093	1
HD 122956	211.30427	-14.85707	0.67	0.17	-1.630	0.068	1
HD 126238	216.37482	-43.64360	0.57	0.11	-1.520	0.054	1
HD 136316 [a]	230.57477	-53.23756	0.82	0.21	-1.740	0.400	1
HD 141531	237.31874	9.61179	0.77	0.26	-1.620	0.042	1
HD 142948	240.01005	-53.85150	0.63	0.21	-0.770	0.138	1
HD 151559 [a]	252.28382	-27.57079	0.59	0.16	-0.630	0.278	1
HD 166161	272.41952	-8.77934	0.69	0.08	-1.160	0.289	1
HD 175305	281.77683	74.72540	0.50	0.15	-1.300	0.047	1
HD 187111	297.16489	-12.12215	0.83	0.22	-1.540	0.133	1
HD 215601	341.70039	-31.87205	0.54	0.14	-1.350	0.015	1
HD 222434	355.17296	-34.69627	0.71	0.24	-1.690	0.012	1
INT 20568	259.54343	57.86928	0.87	0.26	-2.340	0.027	2
INT 31665	259.82304	58.01870	0.96	0.32	-1.990	0.027	2
INT 41498	260.14253	57.89227	0.81	0.38	-1.490	0.027	2
INT 43333	259.92443	57.87208	0.79	0.24	-2.450	0.027	2
INT 43489	259.90134	57.85695	0.82	0.36	-1.890	0.027	2
INT 43525	259.89776	57.97966	0.80	0.34	-1.730	0.027	2
INT 42146	260.06732	57.88229	0.74	0.16	-2.970	0.027	3
INT 42250	260.05647	57.86651	0.76	0.27	-1.860	0.027	3
INT 42560	260.02368	57.96471	0.79	0.26	-1.720	0.027	3
INT 42790	259.99543	57.95587	0.87	0.25	-2.360	0.027	3
INT 43257	259.93643	57.96034	0.93	0.41	-1.670	0.027	3
INT 43504	259.90008	57.94144	0.80	0.37	-1.440	0.027	3
INT 11129	153.17429	-1.75756	0.91	0.35	-1.930	0.048	3
INT 41021	153.27052	-1.65356	0.74	0.25	-2.190	0.048	3
INT 40935	132.47261	63.13937	0.61	0.00	-3.100	0.094	4
INT 40181	133.13957	63.08365	0.64	0.02	-3.230	0.094	4
INT 40065	133.24597	63.09851	0.72	0.12	-2.340	0.094	4
INT 12175	247.81591	12.58238	0.83	0.07	-3.170	0.063	5
INT 42241	247.73849	12.78898	0.82	0.23	-2.030	0.063	5
INT 42149	247.74718	12.79045	0.70	0.11	-2.950	0.063	5
INT 41743	247.78386	12.80170	0.70	0.14	-2.420	0.063	5
INT 42795	247.68541	12.82996	0.67	0.09	-3.170	0.063	5
INT 40789	247.87404	12.74030	0.67	0.10	-2.880	0.063	5
INT 41460	247.80860	12.75741	0.68	0.09	-3.100	0.063	5
INT 42096	247.75261	12.82550	0.66	0.13	-2.600	0.063	5
INT 40993	247.85432	12.75811	0.67	0.13	-2.380	0.063	5
INT 42324	247.73111	12.76968	0.62	0.09	-2.700	0.063	5
INT 12729 [a]	247.78123	12.52606	0.67	0.06	-2.350	0.063	5
INT 41082	247.84564	12.74666	0.78	0.21	-2.040	0.063	6

Column 1 lists the ID. Columns 2 and 3 list the coordinates. Column 4 and 5 list the $(b-y)$ and m_1 indices, respectively. Column 6 lists the spectroscopic [Fe/H]. Column 7 indicates E(B-V) and column 8 the reference. *a* mark stars that were excluded from the multi-linear regression. References: 0 Milky Way (Cayrel et al. 2004), 1 Milky Way (Gratton et al. 1999), 2 Draco (Cohen & Huang 2009), 3 Draco and Sextans (Shetrone et al. 2001), 4 UMaII (Frebel et al. 2010), 5 Hercules (Adén et al. 2011), 6 Hercules (Koch et al. 2008).

7.3. Metallicity distributions

In Sect. 7.1 we provide a new Strömgren metallicity calibration. This calibration is valid for stars with $-3.3 < [Fe/H] < -0.7$. In Fig. 14 we show the resulting histograms of $[M/H]_{phot,new}$ for the RGB stars identified in the Draco, Sextans and Hercules dSph galaxies (see Sect. 5.1). The bin size of 0.3 dex represents the typical error in $[M/H]_{phot,new}$ (see Sect. 7.1). A small fraction of stars for each dSph galaxy have an [M/H] less than the range for which the new metallicity calibration is valid. However, these stars are included in the sample as a slight extrapolation. We note that the MDFs for the Draco and Sextans dSph galaxies look similar, while the MDF for Hercules peaks at a much lower [M/H]. Given that the Hercules dSph galaxy is much fainter than Draco and Sextans, this is expected from the luminosity-metallicity relation (Grebel et al. 2003; Kirby et al. 2011). In Adén et al. (2011) we derived the MDF for the Hercules dSph galaxy, based on a simple metallicity calibration. When compared to the MDF in this study, we find that the spread in metallicity is about the same, i.e., the majority of the stars are located between −2 and −4 dex. However, the MDF for the Hercules in Fig. 14 appears to have a metal-poor tail. This was not observed in Adén et al. (2011).

The average [M/H] for the Draco, Sextans and Hercules MDFs are -2.1, -2.2 and -2.7, respectively. The metallicity spread is about 3 dex for the Draco and Sextans dSph galaxies, and 2 dex for Hercules. In a recent study, Battaglia et al. (2010) studied the Sextans dSph galaxy based on data from the DART survey. They were able to estimate [Fe/H], based on the equivalent widths of the Ca II IR triplet lines, for 174 RGB stars. Our MDF for the Sextans dSph galaxy is in agreement with their results on the metal-rich end of the MDF (i.e., peaks at about -2 dex with a steep slope at the metal-rich end). However, they do differ slightly for the metal poor end. Our MDF indicates a larger fraction of stars with [Fe/H]< −3.5. Additionally, we note that there is a bump in the MDF at [Fe/H]~ -3 in Battaglia et al. (2010). We find no such bump in our MDF. This difference could be due to that Battaglia et al. (2010) are able to probe a much more extended field than in our study. As indicated in their Fig. 9, the bump at [Fe/H]~ -3 is caused by stars at a projected radii $R > 0.8$ degrees. In another recent study by Kirby et al. (2011), [Fe/H] for 141 RGB stars in Sextans were determined based on spectral synthesis of iron absorption lines. Again, our MDF is in agreement on the metal-rich end of the MDF. Given that the sample in Kirby et al. (2011) extend to only 21.4 arcmin, no metal-poor bump is seen in their MDF. Their MDF has more in common with our MDF, although a larger fraction of metal-poor stars are discovered in our MDF.

7.4. Metallicity gradients

Given our large sample of high probability member stars for the Draco, Sextans and Hercules dSph galaxies, and an estimate of [M/H] based on our new calibration, we investigate the presence of metallicity gradients present in these galaxies. In Fig. 15 we show [M/H] vs. distance to the centre for the RGB stars that were determined to have a high probability of being members of the Draco, Sextans and Hercules dSph galaxies. Additionally, for this analysis, we removed stars with [M/H] beyond the range for which the calibration is valid, in order to increase the accuracy. We used the distance to each dSph galaxy as given in Table. 2 to convert angular distance to kpc. For the Draco and Sextans dSph galaxies, we find tentative evidence for the presence of metallicity gradients, -1.5 [M/H]/kpc and -1.4 [M/H]/kpc

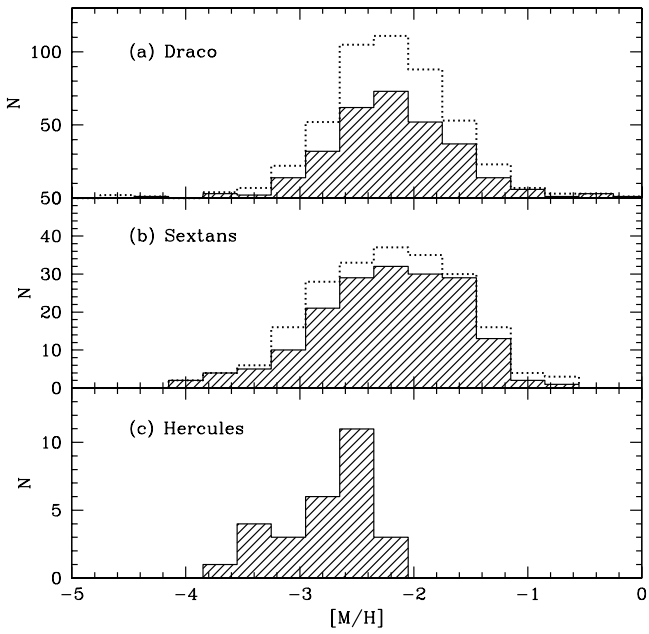

Fig. 14. Metallicity histograms for the Draco, Sextans and Hercules dSph galaxies, as indicated. The dotted line indicates all RGB stars (including those below the blue limit) and the shaded histogram shows the clean sample of RGB stars, as defined in Sect. 5.1

respectively. We do not find any evidence of a metallicity gradient in the Hercules dSph galaxy. This could be due to the low number of RGB stars available for the analysis.

In a similar study, Kirby et al. (2011) determined the metallicity gradients for eight dSph galaxies. They found gradients of -0.45 [Fe/H]/kpc and 0.12 [Fe/H]/kpc for the Draco and Sextans dSph galaxies, respectively. Thus, our metallicity gradients are significantly steeper.

Additionally, to investigate the presence of a metallicity gradient further, we perform the following analysis. Assuming that the metallicity gradient around the semi-minor axis (in the ellipse that desribes the orientation of the dSph) is more likely then around the semi-major axis we can define the "semi-minor axis distance" $d_{mi}(\theta)$ as the distance, perpendicular to the semi-minor axis, between the axis and the star. For each of the RGB stars in the Draco, Sextans and Hercules dSph galaxies we calculate this distance for different position angles θ. We then derive the metallicity gradient , $k_{[M/H]}$, and zeropoint, $m_{[M/H]}$, by solving the following equation with a least-squares fit for each position angle,

$$[M/H] = k_{[Fe/H]} \times d_{mi}(\theta) + m_{[Fe/H]} \quad (8)$$

where [M/H] is the metallicity measurement, as determined by our new calibration (see Sect. 7.1), for each star. The least-squares fit to this function yields a χ^2 value for each θ.

For the Draco, Sextans and Hercules dSph galaxies we find a position angle of 78, 120 and 92 degrees, where χ^2 is minimised, with a metallicity gradient of –0.86, –1.0 and -0.66 [M/H]/kpc, respectively. We note that these values for the metallicity gradients are lower than the values derived above, except for the Hercules where we see a tentative evidence for a gradient. This could be due to the high degree of flattening for the Hercules dSph galaxy (Coleman et al. 2007).

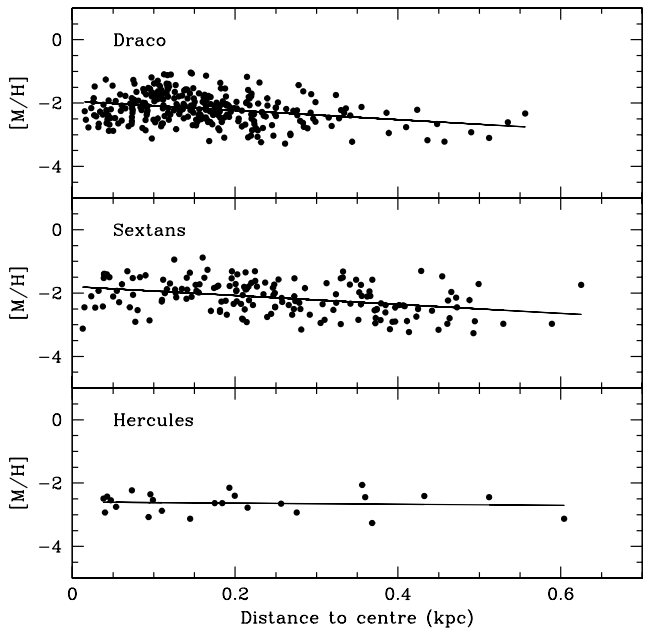

Fig. 15. [M/H] vs. distance to the centre for the Draco, Sextans and Hercules dSph galaxies, as indicated. The solid lines indicate the least-squares fits. The metallicity gradients are -1.5, -1.4 and -0.18 [M/H]/kpc for the Draco, Sextans and Hercules dSph galaxies, respectively.

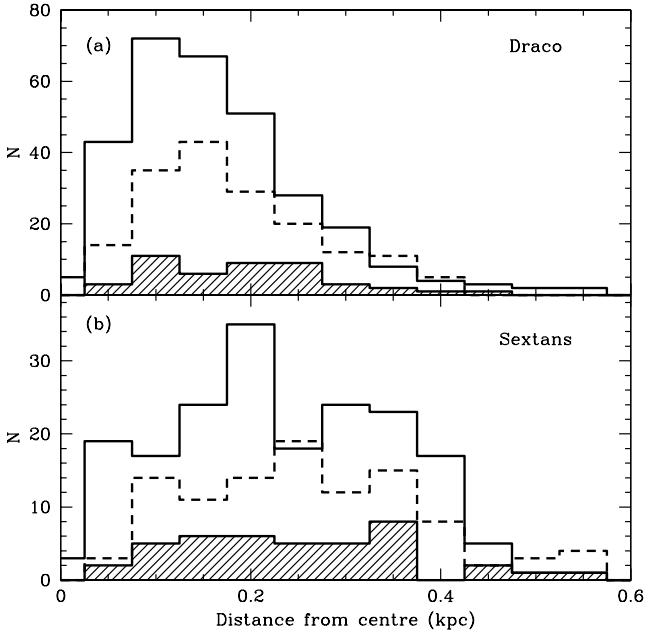

Fig. 17. Distance from centre distributions for the Draco and Sextans dSph galaxies, as indicated. The solid lines mark the distribution for RGB stars. The dashed lines indicate the distribution for the RHB and the shaded histogram for the BHB.

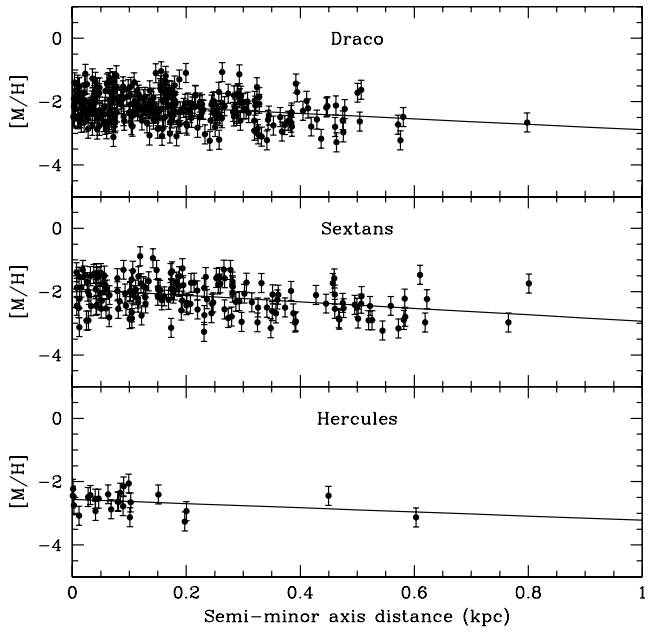

Fig. 16. [Fe/H] vs. the semi-minor axis distance for the Draco, Sextans and Hercules dSph galaxies, as indicated. The solid lines indicate the least-squares fits. The metallicity gradients are -0.9, -1.0 and -0.66 [M/H]/kpc for Draco, Sextans and Hercules, respectively.

8. Population gradients

In Sect. 5.2 we identified a wealth of HB stars in the Draco and Sextans dSph galaxies. HB stars are in general older than ∼ 10 Gyrs, and have He-core burning. The BHB and RHB stars occupy the region blue-wards, and red-wards, of the RR Lyrae instability strip and the RHB, respectively, in a colour-magnitude diagram. In Sect. 5.2 we used the classification from Schuster et al. (2004) to separate the BHB from the RHB (limit at $(b-y)_0 \sim 0.1$). However, as can be seen in Fig. 9b, the RR Lyrae instability strip is more likely to be at $(b-y)_0 \sim 0.2$. Thus, henceforth, we define HB stars with $(b-y)_0 < 0.2$ as BHB, and HB stars with $(b-y)_0 > 0.2$ as RHB. Radial gradients, where the RHB stars are more concentrated toward the centre, for the HB morphology have been reported for Local Group dSph galaxies (see, e.g., Da Costa et al. 1996; Hurley-Keller et al. 1999). In Fig. 17 we show the distance distributions of RHB and BHB in the Draco and Sextans dSph galaxies. Additionally, for comparison, we show the distribution of RGB stars. Unfortunately, The sample of HB stars for the Hercules and UMa II dSph galaxies were not large enough for similar analysis. We find that, for the Draco dSph galaxy, the distance distribution of BHB stars are flatter than the distance distribution of RHB stars, i.e., the distribution of RGB and RHB stars for Draco are similar. However, such a trend is not observable in the Sextans. Indeed, the RHB, BHB and RGB distributions appear to have a similar profile for the Sextans, although the distribution of RGB stars has a sharper cut-off at ∼ 0.42 kpc. We interpret the distance distributions for the Draco dSph galaxies as an indication of a population gradient.

9. The Ursa Major II dSph galaxy

The Ursa Major II dSph galaxy was discovered as a localised stellar over-density in the Sloan Digital Sky Survey (SDSS) (Zucker et al. 2006a). With a total luminosity of only $4 \cdot 10^3\, L_\odot$ (see Table 2), it is one of the faintest dSph galaxies in the Local Group (e.g., Muñoz et al. 2010). Additionally, at a distance of about 30 kpc, it is situated much closer to the Milky Way centre than the other dSph galaxies in this study (compare Table 2). Indeed, using deep CFHT/MegaCam photometry of the UMaII

dSph galaxy Muñoz et al. (2010) was able to conclude that the UMa II shows signs of ongoing tidal interaction with the Milky Way.

9.1. Identifying the Ursa Major II stars

9.1.1. Members based on Strömgren photometry

In Sect. 5.1 we identified RGB members in the Draco, Sextans, Hercules and UMa II dSph galaxies. We note that the search for RGB stars in the UMa II dSph galaxy was much more difficult than for the other fields. This may not come as a surprise given that the stellar content of the UMa II is estimated to be almost ten times as low as for the Hercules dSph galaxy (Martin et al. 2008), which has relatively few RGB stars as compared to Draco and Sextans. In Fig. 21a and 21b, we summarise our search for RGB and HB member of the UMa II dSph galaxy in colour-magnitude diagrams. Additionally, for clarity we draw a horizontal line with y_0 as the average of the HB stars found in Sect. 5.2. With a distance of about 30 kpc, the tip of the RGB for the UMa II should appear at $y_0 \sim 14.5$. However, in the magnitude bin $14.5 < y_0 < 17$, where the majority of the RGB stars above the HB are expected, we found only a few RGB stars. We note that there are three stars at $y_0 \sim 15$ that deviate significantly from the expected RGB. They are about 1 to 2 magnitudes too bright as compared to the isochrone (based on a fit to the turn-off, see below).

In Adén et al. (2009) we investigated the probability of finding foreground RGB stars towards the Hercules dSph galaxy. We found that a Besançon model (Robin & Creze 1986) predicted about 15 RGB stars towards the Hercules dSph galaxy. A Besançon model in the direction of the UMa II dSph galaxy gives about 20 RGB stars in the colour-magnitude region $15 < y_0 < 21$ and $0.3 < (b-y)_0 < 0.8$. However, given that the Hercules dSph galaxy is situated much further away (compare Table 2) than the UMa II, and therefore has fainter RGB stars on average, the foreground RGB stars were easier to disentangle from the Hercules RGB stars since they appeared in brighter magnitudes as compared to the Hercules RGBs. For the UMa II this is difficult given that the UMa II RGB is expected to appear at $y_0 \sim 14.5$. Our conclusion is that the stars identified as UMa II RGB stars most likely suffer from foreground contaminating RGB stars that belong to the Milky Way. Given the modest number of RGB stars identified in the UMa II, this contamination is not negligible.

9.1.2. Comparison with radial velocity membership

Martin et al. (2007) have obtained stellar spectra for 54 stars in the direction of the UMa II dSph galaxy. In order to avoid including foreground dwarf stars they used measurements of the radial velocity and the strength of the Na I lines at 818.3 and 819.5 nm to distinguish between dwarf and giant stars. As discussed in Schiavon et al. (1997) the strength of these lines depend on the gravity of the star. Hence, it enables a distinction between dwarf and giant stars. Out of the 54 stars, 11 were identified as UMa II giant members based on the measurements of the strength of the Na I lines and the radial velocities.

For the stars in common between our photometric study and Martin et al. (2007), we show a c_1 vs. $(b-y)$ diagram in Fig. 18a. From this comparison we find that about 5 of the stars considered as giants in Martin et al. (2007) are likely dwarf stars. Additionally, many of the remaining 6 stars are likely to be subgiant or turn-off stars. This is unfortunate since the Strömgren c_1 diagram is most efficient at disentangling giant stars from dwarf stars at the tip of the RGB (i.e., above the HB). Thus, it is difficult to further clean the sample of members stars presented in Martin et al. (2007). However, we can confirm that about 3 to 5 of the stars in Martin et al. (2007) are likely RGB stars.

We find one star in common, INT40282, that has been identified as an RGB star in both studies. Additionally, one of the stars that fall in the RGB region, INT40874, was excluded from the RGB star sample in this study since it is too faint for our membership determination (see Fig. 18). This star is likely a foreground dwarf star as we find it unlikely that its y_0 magnitude is off by 5 magnitudes (compare Fig. 18b). Also, for star INT40874, Martin et al. (2007) estimated the radial velocity to $502 \pm 10\,\mathrm{km\,s^{-1}}$, which is much higher than the systemic velocity ($-116.5\,\mathrm{km\,s^{-1}}$, Simon & Geha 2007) for the UMa II dSph galaxy.

In a recent study, Frebel et al. (2010) obtained high-resolution spectra for 4 stars, assumed to be UMa II RGB member stars. All of these stars have radial velocities that fall within the 3σ limit of the systemic velocity ($-116.5\,\mathrm{km\,s^{-1}}$, Simon & Geha 2007) of the UMa II dSph galaxy. However, based on distance determination for the stars, derived from the surface gravity, they concluded that one of the stars is not an RGB member of the UMa II dSph galaxy, but instead a dwarf star that belongs to the Milky Way. As can be seen in Fig. 18a, the location of this star in the c_1 vs. $(b-y)$ diagram agrees with their conclusion. For the three remaining star, we agree that they are RGB stars that belong to the UMa II galaxy.

9.1.3. Final member list

Our final sample of RGB and HB UMa II member stars are listed in Table 9. We note that we are in agreement with the stars identified as members in Frebel et al. (2010). These 3 stars are all bright and separate well from the foreground contaminating dwarfs. However, as discussed in Sect. 9.1.2, we are not able to provide a good identification analysis of the stars in Martin et al. (2007) since many of those stars are much bluer than our blue limit for RGB star identification and Fig. 18 shows that most of these are likely dwarf or subgiant stars. Of the 20 stars identified as RGB stars using the Strömgren c_1 diagram, 3 stars deviate from the RGB in a colour-magnitude diagram. These stars are removed from the sample since they are believed to be foreground contaminating RGB stars.

9.2. The metallicity for the UMa II

9.2.1. Based on RGB stars

In Sect. 7.3 we studied the MDFs for the Draco, Sextans and Hercules dSph galaxies. In this section, we do the same for the UMa II dSph galaxy. In Fig. 19a we show the MDF for the UMa II. We note that there is a significant fraction of stars with [Fe/H]> 0. In Fig. 19b and 19c we show the location of these stars in a colour-magnitude diagram and $c_{1,0}$ vs. $(b-y)_0$, respectively. The stars with [M/H]> 0 preferentially position themselves closer to the metal-rich isochrone as indicated in the $c_{1,0}$ vs. $(b-y)_0$ diagram.

The origin of these stars need an explanation. If they are indeed RGB members of the UMa II dSph galaxy, it would suggest that the UMa II has a metal-rich, super solar, component. Given that no other dSph galaxy has a metal-rich peak with [Fe/H]> 0, we find it less likely that the UMa II would display such a feature, given that it is an ultra-faint dSph galaxy (see, e.g., Grebel

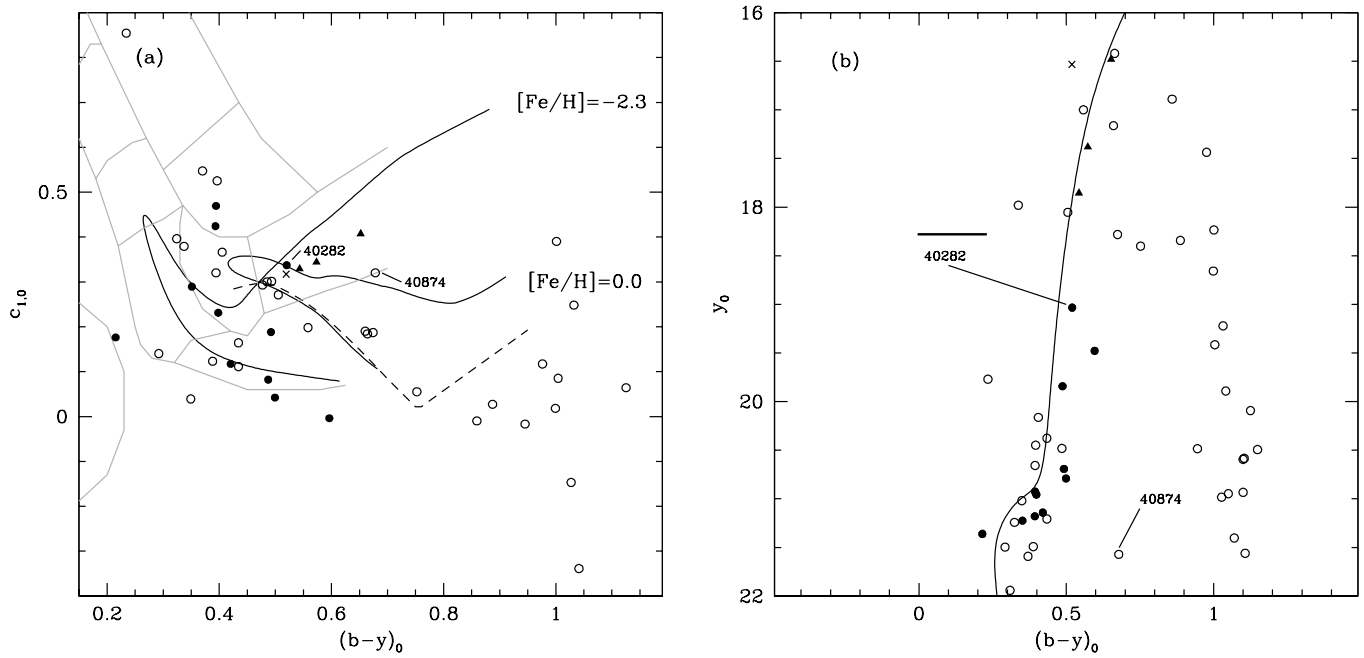

Fig. 18. (a) $c_{1,0}$ vs. $(b-y)_0$ for stars in the direction of the UMa II dSph galaxy for which Martin et al. (2007) and Frebel et al. (2010) have obtained spectra for. The grey solid lines outline the identification scheme for metal-poor stars developed by Schuster et al. (2004), see also Sect. 2. The upper and lower solid lines indicate isochrones for RGB stars by VandenBerg et al. (2006) with colour transformations by Clem et al. (2004). Their metallicities are -2.3 and 0.0 dex, respectively. The dashed line indicates a dwarf star sequence with [Fe/H]=0.0 Árnadóttir et al. (2010). Open circles indicate UMa II non-members, and • indicate UMa II members as determined by Martin et al. (2007). Filled triangles indicate UMa II members, and × indicates a UMa II non-member as determined by Frebel et al. (2010). **(b)** Colour-magnitude diagram for the stars in (a). The solid thick line indicates the location of the HB as determined in Sect. 5.2.

et al. 2003, for a discussion on the luminosity-metallicity relation). Another explanation could be that they are not members of the UMa II dSph galaxy, but instead are foreground contaminating RGB stars. As discussed in Sect. 9.1.1, the contamination of foreground RGB stars towards the UMa II dSph galaxy may not be negligible.

Under the assumption that the remaining RGB stars, i.e., stars with [M/H]< 0, in Fig. 19a belong to the UMa II, we find that the UMa II has a spread in metallicity similar to the spread for the Hercules MDF. The average [M/H] for these stars is –2.6 dex.

As discussed in, e.g., Grebel et al. (2003); Kirby et al. (2011), dSph galaxies follow the metallicity-luminosity relation where the mean metallicity for the galaxy increase with luminosity. In Fig. 20 we show the location of the UMa II dSph galaxy together with the metallicity-luminosity relation derived by Kirby et al. (2011). For the UMa II dSph galaxy, only stars with [M/H]< 0 are considered. We also show the location of the Draco, Sextans and Hercules dSph galaxies. We adopt the luminosities from Table 2. All of the dSph galaxies fit the relation fairly well, albeit with an apparent downward offset for Draco, Sextans and Hercules. Thus, a metallicity-luminosity relation based on our data would be significantly shallower than that derived by Kirby et al. (2011).

9.2.2. Based on Ursa Major II's turn-off

Given the prominent clump of stars at the turn-off for UMa II, we investigate if we are able to determine [Fe/H] for stars in this region. A review of the Strömgren metallicity calibrations for dwarf stars is provided by Árnadóttir et al. (2010). They recommend using the calibration available in Ramírez & Meléndez (2005) for the translation of Strömgren photometry to an estimate of [Fe/H] for dwarf stars. Thus, we adopt this calibration. In Fig. 21a we show the region, indicated by a solid rectangle, that was selected to represent the dwarf stars in the UMa II dSph galaxy. However, as indicated by the amount of stars in neighbouring regions at this magnitude, this area is likely to contain a significant fraction of dwarf stars that do not belong to the UMa II. To put constraints on this problem, we select a second region that we believe is clear of UMa II members. This is indicated in Fig. 9a with a dashed rectangle. In Fig. 9a we show the MDF for these two regions of stars. For the sample of stars in the turn-off region, we see a clear indication of two peaks at [M/H]∼ −0.5 and [M/H]∼ −1.5. By comparing the two distributions we note that the turn-off sample extends to much more metal-poor stars. Thus, one possibility is that the stars in the metal-rich peak of the turn-off sample are the foreground dwarf stars, and the majority of the stars in the metal-poor end belong to the UMa II dSph galaxy.

9.2.3. Discussion

We find that our estimate of [M/H] is in agreement with [Fe/H] as estimated in Frebel et al. (2010) (compare Table 9). Since these stars are included in our sample for the metallicity calibration in Sect. 7.1, this agreement is expected. However, for the star in common, INT40282, between our study and Martin et al. (2007) we find that our estimate is about 1.7 dex more metal-poor. Martin et al. (2007) measured [Fe/H] from the equivalent widths of the Ca II IR triplet lines. The final values of [Fe/H] in Martin et al. (2007) were calculated using the calibration by

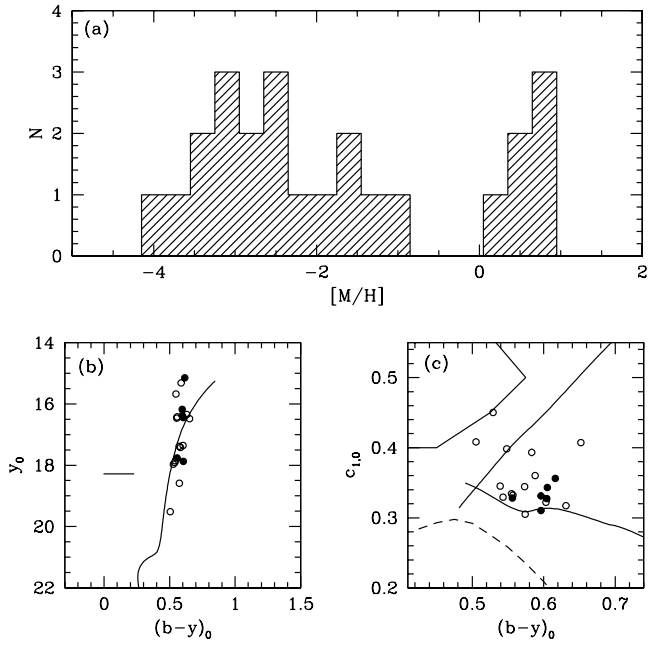

Fig. 19. a) Metallicity histogram for the UMa II dSph galaxy. **b)** Colour-magnitude diagram for the stars identified as RGB stars towards the UMa II. • indicate RGB stars with [M/H]< 0, and open circles indicate RGB stars with [M/H]> 0. **c)** $c_{1,0}$ vs. $(b-y)_0$ diagram for the stars in (b). For a description of the solid lines, dashed line and area marked by solid lines, see Sect. 2.

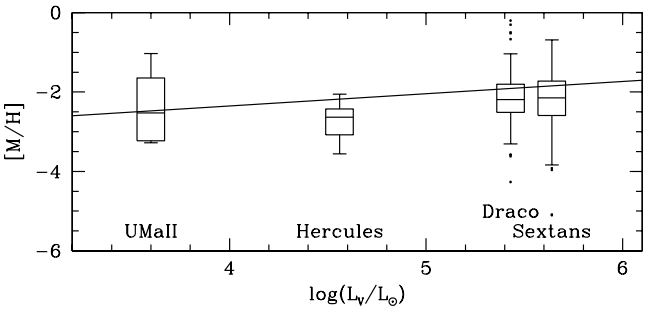

Fig. 20. The [M/H] distribution vs. total luminosity for the Draco, Sextans, Hercules and UMa II dSph galaxies, as indicated. The box-plot for each galaxy indicates the distribution of [M/H] where the central horizontal line represents the median value. The upper and lower quartile are represented by the outer edges of the box, i.e., the box encloses 50 per cent of the sample. The whiskers extend to the farthest data points that lies within 1.5 times the inner quartile distance. Those stars that do not fall within the reach of the whiskers are considered as outliers and are marked by dots. The solid line indicates the metallicity-luminosity relation from Kirby et al. (2011).

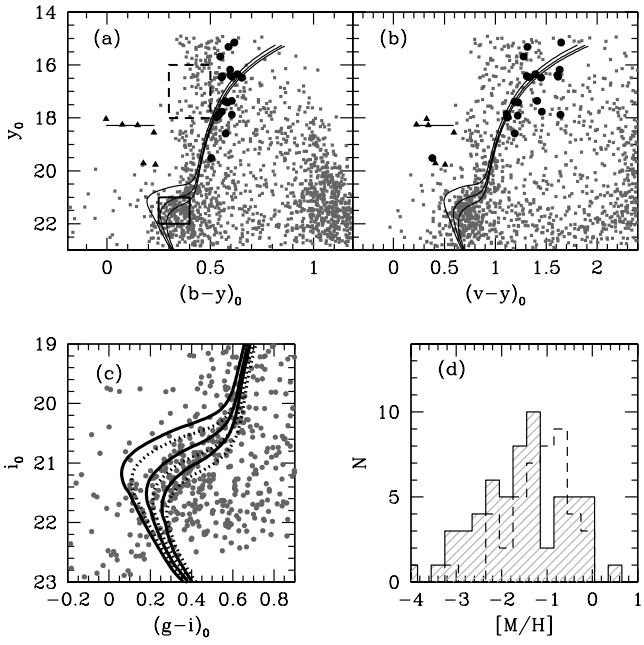

Fig. 21. a) Strömgren colour-magnitude diagram for all stars towards the UMa II dSph galaxy. • are stars identified as RGB stars (see Sect. 5.1). Solid triangles are stars identified as HB stars (see Sect. 5.2). The solid lines indicate 8, 12 and 16 Gyrs old isochrones, from left to right respectively, by VandenBerg et al. (2006) with colour transformations by Clem et al. (2004), with a metallicity of –2.3 dex. The solid rectangle outlines the region for turn-off dwarf stars, and the dashed rectangle shows the region for the selection of foreground dwarf stars. **b)** same as **(a)** but in y_0 vs. $(v-y)_0$ space. **c)** SDSS colour-magnitude diagram for all stars towards the UMa II dSph galaxy. The solid lines indicate 9, 12 and 15 Gyrs old isochrones, from left to right respectively, by Dotter et al. (2008) with colour transformations by Clem et al. (2004), with a metallicity of –2.5 dex. The dashed lines are the same as the solid, however with a metallicity of –2.0 dex. **d)** Metallicity distribution function for stars towards the UMa II dSph galaxy. The shaded histogram is for stars assumed to be turn-off dwarf stars. The dashed histogram is foreground dwarf stars.

Rutledge et al. (1997) onto the metallicity scale of Carretta & Gratton (1997). Thus, one could argue that the discrepancy is not a surprise since the calibration in Rutledge et al. (1997) only extends to [Fe/H] of about −2.4 dex, and is not valid for more metal-poor RGB stars.

In Sect. 9.2.1 we found an average [M/H] for the UMa II dSph galaxy of about −2.6 dex, based on stars identified as UMa II RGB stars. For comparison, in Sect. 9.2.2, we made an attempt to determine [M/H] based on turn-off stars. The MDF for the foreground dwarf stars (dashed line in Fig. 21) extends down to about −2 dex. Thus, based on Fig. 21, one can argue that an average [M/H] less than about −2 dex is more likely. Thus, we find that [M/H] as determined from the RGB stars is in agreement with the average [M/H] as estimated based on the turn-off stars.

9.3. The age of Ursa Major II

Given that the UMa II dSph galaxy is situated much closer than the other dSph galaxies in this study (compare Table 2), it gives us the opportunity to investigate the turn-off dwarf stars in the UMa II. In Fig. 21a and b we can clearly see the position of the turn-off stars at $y_0 \sim 21$. To investigate this further, we include isochrones for RGB stars by VandenBerg et al. (2006), with colour transformations by Clem et al. (2004), with different ages, 8, 12 and 16 Gyr old, in the colour-magnitude diagrams. Based on the analysis of three UMa II RGB stars in Frebel et al. (2010), and three RGB stars in Martin et al. (2007), we choose isochrones with a metallicity of –2.3 dex since this is the average for these six stars. As can be seen in Fig. 21a and 21b, the 8 Gyr old isochrone has a poor fit to the turn-off. Instead, we find that the UMa II dSph galaxy is more likely to be older than 12 Gyrs. To further enhance our study of the age of the turn-off

for UMa II, in Fig. 21c we show the colour-magnitude diagram in the direction of the UMa II dSph galaxy for the SDSS photometric system. In this figure, we have included Darthmouth isochrones (Dotter et al. 2008), with colour transformations by Clem et al. (2004), with different ages, 9, 12 and 15 Gyrs old, and different metallicities, –2.0 and –2.5 dex. We find that the UMa II is likely to be a very old stellar system (older than 12 Gyrs).

10. Summary

We have used Strömgren photometry towards the Draco, Sextans, Hercules and UMa II dSph galaxies to identify RGB and HB that are members of the dSph galaxies. This enabled us to create a clean sample of member stars for each dSph galaxy. To further enhance our analysis, we combined our Strömgren photometry with SDSS photometry.

In Sect. 8 we analysed population gradients in the Draco and Sextans dSph galaxies. We found that the Draco dSph galaxy had a much flatter distribution of RGB and HB stars than Sextans dSph galaxy. Additionally, the distribution of BHB stars in the Draco dSph galaxy is flatter than the distribution of RGB and RHB stars.

We have established a new metallicity calibration that translates Strömgren photometry to an estimate of [Fe/H]. This calibration is valid down to at least [Fe/H]= −3.3 dex. This is more metal-poor than previous similar calibrations.

We have investigated the ability of SDSS *ugriz* filters to identify late K giants. We found that the success rate is about 50 per cent.

We have, for the first time, presented a list of UMa II dSph galaxy members based on an analysis of the evolutionary stage obtained from Strömgren photometry. In detail we provide the following inventory of the UMa II dSph galaxy

- 20 stars as tentative RGB members based on their evolutionary stage, see Sect. 5.1. 3 of these stars deviate from the RGB in a colour-magnitude diagram and are therefore removed from the sample. 5 of the remaining 17 RGB stars have a dubious metallicity, as derived using our calibration, and are therefore removed. Thus, 12 stars remain that are believed to be true RGB members of the UMa II dSph galaxy.
- 4 stars as HB members based on their evolutionary stage, see Sect. 5.2. Based on these stars, we have estimated the mean magnitude of the HB of the UMa II dSph galaxy to $V_0 = 18.3$

Stellar metallicities have been determined using the Strömgren m_1 index with our new calibration that translates $m_{1,0}$ to [Fe/H] for RGB stars (Sect. 7.1). We found a mean metallicity of −2.6 dex for the UMa II dSph galaxy. In addition, we estimated the metallicity of the UMa II dSph galaxy using turn-off stars. We found it to be in agreement with the metallicity as determined using the RGB stars. We also derived metallicities for RGB stars in the Draco, Sextans and Hercules dSph galaxies (Sect. 7.3), using our new metallicity calibration.

Using isochrones, we have determined that the UMa II dSph galaxy is likely to be older than 12 Gyrs.

Acknowledgements. D.A. thanks Jennifer Johnson for her help with the ability of the SDSS *ugriz* filters to identify late K giants. S.F. is a Royal Swedish Academy of Sciences Research Fellow supported by a grant from the Knut and Alice Wallenberg Foundation. Funding for the SDSS and SDSS-II has been provided by the Alfred P. Sloan Foundation, the Participating Institutions, the National Science Foundation, the U.S. Department of Energy, the National Aeronautics and Space Administration, the Japanese Monbukagakusho, the Max Planck Society, and the Higher Education Funding Council for England. The SDSS Web Site is http://www.sdss.org/. The SDSS is managed by the Astrophysical Research Consortium for the Participating Institutions. The Participating Institutions are the American Museum of Natural History, Astrophysical Institute Potsdam, University of Basel, University of Cambridge, Case Western Reserve University, University of Chicago, Drexel University, Fermilab, the Institute for Advanced Study, the Japan Participation Group, Johns Hopkins University, the Joint Institute for Nuclear Astrophysics, the Kavli Institute for Particle Astrophysics and Cosmology, the Korean Scientist Group, the Chinese Academy of Sciences (LAMOST), Los Alamos National Laboratory, the Max-Planck-Institute for Astronomy (MPIA), the Max-Planck-Institute for Astrophysics (MPA), New Mexico State University, Ohio State University, University of Pittsburgh, University of Portsmouth, Princeton University, the United States Naval Observatory, and the University of Washington.

References

Adén, D., Eriksson, K., Feltzing, S., et al. 2011, A&A, 525, A153+
Adén, D., Feltzing, S., Koch, A., et al. 2009, A&A, 506, 1147
Anthony-Twarog, B. J. & Twarog, B. A. 1994, AJ, 107, 1577
Aoki, W., Arimoto, N., Sadakane, K., et al. 2009, A&A, 502, 569
Arce, H. G. & Goodman, A. A. 1999, ApJ, 512, L135
Árnadóttir, A. S., Feltzing, S., & Lundström, I. 2010, A&A, 521, A40+
Battaglia, G., Tolstoy, E., Helmi, A., et al. 2010, MNRAS, 1817
Beers, T. C., Drilling, J. S., Rossi, S., et al. 2002, AJ, 124, 931
Belokurov, V., Walker, M. G., Evans, N. W., et al. 2008, ApJ, 686, L83
Belokurov, V., Walker, M. G., Evans, N. W., et al. 2009, MNRAS, 397, 1748
Belokurov, V., Zucker, D. B., Evans, N. W., et al. 2007, ApJ, 654, 897
Belokurov, V., Zucker, D. B., Evans, N. W., et al. 2006, ApJ, 647, L111
Bonanos, A. Z., Stanek, K. Z., Szentgyorgyi, A. H., Sasselov, D. D., & Bakos, G. Á. 2004, AJ, 127, 861
Bond, H. E. 1980, ApJS, 44, 517
Calamida, A., Bono, G., Stetson, P. B., et al. 2007, ApJ, 670, 400
Carretta, E. & Gratton, R. G. 1997, A&AS, 121, 95
Cayrel, R., Depagne, E., Spite, M., et al. 2004, A&A, 416, 1117
Clem, J. L., VandenBerg, D. A., Grundahl, F., & Bell, R. A. 2004, AJ, 127, 1227
Cohen, J. G. & Huang, W. 2009, ApJ, 701, 1053
Coleman, M. G., de Jong, J. T. A., Martin, N. F., et al. 2007, ApJ, 668, L43
Da Costa, G. S., Armandroff, T. E., Caldwell, N., & Seitzer, P. 1996, AJ, 112, 2576
Dotter, A., Chaboyer, B., Jevremović, D., et al. 2008, ApJS, 178, 89
Faria, D., Feltzing, S., Lundström, I., et al. 2007, A&A, 465, 357
Ferrara, A. & Tolstoy, E. 2000, MNRAS, 313, 291
Frebel, A., Simon, J. D., Geha, M., & Willman, B. 2010, ApJ, 708, 560
Gratton, R. G., Sneden, C., Carretta, E., & Bragaglia, A. 1999, VizieR Online Data Catalog, 335, 40169
Grebel, E. K., Gallagher, III, J. S., & Harbeck, D. 2003, AJ, 125, 1926
Grebel, E. K. & Richtler, T. 1992, A&A, 253, 359
Hauck, B. & Mermilliod, M. 1998, A&AS, 129, 431
Hilker, M. 2000, A&A, 355, 994
Howell, S. B. 1989, PASP, 101, 616
Hurley-Keller, D., Mateo, M., & Grebel, E. K. 1999, ApJ, 523, L25
Irwin, M. & Lewis, J. 2001, New Astronomy Review, 45, 105
Kirby, E. N., Lanfranchi, G. A., Simon, J. D., Cohen, J. G., & Guhathakurta, P. 2011, ApJ, 727, 78
Koch, A., McWilliam, A., Grebel, E. K., Zucker, D. B., & Belokurov, V. 2008, ApJ, 688, L13
Lind, K., Charbonnel, C., Decressin, T., et al. 2010, ArXiv e-prints
Lind, K., Primas, F., Charbonnel, C., Grundahl, F., & Asplund, M. 2009, VizieR Online Data Catalog, 350, 30545
Martin, N. F., de Jong, J. T. A., & Rix, H. 2008, ApJ, 684, 1075
Martin, N. F., Ibata, R. A., Chapman, S. C., Irwin, M., & Lewis, G. F. 2007, MNRAS, 380, 281
Mateo, M. L. 1998, ARA&A, 36, 435
Muñoz, R. R., Geha, M., & Willman, B. 2010, AJ, 140, 138
Olsen, E. H. 1983, A&AS, 54, 55
Olsen, E. H. 1984, A&AS, 57, 443
Olsen, E. H. 1993, A&AS, 102, 89
Olsen, E. H. 1994, A&AS, 104, 429
Olsen, E. H. 1995, A&A, 295, 710
Perryman, M. A. C., Lindegren, L., Kovalevsky, J., et al. 1997, A&A, 323, L49
Ramírez, I. & Meléndez, J. 2005, ApJ, 626, 446
Robin, A. & Creze, M. 1986, A&A, 157, 71
Rutledge, G. A., Hesser, J. E., & Stetson, P. B. 1997, PASP, 109, 907
Schiavon, R. P., Barbuy, B., Rossi, S. C. F., & Milone, A. 1997, ApJ, 479, 902
Schlegel, D. J., Finkbeiner, D. P., & Davis, M. 1998, ApJ, 500, 525

Schuster, W. J., Beers, T. C., Michel, R., Nissen, P. E., & García, G. 2004, A&A, 422, 527
Schuster, W. J. & Nissen, P. E. 1988, A&AS, 73, 225
Searle, L. & Zinn, R. 1978, ApJ, 225, 357
Shetrone, M. D., Côté, P., & Sargent, W. L. W. 2001, ApJ, 548, 592
Simon, J. D. & Geha, M. 2007, ApJ, 670, 313
Sneden, C., Pilachowski, C. A., & Kraft, R. P. 2000, AJ, 120, 1351
Springel, V., White, S. D. M., Jenkins, A., et al. 2005, Nature, 435, 629
Starkenburg, E., Hill, V., Tolstoy, E., et al. 2010, A&A, 513, A34+
Strömgren, B. 1963, QJRAS, 4, 8
Tafelmeyer, M., Jablonka, P., Hill, V., et al. 2010, A&A, 524, A58+
Tollerud, E. J., Bullock, J. S., Strigari, L. E., & Willman, B. 2008, ApJ, 688, 277
VandenBerg, D. A., Bergbusch, P. A., & Dowler, P. D. 2006, ApJS, 162, 375
Walker, M. G., Mateo, M., Olszewski, E. W., et al. 2006, AJ, 131, 2114
Walker, M. G., Mateo, M., Olszewski, E. W., et al. 2009, ApJ, 704, 1274
Walsh, S. M., Jerjen, H., & Willman, B. 2007, ApJ, 662, L83
Yasuda, N., Fukugita, M., & Schneider, D. P. 2007, AJ, 134, 698
Zucker, D. B., Belokurov, V., Evans, N. W., et al. 2006a, ApJ, 650, L41
Zucker, D. B., Belokurov, V., Evans, N. W., et al. 2006b, ApJ, 643, L103

Appendix A: Finding the RGB stars using Strömgren photometry

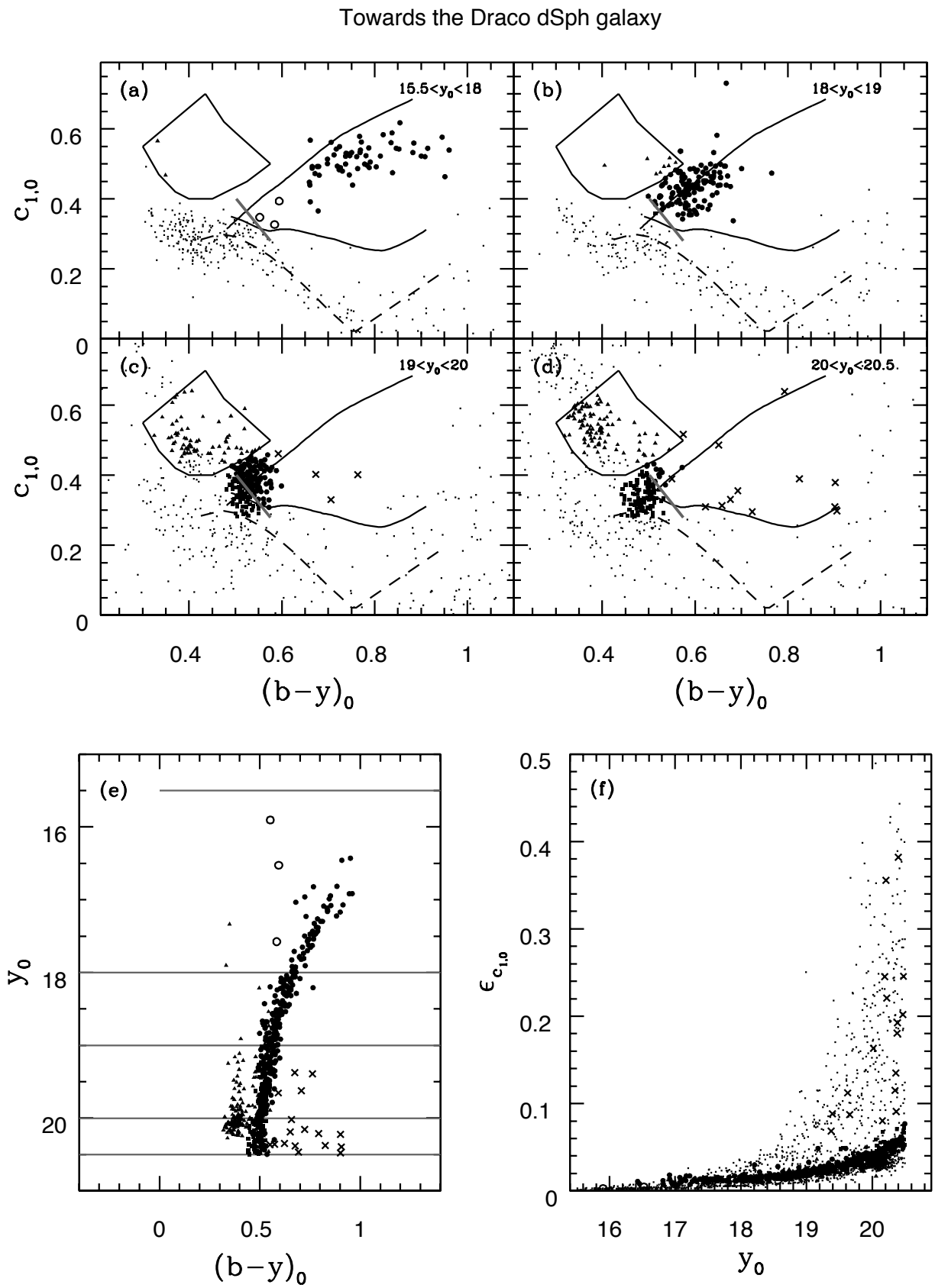

Fig. A.1. a), b), c) and **d)** $c_{1,0}$ vs. $(b-y)_0$ diagram for stars in the direction of the Draco dSph galaxy. The range of magnitude is indicated at the top of each panel. Dots are stars within the given magnitude range. • are stars that fall within the RGB region. ○ indicate stars that fall within the RGB region, but they deviate from the bulk of the RGB stars as outlined by •. × mark stars that fall in the RGB region, but have a large error (see **(f)**). Filled squares mark stars that fall in region occupied by both RGB and dwarf stars. Filled triangles indicates stars that fall in the RHB-AGB region. The upper and lower solid lines indicate isochrones for RGB stars by VandenBerg et al. (2006) with colour transformations by Clem et al. (2004). Their metallicities are -2.3 and 0.0 dex, respectively. The dashed line indicates a dwarf star sequence with [Fe/H]=-1.0 (Árnadóttir et al. 2010). The thick grey line marks the empirically determined blue limit for the foreground contamination. The box outlined by a solid black line indicates the region for RHB-AGB stars. **e)** Colour-magnitude diagram for the stars highlighted above. The solid lines mark the range of magnitude. Symbols as given above. **f)** $\epsilon_{c_{1,0}}$ vs. y_0. Symbols as given above.

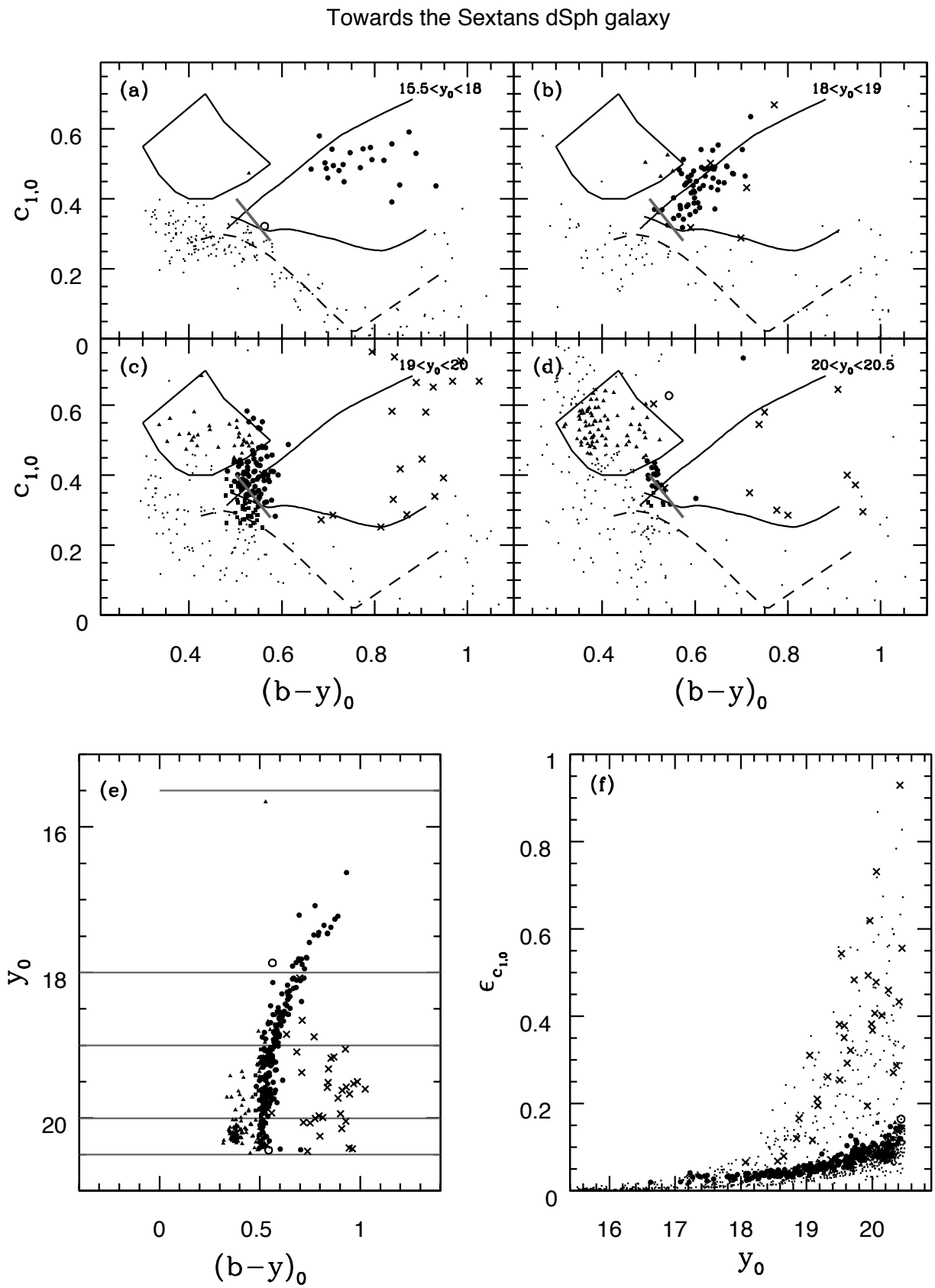

Fig. A.2. Same as for Fig. A.1, but for stars towards the Sextans dSph galaxy.

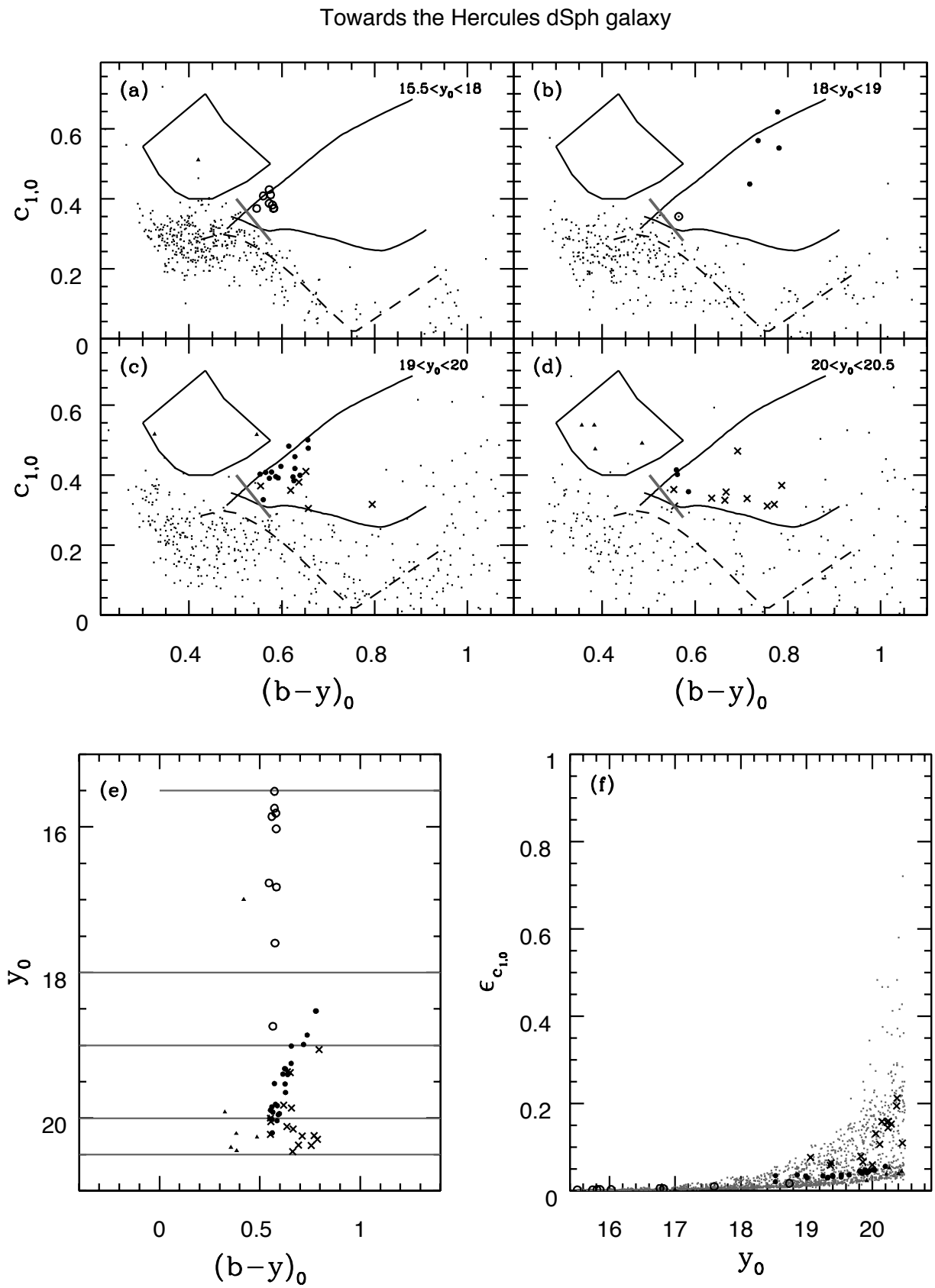

Fig. A.3. Same as for Fig. A.1, but for stars towards the Hercules dSph galaxy.

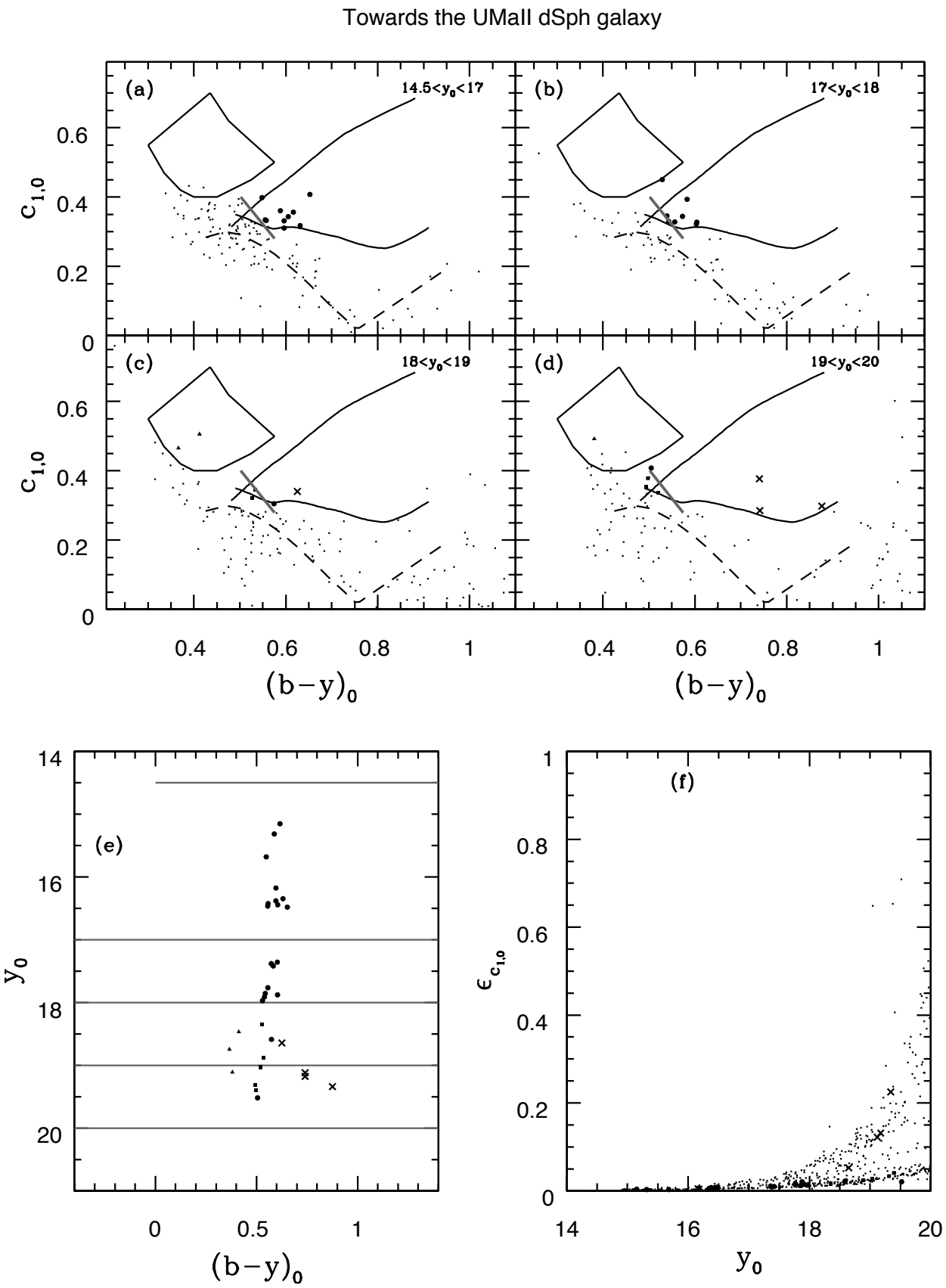

Fig. A.4. Same as for Fig. A.1, but for stars towards the UMa II dSph galaxy.

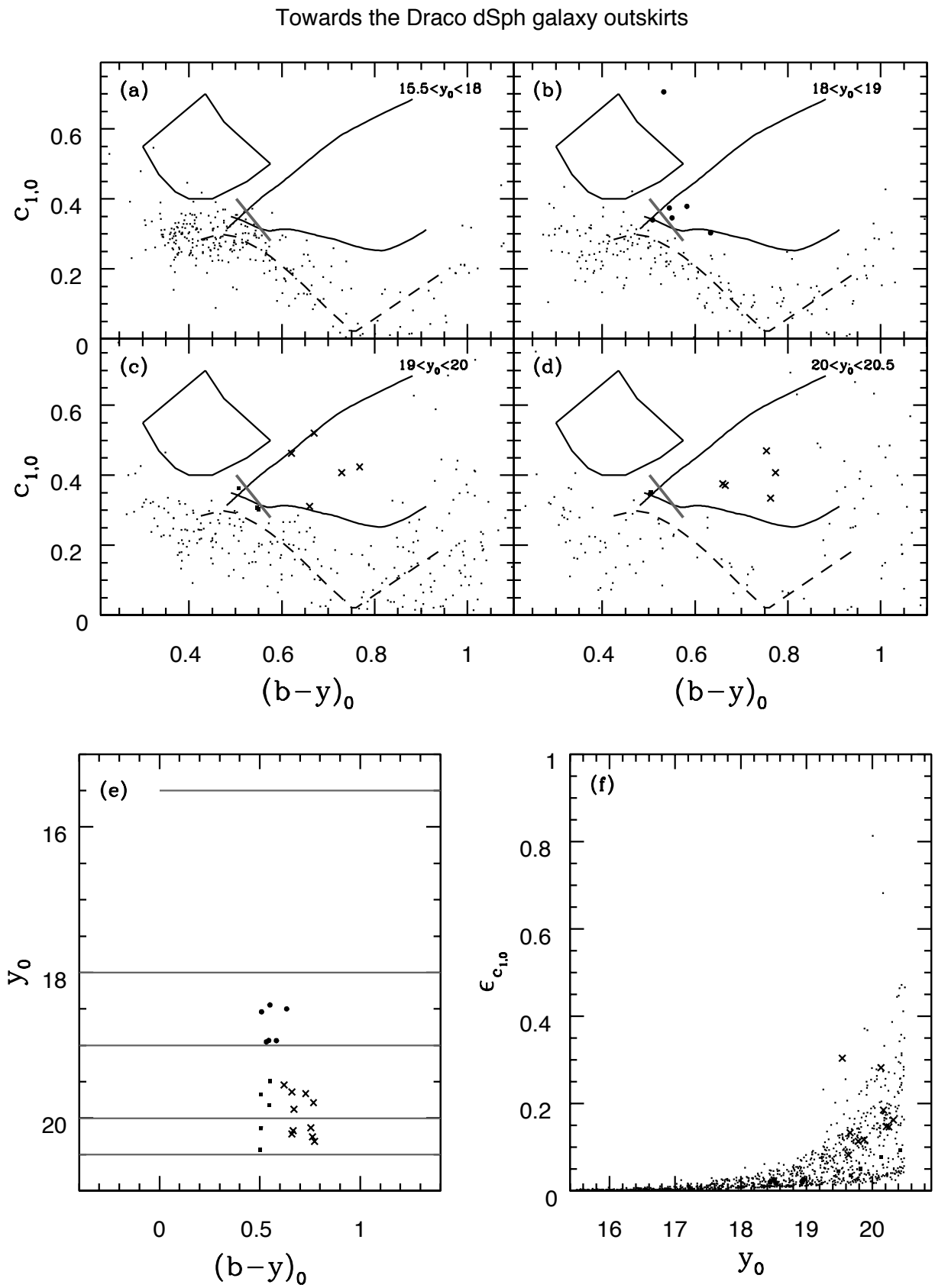

Fig. A.5. Same as for Fig. A.1, but for stars towards the Draco dSph galaxy outskirts.

Table 9. Ursa Major II dSph galaxy members.

ID	RA(2000)	DEC(2000)	*y*	*b*	*v*	*u*	[M/H]		[Fe/H]	Note
10140	133.10652	62.98562	18.06	18.68	19.63	20.92	0.28	RGB	...	*c*
10395	132.83014	62.98528	15.97	16.59	17.36	18.55	-1.51	RGB	...	*d*
10461	132.76676	62.96444	18.20	18.81	19.54	20.62	-1.91	RGB	...	...
10575	132.62416	62.89722	18.88	19.52	20.18	21.17	-3.23	RGB	...	...
20009	132.34902	63.21586	18.17	18.84	19.92	21.35	0.72	RGB	...	*c*
20088	132.08378	63.17971	16.67	17.34	18.40	19.78	0.66	RGB	...	*c*
20195	132.32180	63.14079	16.74	17.41	18.47	19.88	0.45	RGB	...	*c*
20387	132.33224	63.05042	16.76	17.38	18.21	19.39	-1.03	RGB	...	...
30663	132.72230	63.32804	15.61	16.27	17.04	18.19	-2.24	RGB	...	*d*
30679	132.71777	63.39723	17.65	18.32	19.18	20.37	-1.65	RGB	...	...
30725	132.67002	63.39434	16.64	17.34	18.14	19.28	-2.57	RGB	...	...
40065	133.24597	63.09851	16.77	17.49	18.34	19.60	-2.52	RGB	-2.34	*a*
40181	133.13957	63.08365	17.67	18.32	18.98	20.00	-3.23	RGB	-3.23	*a*
40248	133.08452	63.09378	16.72	17.34	18.14	19.28	-1.43	RGB	...	...
40323	133.01025	63.16333	16.47	17.13	18.21	19.64	0.89	RGB	...	*c*
40703	132.66468	63.15154	15.45	16.13	17.21	18.65	0.43	RGB	...	*c*, *d*
40712	132.65636	63.16910	18.26	18.86	19.50	20.60	-2.79	RGB	...	...
40861	132.52090	63.16877	17.71	18.36	19.05	20.14	-3.10	RGB	...	...
40935	132.47261	63.13937	18.15	18.76	19.37	20.33	-3.28	RGB	-3.10	*a*
40157	133.17123	63.15499	19.60	20.17	20.69	21.58	-3.57	RGB2	...	...
40282	133.05116	63.09313	19.33	19.91	20.48	21.39	-3.53	RGB2	-1.80	*b*
40312	133.02236	63.11373	19.69	20.25	20.85	21.83	-2.76	RGB2	...	...
40359	132.97759	63.16838	18.64	19.24	19.88	20.87	-2.62	RGB2	...	...
40480	132.86818	63.05665	19.17	19.77	20.32	21.24	-3.86	RGB2	...	...
20509	132.24149	62.97757	18.84	19.14	19.55	20.74	...	HB	...	...
20622	132.28985	62.90170	18.33	18.40	18.77	18.96	...	HB	...	...
20657	132.17906	62.88195	18.57	18.79	19.03	20.50	...	HB	...	...
40379	132.95696	63.06244	20.06	20.36	20.68	21.87	...	HB	...	...
40422	132.91973	63.17863	20.01	20.25	20.53	21.79	...	HB	...	...
40465	132.87424	63.10475	18.55	18.69	18.89	20.36	...	HB	...	...

Column 1 lists the INT ID. Column 2 and 3 list the coordinates. Column 4 to 7 list the Strömgren magnitudes *y*, *b*, *v* and *u*. Column 8 lists the photometric metallicity as derived in Sect. 9.2. Column 9 lists the evolutionary stage of the star. Note that RGB2 mark stars that are bluer than the blue limit for membership identification (see Sect. 5). Column 10 lists the spectroscopic [Fe/H], if available. Column 11 Notes: *a*) [Fe/H] as determined in Frebel et al. (2010); *b*) [Fe/H] as determined in Martin et al. (2007); *c*) Possible foreground stars given that [M/H]>0 (see Sect. 9.1.1); *d*) Possible foreground stars given that they deviate significantly from the RGB in a colour-magnitude diagram.